UNIVERSITY OF TECHNOLOGY SYDNEY
Faculty of Engineering and Information Technology

Analysis of Uncertainty for Dynamic Pricing: Models, On-demand Attractors, and Artificial Chaos

by

Shuixiu Lu

A Thesis Submitted in Fulfillment of the Requirements for the Degree

Doctor of Philosophy

Sydney, Australia

August, 2022

Certificate of Original Authorship

I, Shuixiu Lu, declare that this thesis is submitted in fulfilment of the requirements for the award of Doctor of Philosophy in the Faculty of Engineering and Information Technology at the University of Technology Sydney.

This thesis is wholly my own work unless otherwise referenced or acknowledged. In addition, I certify that all information sources and literature used are indicated in the thesis.

This document has not been submitted for qualifications at any other academic institution. This research is funded by a scholarship from Southern University of Science and Technology and a UTS FEIT International Research Scholarship. This research is supported by the Australian Government Research Training Program.

SIGNATURE: Production Note: Signature removed prior to publication.

[Shuixiu Lu]

DATE: 19th August, 2022

Acknowledgments

Between August 2017 and August 2021, I concentrated my efforts and attention solely on completing this thesis. Everyday conversations with my family, the supervisor panel, colleagues, and friends make the four years memorable. Their valuable help makes a smooth completion of this thesis.

I would like to thank my supervisor panel. A/Prof. Sebastian Oberst spent thousands hours in discussing every detail of this thesis, including the methods, the arguments, the writings, and the structures of the whole thesis and individual chapters. Thanks to, A/Prof. Oberst, for constantly critical reviews and challenging my results. Thanks to Prof. Georgios Theodoropoulos, for letting me realize "the power of now". Thanks to Dr. Guoqiang Zhang, for fruitful discussions on machine learning methods and for reviewing my work. Thanks to Dr. Zongwei Luo, for giving me the freedom to study a new research domain and for initializing the PhD program.

Thanks to my former supervisors of Xiamen University. Prof. Shuihua Han and Prof. Bo Zhou encouraged my pursuit of a PhD and initialized the research topic in dynamic pricing problems. Thanks to, Prof. Han and Prof. Zhou, for the amazing insights that help me decide and for letting me know what more I could achieve.

I would like to thank two autonomous reviewers of PNAS for their valuable and insightful comments on Chapter 5. The use of the both, a flow and a map, for experiments

is to address their comments. I would also like to thank Prof. Joseph Lai, Prof. Norbert Hoffmann, and Dr. Merten Stender. In the seminar about machine learning methods applied to complex dynamics, their advice on machine behaviors was highly appreciated.

I would like to thank the members of Georgios Theodoropoulos's lab. Yaru Zhao, Nan Zhang, Zhengchang Hua, and Suyi Chen. Everyday conversations and warm cares made me be a member of a group and enjoyed every minute of it.

To my friends. Thank you, Yiqing, for posting PPEs from China when they were diÿcult to be bought in Sydney in March 2020. Those PPEs reduced a lot of my fears and anxieties when the border was suddenly closed. Thank you, Caiqin, for trivial WeChat and for standing firm. Thank you, Yixin, Lin, Lingling, Qing, Xiaocui, Chun, Bin, and Qin, for persistent help and encouragement.

Last but not least, I thank my family for unconditional and unending support and for daily trivial talkings regardless of differences in time zones. You laid and have become the foundations of those years. Most importantly, this thesis is dedicated to you, Chahua Liu, Jianping Lu, Shuihong Lu, and Yan Yao.

Abstract

Dynamic pricing is a pricing strategy that adapts and optimizes prices based on information about demand. The optimization models interactions between price and demand. Uncertain demand poses a challenge in the modeling. In addressing the uncertainty, stochastic demand is widely assumed. From dynamical systems' perspective, nonlinear interactions between variables yield a rational route that can exhibit uncertainty. However, uncertain demand because of nonlinear interactions remains to be elucidated.

This thesis analyzes uncertain demand from theoretical and empirical perspectives. A theoretical model addresses a hypothetically rational route to uncertain demand. The rational route has discontinuities in demand functions and optimizations. By a bifurcation analysis, the theoretical impacts of discontinuous interactions are investigated. A reconstruction of real-life on-demand attractor addresses a data-driven identification of uncertain demand. Recurrence-based attractor reconstruction is proposed and applied on empirical data from RideAustin, a company providing ride share service in the city of Austin, Texas, the United States. Recurrence plots and Pareto optimality are applied to find optimal embedding and time delay dimensions. The ones under which recurrence plots yield optimal recurrence quantification measures, the determinism and the trapping time, are chosen for an attractor reconstruction.

Border collision bifurcations are observed from the theoretical mode, justifying dynamic pricing from dynamical systems' perspective. A period-7 limit cycle is recon-

structed from empirical data. Results suggest that nonlinear interactions could cause uncertain demand of which a rational route is a constituent part. The findings emphasize data-driven modeling of uncertain demand. For optimal revenue, demand dynamics should be identified.

Finally, uncertainty in deterministic chaos or dynamic pricing is increasingly analyzed by machine learning methods. However, for an artificial system, a system that employs machine learning methods for mimicking deterministic chaos, the role of initial conditions remains unclear. This thesis analyzes the sensitive dependence of an artificial system on initial conditions. Nonlinear time series analysis is introduced to study machine behavior, the behavior of an artificial system under varying initial conditions. We observe that machine behaviors coincide chaotic trajectories, however, alter original basins. Garbled symbolic dynamics is observed, further indicating that a coincidence of a single chaotic trajectory could mislead conclusions. The results highlight that when machine learning meets complex dynamics, an artificial system should be performed under varying initial conditions, instead of a single chaotic trajectory. Machine behaviors would help showing and comparing the sensitive dependence on initial conditions between a mimicked chaotic and an artificial systems.

List of Publications

Related to the Thesis :

Journal Papers

J-1. **Lu S**, Oberst S, Zhang G, Luo Z (2019). "Bifurcation analysis of dynamic pricing processes with nonlinear external reference effects", *Communications in Nonlinear Science and Numerical Simulation*, 79:104929. Doi: 10.1016/j.cnsns.2019.104929.

Conference Papers

C-1. **Lu S**, Oberst S, Zhang G, Luo Z. "Comparing complex dynamics using machine learning-reconstructed attracting sets", *Colloquium on "Irregular Engineering Oscillations and Signal Processing"*. Hamburg, Germany, Sep., 2018. Doi: 10.13140/RG.2.2.27988.96647.

C-2. **Lu S**, Oberst S, Zhang G, Luo Z. "Period adding bifurcations in dynamic pricing processes", *2019 IEEE Conference on Computational Intelligence for Financial Engineering & Economics (CIFEr)*. Shenzhen, China, 2019, pp. 1-6. Doi: 10.1109/CIFEr.2019.8759118.

C-3. **Lu S**, Oberst S, Zhang G, Luo Z. "Capturing determinism buried in surrogate time series of dynamic pricing processes: applying transition networks on order pattern

plots", 8^{th} *International Symposium on Recurrence Plots*. Zhenjiang, China, Aug. 2019.

Book Chapter

B-1. **Lu S**, Oberst S, Zhang G, Luo Z. "Novel Order Patterns Recurrence Plot-Based Quantification Measures to Unveil Deterministic Dynamics from Stochastic Processes", *Theory and Applications of Time Series Analysis*. 2019, pp 57–70. editor: Valenzuela, Olga, Rojas, Fernando, Pomares, Héctor, and Rojas, Ignacio. Springer International Publishing (Cham). Doi: 10.1007/978-3-030-26036-1_5.

Poster

P-1. **Lu S**, Luo Z, Zhang G, Oberst S. "Order pattern recurrence plots: unveiling determinism buried in noise", University of Technology Sydney, Faculty of Engineering and IT Research Showcase. Sydney, Australia. Jun., 2018. Doi: 10.13140/RG.2.2.32482.02249.

Fundings

F-1. Visualizing the Topology of Irregular Oscillations of Complex Dynamics. Funding provider: UTS Data Arena.

F-2. A Scholarship of the 8^{th} International Symposium on Recurrence Plots (2019). Funding provider: Jiangsu University of Science and Technology.

F-3. HDR Tech Lab Collaboration Grant. Funding provider: UTS Tech Lab.

Contents

List of Figures

Figure **Page**

List of Tables

Table **Page**

Chapter 1

Introduction

Recurrence is a fundamental property of many real-life dynamical systems. Uncertainty is an inherent problem to the dynamical system. The subject of this thesis is deterministic chaos and nonlinear time series analysis in the application of dynamic pricing problems. A theoretical model is provided to justify dynamic pricing from nonlinear dynamical systems' perspective and to fresh knowledge about uncertain demand. Recurrence-based attractor reconstruction is then proposed to identify demand dynamics for data-driven dynamic pricing. Finally, the behavior of an artificial intelligence system in mimicking deterministic chaos is studied.

1.1 Dynamic pricing

Price, *demand*, and *supply* are the three variables that affect social behaviors of economically acting human individuals [297, 361]. The buying and the selling decisions, for example, are affected. While demand is related to consumers' buying behavior, supply is related to sellers' selling behavior. Price is the critical variable that connects and interacts with both demand and supply. In a transaction, consumers are a price-taker, and sellers are a price-maker. A seller makes a pricing decision and sets the price of goods or services [297, 361].

Dynamic pricing is concerned with the price that a seller sets for optimal revenue [70, 297, 361]. Different from an equilibrium price, dynamic pricing utilizes a demand-based pricing strategy. An equilibrium price is the price where the quantity demanded equals the quantity supplied. Dynamic pricing adjusts a price of an individual unit of supply based on real-time information of demand [232]. Increasing availability in data improves revenue that a seller realizes from dynamic pricing [45, 119, 297, 361]. Airline industry of the United States initialized dynamic pricing in the late 1970s [73, 297, 361]. Since then many businesses of our daily routes have implemented dynamic pricing, including energy providers [114, 182], retailers [209], and the hospitality industry [2].

For a seller, improving revenue is one of the strongest motivations for an implementation of dynamic pricing. As shown by Cohen et al. [85], an increase of 3% profit can be achieved from dynamic pricing for a grocery retailer in the United States. Kemper and Breuer [190] show that dynamic pricing could eÿcien tly improve the revenue of FC Bayern Munich, the famous soccer club in Bavaria, Germany. The empirical studies highlight that consumers' willingness to pay is at least 75% higher than the current price for some game [190]. Implementing dynamic pricing is thus economically inspired. From empirical evidence Fisher et al. [130] demonstrate that an 11% increase of revenue can be achieved when a Chinese online retailer who sells baby-feeding bottles implements dynamic pricing.

For a policy maker of governments, flattening the demand curve is the main reason for accepting dynamic pricing. Zheng and Geroliminis [418] conduct a case study on public parking facilities. The study suggests that dynamic pricing can effectively reduce parking congestion and the time delay in cruising. Eliasson et al. [118] report that dynamic pricing enables a reduction of 20% traÿc flows, in particular, the traÿc jam, in Stockholm, Sweden. As Cramton et al. [92] emphasize, "dynamic pricing is the only way forward for roads".

For consumers, dynamic pricing is a benefit as well [73]. Chen and Sheldon [72] show that dynamic pricing enables a significant increase of supply in a ride-sharing market,

contributing to an improvement of consumers' welfare. Garbarino and Lee [137] show that because of dynamic pricing online consumers' trust levels towards a seller's behavior increase. Stamatopoulos et al. [348] demonstrate that the cost savings from dynamic pricing can be passed on to consumers, thus improving consumers' welfare.

Machine learning methods further enable updating information about demand in a timely manner. Amazon [69], Lyft and Uber [160], and Airbnb [141] are well-known companies that conduct dynamic pricing.

However, demand fluctuations are driven by human behavior. A fundamental problem of a human-driven system is uncertainty [262, 368]. The main source of uncertainty comes from our lack of knowledge about how a human-driven system works [368]. For example, mathematical equations that universally describe the interactions between price, demand, and supply remain unknown.

Uncertain demand affects each market participant, including the consumers, the sellers, and the policy makers of government [84, 232]. Facing a purchase decision, consumers often anticipate the price at which they are willing to pay [129, 175, 205, 232, 270, 300]. That price represents consumers' *price expectations*. Lu et al. [232] show that uncertainty in initial conditions causes demand exhibiting different dynamics. Consumers' price expectations are thus easily manipulated by a change of initial conditions. Chen, Mislove, and Wilson [68] indicate that without audits uncertainty in demand imposes a concern to consumers' welfare, such as the fairness and the transparency. For a seller, coping with uncertainty in demand is the essence of dynamic pricing [70, 297, 361]. For policy makers, ignoring uncertainty makes them fail a target level of public welfare [84].

Existing approaches often rely on assuming stochastic demand to cope with uncertain demand [40, 44, 111, 191, 261]. Under the assumption, an external force behaves like noise, and drives the interactions between price, demand, and supply. In this thesis, noise is a stochastic variable of a high-dimensional system. From the assumption, the uncertainty is because of a force in a complex high-dimensional system [262, 368]. A low-dimensional system is incapable of quantifying the force by known and limited variables.

On the other hand, contemporary statistics can be applied to analyze and quantify the uncertainty of randomness. For example, statistics provides an effective tool to model and predict the state of stochastic demand [70, 104, 105].

1.2 Equilibrium price

Another mechanism, equilibrium price, exists in addressing a pricing problem. Dynamic pricing is different from an equilibrium price from three perspectives. Firstly, the role that price, demand, and supply plays in dynamic pricing is different from that in equilibrium price models. Dynamic pricing aims for maximal revenue as a seller has a fixed amount of supply [45, 70, 119]. An equilibrium price occurs when a balance is achieved between demand and supply as they are both adjustable.

Secondly, dynamic pricing is an operational issue of the seller [297, 361]. Facing a given amount of supply, the seller utilizes optimizations to harvest optimal revenue that is realized from the quantity supplied. From the perspective of day-to-day business operations, a seller has a multiple-objective problem. At time t, one objective of the seller could be to maximize the revenue that is realized from one inventory by increasing price. The other one could be to minimize the risk of a non-zero inventory at the end of the selling period by decreasing price. An inventory is one unit of supply that holds for a future satisfaction of one unit of demand. Dynamic pricing is thus applied to address the multiple-objective problem related to daily operations [297, 361].

Thirdly, as non-equilibrium prices occur, it becomes profitable to adopt dynamic pricing strategy. Dynamic pricing is to find the price where optimal revenue can be achieved. Nevertheless, an equilibrium is a situation deviating from which there does not exists any profitable strategy [240, 269]. At the situation where supply is unable to be adjusted as easy as demand, dynamic pricing, however, provides a strategy that harvests an optimal revenue from the delay of interactions between demand and supply [232]. Here, deviating from a previous equilibrium price can be profitable until a new equilibrium price is reached. For example, Schröder et al. [332] show that dynamic

pricing can be used to improve revenue when a ride-sharing market goes through a shortage of supply (drivers) where non-equilibrium prices occur.

An equilibrium price can be an optimal solution to a dynamic pricing problem. At the situation where supply is adjustable as easy as demand, an equilibrium price is the optimal price that dynamic pricing aims for. A seller thus can implement a dynamic pricing strategy to approach the equilibrium price for daily operations.

In the study of equilibrium prices, studies find that a rational route with uncertainty can be an alternative source to apparent randomness. Brock and Hommes [51] show that nonlinear interactions between demand and supply cause a deterministic route to apparent randomness. Corcos et al. [89] demonstrate that intermittency emerges from two contradicted human behaviors, imitation and contrarian. Intermittency is an irregular alternation of different deterministic routes [333]. The intermittency phenomenon also explains bubbles and crashes of a stock market [89]. Anufriev et al. [11] show that a deterministic model with discontinuity fits fluctuations of real markets.

1.3 Motivation for dynamic pricing

When it comes to the modeling of dynamic pricing problems, a rational route to irregular demand fluctuations remains rare. Rump and Stidham [319] show that consumers' adaptive price expectations lead to irregular arrivals as dynamic pricing aims for an equilibrium price. The irregularity is attributed to a rational way that consumers adapts price expectations. As dynamic pricing is unrelated to equilibrium prices, Hu et al. [175] illustrate that a discontinuity in consumers' adaption of price expectations leads to a rational route to uncertain demand.

A rational route to irregular demand remains to be elucidated for four reasons. Dynamic pricing problems are held by human behavior-driven systems [322]. However, a universal equation has not been identified to describe the behavior of human beings responding to a change of prices or market environments [368]. Facing dynamic pricing problems, a seller needs to have a current action (pricing decision), but expects an

optimal future revenue. Nevertheless, in the absence of deterministic equations, "...who knows what the future might hold?" [361]. Also, empirical studies that identify the underlying equations of the interactions between price, demand, and supply are limited to contemporary regression methods. The idea of a regression is that hypothetical equations fit the fluctuations of data. For example, Kopalle and Lindsey-Mullikin [203] use a linear, a quadratic, an inverted U-shaped (e.g., the logarithmic function), and an S-shaped (e.g., the logistic model) functions to model the interactions between price, demand and supply. Li et al. [223] introduce a time delay term to a linear function for modeling the interactions. Regressions rely on our contemporary knowledge about mathematical equations. However, that knowledge remains elusive [53]. Another two reasons are related to the modeling and the identification of a rational route in the research field that is concerned with deterministic chaos and nonlinear time series analysis. We will discuss the remaining two reasons in section 1.5 after introducing mathematical definitions of deterministic chaos and nonlinear time series analysis.

1.4 Complex dynamics

A rational route to apparent randomness is fundamentally different from the route to randomness that noise takes. Randomness of noise results from the incapacity to model a high dimensional system by means of known variables of a low dimensional system [262, 368]. Randomness is driven by an external force and quantified by noise [262, 368]. However, apparent randomness of a rational route results from nonlinearity that connects known variables of a low dimensional system [51, 277]. The nonlinearity can be described by deterministic equations. Apparent randomness is thus driven by an internal force and quantified by deterministic equations [51, 175, 319].

1.4.1 Deterministic and stochastic dynamics

If fixing a system's present state can lead to a deterministic future state, then the system underlies *deterministic dynamics* [333] and exhibits a rational route to apparent randomness. The rationality can be quantified by deterministic equations that describe

the relationship between the system's present and future states. However, the equations may be unknown. We take a natural system as an example. Deterministic dynamics has been identified from the climate system in some intervals of the last 66 million years [397]. Nevertheless, explicitly mathematical formulas that describe the climate system are yet to be addressed.

Stochastic dynamics is the dynamics of randomness as a result of noise. Deterministic dynamics and stochastic dynamics have similarities in (1) irregular fluctuations of the time series [277, 315]; and, (2) a broadband power spectrum in the frequency domain [234, 315]. The topic, an identification of nonlinear dynamics, is to distinguish between deterministic and stochastic dynamics. The identification is based on deterministic patterns, such as recurrent properties [246, 277, 397] or symbolic patterns [7, 234, 317], which can be seen in a system underlying deterministic dynamics.

1.4.2 Deterministic and artificial chaos

Chaos theory is a theory to understand apparent randomness arisen from a rational route and to analyze the behavior of a dynamical system. The following concepts have been introduced in chaos theory. Let $\phi(t,x)$ denote a flow generated from a vector field $\frac{dx}{dt} = f(x)$ where f is the governing equation, t denotes time, x represents a state of the system, and x_0 is an initial point. *Phase space* [398] is a phase of dependent variables that define f. Given an initial point in phase space, a *trajectory* [398] is a solution to $\frac{dx}{dt} = f(x)$. An *invariant set* [398] is a set of points in phase space satisfying that a trajectory taking the point in the set as initial points remains in an identical set forever. An *attracting set* [398] is a closed invariant set A, and there exists some neighborhood U of A satisfying $\forall t \geq 0$, $\phi(t,U) \subset U$ and $\bigcap_{t>0} \phi(t,U) = A$. A closed invariant set A satisfies *topological transitivity* [398] if for any two open sets, $U,V \subset A$, $\exists t \in R$ such that $\phi(t,U) \cup V \neq \emptyset$. An *attractor* [398] is an attracting set that satisfies topological transitivity.

We assume that Λ is a compact set, and for all $t \in R$, $\phi(t,\Lambda) \subset \Lambda$. A flow $\phi(t,x)$ exhibits *sensitive dependence on initial conditions* [398] on Λ if there exists an $\epsilon > 0$

holding the following property. For any $x \in \Lambda$ and any neighborhood U of x, there exists $y \in U$ and $t > 0$ satisfying $|\phi(t,x) - \phi(t,y)| > \epsilon$. Sensitive dependence on initial conditions is related to a diverging behavior. For any point $x \in \Lambda$ and an arbitrarily small neighborhood U of x, there exists at least one point $y \in U$ satisfying a diverging behavior, that is, under ϕ the passing of finite time $t > 0$ makes y diverge from x by a fixed distance ϵ. An attractor with $\phi(t,x)$ exhibits sensitive dependence on initial condition is called chaotic, and the corresponding system is a chaotic system.

Deterministic chaos represents a phenomenon that takes place in a chaotic system [333]. The system is (1) governed by deterministic equations and (2) bounded in phase space. Also, the system (3) has aperiodic long-term fluctuations and (4) sensitive dependence on initial conditions [116, 143, 150, 333, 353, 360, 398]. Deterministic chaos has been observed in natural systems [25, 158, 284, 286, 294] as well as in engineered [93, 107, 216, 281] systems.

Machine learning methods are increasingly employed to mimic deterministic chaos [64, 179, 237, 293, 303, 318, 383, 423]. Related to machine learning methods, we introduce the terms, artificial system, mimetic trajectory, ML-mimetic attractor, and artificial chaos. An *artificial system* is an exclusive term for an artificial intelligence system that is designed to mimic deterministic chaos. It is a system equipped with machine learning methods and often takes an input/output framework. *Mimetic trajectory* is a trajectory that an artificial system synthesizes. An *ML-mimetic attractor* is an attractor that a mimetic trajectory approach. In section 5.1.1, we will give the mathematical definitions of above-mentioned new terms.

Artificial chaos represents a phenomenon that takes place in an artificial system as it mimics deterministic chaos. The system (1) takes an input/out framework, and (2) has the supposed and the actual behaviors. Supposed behavior is the behavior that an artificial system is designed to mimic, thus being chaotic. Actual behavior is the behavior that an artificial system actually exhibits under given initial conditions. The dynamics of actual behavior can be chaotic or non-chaotic. If an artificial system satisfies the

sensitive dependence on the initial conditions to which the input is sensitive, then the system exhibits deterministic chaos. Artificial chaos is related to the actual dynamics of an artificial system, which is not necessarily chaotic.

We introduce *machine behavior* to study the supposed and actual behaviors of an artificial system. In computer science, machine behavior is the behavior of an artificial intelligence system as it is integrated into an environment for a fulfillment of a designed task [304]. A study of machine behavior is to mitigate unfavorable effects or maximize the benefit of the artificial intelligence system [304]. Here, machine behavior represents the behavior of an artificial system under varying initial conditions. We study machine behavior for an analysis of the sensitive dependence of an artificial system on initial conditions.

Theoretical analysis of machine behavior is diÿcult. Machine learning methods behave like a black box [145, 218, 410]. For an artificial system, optimizations are involved in mimicking the behavior of an input in a training process [145, 218]. Explicit solutions to optimizations are often diÿcult to be obtained [145, 218], which holding back explicit formulas that describe machine behavior.

However, nonlinear time series analysis can be applied to an output for the study of machine behavior. An output can be regarded as the time series of an artificial system for two reasons. An output is collected from an artificial system that takes an input/output framework. In a sense, we place a sensor at the output layer and measure the oscillation of the system by an output. In addition, as a mimetic trajectory is delivered, an output is characterized by the supposed and the actual dynamics. Supposed dynamics is what the artificial system targets for, which is consistent with the fulfillment of the system. Actual dynamics represents the dynamics what the output actually displays, which is consistent with our observation. An output thus represents an observable of the system by the supposed and the actual behaviors.

1.4.3 Nonlinear time series analysis

Takens' embedding theorem [360] provides a theoretical foundation for nonlinear time series analysis. Consistent with Kantz and Schreiber [188], the method that analyzes the dynamics of phase space based on a time delay embedding is called *nonlinear time series analysis*. A *time series* is an observable that can be taken from measurements or collected via real-life sensors. We assume that a time series $\left\{x_1, x_2, \cdots, x_t, \cdots\right\}$ underlies deterministic dynamics. Here, x_t is a scalar that represents the $t-$th state of a system. Takens' embedding theorem ensures the existence of an embedding dimension m and a time delay dimension τ. From m and τ, we can reconstruct a time delay vector $\boldsymbol{s}_t$ via

$$\boldsymbol{s}_t = (x_t, x_{t+\tau}, \cdots, x_{t+(m-1)\tau}) \tag{1.1}$$

Also, $\left\{\boldsymbol{s}_1, \boldsymbol{s}_2, \cdots, \boldsymbol{s}_t, \cdots\right\}$ is equivalent to the system that yields $\left\{x_1, x_2, \cdots, x_t, \cdots\right\}$. Here, x_t is a scalar state of an original attractor, $\boldsymbol{s}_t$ is a vectorial state of a reconstructed attractor. In this thesis, an *original attractor* is the attractor that $\left\{x_1, x_2, \cdots, x_t, \cdots\right\}$ approaches. A *reconstructed attractor* is an attractor that $\left\{\boldsymbol{s}_1, \boldsymbol{s}_2, \cdots, \boldsymbol{s}_t, \cdots\right\}$ approaches. Eq. (1.1) describes an attractor reconstruction from a univariate time series [188, 295]. However, attractor reconstruction is applicable for a multivariable time series [188].

As instructed by nonlinear time series [49, 60, 188, 208, 278, 295], m and τ can be found in following sequential steps. The idea is to firstly find τ, and then to find m by fixing τ.

(1) Find τ. As τ increases, we plot how mutual information or auto correlation changes. A practical criterion is to choose the first τ under which mutual information reaches the first local minimum [188]. Multiple local minima should be observed for avoiding pitfalls of nonlinear time series analysis.

(2) Find m under τ. Here τ is derived from (1). As m increases, we plot how the fraction of false nearest neighbors changes under the given τ [60]. A practical criterion is to define a threshold such as 10% and then choose m whose corresponding fraction of false nearest neighbors goes under the given threshold for the first time.

1.4.4 Symbolic dynamics

Symbolic analysis provides an alternative way to analyze deterministic chaos [143, 312]. The idea is to study the dynamics in symbolic space instead of phase space. A shift map decomposes an original phase space to non-overlapping blocks [143]. Different symbols are then used to label individual blocks. All used symbols constitute a new space (symbolic space) [110]. *Symbolic dynamics* is concerned with the dynamics of those symbols under the time evolution [110, 143, 312].

A shift map δ is the key for symbolic analysis [143]. A symbolic sequence can be calculated from a time series via

$$\begin{array}{ccccccc} \Big\{x_1, & & x_2, & \cdots, & x_t, & \cdots\Big\} \\ \delta\downarrow & & \delta\downarrow & \cdots, & \delta\downarrow & & \\ \Big\{\delta(x_1), & \delta(x_2), & \cdots, & \delta(x_t), & \cdots\Big\} \end{array} \tag{1.2}$$

where $\delta(x_t)$ is a symbol to which x_t is encoded under δ. Eq. (1.2) translates individual states to their corresponding symbols.

We introduce terms related to symbolic dynamics. A finite set $\mathcal{A}$ of symbols are called *alphabet* [110]. An element of $\mathcal{A}$ is called a *letter* [110] . A *k-word* is a sequence containing k letters over $\mathcal{A}$ [110]. For example, the alphabet of binary number is $\mathcal{A} = \{0, 1\}$, 0 and 1 are letters, and "1100" is a 4-word. For a set $\mathcal{A}$ with q different letters, it has q^q different permutations. A *forbidden word* [110] of length k is the permutation that is not allowed in the k-words of $\Big\{\delta(x_t)\Big\}_{t=1}^{\infty}$. The existence of forbidden words is determined by the underlying dynamics of deterministic chaos [143].

Symbolic dynamics can be applied to examine an equivalence between two chaotic systems [143]. If δ satisfies one-to-one correspondence, then a symbolic dynamical representation $\Big\{\delta(x_t)\Big\}_{t=1}^{\infty}$ preserves the nonlinear dynamics of $\Big\{x_t\Big\}_{t=1}^{\infty}$, thus being faithful [143]. In addition, the presence or the absence of a forbidden word is related to the topological invariants of deterministic chaos [143]. Symbolic dynamics is thus used to distinguish two dynamical systems [143].

1.5 Motivation for nonlinear dynamics

The modeling and the identification of uncertain demand remain to be elucidated for four reasons. In section 1.3, we have shown the two reasons, the absence of universal equations of human behavior and limit knowledge as a result of contemporary regressions. The remaining two reasons are related to deterministic chaos and nonlinear time series analysis for real-life applications.

Nonlinear time series analysis methods remain understudied when a dynamical system is contaminated by noise or with non-stationarity [188]. However, it is often the case that real-life data are contaminated by noise. For dynamic pricing problems, the interactions between price, demand, and supply are made in a social system. It is difficult to collect data in a social system without noise. A stochastic demand is thus widely assumed to model uncertainty. Moreover, an attractor reconstruction relies on the choices of m and τ (Eq. 1.1). However, there is no unique choice for m and τ [188]. In particular, a diÿcult y occurs in finding appropriate choices when no obvious ups or downs can be seen from the plot of mutual information or that of auto correlation in a deterministic system. This will be shown in chapter 4.

The last but not least reason comes from chaos predictions and optimizations in the context of deterministic chaos. Dynamic pricing models and predicts demand for optimal revenue. If demand was deterministic or chaotic, then demand predictions belonged to chaos predictions. Besides, machine learning methods have been applied for chaos predictions [293, 421] and data-driven dynamic pricing models [59, 157]. However, (1) chaos prediction is a challenging problem. (2) It remains unclear for the behavior of an artificial system as initial conditions are varied. In particular, the problem remains unaddressed that whether a coincidence between an original and a mimetic trajectories is a conclusive evidence of an equivalent sensitive dependence on initial conditions between an original and an artificial systems. (3) If a gap exists between an original and an artificial systems under the coincidence, then its impact should be identified.

Those four reasons include the equations-based thinking to model and fit demand,

noise contaminating real-life data, and issues related to the supposed and actual dynamics of an artificial system. They motivate us to develop attractor-based models. The models justify dynamic pricing and explain uncertain demand from nonlinear dynamical systems' perspective (Chapter 3). Also, we are motivated to reconstruct an attractor from a real-life dynamic pricing scenario (Chapter 4). Finally, the sensitive dependence on initial conditions between deterministic and artificial chaos is motivated to be compared (Chapter 5).

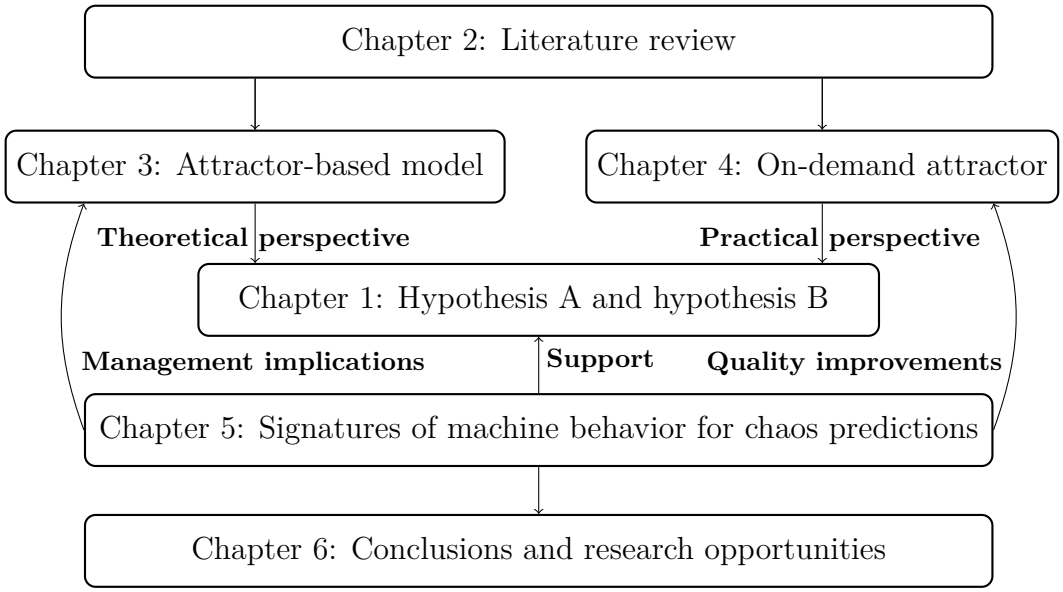

Figure 1.1 : An organization of this thesis. Chapter 1 proposes two hypotheses. Chapter 2 makes a literature review and identifies research problems. Chapters 3 and 4 base on nonlinear dynamical systems and support the hypotheses from theoretical and practical perspectives. Chapter 5 examines the sensitive dependence on initial conditions as an artificial system mimics deterministic chaos. Chapter 6 concludes the observations and the findings. Also, managerial implications are provided.

1.6 Objectives and hypotheses

1.6.1 Objectives

In this thesis we analyze uncertainty in dynamic pricing problems from the perspective of deterministic chaos. We aim to improve pricing decisions and to improve nonlinear

time series analysis. With a focus on nonlinear time series analysis being applied to a social system, three objectives are included.

(1) Nonlinear interactions between price and demand will be studied under a fixed amount of supply (Chapter 3). We will justify dynamic pricing using a hypothetical model that considers the influence of consumers' behavior on demand. The mode will quantify consumers' price expectations. Bifurcation analysis will be conducted by modeling a change in the intensity of nonlinear interactions.

(2) The underlying dynamics of real-life demand from a ride-sharing market will be identified (Chapter 4). The dataset records a timestamp of arrivals of each transaction of a ride-sharing company who provided a ride sharing service in greater Austin, Texas, the United States. We will propose a recurrence-based attractor reconstruction, and use the proposed approach to reconstruct an on-demand attractor.

(3) Signatures of machine behaviors will be analyzed (Chapter 5). We will apply nonlinear time series analysis to study machine behaviors and compare the sensitive dependence on initial conditions between mimicked chaotic systems and artificial systems.

1.6.2 Hypotheses

This thesis introduces deterministic chaos, nonlinear time series, symbolic dynamics, and machine learning for testing two hypotheses:

Hypothesis A: Nonlinear interactions between price, demand, and supply can result in a rational route to uncertain demand in dynamic pricing problems.

Hypothesis B: A coincidence between a chaotic trajectory that an original system yields and a mimetic trajectory that an artificial system synthesizes is incapable of leading to an equivalent sensitive dependence on initial conditions between the original and the artificial systems.

Hypothesis A is concerned with the root of uncertainty in dynamic pricing problems. We provide a theoretical and a practical perspectives to study Hypothesis A (Fig. 1.1).

A hypothetical model justifies dynamic pricing from dynamical systems' perspective. It aims to address a hypothetically rational route to apparent randomness (Chapter 3). In addition, attractor reconstruction identifies a practically rational route to uncertain demand from a real-life dynamic pricing setting (Chapter 4).

Hypothesis B is concerned with the learnability of machine learning methods in mimicking deterministic chaos. It remains a debate when it comes to the learnability of machine learning methods in computer science [31]. We therefore focus on a question related to the sensitive dependence on initial conditions between deterministic and artificial chaos. Let assume that a mimetic trajectory coincides a chaotic trajectory. The question is that under the coincidence can we conclude the learnability of artificial systems in the sense of an equivalence in the sensitive dependence on initial conditions.

Hypothesis A will be confirmed in Chapters 3 and 4 (Fig. 1.1). The confirmation opens a new door for a data-driven dynamic pricing modeling by means of deterministic chaos. Along the direction, we take a small step towards a gap between the supposed and the actual dynamics that an artificial system exhibits in mimicking deterministic chaos. This motivates Hypothesis B (Fig. 1.1). The confirmation of Hypothesis B will gives implications for the data-driven dynamic pricing modeling (Chapter 6).

1.7 Thesis outlines

In this thesis, we propose an attractor-based model to justify dynamic pricing strategy (Chapter 3) and an attractor-based thinking to identify uncertain demand (Chapter 4). Deterministic chaos, nonlinear time series analysis and machine learning methods are introduced. Three main chapters are used to achieve the goals and deliver the objectives. Fig. 1.1 outlines this thesis. Each chapter discusses the following topics, respectively.

Chapter 1: A general introduction of the research topics are covered; hypotheses are developed; and, motivations and objectives are presented.

Chapter 2: A literature review identifies research problems that are needed to be solved in the modeling of uncertain demand.

Chapter 3: An attractor-based model is proposed to justify dynamic pricing strategy from nonlinear dynamical systems' perspective. The focus is on how uncertainty emerges from the nonlinear interactions between price and demand. Bifurcation analysis is conducted by changing the intensity of the interactions. In this chapter we build a theoretical model for a support of Hypothesis A (Fig. 1.1).

Chapter 4: Nonlinear time series analysis is conducted on demand of a real-life ride-sharing market. Recurrence-based attractor reconstruction is developed. A statistics of two different recurrence quantifications are applied for Pareto optimality. The optimization aims to find the Pareto optimal parameters of recurrence plots. A range of parameters of recurrence plots are searched for an optimal attractor reconstruction. In this chapter we reconstruct a real-life attractor for a support of Hypothesis A (Fig. 1.1).

Chapter 5: Initial conditions of an artificial system are identified. By varying initial conditions, basins of an ML-mimetic attractor are calculated and compared with the basins of an original attractor. Symbolic dynamics is conducted. The supposed and the actual behaviors of artificial systems are analyzed. In this chapter we identify the gap between the supposed and the actual behaviors of artificial systems for a support of Hypothesis B (Fig. 1.1).

Chapter 6: Managerial implications for the data-driving dynamic pricing modeling are discussed. Research opportunities are proposed as well.

Chapter 2

Literature survey

> All models are wrong, but some are useful.
>
> — George E. P. Box

2.1 Introduction

As discussed in Chapter 1, the modeling of demand is essential for solving a dynamic pricing problem. The booming of online marketplaces further increases the availability of demand information [69, 144]. This chapter reviews uncertainty that has been considered to capture "the abstractions of reality" [40] for dynamic pricing problems. The emphasis is putted on two perspectives. The first one is on the dispute, stochastic versus deterministic demand, to uncertainty. The second one is on the force that induces uncertainty. Finally, research problems are identified.

Two different ways exist in the modeling of demand for dynamic pricing. The one proposes a hypothetical model for obtaining managerial implications from analytical solutions to optimizations [36, 46, 133, 133, 144, 271, 300, 354, 416]. The other one proposes a practical model that fits real-life data, such as sales transactions [180], for improving the accuracy of demand predictions [130, 180, 190, 203, 223]. This thesis proposes a hypothetical model (Chapter 3) and bridges a gap (Chapter 4) between a fitting

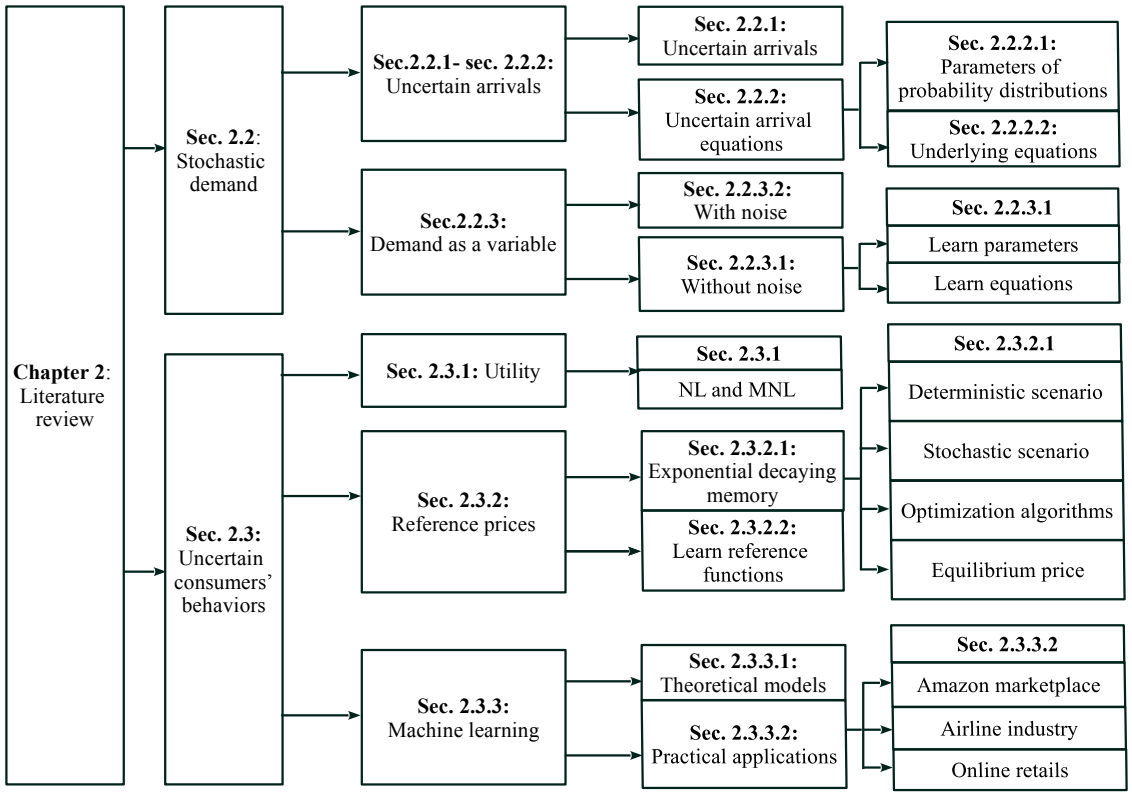

Figure 2.1 : An organization of Chapter 2. In sections 2.2 to 2.4, the modeling of uncertain demand is reviewed. In section 2.2, uncertain demand is assumed to be a stochastic variable being either discrete or continuous. In section 2.3, uncertain demand is quantified by stochastic human behavior that follows some economic theory. In section 2.4, rational routes to apparent randomness are reviewed in equilibrium price models. In section 2.5 research problems are stated

of data and a practical model for improving data-driven predictions (Chapter 5). Many books and papers have reviewed the modeling of demand and the optimization methods for addressing dynamic pricing problems. Classical books for revenue management are written by Phillips [297] and Talluri and Van Ryzin [361]. Papers, including Bitran and Caldentey [45], Elmaghraby and Keskinocak [119], van Ryzin [380], Shen and Su [334], Chen and Chen [70], and den Boer [100], provide detailed reviews of the modeling of demand. Also, literature reviews exist for dynamic pricing with a focus on some special industry. For example, Dutta and Mitra [114] provide an overview of dynamic pricing in electricity markets. Limmer [227] reviews dynamic pricing for electric vehicle charging.

Fig. 2.1 outlines the structure of this chapter. In section 2.2, we review the modeling of uncertain demand in the form of stochastic demand. Interactions between price and demand are modeled by deterministic equations and an involvement of a stochastic term. The equations model the interactions from a hypothetical perspective by allowing a deviation from economic theory. For example, a dynamic pricing problem can be modeled by a linear equation that allows deviations from actual human behaviors [40]. In section 2.3, we review the modeling of uncertain demand in the form of uncertain human behavior. The modeling is supported by an economy theory that quantifies how human beings behave as a price fluctuates. Stochastic human behaviors are considered in the modeling. In section 2.4, we review deterministic chaos with an application in the modeling of equilibrium prices. In section 2.5, we identify research problems.

2.2 Stochastic demand

Three main models exist in the modeling of stochastic demand [297, 361, 380]. They are (a) additive noise $D(p, \epsilon) = d(p) + \epsilon$; (b) multiplicative noise $D(p, \epsilon) = \epsilon d(p)$; and, (c) Poisson or Bernoulli process. Here, $d(p)$ is a hypothetical equation that directly quantifies the relationship between price and demand. The equation is allowed to deviate from the governing equation that actually describes the interactions between price and demand. Also, ϵ represents noise, which is an external force to model uncertain demand. In (a) and (b), demand is assumed to be a stochastic continuous variable. However, in (c) the arrival of consumers is assumed to be a random and discrete variable.

The modeling of stochastic demand can be categorized into conventional parametric, Bayesian parametric, and nonparametric approaches [104]. The categorization is based on how to model uncertainty. Conventional parametric approaches assume that demand function is chosen from a parametrized family of distributions [104]. Classic statistical approaches such as maximum likelihood or least square regressions can be applied to obtain a demand function. Bayesian parametric approaches apply Bayesian estimation to update the knowledge of demand function [104]. Nonparametric approaches do not assume a known parametric equation of a demand. Instead of maximizing expected

revenue, nonparametric approaches often maximize revenue in the worst cases [104].

We narrate the modeling of stochastic demand in an alternative way by the passage of time. The reason is that the availability of data is improved by the passage of time. The data, however, change the way that researchers model and tackle uncertain demand. We put the emphasis on the root and the meaning of uncertainty that the modeling of uncertain demand involves. Three stages are recognized, including uncertain arrivals, uncertain arrival functions, and uncertain demand functions. The former two stages model a discrete demand by consumers' arrivals (Fig. 2.1). The latter one models a continuous demand (Fig. 2.1).

2.2.1 Uncertain arrivals in known functions

At the first stage the uncertainty is examined from the perspective of the arrivals of consumers. The uncertainty comes from the time when consumers arrive. Dynamic programming is a common tool to solve an optimization of expected revenues. Dynamic programming is a recursive algorithmic technique to solve optimization problems [28, 29, 99]. The recursive equation is called a Bellman equation.

The initial study on dynamic pricing with stochasticity is credited to Gallego and Van Ryzin [133]. A Poisson process is assumed to model the realization of consumers' arrivals. Under the assumption a one-to-one correspondence between a unit of inventory and a price exists, that is, $\lambda = \lambda(p)$. Here λ is the number of arrivals in a unit time, and p represents a price. A Bellman equation is used to solve dynamic programming involved in the optimization of expected revenues. In a similar manner, Gallego and Van Ryzin [134] extend their model to a dynamic pricing problem of multiple products. Arrivals thus become a vector, $\boldsymbol{\lambda} = \boldsymbol{\lambda}(\boldsymbol{p})$, where $\boldsymbol{\lambda}$ and $\boldsymbol{p}$ are vectorial arrivals and prices of individual products. Zhao and Zheng [416] use a nonhomogeneous Poisson process to study hetergeneous arrivals, thus $\lambda = \lambda(p, t)$. Here, the arrival λ is a function of the price p and the time t together. Zhao and Zheng [416] address uncertainty through a known cumulative probability distribution and a backward dynamic programming algorithm.

A Bernoulli process and a relative entropy can also be introduced for dynamic pricing problems. Maglaras and Meissner [239] use a Bernoulli process to model consumers' arrivals as a discrete process. The uncertainty is in the form of heterogeneous arrivals. Dynamic programming is then applied to address optimal arrival rates. Feng and Xiao [125], Subramanian et al. [355], Feng and Xiao [124], and Chatwin [65] apply a similar method to model the uncertain arrivals of consumers. Lim and Shanthikumar [226] introduce relative entropy to mitigate a revenue loss due to deviations that the modeling of uncertain consumers' arrivals induces. The entropy measures the distance of consumers' arrival rates between a model-based calculation and a real-life realization.

A stochastic arriving process transforms a dynamic pricing problem to a dynamic optimization problem [39], such as dynamic programming. However, the arrivals of consumers are assumed to be in a form of known equations. Those equations can be described either by a known probability distribution [416] and or by known mathematical formulas [239]. In practice, the probability distribution and mathematical formula are both diÿcult to be understood when a seller faces a pricing decision [39, 226].

2.2.2 Uncertain arrival equations

At the second stage the uncertainty is studied from the perspective of arrival equations. The uncertainty comes either from unknown parameters or from unknown equations that quantify when consumers arrive. Optimizations have two objectives: exploration and exploitation, in addressing the uncertainty [39]. An exploration aims to learn the underlying arrival equations for future revenues. An exploration aims to harvest current revenues from current pricing decisions.

In this chapter, the learning is not about machine learning methods but about the identification of either parameters or equations that quantify a relationship between demand and price. The learning of parameters is related to identify the parameters of a given equation. The learning of equations is related to identify the underlying equations of a realized demand.

2.2.2.1 Unknown parameters of probability distributions

Two different approaches exist in modeling and addressing unknown parameters of a given equation. In the first category an optimization is still solved by dynamic programming. However, the parameter of the Bellman equation is updated by a Bayesian scheme based on a realization of demand.

Aviv and Pazgal [16] consider the uncertainty of consumers' arrivals in a changing environment. Their model considers the influence of unknown external forces on demand realizations. A Markov process is introduced in the modeling of uncertain demand realizations [16]. The parameter of Bellman equation is updated by a series of posterior probabilities. Aviv and Pazgal [15], Lin [228], and Farias and Van Roy [120] use a Gamma distribution to describe uncertain beliefs of a seller about its consumers or uncertain arrivals. The Gamma distribution has unknown parameters. Real-time posterior distributions of demand are used to update the unknown parameters. Araman and Caldentey [12] introduce two types of uncertainty: the arrival of consumers λ and a scaling factor θ. Here, θ captures the influence of an unknown market size on consumers' purchase decisions, and λ is a known function. Both θ and the Bellman equations are updated by posterior distributions [12].

2.2.2.2 Unknown underlying equations

In the second category a different thinking is developed to model the uncertainty in the arrivals of consumers. The idea is to learn the underlying equations of arrivals $\lambda = \lambda(p(t))$ [39, 389]. The unknown equations elucidate the relationship between the arrival (λ) and the price (p).

Besbes and Zeevi [39] introduce the exploration and the exploitation, which changes previous studies that apply the Bellman equations to solve optimal revenue. The uncertainty is assumed to remain in the arrivals of consumers and their underlying arrival equations. Let assume that the arrivals follow a Poisson process, then a dynamic pricing problem is split into two sequential problems [39]. The first problem aims to learn the

underlying equations that describe the arriving of consumers (exploration). The second problem intends to compute optimal prices based on the learned equations (exploitation). Besbes and Maglaras [37] follows the same idea, exploration first and then exploitation. However, a constraint is added into dynamic pricing problems with financial milestones [37]. The constraint approximates a sequence of financial milestones imposed on a seller, such as the sales targets and the revenue targets. Wang et al. [389] focus on the dynamic pricing problem studied in [39]. A learning-while-doing algorithm is proposed to improve revenue [389] by a shrinking mechanism [389]. The mechanism iteratively decreases the price interval that accommodates the optimal prices while learning about the uncertain arrival functions.

In section 2.2.1, the uncertainty is modeled by consumers' arrivals that satisfy a stochastic process with known properties. In section 2.2.2, the uncertainty is modeled by explicit equations that describe consumers' arrivals in the form of unknown parameters or unknown formulas. Consumers' arrivals address the uncertainty of discrete demand. However, an alternative perspective is to address the uncertainty of continuous demand.

2.2.3 Uncertain demand functions

At the third stage a demand is regarded as a variable that describes the quantity demanded. Uncertain demand is due to a lack of information about the underlying equations that elucidate the interactions among price, demand, and supply. We classify existing studies by an involvement of noise (Fig. 2.1).

2.2.3.1 Demand equations without noise

In the first category the uncertainty is addressed is a similar way as unknown arrival equations shown in section 2.2.2. An equation is used to describes the relationship between the mean $E[D(p)]$ of demand $D(p)$ and the price p [83]. Here, E is the first moment of the distribution of a random variable. It is calculated by the mean of demand D. Also, $E[D(p)]$ represents the uncertainty of a demand realization, and $d(p) = E[D(p)]$ stands for a demand equation.

The learning of parameters of a known equation. Apart from $E[D(p)]$, den Boer and Zwart [104] utilize the variation $\mathrm{Var}[D(p)]$ of demand distribution to model the uncertainty of a demand realization. Here, "Var" is the second moment of a distribution of a random variable. It is calculated by the variance of demand. The underlying equations of $E[D(p)]$ and $\mathrm{Var}[D(p)]$ are assumed to be known. Nevertheless, the values of their parameters are unknown. den Boer and Zwart [105] further impose a lower and an upper bounds on uncertain parameters for containing $d(p)$. The bounds represent the influence of finite inventories on demand. For example, stockout affects a demand realization [105]. Broder and Rusmevichientong [52] assume that the unknown parameters are in a compact and convex set to ensure the boundness of demand. den Boer and Keskin [102] allow discontinuity in demand functions, and consider the uncertainty in the location where a jump occurs. Demand becomes a known function of two random vectors, $d(p,\boldsymbol{\kappa},\boldsymbol{\theta})$. Here, $\boldsymbol{\kappa}$ stands for the uncertainty in the location of jumps, and $\boldsymbol{\theta}$ stands for unknown parameters. Maximum likelihood estimations are used to calculate the unknown parameters [102].

The learning of equations. Cheung et al. [83] relax the assumption that $d(p)$ is quantified by a known equation. In [83], demand equation is learned from a library of basis functions. Exploration first and then exploitation [39] is introduced to learn the true $d(p)$ from the given library. Chen and Gallego [74] further relax the knowledge of $d(p)$, and consider the uncertainty in demand due to personalized information (covariates) of online marketplaces. In [74], an adaptive binning and exploration algorithm is proposed. The algorithm splits the covariate space, clusters consumers, simultaneously learns demand (clustering rules), and earns current revenues.

2.2.3.2 Demand equations with noise

A natural idea is to involve noise in the equations that describe the relationship between price and demand. Additive and multiplicative noise and a combination of the both can be used to model the effect of noise on demand [297, 361, 380]. Here, we mainly review models that take additive noise to exemplify the modeling of a stochastic demand.

However, a choice between additive and multiplicative noise relies on the existence and uniqueness of an optimal solution when a hypothetical model aims for an analytical solution to dynamic pricing problems [380]. For real-life applications the choice should agree with the process from which demand realizes [361, 380].

Noise can be used to represent either demand shocks or stochastic forces. Both parametric and non-parametric approaches are applied for a solution to a dynamic pricing problem. Besbes and Zeevi [40] assume that demand satisfies $d(p_t) = E[D(p_t)] + \epsilon_t$. Here, two types of uncertainties are modeled, where $E[D(p_t)]$ addresses unknown demand equations, and ϵ_t captures random demand shocks. Simultaneous explorations and exploitations are utilized to address the learning of demand functions and the earning of immediate revenues. Examples in Besbes and Zeevi [40] show that a mismatch between the true and the learned demand functions changes the optimal price from a fixed point to period-2 oscillations. However, their results leave an open question to the bifurcating phenomenon. Den Boer [101] uses additive noise to represent a stochastic market process. Keskin and Zeevi [192] introduce another two types of uncertainty in a model with additive noise. The one is related to additive Gaussian noise. The other one is related to unknown parameters of a known function. The values of unknown parameters are selected from a sequence of demand parameter vector. A variation in demand parameter vectors reflects the uncertainty of market environment. Chen et al. [75] relax the assumption of a prior knowledge of demand function, use a spline function to approximate real demand function, and learn unknown parameters of the spline approximation.

An advanced study is to consider uncertainty over multiple time periods. Cohen et al. [86] provide a sample-based optimization to address uncertainty over multiple time periods. The data are divided into N samples. At time t, for a sample i, a random scaler ϵ_t^i stands for the errors between the realized and the estimated demand. The uncertainty lies in the disparity $\boldsymbol{\epsilon} = (\epsilon_t^1, \cdots, \epsilon_t^N)$ between a realization and an estimation of demand across N samples [86].

Furthermore, stochastic dynamic programming, least square regression, and Bayesian inferences have advanced considerably thanks to contemporary optimizations. It is easier than ever to identify underlying equations that describe the interactions between demand and price. On the one hand, the uncertainty either in the arrivals of consumers or in the equations that describe price and demand entails a learn-and-earn tradeoff in dynamic pricing problems [102]. The tradeoff is made between the learning of the underlying equations for future revenues and the earning of immediate revenues [102].

On the other hand, the availability of data leverages the learning of the underlying equations of demand and consumers' arrivals. Transactions of realistic (offline) supermarket retailers [88] and consumers' online product reviews [123] are examples. The data are closely related to human behaviors. Economic theory can be applied to describe human behaviors when it comes to a response of human beings to a change of price. The modeling of uncertain demand, therefore, borrows economic theory for solving dynamic pricing problems.

2.3 Uncertain consumers' behavior

Consumers' behavior is entailed in a seller's pricing decision. Mead and Hardesty [255] show that a display of disfluent fonts can affect consumers' price expectations. Xu et al. [401] provide empirical evidence that online product reviews significantly affect consumers' choices for physicians. Ajorlou et al. [4] shows that word-of-mouth marketing has a similar effect on consumers in the smartphone APP market [4]. Xu et al. [400] indicate that consumers' characteristics, such as the arriving time, considerably affect different choices for Major League Baseball tickets.

2.3.1 Consumers' utility

Data, including transaction information [18, 88] and online product reviewers [123, 401], improve the data-driven modeling and the calibration of consumers' behavior for many businesses [400]. Above-mentioned dynamic pricing models capture homogeneous consumers' behavior by a unified equation. Homogeneous behavior assumes that a group

exhibits a collective behavior, so a unified equation represents all consumers in that group. Human behavior, however, can exhibit heterogeneities. Above-mentioned dynamic pricing models are unable to model a heterogeneity. Consumers' utility is thus borrowed from economics for a modeling of demand.

Consumers' utility is an economic concept related to a measure of consumers' personal preference [361]. It captures heterogeneities in consumers' behavior by two basic models [70, 135], the nested logit (NL) model and the multinomial logit (MNL) model. An MNL model is a special case of an NL model [236]. The similarities and the differences between an NL and an MNL models have been identified by Gallego and Wang [135]. An individual consumer's utility (U_i) is described by random noise ϵ_i and the mean utility of all consumers V_i via

$$U_i = V_i + \epsilon_i \tag{2.1}$$

Here, ϵ_i represents heterogenous behaviors of individual consumers. A heterogeneity among different groups is represented by different equations that quantify V_i or different parameters of a unified function.

The modeling of uncertain demand is often in the form of Eq. (2.1) or its extensions as heterogeneous consumers' behavior is considered. Chen et al. [81] consider uncertainty in contextual information that features the heterogenous buying behavior of individual consumers. Eq. (2.1) is assumed to have a known formula, however, its parameters are unknown due to insuÿcien t data. Maximum likelihood estimation is applied for a learning of unknown parameters. Valogianni et al. [379] apply dynamic pricing to smooth peaking demand of electricity. The study employs an MNL model for a consideration of heterogeneous electric vehicle owners. A cost function and constraints are incorporated in the modeling of consumers' utility [379]. The uncertainty is modeled by stochasticity in total demand, unknown parameters of some given formulas of Eq. (2.1). A learning of unknown parameters is introduced to approximate an optimal price.

Consumers' utility is also applicable in the modeling of multiple products. Sauré and Zeevi [325] use an MNL model to address optimal prices of multiple products. Two

types of uncertainties exist in consumers' behavior. The one is related to unknown consumers' preference over multiple products. The other one is related to unknown formula of Eq. (2.1). Algorithms that simultaneously trade off the learning of Eq. (2.1) and the earning of immediate revenue are proposed to address those two types of uncertainties [325]. Du et al. [111], Besbes and Sauré [38], Rusmevichientong et al. [321], Rusmevichientong et al. [320], Li and Huh [222], and Wang [385] are selections of studies that utilize an MNL or an NL models for dynamic pricing of multiple products. Chen and Chen [70] provide an overview of recent advances in dynamic pricing with multiple products.

The concept of utility captures consumers' heterogeneous preference behavior when facing multiple choices. A premise is that individual consumers maximize their utilities when making purchase decisions [70, 297, 361]. However, consumers do not always maximize utilities for a buying choice [70]. They may use an alternative rule to make a purchase decision [70, 203, 205]. The rule is related to an observation of historical prices. Price expectations are thus assumed in the modeling of consumers who make purchase decisions via an observation of historical prices.

2.3.2 Reference prices

Consumers' availability to data has been increased as well [88]. Consumers have data-driven behaviors, which is supported from four perspectives. Firstly, for individual consumers, accesses to online communities and social networks become easy owning to a rapid growth of digital technology. Empirical study shows that consumers learn from past buying experiences and utilize social information for a future purchase decision [98].

The second perspective is related to a reduction of *search frictions* in online marketplaces. A search friction is an impediment that imperfect information between sellers and consumers induces [108]. In a dynamical market, a set of information changes regularly and irregularly. The changes occur in a high dimensional system that consumers can neither access nor be aware of [108]. The inaccessibility or the unawareness induces a search friction. More details can be found at the Prize in Economic Sciences in Memory

of Alfred Nobel [365, 366]. The prize was awarded jointly to Peter A. Diamond, Dale T. Mortensen and Christopher A. Pissarides "for their analysis of markets with search frictions" [365]. Dinerstein et al. [108] point out that the design of an online platform, which makes a tradeoff between reducing search frictions and intensifying price information, considerably affects consumers' buying behavior. The accuracy of demand predictions thus relies on the ability to capture consumers' data-driven behavior.

Thirdly, price expectations are unignorable for consumers to make a purchase decision. As consumers repeatedly buy goods or services, "consumers' purchase decisions are also determined by past observed prices" [300]. Consumers can develop a price expectation from historical prices [300]. The price expectation, also termed reference price, becomes a benchmark against current sales prices. The benchmarking behaviors are supported by prospect theory [183, 377] in economics and empirically observed by Kopalle and Lindsey-Mullikin [203] and Tereyagoglu et al. [364].

Finally, many online platforms have records of historical prices of a product or a service, which enables consumers' benchmarking behaviors. For example, a proliferation of web tools help consumers' purchase decisions for airline tickets [223]. Those web tools include Expedia, Booking, Kayak, and so on.

Those four reasons motivate the modeling of reference prices for dynamic pricing problems. Two ways exist in the modeling of reference prices: an exponential decaying memory of historical prices and a learning of underlying equations that describe consumers' reference price (Fig. 2.1). The former way utilizes a given function to quantify the relationship between a price and a reference price (reference function). The latter way learns the underlying equations of reference prices from data.

2.3.2.1 Exponential decaying memory

The first way is based on the assumption that consumers' reference prices satisfy

$$r_{t+1} = \alpha r_t + (1-\alpha) p_t \tag{2.2}$$

where at time t, r_t represents consumers' reference price, p_t represents the sales price, and α is a memory rate representing consumers' adaptions to historical prices. Eq. (2.2) describes how human beings' memory fades [300], which likes an exponential function.

Deterministic scenario. A use of Eq. (2.2) is for obtaining managerial implications by an analytical solution to a hypothetical model. Some phenomena that are observed in practical dynamic pricing problems are captured by the hypothetical model. Popescu and Wu [300] utilize the exponential smoothing (Eq. 2.2) to model reference price mechanism. The authors propose a deterministic demand equation and develop a Bellman equation to address optimizations. The focus is on analytical solutions for managerial implications under different dynamic pricing settings. Fibich et al. [129] develop a hypothetical model by a continuous version of the exponential smoothing (Eq. 2.2), that is, $r^{'} = \alpha(p - r)$. Similar to Eq. (2.2), r represents the reference price, p represents the sales price, and α represents the memory rate. The attentions are on methods that lead to an explicitly analytical solutions to the hypothetical model.

Eq. (2.2) can also be used to capture consumers' asymmetric behaviors when sales prices and reference prices are compared. Fibich et al. [129] utilize a discontinuous demand function to reflect asymmetric responses of consumers to a perceived gain, $p \leq r$, and to a perceived loss, $p > r$. Nasiry and Popescu [270] consider the discrete version (exponential smoothing) of optimization models of Fibich et al. [129]. The focus is on the so-called loss-averse consumers [270] . If consumers are more sensitive to a perceived loss, $p_t > r_t$, than to a perceived gain, $p_t \leq r_t$, then consumers are loss averse. Analytical solutions are addressed by a Bellman equation [270]. Hu et al. [175] consider gain-seeking consumers. If consumers are more sensitive to a perceived gain than to a perceived loss, then consumers are gain-seeking. Border collision bifurcations are observed in [175], however, a bifurcation analysis of the discontinuity in demand functions is absent. Hsieh and Dye [173] extend the study of reference prices to perishable products where consumers can be gain seeking, loss averse, or neutral. The optimization problem is transformed to a differential equation with known boundary conditions. Wang [388] introduces heterogeneity in consumers' arrival periods, thus consumers have been divided

into different groups and assigned to different time periods. The assumption that the arrivals of consumers are periodic allows to directly obtain analytical solutions. However, the assumption is made without an identification of demand dynamics

Stochastic scenario. Noise can be involved in the modeling of reference prices. Güler et al. [161] introduce additive noise to the model that Popescu and Wu [300] develop. Maximizing expected revenue becomes the object of the hypothetical model. The optimization is then solved by dynamic programming [161]. Chen et al. [78] consider additive noise in the model developed by Hu et al. [175]. The focus is on loss-averse consumers. Bellman equations are proposed to solve maximal expected revenue of the hypothetical model [78]. Wu et al. [399] consider multiplicative noise for the analysis of maximal revenue by dynamic programming.

Optimization algorithms. An analytical solution is diÿcult to be obtained from a hypothetical model with discontinuity. However, asymmetric behaviors of consumers induce a discontinuity. One stream of studies therefore focus on algorithms that lead to an analytical solution in the modeling of reference prices. Chen et al. [77] provide a dynamic programming algorithm. The algorithm costs a polynomial time for a solution to discontinuous optimization problems. Cohen et al. [87] extend the hypothetical model of Popescu and Wu [300] to multiple products (reference price model). Maximizing revenue is translated into the longest path problem in a weighted graph. The results show that a hypothetical model considering reference prices and multiple products is an NP-hard problem [87]. Indeed, "maximizing a submodular function is generally NP-hard" [85]. Discontinuity in demand function often leads to budget-additive demand functions, for example, in terms of multiple products or intertemporal pricing decisions. A budget-additive function is a function in the form of $f(S) = \min\left\{B, \sum_{i \in S} \omega_i\right\}$ [55] where S and B are a set.

Equilibrium price. Eq. (2.2) can also be used to model equilibrium prices. Game theory is then applied to model interactions between agents. Zhang et al. [411] utilize the continuous version of the exponential smoothing for the modeling of consumers' sen-

sitivity to reference prices. An equilibrium price between a manufacture (a Stackelberg leader) and a retailer (a follower) is derived from Stackelberg differential game. Chen et al. [67] extend the hypothetical model of Zhang et al. [411]. Two sequential events are considered related to consumers' purchase decisions. Consumers firstly develop reference prices, and then choose a purchasing time. A two-period Stackelberg game is introduced to obtain an equilibrium price [67]. Coulter and Krishnamoorthy [91] consider reference prices in a competitive market with multiple sellers. Consumers show different sensitivity to reference prices for different products. Nash equilibrium gives a solution to competitive demand [91].

2.3.2.2 A learning of reference functions

Another stream of studies do not use a fixed equation such as Eq. (2.2) in the hypothetical model. The underlying equation of reference prices is learned from data (Fig. 2.1). The modeling is similar to the modeling of unknown arrivals (section 2.2.2) or unknown demand equations (section 2.2.3). Cao et al. [61] extend the hypothetical model of Araman and Caldentey [12] where the market size is assumed to be a proxy of arrivals. Consumers are assumed to have the exponential smoothing of reference prices (Eq. 2.2) and be neutral to losses. The knowledge of the market size is updated by a Bayesian inference. The learning of equations that describe reference prices is addressed by dynamic programming [61]. den Boer and Keskin [103] consider two types of uncertainty. The one is in the form of demand shocks. The other one remains in unknown parameters of some known equations. Consistent with the modeling in [40, 191], a demand shock is represented by additive noise. The parameters defining the equation of reference prices are relaxed to be unknown vectors with known bounds. The algorithm, simultaneous explorations and exploitations, is applied to learn the unknown parameters [103].

2.3.3 Machine learning methods

Digital technology has changed the behavior of individual agents in a market. Consumers have changed the way to search for information on products and services [142].

Sellers are turning to data-centric analytics of businesses, such as the use of individual-level consumer data for a business [142]. Regulators of governments urge for data-drive methods to make a decision and take actions. Data-drive methods are needed to decide whether a colluding behavior occurs as a dynamic pricing policy is implemented [59]. Once a colluding behavior is identified, data-driven methods are needed to intervene the colluding [59]. Data-driven methods, particularly machine learning methods, have been applied to improve a pricing decision. Machine learning methods have improved the price predictions for Bitcoin [253] and crude oil [224, 417], the price formation of financial markets [338], and empirical asset pricing [157].

Similar to the narrative in previous sections, we review the models that apply machine learning methods for dynamic pricing problems from two perspectives. The first one is what kinds of uncertainty machine learning models consider. The second one is how to solve the uncertainty in the modeling.

Two basic categories existing in the modeling of uncertain demand by means of machine learning methods (Fig. 2.1): hypothetical models and practical applications. hypothetical models mainly focus on developing a data-driven method to approximate demand. The idea is to obtain either parameters of a given equation or to learn the underlying equations for the modeling of demand. Practical applications, however, mainly focus on solving a real-life pricing problem. The application proposes a date-driven algorithm either for implementing or for detecting dynamic pricing policies of a business.

2.3.3.1 Hypothetical models

In this category, machine learning methods address the uncertainty that remains in unknown parameters of a known equation or that in unknown equations. Ban and Keskin [19] propose demand equations with additive noise. Unknown parameters are learned by the LASSO (Least Absolute Shrinkage and Selection Operator) regression, a widely used regression algorithm for machine learning [369]. The LASSO regression provides a reasonable performance bound for a selection of a true model from high-dimensional sparse data [30]. Ban and Keskin [19] consider demand shock and high-

dimensional consumers' features. A known equation with unknown parameters and additive noise describes demand shocks [19]. A solution to the hypothetical model is addressed by the LASSO regression as well [19]. Rana and Oliveira [309] assume that the arrivals of consumers follow a Markov process. The uncertainty is modeled by unknown parameters of known equations. Those unknown parameters are selected from a given set. A solution is derived from reinforcement learning [309]. Similarly, Kim et al. [196] introduce a Markov decision process to model stochastic arrivals of energy consumption. Reinforcement learning gives a solution for an update of the unknown parameters [196]. den Boer and Zwart [105] review studies that apply machine learning methods for a solution to a hypothetical model of dynamic pricing problems.

2.3.3.2 Practical applications

Machine learning methods in a hypothetical model mainly focus on an analytical solution for managerial implications. However, one advantage of machine learning methods is their ability to approximate real-life scenarios by a model-free framework. In the second category, machine learning methods are designed for the data-driven modeling that improves a practical pricing decision. An attention is on algorithms that approximate real-life phenomena without any prior knowledge or sophisticated hypothetical models. Amazon marketplace, the airline industry, and online retails are businesses that have been attracted to machine learning methods for solving dynamic pricing problems.

Amazon marketplace. Chen et al. [69] consider the uncertainty that remains in a lack of transparency in a total number of demand for a product on Amazon marketplace. The opacity results in consumers and regulators without comprehensive knowledge about dynamic pricing algorithms that a seller implements [69]. Chen et al. [69] thus propose an algorithm to crawl the website of Amazon at a given frequency [69]. A dataset with information about sellers, prices, and products is created, contributing to many time series of prices [69]. A correlation analysis among those prices is conducted for identifying the dynamic pricing algorithms of sellers under a lack of price transparency [69]. Schlosser and Boissier [330] study optimal pricing strategies that optimize expected rev-

enue of some seller on Amazon. The uncertainty is assumed to be (1) stochastic arrivals of consumers [330], and (2) stochastic inventory of the seller and that of its competitors [330]. Schlosser and Boissier [330] provide data-driven algorithms to calibrate the unknown parameters.

Airline industry. Shukla et al. [336] propose machine learning algorithms to price airline ancillaries based on consumers features. Departure time, market size, and the length of a stay together constitute consumers features. The uncertainty comes from stochastic arrivals of consumers and their features. By deep neural network, Shukla et al. [336] provide an evaluation metric to classify consumers and harvest expected revenue.

Online retails. Ferreira et al. [126] use machine learning algorithms, regression trees, to predict demand of an online fashion retailer. Three types of uncertainty are considered [126]: (1) stochastic demand, (2) unknown parameters of given demand equations, and (3) limited data for some products. Ferreira et al. [126] apply regression trees to predict expected demand and learn the parameters. Limited data are addressed by transferring knowledge from products with suÿcien t data [126].

We have reviewed the modeling of demand in dynamic pricing problems. The uncertainty is represented by stochastic demand (section 2.2) or by stochastic consumers behavior supported by an economic theory (section 2.3). Apart from the modeling of demand, there are studies that empirically analyze the welfare and the influence of dynamic pricing on agents. Just to mention a few, Cui et al. [94] conduct empirical studies that analyze the influence of dynamic pricing on a seller's revenue and consumer welfare. The attention is on the upgrading in the airline industry [94]. Phillips et al. [296] compare the benefits of static and dynamic pricing strategies for an automotive lender. Abrate et al. [2] analyze the impact of dynamic pricing strategies for hoteliers. Schlereth et al. [329] explain a phenomenon that consumers prefer to refuse an adoption of dynamic pricing in an electricity market. A common feature of empirical studies is that they are equation-centric [94, 296, 329]. The studies rely on a prior knowledge of the underlying equations, since the knowledge affects the accuracy of regressions. Empirical

studies therefore face another type of uncertainty, which remains in the prior knowledge about the underlying equations.

2.4 Deterministic chaos in equilibrium price

According to deterministic chaos [143, 333, 345, 353, 398], nonlinear interactions among variables are a critical source of uncertainty. As shown in the above-mentioned demand models, dynamic pricing problems rely almost entirely on the assumption of stochasticity. Nevertheless, studies exist in equilibrium prices when it comes to a rational route to apparent randomness. The route is attributed to nonlinear interactions between price, demand, and supply. Since this thesis does not focus on equilibrium prices, we just mention a few of studies. Anufriev et al. [10] provide a comprehensive overview of the modeling of equilibrium prices by deterministic chaos in economics and finance.

Uncertainty in demand is the topic. We thus narrate the modeling of equilibrium prices by a rational route from two perspective. The one is what contributes to uncertain demand. The other one is a difference in the modeling of uncertainty between randomness of stochasticity and apparent randomness of deterministic chaos.

A rational route is the focus of the modeling. Brock and Hommes [51] consider the interactions between price, demand, and supply. The interactions are described by heterogeneous beliefs (utility functions), contributing to a rational route [51]. Consumers are allowed to switch among different predicting models. The intensity of the switching behavior is regarded as a bifurcation parameter [51]. A change of the intensity leads to uncertain and even chaotic price fluctuations. Since a nonlinear equation quantifies the switching, apparent randomness occurs due to an internal force, the rational switching behavior [51]. Corcos et al. [89] consider two typical contradict attitudes in stock markets: imitative and contrarian. In [89], the rational route is described by the switching behavior between those two contradicted attitudes. An intermittency of a chaotic system well explains the bubbles and the crashes of stock markets [89]. The uncertainty that circulates stock markets is as a result of the deterministic interactions between imitative

and contrarian consumers[89]. The uncertainty is of internal and belongs to deterministic chaos [89]. Anufriev et al. [11] provide a discontinuous model to fit an asset pricing problem. Two types of traders are placed in a market, both of which have discontinuity in demand [11]. Equilibrium price connects the selling and the buying behaviors of different types of traders [11], constituting a rational route. Internal discontinuities instead of external random forces explain the uncertain fluctuations [11].

2.5 Problem statements

We have shown two different mechanisms in the modeling of uncertainty. The one applies an external force to approximate uncertainty by randomness in a dynamic pricing problem. The other one applies a rational route to approximate uncertainty by apparent randomness in an equilibrium price model. However, a rational route to apparent randomness in the modeling of dynamic pricing problems remains to be elucidated.

2.5.1 Nonlinear interactions

A few studies apply deterministic chaos in the modeling of a dynamic pricing problem. Rump and Stidham [319] introduce an adaption of consumers' price expectations to an equilibrium price model. In the model, an equilibrium price is a solution to a dynamic pricing problem. The adaption represents a rational route to chaos as consumers respond to a queueing congestion. Aperiodic and seemingly random behaviors are observed in the modeling of demand fluctuations [319]. Hu et al. [175] introduce a discontinuous demand function to the modeling of reference prices. Irregular changes in the periodicity of optimal pricing solutions are observed from the hypothetical model [175]. Besbes and Zeevi [40] consider a misspecification of true demand function and observe periodic-2 oscillations. However, the following problems have yet to be fully elucidated.

1. **A rational route to apparent randomness.** Randomness is widely assumed in the modeling of dynamic pricing problems. Demand can be in the form of a random discrete variable [40, 44, 104, 105, 111, 127, 191, 261] or a random continuous variable[18, 35, 140, 287, 389]. As shown in equilibrium price models, a rational

route is able to approximate uncertainty that occurs in real-life financial markets [10, 11, 51, 89]. However, in the modeling of dynamic pricing problems, a rational route still remains to be studied from dynamical systems' perspective.

2. A mutual influence between a rational route and an optimization. For existing studies [40, 175, 319] that exemplify a rational route, an observation of deterministic chaos is a byproduct of simplifying the hypothetical models. The focus is on an analytical solution to the hypothetical model with a purpose for managerial implications. The occurrence of a rational route is due to nonlinearity in the analytical solutions [40, 175, 319]. However, two issues remain unsolved. (1) How does a rational route affect optimal pricing solutions in the absence of an analytical solution to optimizations? (2) How does an optimization affect a rational route? The former issue examines the influence of apparent randomness on optimizations in the modeling of demand. The later issue examines the influence of optimizations on the occurrence of apparent randomness.

3. Bifurcation analysis. For a mathematical curiosity, bifurcation analysis has not been conducted in terms of demand as a continuous variable that quantifies a rational route. Both Hu et al. [175] and Besbes and Zeevi [40] model demand as a continuous variable, the quantity demanded. However, bifurcation analysis has yet been conducted. Rump and Stidham [319] conduct a bifurcation analysis, however, demand is modeled by a discrete variable, an arrival of consumers. Many studies exist in a learning of unknown parameters to address uncertainty in demand equations [16, 19, 52, 102, 103, 120, 228, 268]. Bifurcation analysis provides an alternative method to examine the uncertainty that remains in parameters of a hypothetical model for managerial implications.

4. Discontinuity in optimizations. The algorithms, such as dynamic programming [12, 61, 133, 175, 270, 399], explorations first and then exploitations [37, 39, 83], and simultaneous explorations and exploitations [40, 74, 103, 268, 389], navigate a critical way to an optimal solution for a dynamic pricing problem. Those algorithms

aim either for an analytical solution [40, 115, 129, 133, 175, 270, 319] or for the approaching of a solution [39, 83, 103, 268, 389], yielding a function that describes a relationship between price and demand. The smoothness of the function is not necessarily assured. A discontinuity thus can occur in an optimization that a dynamic pricing problem involves. However, it remains unclear the influence of a discontinuity in an optimization on demand.

2.5.2 Demand dynamics

The modeling of uncertain demand can be based on the assumed randomness of noise (stochastic) [18, 35, 44, 105, 111, 127, 140, 261, 287, 389] and the assumed apparent randomness of a rational route (deterministic) [10, 11, 40, 51, 89, 175, 319]. However, most of hypothetical models directly assume a stochastic demand for dynamic pricing problems [18, 35, 44, 105, 111, 127, 140, 261, 287, 389]. Identifying the dynamics that is responsible for the uncertainty becomes critical in a dynamic pricing problem for two reasons.

An assumption is useful only when it reflects reality. Identifying demand dynamics is to confirm which assumption is suitable in the modeling of uncertainty related to the randomness of noise and the apparent randomness. If one could not observe apparent randomness of a rational route in a real-life dynamic pricing settings, then doubts can be casted to a hypothetical model of the rational route. Similarly, if one could not confirm that the randomness of noise is responsible for the dynamics of a real-life dataset, then a direct assumption of a stochastic demand is always open to a suspicion. For bridging the gap between an assumption and reality, demand dynamics is thus needed to be identified.

The second reason is related to data-driven dynamic pricing for improving revenue. Dynamic pricing relies on optimizations and algorithms that lead to an optimal solution. Dynamic programming [133], explorations first and then exploitations [37, 39, 83], and simultaneous explorations and exploitations [40, 74, 103, 268, 389] are algorithms that are proposed to improve revenue. Those algorithms are mainly for harvesting expected

revenue from the assumed randomness [37, 39, 40, 74, 83, 103, 133, 268, 389]. However, a rational route exists in the apparent randomness [10, 11, 51, 89, 175, 319], which is fundamentally different from the randomness of noise. An identification of deterministic dynamics in real-life dynamic pricing settings is needed to open a new door for data-driven algorithms. The algorithm could exploit the rational route, thus potentially improving revenue.

Nonlinear time series analysis is employed to identify demand dynamics. A time series is the data that are collected in a real-life dynamic pricing setting. Empirical studies focus on the data as well. However, nonlinear time series analysis looks at the data from dynamical systems' perspective. Empirical studies primarily fit the data with known equations [2, 94, 296, 329]. The fitting neglects the points that have no obvious statistical meanings. Nevertheless, every part of a nonlinear system counts, including those points without a statistical significance. Nonlinear time series analysis takes the data as a whole [188]. The dynamics is then studied in a phase space [188].

Identifying demand dynamics covers dynamic pricing and nonlinear time series analysis, thus closing the gap between the two research fields. On the one hand, the application of nonlinear time series analysis is extended to a real-life dynamic pricing setting. On the other hand, nonlinear time series analysis gives fresh knowledge of the data that are widely assumed to be stochastic.

2.5.3 Attractor-based demand predictions

Once deterministic dynamics is identified from a real-life dynamic pricing setting, a future study is to use the rational route for data-driven demand predictions. The prediction is then placed into chaos prediction, which is a problem to be solved in deterministic chaos. On the one hand, machine learning methods seemingly promise chaos predictions [293]. The methods show the ability to approximate maximal Lyapunov exponent [292] and to calculate other invariant measures, such as correlation dimension [248]. On the other hand, machine learning methods are transforming the way to model and solve dynamic pricing problems [19, 30, 69, 105, 126, 142, 196, 309, 330, 336, 369]. A question

is raised, how can we apply machine learning methods that mimic deterministic chaos for demand predictions?

The following two problems are needed to be addressed to pave the way for an answer to the question. (1) Can an artificial system that mimics deterministic chaos in the sense of a coincidence in chaotic trajectories be applied for high-fidelity predictions, such as demand predictions? (2) What property does an artificial system have could lead to a good performance in mimicking deterministic chaos for high-fidelity predictions?

2.5.4 Challenges

We have identified three research gaps in the modeling of dynamic pricing problems. Those gaps are a hypothetical model with a rational route to apparent randomness, an identification of demand dynamics from dynamical systems' perspective, and the learnability of an artificial system. Hypothesis A (cf. Chapter 1 section 1.6.2) is concerned with the first and the second gaps. Hypothesis B (cf. Chapter 1 section 1.6.2) is concerned with the third gap. Three challenges exist in bridging the gaps

1. A hypothetical model that describes reality. As May indicates [249], a simple logistic map ($x_{n+1} = rx_n(1-x_n)$) with one nonlinear term is enough to exhibit uncertainty in its fluctuations. However, a challenge comes from the type of nonlinearity that explains demand fluctuations and that approximates reality.

2. Reconstructed attractors from real-life demand. For real-life demand, its nonlinear dynamics should be identified prior to assumptions. To make an assumption that approximates reality, nonlinear time series analysis should be further conducted. However, a challenge comes from signals in real-life scenarios, which are inevitably contaminated by noise [188]. A novel method being consistent with the dynamics that the data underlies should be proposed. Also, an attractors should be reconstructed from real-life demand signals.

3. Artificial systems' sensitive dependence on initial conditions. Machine learning methods are increasingly applied for chaos predictions. The sensitive depen-

dence on initial conditions remains unclear and to be compared between a mimicked chaotic system (input) and an artificial system (output). The challenge comes from machine learning methods, which work in a black box without analytical formulas that describe the dynamics. Experiments should be conducted to compare between the supposed and the actual behaviors of an artificial system under varying initial conditions for high-fidelity chaos predictions.

This thesis is to bridge the above-mentioned three gaps. Chapter 3 resolves the four problems related to a hypothetical mode that applies a rational route to approximate uncertain demand. Chapter 4 provides a new recurrence-based paradigm to reconstruct an attractor from real-life demand signals. Finally, chapter 5 applies nonlinear time series analysis on artificial systems. The focus is on the supposed and the actual behaviors under varying initial conditions.

Chapter 3

Bifurcation analysis of dynamic pricing processes with nonlinear external reference effects

Abstract

Dynamic pricing has been widely implemented to hedge against volatile demand. One challenging problem is the study of optimal price choices under the influence of this volatility. Stochastic demand is a prevalent assumption when it comes to modeling the volatility on pricing decisions. However, demand volatility might also be produced by deterministic chaos, which has rarely been studied in this field of research to-date. We propose deterministic dynamic pricing processes that aim to maximize revenue and to mimic a real pricing decision. Our model includes nonlinear consumer expectations that explain the effects of external information on consumers and discrete optimizations. A non-smooth demand function models asymmetries in the perceptions of gains or losses of consumers, and finite price choices of companies are considered in the optimizations. Volatility can show up because of non-periodic consumer expectations, period adding bifurcations, codimension-2 points, and coexisting solutions.

Our results highlight that optimal pricing strategies should agree with the dy-

namics of consumer expectations. Disregarding deterministic dynamics may not only cause revenue losses in practice but might also mislead regulators about the underlying mechanisms that consumers and companies respond. We introduce an *irregular pricing strategy*: a company can make the first return iteration of each sales price non-periodic to follow non-periodic consumer expectations when having finite price choices. The results may justify implementing irregular pricing strategies in the case of practical pricing decisions. Here, the existence of coexisting solutions can assist in identifying potential market manipulations within a monopoly market. This contributes to a fresh look in volatile markets and emphasizes the importance of initial conditions to pricing decisions and price regulations.

3.1 Introduction

Pricing decisions always involve a dilemma. A high price may lead to losses in numbers of potential consumers. A low price, however, may lead to losses in potential revenue [297, 361]. Therefore, many businesses, including the airline, the hospitality industry, also energy providers, and retailers, have already implemented dynamic pricing models for harvesting optimal revenue [70, 297, 361].

Dynamic pricing works as a pricing tool in a seller's decision. While implementing a dynamic pricing strategy, companies (sellers) monitor and update their knowledge of demand [41, 71, 297, 361]. This demand-based knowledge enables companies to optimize their revenue by setting the sales price as the optimal one [41, 71, 297, 361], turning a price into a useful hedge against volatile markets. An optimal price choice is different from an equilibrium price. An equilibrium price results from demand quantity equalling supply quantity. An optimal price choice is derived from an optimization process that satisfies the objectives of a company. An equilibrium price is widely used to model a market in which an equilibrium can be reached infinitely fast [51, 162, 265, 407]. However, dynamic pricing addresses an optimal price during a transition to the equilibrium.

The transition can be either instantaneous or delayed, depending on market struc-

ture. In a competitive market, demand and supply quickly respond to each other. A transition to an equilibrium is negligible. An equilibrium price is thus reached almost instantaneously. However, there exists a market in which the supply of goods is often scarce or diÿcult to be adjusted within a short time frame [297], for example, a monopoly market. An extended duration of a transition occurs.

Prolonged transition time, however, is advantageous both for pricing decisions and price regulations, since market participants can learn from the evolution of demand. Prolonged transition time allows a seller to benefit from a dynamic pricing strategy. The strategy utilizes engineered revenue management tools and fixed distribution systems for optimal revenue [297, 361]. On the other hand, prolonged transition time allows a policy-maker or a regulator to understand how companies react to demand by observing a change of prices. Based on the understanding, the policy-maker or the regulator can counteract and re-establish market mechanisms in line with competition laws or discourage abusive pricing strategies [186].

A diÿcult y in implementing a dynamic pricing strategy comes from obtaining an optimal price choice in strong market volatility [297]. To achieve it, hypothetical models exist to model the volatility [4, 41, 71, 90, 165, 175, 220, 319]. The idea is to obtain a solution from a hypothetical model that approximates some phenomena in reality, so one can derive managerial implications for guiding actions as a similar situation occurs in practice. A stochastic demand and probabilistic approaches are prevalent in the modeling of a volatile market [4, 41, 71, 90, 165, 220]. Ajorlou et al.[4] model the arrival of consumers using a Poisson process. Cosguner et al. [90] and Harsha and Dahleh [165] assume that demand follows a Markov process. Chen and Chen [71] take the bound of demand as a stochastic variable with known expected value.

Deterministic chaos provides an alternative way to model the volatility [1, 22, 188, 277]. In the modeling of an equilibrium price, a rational route is used to approximate volatile markets. [51, 162, 220, 407]. Brock and Hommes [51] allow a rational adaption of price predictions in a demand-supply model that quantifies the relationship between

equilibrium prices, demand, and supply. The rational adaption results in apparent randomness that explains the volatility of equilibrium prices. Similarly, a rational route with aperiodic dynamics explains the dynamic behavior in advertising decisions [162], the market collapses [220], or the volatile behavior within a market that contains social interactions [407]. As indicated by Abrams et al. [1], a dynamical system that underlies deterministic dynamics is able to explain social group competition. The system can evolve in a nearly identical way as that of a discrete stochastic model [1].

A rational route that explains uncertain demand remains rare in operation research that focuses on a hypothetical model of dynamic pricing problems for managerial implications. Rump and Stidham [319] allows a rational adaption of price expectations. The rational route that follows equilibrium prices explains irregular arrivals of consumers [319]. Hu et al. [175] build a hypothetical model to obtain an analytical solution that quantifies the relationship between an optimal price and demand. The analytical solution contributes to a rational route, which explains irregular dynamics in the periodicity of periodic solutions. Rump and Stidham [319] look at explicit solutions and analyze the volatility of consumers' arrivals from dynamical systems' perspective. Hu et al. [175] consider the quantity demanded and focus only on periodic solutions for managerial implications. Demand, as the quantity demanded, remains to be elucidated from dynamical systems' perspective in the modeling of a dynamic pricing problem.

This chapter extends the hypothetical model of Hu et al. [175] by allowing adaptive and aperiodic consumers' price expectations. The focus is on a dynamic pricing problem where optimizations are involved. We aim to explain volatile demand from dynamical systems' perspective. A hypothetical dynamic pricing model is proposed merely to justify the alternative and rational route to volatile demand. This chapter does not aim for a practical model that fits a real-life dynamic pricing dataset. However, we aim for the strategies and the actions of market participants under the volatility that a rational route induces.

3.2 Background

This chapter analyzes the volatility according to the theory of deterministic chaos. Three types of knowledge will help understanding the hypothetical model and the analysis. They are the reference effect, the logistic map as a canonical model in deterministic chaos, and the border collision bifurcations.

3.2.1 Reference effects

Expectations are indispensable to influence individual decision making processes [356], including consumers' purchase decision. When consumers are trying to make purchase decisions, their price expectations act as a reference [129, 175, 205, 270, 300]. If a price expectation is higher than the current sales price, then consumers may perceive a discount in the price of a product. The transaction thus appears as a potential *gain* for a consumer. By contrast, if a price expectation is lower than the current sales price, then consumers may perceive a price surcharge. The transaction is thus perceived as a potential *loss*. A gain is more likely to initiate a purchase. However, a loss is less likely to achieve the same effect [78]. The effect of a perceived gain or loss on the quantity demanded is called *reference effect*.

In pricing decisions, a consideration of consumer expectations may allow companies to take countermeasures avoiding revenue losses [300]. However, the modeling of a volatile market rarely considers consumer expectations [70]. The main reason to the rareness is a lack of universal equations to model a reference effect. Our hypothetical model considers consumer expectations. We shall need to formulate consumer expectations.

In a purchase decision, an estimation of consumer expectation is often based on historical prices [175, 206, 250, 270]. Our hypothetical model will consider consumer expectations. The expectations are developed from two sources. The one is solely based on historical prices. The other one is based on information that is unrestricted to historical prices. We introduce *internal reference price* (IRP) and *external reference price* (ERP) to model those two types of consumer expectations, respectively. Expectations,

which are solely developed from historical prices, are here referred to as an IRP [250]. Optimal price choices have been studied when demand fluctuates according to the IRP [129, 175, 205, 206, 270, 300]. A *constant pricing strategy* is optimal when consumers are more sensitive to a loss than to a gain [129, 205, 206, 300]. A *cyclic pricing strategy* becomes optimal when consumers are more gain sensitive [175, 205, 300]. Since the both, constant and cyclic pricing strategies follow regular patterns, they are referred to as *regular pricing strategies* in the following.

Yet the IRP fails to model information other than historical prices on optimal price choices. This other information, which will be called in the following *external information*, is shown to be measurable on consumer expectations. Examples include the inventory availability [364], the text font in printing a price tag [255], the list price [203] or the prices of competitors [130].

External information may also account for nonlinearity in consumer expectations. On the one hand, external information can lead to opposing effects on consumer expectations [167, 265]. Imitation and distinction both play an important role in purchase decisions such as in the case of fashion products [265]. Here, external information is represented by the number of individuals who choose an identical product. The greater that number is, the more likely consumers become satisfied due to a so-called imitation effect. Yet, consumers can also get more dissatisfied expectations due to a so-called distinction effect. As a result, consumers can get contradicted expectations out of identical external information [265]. The contradiction thus results in nonlinear consumer expectations.

On the other hand, consumer expectations interact with external information [407]. The observation of consumer expectations is influential in individual purchase decisions, contributing to a realization of external information. Nonlinear interactions between external information and consumer expectations can thus be observed [407]. To overcome the limitation of the IRP, we incorporate nonlinearity and allow consumers to develop two levels of price expectations: an IRP and an ERP. Here, an ERP represents consumer expectations that are nonlinear and developed via external information. Consistent

with the IRP-induced reference effects [129, 175, 205, 206, 270, 300], we assume that comparisons between the ERP and the sales price also can lead to the perception of either a gain or a loss. In the following, reference effects that an IRP induces are named internal reference effects, and those an ERP induces are named external reference effect.

3.2.2 Logistic map

Logistic map is a toy model that exemplifies complicated behavior emerging from a rational route in deterministic chaos [106, 143, 170, 249, 333, 353]. Its mathematical formula is $x_n = F(x_{n-1}) = rx_{n-1}(1-x_{n-1})$ where r is a parameter that determines the system's behaviors. The map is a canonical form of the logistic equation that models the population growth in an ecosystem [249]. Varying the parameter r allows the logistic map to exhibit "an extraordinarily rich spectrum of dynamical behavior, from stable points, through cascades of stable cycles, to a regime in which the behavior (although fully deterministic) is in many respects "chaotic", or indistinguishable from the sample function of a random process" [249].

The complicated behavior depends on the stability of fixed points [249, 346]. A fixed point x^* is a solution to $x^* = rx^*(1-x^*)$. Two solutions exist, $x^* = 0$ and $x^* = 1 - \frac{1}{r}$. The stability is characterized by the Jacobian at the point x^*, that is, $J = |\frac{dF(x)}{dx}| = |\frac{dx_n}{dx_{n-1}}| = |r(1-2x_{n-1})|$ [392]. If $J(x^*) < 1$, then x^* is a stable solution; otherwise, x^* an unstable solution. For $0 < r < 1$, the map converges to the stable solution $x^* = 0$, and $x^* = 1 - \frac{1}{r}$ is unstable [346, 392]. At $r = 1$, a bifurcation occurs where $x^* = 0$ becomes unstable, however, $x^* = 1 - \frac{1}{r}$ becomes stable [346]. For $1 < r < 3$, the map converges to the stable solution $x^* = 1 - \frac{1}{r}$ [346]. For $r = 3$, both $x^* = 0$ and $x^* = 1 - \frac{1}{r}$ become unstable [346].

We then focus on successive two iterations in the map, that is, $x_{n+2} = F(F(x_n))$, a quartic equation. By letting $x^* = F(F(x^*))$, four solutions are derived. They are $x^* = 0$, $x^* = 1 - \frac{1}{r}$, and another two solutions $x^*_{\pm} = \frac{r+1\pm\sqrt{(r-3)(r+1)}}{2r}$ [346]. At $r = 3$, $x^* = 1 - \frac{1}{r} = x^*_{\pm}$. Only for $r \geq 3$, $x^*_{\pm}$ are real numbers [346]. So for $r > 3$, the map exhibits oscillations on successive iterations. As before, the stability of $x^*_{\pm}$ depends on

the Jacobian, $J = |\frac{dF(F(x))}{dx}|$. For $3 < r < 1+\sqrt{6}$, x_n oscillates between $x^*_{\pm}$. The map is a period-2 orbit. This process continuous as r increases. A period-2^{k-1} cycle with $k = 1, 2, \cdots$ becomes unstable, simultaneously bifurcating to a period-2^k orbit. This is called period doubling routine [346]. The doubling routine is quantified by a universal number [170, 346], known as the Feigenbaum constant, $\delta = \lim_{k\to\infty} \frac{r_k - r_{k-1}}{r_{k+1} - r_k} = 4.669201\ldots$ [121, 122]. Here, r_k is the parameter where the period-2^k orbit appears. For the logistic map, the Feigenbaum sequence is $r_1 = 3$ (period-2), $r_2 = 1+\sqrt{6} = 3.449490\ldots$ (period-4), $r_3 = 3.544090\ldots$ (period-8), $r_4 = 3.564407\ldots$ (period-16), $r_5 = 3.568759\ldots$ (period-32), $r_6 = 3.569692\ldots$ (period-32), $r_7 = 3.569891\ldots$ (period-128), $r_8 = 3.569934\ldots$ (period-256), $r_9 = 3.569943\ldots$ (period-512), $r_{10} = 3.569945\ldots$ (period-1024), $\cdots$, $r_\infty = 3.569945\ldots$ [346, 392]. The Feigenbaum number $\delta = 4.669201\ldots$ is universal for arbitrary unimodal maps with quadratic maximum. The bifurcating behavior is called a period doubling bifurcation.

Beyond some critical value r_∞, the logistic map can become aperiodic and never revisit previously exact states [249, 346], although it visits arbitrarily small neighborhoods of previous states. The period doublings give way to chaos [249, 346]. Those complex behaviors can be visualized from a bifurcation diagram (Appendix C, Fig. C.3A). The diagram plots all possible steady states (transients has been disposed) of x_n as a function of the parameter r [346, 374].

3.2.3 Border collision bifurcation

As shown in empirical studies [153, 185, 206, 339], a positive effect of a perceived gain on demand can be unequal to a negative effect of a perceived loss on demand. A smooth demand function is incapable of reflecting that asymmetrical phenomenon. Conversely, a non-smooth function can reflect the asymmetrical phenomenon. One can let a point fail to be differentiable at those points where an asymmetrical phenomenon occurs. For example, Hu et al. [175] use a demand function that does not have a differential at the point where the price equals an IRP. We will discuss the modeling of an asymmetrical phenomenon by a non-smooth function in section 3.4.

However, a non-smooth demand function can cause border collision bifurcations (BCB) in dynamic pricing processes [175, 233]. The BCB or grazing bifurcations are widely observed in non-smooth or piece-wise smooth systems. Impact or friction oscillators, aeroelastic systems, or mathematical models with economic applications are known to exhibit complex dynamic changes [148, 225, 372, 382, 404]. BCB is a discontinuity-induced bifurcation [274, 275]. Its mathematical definition can be summarized as follows. Assume a map f_m is defined over two non-overlapping regions S_1 and S_2. The definition satisfies [34]

$$f_m(x,r) = \begin{cases} F_1(x,r), \text{ if } x \in S_1 \\ F_2(x,r), \text{ if } x \in S_2 \end{cases}$$

where F_i with $i = 1,2$ is a smooth function defined in S_i, and r is a parameter that determines the dynamical behavior of the system. Assume that a smooth boundary ∂S exists between S_1 and S_2, and f_m is continuous across the boundary, then a smooth function $E(x,r)$ exists such that [34]

$$F_2(x,r) = F_1(x,r) + E(x,r)$$

where $E(x,r)$ is defined in $S_1 \cup S_2 \cup \partial S$. At a given parameter $r = r^*$, a fixed point x^*, a solution to $x^* = f_m(x^*)$, undergoes a BCB, if $x^* \in \partial S$ satisfies $F_1(x^*,r^*) = F_2(x^*,r^*)$, however, the Jacobian calculated in S_1 is unequal to that in S_2 [34, 422], that is,

$$\frac{\partial F_1}{\partial x}(x^*,r)\bigg|_{r=r^*} \neq \frac{\partial F_2}{\partial x}(x^*,r)\bigg|_{r=r^*}$$

The definition can be extended to a period-k point undergoing BCB by the k^{th}-iteration map f_m^k and the Jacobian at the point.

Period incrementing and adding bifurcations are essential elements of systems that exhibit border collisions [139, 149, 265, 289]. Period incrementing bifurcations correspond to an increase or decrease in the period by a positive integer [289, 372]. Period adding bifurcations can be observed when the period follows the Farey sequence [139, 148, 265, 289] and have been recently shown by Lu et al. [233] in a dynamic pricing model with asymmetrical reference effects. The Farey sequence is a sequence with some fixed order [391]. In Appendix B Figs. B.3 and B.4 exemplify a Farey sequence.

3.3 Model

Dynamic pricing processes involve consumers that make a purchase decision and companies that make a pricing decision. In the period $n \in \mathbb{N}$, consumers have an internal (^{I}) reference (r) price (IRP) r_n^I and an external (^{E}) reference price (ERP) r_n^E. Observing an IRP and an ERP, a company maximizes the revenue by a sales price p_n. Yet, the IRP and the ERP evolve from that sales price [203, 250]. The following map expresses the interdependence among the IRP r_n^I [129, 175, 205, 270, 300], the ERP r_n^E [167, 202, 203, 250, 265, 407], and the sales price p_n [129, 175, 205, 270, 300]

$$r_n^I = \alpha r_{n-1}^I + (1-\alpha) p_{n-1} \tag{3.1a}$$

$$r_n^E = h(r_{n-1}^E, r_{n-1}^I, p_{n-1}) \tag{3.1b}$$

$$p_n = f(r_n^E, r_n^I) \tag{3.1c}$$

where α is a memory rate, and the function h models an ERP. Importantly, the function f describes a solution to an optimal revenue. Also, f represents an optimal pricing strategy that companies should follow for avoiding potential revenue losses. The following subsections will define each function and explain the IRP and the ERP, and the optimal choices of a sales price. Appendix A, section A.1, provides a pseudo-algorithm (cf. Algorithm A.1) to iterate Eq. (3.1).

3.3.1 Internal reference price

Eq. (3.1a) represents a memory-based process that models an IRP based on historical sales prices [129, 175, 205, 270, 300]. Given an initial IRP r_0^I, Eq. (3.1a) is equivalent to

$$r_n^I = \alpha^n r_0^I + (1-\alpha)(\alpha^{n-1} p_0 + \alpha^{n-2} p_1 + \cdots + \alpha^0 p_{n-1})$$

The memory rate $\alpha \in [0,1]$ weighs consumer adaptations to historical prices p_k with $k = 0, \cdots, n-1$. When $\alpha = 0$, an IRP is retrieved from the last sales price p_{n-1}. The larger α is, the slower consumers adapt to historical prices. When $\alpha = 1$, no adaptation exists, and an IRP becomes a constant being equal to r_0^I. Here, r_0^I is intrinsically related to the value of products, and it reflects the price evaluation of consumers on their first

purchase. Following Hu et al. [175], we let $r_0^I \in [0,U]$ and $p_n \in [0,U]$. Here, U is the maximal price representing a price celling or a price that renders demand to be zero.

3.3.2 External reference price

Eq. (3.1b) represents the evolution of an ERP. Three empirical observations are considered in the modeling of an ERP.

A. Based on empirical evidence [202, 203], a nonlinear model especially a quadratic model should be better suited than a linear model to evaluate the ERP.

B. Interactions between external information and consumer expectations are common in reality [167, 265, 407].

C. Historical prices are an important determinant on consumer expectations [250].

The key idea behind observations A and B is that consumers often use external information to develop contradicted expectations in a purchase decision [167, 265]. Observation C originates from the importance of price stimuli that consumers absorb in their expectations [250].

Based on those observations, we assume that an ERP comprises two components: evaluating external information and absorbing an ERP into an IRP. The model is expressed by

$$\frac{r_n^E}{\tau_E} = \beta V_n + (1-\beta)\frac{r_n^I}{\tau_I} \tag{3.2a}$$

$$V_n = \mathcal{A}\frac{F_n}{\tau_F}(1-\frac{F_n}{\tau_F}) \tag{3.2b}$$

$$\frac{F_n}{\tau_F} = \mathcal{B}\sin\frac{\pi r_{n-1}^E}{\tau_E} \tag{3.2c}$$

In Eq. (3.2a) $V_n \in [0,1]$ represents consumer evaluations of external information, and $\beta \in [0,1]$ weights the effect of absorption. The larger β is, the less effective the absorption is. For $\beta = 0$, any external information is excluded, which results in an ERP being absorbed by an IRP. In this setting, the model degenerates into that of Hu et al. [175]. At $\beta = 1$, an ERP is free from the influence of an IRP. Eq. (3.2a) models the observation C and describes the dependence of an ERP on historical price by an IRP.

In Eq. (3.2b) F_n represents the value of external information that produces opposite effects on consumer expectations. Here $\mathcal{A} \in [0,4]$ is the coefficient of consumer evaluations of external information. Eq. (3.2b) models the observation A. It exemplifies the opposite effects of external information on consumers' evaluation of ERP by means of a quadratic term. Although many types of nonlinearity exist, we use a quadratic term in the hypothetical model to be consistent with the empirical observations [202, 203]. For real-life dynamic pricing models, the choice of the type of nonlinearity should be consistent with the dynamics of data.

In Eq. (3.2c) $\mathcal{B} \in [0,1]$ represents the amplitude of the interactions between external information and an ERP. We simplify the evolution of an ERP for obtaining managerial implications, and thus introduce the parameters τ_E, τ_F, and τ_I that nondimensionalize an ERP, external information and an IRP, respectively. Also we let $\tau_E = \max\{r^E\}, \tau_F = \max\{F_n\}$, and $\tau_I = U$. Here, $r_0^E \in [0, \tau_E]$ is an initial ERP, which represents an expectation that consumers hold on the first purchase. Eq. (3.2c) models the observation B and describes the interactions between external information and an ERP. Since $\frac{r_{n-1}^E}{\tau_E} \in [0,1]$ (Eq. 3.2c), we use a sine term only for an approximation of nonlinear interactions with unimodality such as a quadratic effect. Generally, a sine function can be used to model a seasonal force [167], so Eq. (3.2c) can approximate a seasonal force with unimodality. Our model does not consider seasonal forces. The use of a sine term is for mathematical curiosity. Fresh knowledge can be derived from dynamical systems' perspective, in case a similar season force is involved in a hypothetical model.

Finally, h in Eq. (3.1b) has an explicit formula. Plugging Eqs. (3.1a), (3.2b) and (3.2c) to Eq. (3.2a) yields an explicit definition of h

$$\begin{aligned} \frac{r_n^E}{\tau_E} &= h(r_{n-1}^E, r_{n-1}^I, p_{n-1}) \\ &= \beta\mathcal{A}\mathcal{B}\sin\frac{\pi r_{n-1}^E}{\tau_E}(1 - \mathcal{B}\sin\frac{\pi r_{n-1}^E}{\tau_E}) + (1-\beta)\frac{\alpha r_{n-1}^I + (1-\alpha)p_{n-1}}{\tau_I} \end{aligned} \tag{3.3}$$

3.3.3 Demand

Eq. (3.1c) models the evolution of an optimal price as a company aims for a maximal revenue based on demand knowledge $d(p_n)$. In general, $d(p_n)$ is defined by a base demand and internal reference effects [129, 175, 205, 270, 300]. We incorporate external reference price effects into the definition of $d(p_n)$ by

$$d(p_n) = \underbrace{b - ap_n}_{\text{base demand}} + \underbrace{\lambda^I \gamma (r_n^I - p_n)}_{\text{internal reference effects}} + \underbrace{\lambda^E \gamma (r_n^E - p_n)}_{\text{external reference effects}} \tag{3.4}$$

In Eq. (3.4), the base demand describes the influence of the sales price on demand, and the internal and external reference effects describe demand fluctuations that an IRP and an ERP induce, respectively. Here, λ^I and λ^E represent the intensity of internal and external reference effects on demand, respectively. Further, γ represents the consumer sensitivity to a gain or a loss, defined by

$$\gamma = \begin{cases} \gamma^g, & r_n^j > p_n, \text{ with } j \in \{E, I\} \\ 0, & r_n^j = p_n, \text{ with } j \in \{E, I\} \\ \gamma^l, & r_n^j < p_n, \text{ with } j \in \{E, I\} \end{cases} \tag{3.5}$$

where γ^g and γ^l are the consumer sensitivity to a gain and a loss, respectively. Plugging Eq. (3.5) into Eq. (3.4) and substituting these three terms, $c_n = b - ap_n$, $\Delta_n^I = r_n^I - p_n$ and $\Delta_n^E = r_n^E - p_n$, provide a full piece-wise demand function,

$$d(p_n) = \begin{cases} c_n + \lambda^I \gamma^g \Delta_n^I + \lambda^E \gamma^g \Delta_n^E, & r_n^I, r_n^E \geq p_n \\ c_n + \lambda^I \gamma^g \Delta_n^I + \lambda^E \gamma^l \Delta_n^E, & r_n^E < p_n < r_n^I \\ c_n + \lambda^I \gamma^l \Delta_n^I + \lambda^E \gamma^g \Delta_n^E, & r_n^I < p_n < r_n^E \\ c_n + \lambda^I \gamma^l \Delta_n^I + \lambda^E \gamma^l \Delta_n^E, & r_n^I, r_n^E \leq p_n \end{cases} \tag{3.6}$$

In Eq. (3.6) if $r_n^j = p_n$ ($j \in \{E, I\}$), then $\Delta_n^j = 0$, so the corresponding reference effects (cf. Eq. 3.4) disappear. In this setting, the value of γ has no influence on $d(p_n)$.

3.4 Optimization solutions and bifurcation analysis

The function f (cf. Eq. 3.1c) depends on the solutions to an optimization problem. In this section we will present an optimization method, use a symbolic representation to visualize f, and introduce new pricing strategies. Numerical bifurcation analysis is introduced as well.

3.4.1 Optimal price choices

We focus on a short-term dynamic pricing problem. A company maximizes revenue Π in the period n. Here, Π satisfies

$$\Pi = p_n d(p_n) \tag{3.7}$$

where $d(p_n)$ follows Eq. (3.6). Maximizing Eq. (3.7) leads to an optimal price p_n^* via

$$p^*(r_n^E, r_n^I) = \arg\max_{p_n \in [0,U]} \Pi = \arg\max_{p_n \in [0,U]} p_n d(p_n) \tag{3.8}$$

A solution to Eq. (3.8) exists since $p \in [0,U]$ is compact and Π is continuous [129, 175, 270, 300]. If multiple solutions are derived from Eq. (3.8), then the smallest among them is selected for the uniqueness of an optimal price. It is straightforward to get an analytical solution if $\gamma^g = \gamma^l$ (symmetric case). However, if $\gamma^g \neq \gamma^l$ (asymmetric case), the optimization becomes non-smooth, and only numerical approximations of an optimal price can be extracted [77, 129, 204].

However, many promotion-driven consumers exhibit asymmetric sensitivity. Those consumers are more sensitive to a perceived gain than a perceived loss [153, 175], that is, $\gamma^g > \gamma^l$. The phenomenon can be understood in this way. For a promotion where $r_n^j > p_n$ those consumers perceive a gain. According to Eq. (3.6), $r_n^j - p_n$ is the amount of perceived gain, and $\gamma^g(r_n^j - p_n)$ represents an increased amount of demand due to a gain. For a situation where $r_n^j < p_n$ those consumers perceive a loss. According to Eq. (3.6), $p_n - r_n^j$ is the amount of perceived loss, and $\gamma^l(p_n - r_n^j)$ represents a decreased amount of demand due to a loss. Promotion-driven consumers have a following feature. Let assume that a perceived gain is equal to a perceived loss, then the effect of a perceived gain on

demand is larger than that of a perceived loss [153], since $\gamma^g(r_n^j - p_n) > \gamma^l(p_n - r_n^j)$. In line with [175], we focus on those promotion-driven consumers where $\gamma^g > \gamma^l$, although the model is applicable when $\gamma^g < \gamma^l$.

3.4.2 Asymptotically optimal price

We introduce an asymptotical algorithm proposed by Chen et al. [77] for a solution to Eq. (3.8). The asymptotically optimal price p^{**} (a solution) is chosen from a finite set $\mathbb{P}_\epsilon = \{\kappa\epsilon : \kappa = 0, 1, 2, \ldots, N_\epsilon\}$ rather than from $[0, U]$. Here N_ϵ is the number of the divisions of the interval $[0, U]$, with $\epsilon = \frac{U}{N_\epsilon}$. The distance between $\mathbb{P}_\epsilon$ and any feasible solution in $[0, U]$ is smaller or equal to ϵ. The accuracy of the approximation is thus of the order $\mathrm{O}(\epsilon)$. The calculation follows

$$p^{**}(r_n^E, r_n^I) = f = \arg\max_{p_n \in \mathbb{P}_\epsilon} \Pi = \arg\max_{p_n \in \mathbb{P}_\epsilon} p_n d(p_n) \tag{3.9}$$

Eq. (3.9) is incapable of yielding an explicitly analytical solution. However, Eq. (3.9) approximates a real-life pricing decision in which an optimal price is chosen from a set of finite choices. For example, in practice, prices are more attractive when taken from a discrete set, e.g., ending with 99 such as \$9.99 or \$99 [70, 327, 361]. In the following, we refer to "asymptotically optimal price" simply as the optimal price.

3.4.3 Irregular pricing strategies

A pricing path is an orbit of optimal prices [175, 300]. If the steady states of optimal prices (Eq. 3.9) are a constant or periodic, then the pricing path is regular. In this setting, the corresponding optimal pricing strategy is defined as a *regular* one. However, a regular pricing strategy has limitations. The market is highly complex and full of irregularities such as demand spikes [184]. A regular pricing strategy precludes a pricing strategy that follows irregularities of markets. Also, a regular pricing strategy is vulnerable in that consumers can learn the pricing pattern and defer their purchase decisions until the occurrence of lower prices [300]. To overcome these limitations, we introduce the terms *irregular* and *chaotic* pricing strategies.

1. If the steady states of optimal prices (Eq. 3.9) are aperiodic, then the pricing path exhibits irregularities. In this setting, we define the optimal pricing strategy as an *irregular* pricing strategy.

2. If the steady states of optimal prices (Eq. 3.9) are chaotic, then we define the optimal pricing strategy as a *chaotic* pricing strategy.

In the absence of an analytical model, two ways exist in identifying irregularities of a dynamical system. They are to examine the time series and to look at time intervals between successive states. The former is applicable to systems that include infinite steady-state solutions such as the logistic map running into a chaotic window [277, 349]. The latter is applicable when systems include finite steady-state solutions, or when it is diÿcult to measure steady-state solutions such as the dripping faucet [242, 284]. Facing finite price choices, we investigate the time intervals between successive states and define a *first return iteration* [284]. A minimal iteration $k \in \mathbb{N}$ of a steady-state solution s_i is the minimal integer that satisfies $s_i = s_{i+k}$. The first return iteration is the time series of the minimal iteration of a pricing path. Let assume a pricing path as follows, then we can calculate its first return iteration via

$$\begin{aligned} &\text{Pricing path:} \quad 0.276 \longrightarrow \underbrace{0.276 \longrightarrow 0.337}_{\text{repeat 4 times}} \longrightarrow 0.276 \longrightarrow 0.337 \\ &\text{First return iteration:} \quad 1 \longrightarrow \underbrace{2 \longrightarrow 2}_{\text{repeat 4 times}} \longrightarrow 2 \longrightarrow 3 \end{aligned} \tag{3.10}$$

where the pricing path starts with the state 0.276, and returns to 0.276 after five repetitions of the low-high pattern, $0.276 \to 0.337$. In Eq. (3.10) the state 0.276 sitting in the first position reoccurs in the next iteration, so its minimal iteration is 1. The state 0.276 sitting in the second position reoccurs after two iterations, so its minimal iteration is 2, and so on.

3.4.4 Symbolic representations

We have defined a dynamic pricing model (Eq. 3.1), where h and f follow Eqs. (3.3) and (3.9), respectively. Despite three variables shown in Eq. (3.1), the underlying system

is a two-dimensional map. For a given set of parameters, the system has a correlation dimension estimation $D_2 = 1.26 \in \mathrm{CI} = [1.11, 1.41]$, cf. Appendix A Fig. A1. In addition, the map (Eq. 3.1) is plotted in the $(r_n^E, r_n^I, p_n^{**})-$plane for a further visualization of the system, cf. Appendix A, Fig. A2.

The dynamic pricing map (Eq. 3.1) considers discrete price choices (Eq. 3.9) and the asymmetrical effect between a gain and a loss (Eq. 3.6). Those two considerations are to approximate reality. However, Eqs. (3.6) and (3.9) together prevent an explicit formula of f. It thus becomes diÿcult to mathematically analyze the map.

Eq. (3.6) defines a non-smooth system of which the derivative contains discontinuity at $p_n = r_n^I$ or $p_n = r_n^E$. Symbolic representations are widely used to visualize dynamic manifolds and to study a switch behavior among manifolds within non-smooth systems [139, 148, 289, 357]. We, therefore, use symbolic representations to visualize and analyze f. The symbolic representation satisfies

$$I_1 = \{p_n^{**} : p_n^{**} < r_n^I \quad \text{and} \quad p_n^{**} < r_n^E\}; \tag{3.11a}$$

$$I_2 = \{p_n^{**} : p_n^{**} > r_n^I \quad \text{and} \quad p_n^{**} > r_n^E\}; \tag{3.11b}$$

$$I_3 = \{p_n^{**} : r_n^E < p_n^{**} < r_n^I\}; \tag{3.11c}$$

$$I_4 = \{p_n^{**} : r_n^I < p_n^{**} < r_n^E\}; \text{ and} \tag{3.11d}$$

$$I_5 = \{p_n^{**} : r_n^I = p_n^{**} \text{ or } r_n^E = p_n^{**}\} \tag{3.11e}$$

Eq. (3.11) symbolizes p_n^{**} by comparingp_n^{**}, r_n^I and r_n^E. We use the symbols $\mathcal{L}$, $\mathcal{R}$, $\mathcal{M}^I$, $\mathcal{M}^E$, and $\mathcal{M}$ to denote the results of comparisons I_1 (Eq. 3.11a), $\cdots$, I_5 (Eq. 3.11e), respectively. Let assume, for example, that $r_n^I = 0.3$, $r_n^E = 0.3$, and $p_n^{**} = 0.213$ where p_n^{**} is derived from Eq. (3.9), then p_n^{**} gets an assigned symbol $\mathcal{L}$ ($p_n^{**} \in I_1$) since $p_n^{**} = 0.213 < 0.3 = r_n^I$ and $p_n^{**} = 0.213 < 0.3 = r_n^E$.

Two sources of nonlinearity are noticeable in the map (Eqs. 3.1, 3.3 and 3.9). They are related to the definition of h (Eqs 3.2 and 3.3) and f (Eq. 3.9), respectively. For h, Eq. (3.2) contains two nonlinear equations. A quadratic equation (Eq. 3.2b) models nonlinear evaluations of external information and considers contradicted consumer

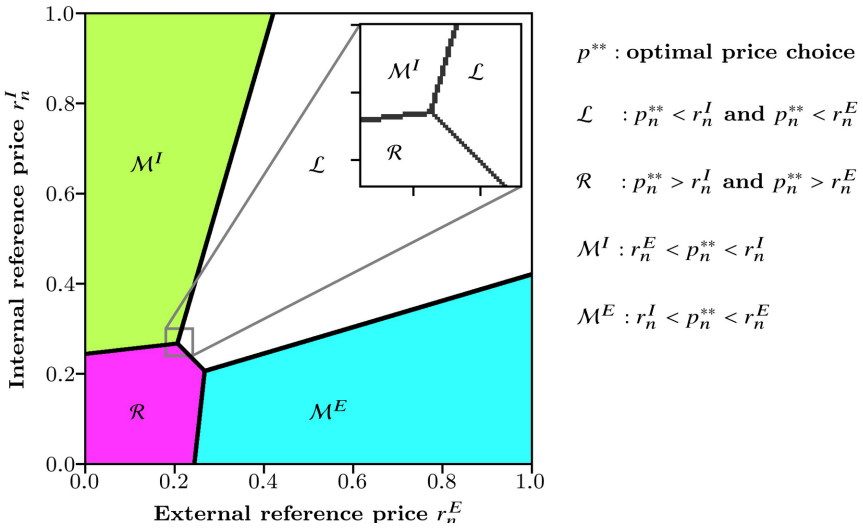

Figure 3.1 : Visualization of the function f (Eq. 3.1c) by symbolic representations (Eq. 3.11). The symbol $\mathcal{L}$ indicates that consumers perceive gains from both the internal and external reference effects. The symbol $\mathcal{R}$ that losses from the both. The symbol $\mathcal{M}^I$ that gains from the internal reference effects but losses from external reference effects. The symbol $\mathcal{M}^E$ that gains from external reference effects but losses from the internal reference effects. (Zoomed plot): Visualization of stepwise changes of the borders where $r_n^E \in [0.18, 0.24]$ (x-axis) and $r_n^I \in [0.24, 0.3]$ (y-axis).

expectations. A sine function (Eq. 3.2c) models nonlinear interactions between price expectations (ERP) and external information. For f, Eq. (3.9) contains a new source of nonlinearity, the discontinuity in optimizations, cf. Fig. 3.1. The two sources of nonlinearity describe the interdependence between consumers and companies, thus being entailed and difficult to be disentangled.

This chapter aims to explain volatile demand by a rational route from dynamical systems' perspective. The rational route is described by the dynamic pricing map (Eqs. 3.1, 3.3 and 3.9) with those two sources of nonlinearity. We let the amplitude of the interactions between external information and price expectations $\mathcal{B}$ be the changeable parameter and fix the following parameters to be consistent with Hu et al. [175]

$$b = 582,\ a = 569.4,\ \alpha = 0.95,\ \beta = 0.95,\ \gamma^g = 1335.6,\ \gamma^l = 267.1, \text{and}$$
$$\mathcal{A} = 4,\ U = \lambda^I = \lambda^E = \tau_E = \tau_F = \tau_I = 1$$

We will show nonlinear dynamics of steady-state solutions of the ERP as $\mathcal{B}$ changes.

Three reasons exist for the choose of an ERP over other variables such as an IRP, an optimal price, and demand. An ERP is formulated by two nonlinear functions, cf. Eqs. (3.2b) and (3.2c). It is expected that an ERP will exhibit complex dynamics. In addition, an ERP is firstly modeled in pricing decisions. The analysis of the ERP will provide a fresh impetus to our knowledge of possible acting mechanisms of volatile markets. Finally, according to Takens' embedding theorem [333, 360], the dynamics of one variable is consistent with the whole system. Therefore, the dynamics of ERP represents that of other variables.

3.4.5 Numerical bifurcation and period diagrams

An absence of an analytical solution to Eq. (3.9) causes a lack of an analytical formula of the map f. It becomes difficult to analyze the bifurcations by the fixed points, the $k^{\text{th}}-$iteration, or the corresponding Jacobian as shown for the logistic map (sections 3.2.2 and 3.2.3). We therefore conduct bifurcation analysis using a time series, instead of analytics or associated eigenvalues.

Numerical bifurcation diagram. Two sets of initial conditions are employed for a numerical bifurcation diagram. They are $(r_0^E, r_0^I) = (0.3, 0.3)$ and $(r_0^E, r_0^I) = (0.3, 0.6)$. For a given set of initial conditions, we plot all possible steady-state solutions of the dynamic pricing map (Eq. 3.1) against an increase of $\mathcal{B} \in \{0.0001 * k : k = 0, 1, \cdots, 10000\}$ (Eq. 3.3). BCB is expected due to the discontinuity of demand function (Eq. 3.6). For identifying a BCB, the parameter should be close enough to the point where BCB appears [34]. When an evident jump is observed in the bifurcation diagram, we then zoom into the interval where the jump is observed. In a zoomed plot, initial conditions are randomized, and a bootstrapping [279] is introduced. For a given $\mathcal{B} \in \{\mathcal{B}_L + k(\mathcal{B}_U - \mathcal{B}_L)/10000 : k = 0, 1, \cdots, 10000\}$ both r_0^E and r_0^I are uniformly distributed over $[0, 1]$. Here, $\mathcal{B}_L$ and $\mathcal{B}_U$ are the lower and the upper bounds of the interval where the jump is observed.

Numerical identification of doublings. We iterate the dynamic pricing map and shrink the interval that accommodates the parameter at which a doubling occurs. The idea is to sequentially approximate the decimals from the tenths until the millionths. To locate $\mathcal{B}_1^F$ at which a period-2 solution occurs, we look at the bifurcation diagram, let $\mathcal{B}_U^2 = \{0.1, 0.2, \cdots, 1\}$, and identify the interval $\mathcal{B}_1^F \in [\mathcal{B}_L^2, \mathcal{B}_U^2]$ with $\mathcal{B}_L^2 = \mathcal{B}_U^2 - 1 \times 10^{-1}$. The bifurcation diagram shows one branch at $\mathcal{B}_L^2$, whereas two branches at $\mathcal{B}_U^2$. We then move to the hundredths place by letting $\mathcal{B}_L^2 = \mathcal{B}_U^2 - 1 \times 10^{-2}$. If at $\mathcal{B}_L^2$ one branch is observed, then we move to the thousandth place. Otherwise, we let $\mathcal{B}_U^2 = \mathcal{B}_L^2$ firstly and then $\mathcal{B}_L^2 = \mathcal{B}_U^2 - 1 \times 10^{-2}$. The process is repeated until that at $\mathcal{B}_L^2$ one branch is observed for the first time. For the thousandth place, we then let $\mathcal{B}_L^2 = \mathcal{B}_U^2 - 1 \times 10^{-3}$ and follow the same way to shrink the interval $[\mathcal{B}_L^2, \mathcal{B}_U^2]$. The shrinking continues until seven decimal places where $\mathcal{B}_1^F \in [\mathcal{B}_L^2, \mathcal{B}_U^2]$ with $\mathcal{B}_L^2 = \mathcal{B}_U^2 - 1 \times 10^{-7}$. Therefore, $\mathcal{B}_L^2$ and $\mathcal{B}_U^2$ correspond to an identical number when the seventh digit after decimal point is dropped. That number represents $\mathcal{B}_1^F$. Similarly, we shrink the interval $\mathcal{B}_k^F \in [\mathcal{B}_L^k, \mathcal{B}_U^k]$ by the rule that $\mathcal{B}_L^k$ corresponds to 2^{k-1} branches and $\mathcal{B}_U^k$ that 2^k branches with $k = 1, \cdots, 10$ for locating a period-2^k solution in the doubling.

Numerical period diagram. Bifurcation diagrams are ineffective to detect a change in dynamics if period adding bifurcations occur [272]. However, period diagrams improve the detection [132, 138, 148]. A period diagram is a diagram that records the periodicity of a solution. If a period adding bifurcation is observed in a bifurcation diagram, then we plot the periodicity of a solution against an increase of $\mathcal{B} \in \{\mathcal{B}_L + k(\mathcal{B}_U - \mathcal{B}_L)/10000 : k = 0, 1, \cdots, 10000\}$. Here, $\mathcal{B}_L$ and $\mathcal{B}_U$ are the lower and the upper bounds of the interval where the period adding bifurcation is observed. We only calculate a period-k solution with k smaller than 300. Period-300 in the diagram thus represents a periodic-300 solution, a solution with periodicity larger than 300, or an aperiodic solution.

A numerical bifurcation diagram can be different from an analytical bifurcation diagram of which the analysis is based on the Jacobian [34, 96]. In particular, an identification of a BCB from a bifurcation diagram needs a high accuracy in locating the small

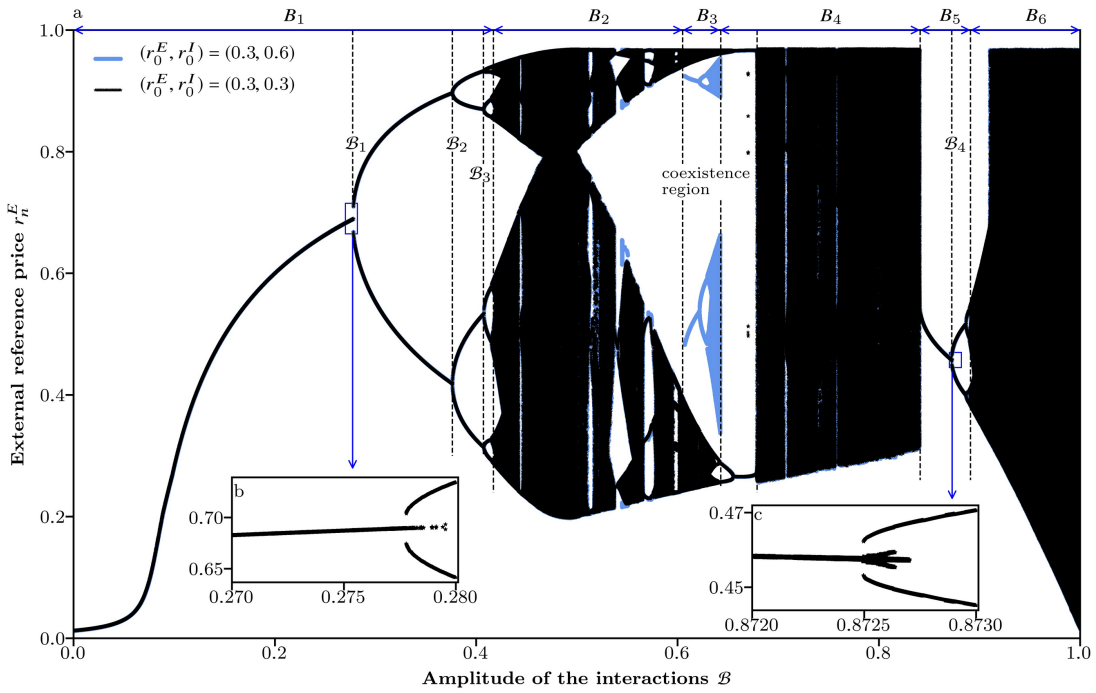

Figure 3.2 : Bifurcation diagram of an ERP against the amplitude of the interactions, $\mathcal{B}$ (Eq. 3.3). (a) Numerical bifurcation analysis is conducted over two sets of initial conditions, $(r_0^E, r_0^I) = (0.3, 0.3)$ and $(r_0^E, r_0^I) = (0.3, 0.6)$. Panels (b) and (c) are a zoomed plot to visualize a jump in the bifurcation diagram. Random initial conditions are applied to the dynamic pricing map (Eqs. 3.1, 3.3 and 3.9) for a plot. The map exhibits different dynamics in the intervals, $B_1, \cdots, B_6$. In B_3 coexisting solutions occur. A doubling behavior is evident at $\mathcal{B}_1 \approx 0.2772$, $\mathcal{B}_2 \approx 0.3763$, $\mathcal{B}_3 \approx 0.4072$, and $\mathcal{B}_4 \approx 0.8724$.

neighborhood of the exact position where a BCB occurs [34, 96]. This thesis does not focus on identifying a BCB. A use of a period diagram is merely to exemplify a rational route to apparent randomness in the periodicity of a solution. An advanced numerical method that improves the identification would be of interest for mathematical curiosity. In addition, obtaining analytics for optimizations (Eq. 3.9) would further improve the identification.

3.5 Mechanisms for volatile markets

A dynamic pricing map has been proposed. We then conduct a bifurcation analysis to look at a rational route to apparent randomness. The rational route is interpreted

from dynamical systems' perspective. The interpretation includes a plot of a bifurcation diagram, an analysis of a BCB, and basins of coexisting solutions.

3.5.1 Bifurcation analysis

Fig. 3.2 shows the bifurcation diagram of the dynamic pricing map as $\mathcal{B}$ changes. The sequence that associates with the occurrence of possible doublings is $\mathcal{B} = \mathcal{B}_1^F \approx 0.277786\ldots$ (period-2), $\mathcal{B} = \mathcal{B}_2^F \approx 0.376428\ldots$ (period-4), $\mathcal{B} = \mathcal{B}_3^F \approx 0.409111\ldots$ (period-8), $\mathcal{B} = \mathcal{B}_4^F \approx 0.415522\ldots$ (period-16), $\mathcal{B} = \mathcal{B}_5^F \approx 0.416644\ldots$ (period-32), $\mathcal{B} = \mathcal{B}_6^F \approx 0.417249\ldots$ (period-64), $\mathcal{B} = \mathcal{B}_7^F \approx 0.417449\ldots$ (period-128), $\mathcal{B} = \mathcal{B}_8^F \approx 0.417452\ldots$ (period-256), $\mathcal{B} = \mathcal{B}_9^F \approx 0.417453\ldots$ (period-512). Our numerical method is difficult to locate the position where a period-1024 solution occurs. The calculation of $\frac{\mathcal{B}_k^F - \mathcal{B}_{k-1}^F}{\mathcal{B}_{k+1}^F - \mathcal{B}_k}$ yields 3.018, 5.098, 5.714, 1.855, 3.025, 66.667, 3.000 with $k = 2, \cdots, 8$, respectively. The sequence is different from the Feigenbaum sequence of the logistic map (section 3.2.2). Also, we are unable to observe the Feigenbaum constant. The reason can be the errors induced by a numerical bifurcation diagram [34, 96] or the discontinuity of the dynamic pricing map (Eqs. 3.1, 3.3 and 3.9), which fundamentally changes the bifurcating behaviors.

Jumps are visible in the bifurcation diagrams, cf., Figs. 3.2b and 3.2c. The occurrence of those jumps is consistent with the observations of discontinuous jump phenomena near a grazing point [229, 404]. The jumps are likely to be related to Neimark-Sacker bifurcations as a switching from periodic to quasi-periodic solutions occurs [346, 415]. However, the exact determination would require a normal form of Eq. (3.1), which is difficult to be retrieved because of the lack of analytical formula in the function f (Eq. 3.9).

Six intervals are used for a summary of the complex dynamics. The intervals are $\mathcal{B} \in B_1 = [0, 0.417), B_2 = [0.417, 0.605), B_3 = [0.605, 0.642)$ where coexisting solutions occur, $B_4 = [0.642, 0.679)$, $B_5 = [0.679, 0.891)$, $B_6 = [0.891, 1]$. Complex changes and many bifurcation structures are observed in Fig. 3.2a. Intervals B_1 and B_5 exhibit almost periodic solutions. The interval B_3 exhibits coexisting solutions. In addition, complex bifurcation structures are found in the Figs. 3.2b and 3.2c.

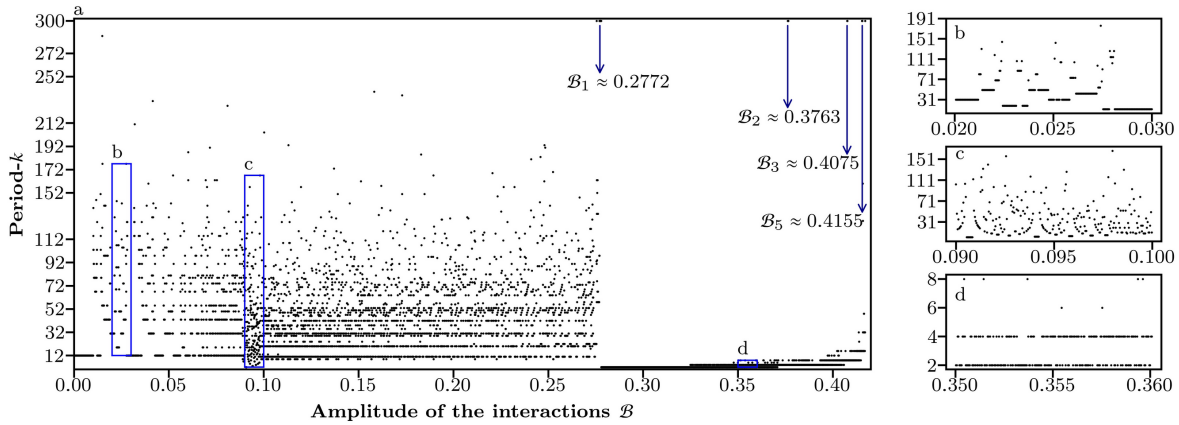

Figure 3.3 : Period diagrams. (a) The periodicity of an ERP against an increase of $\mathcal{B} \in B_1$ is plotted. The initial condition $(r_0^E, r_0^I) = (0.3, 0.3)$ is applied. (b) A zoomed plot where $\mathcal{B} \in [0.2, 0.3]$ shows overlapping structures in the periodicity of the ERP. (c) A zoomed plot where $\mathcal{B} \in [0.09, 0.1]$ shows increasing and decreasing increments. (d) A zoomed plot where $\mathcal{B} \in [0.35, 0.36]$ shows a period doubling routine undergoing a BCB.

The ERP is regular in almost periodic windows (B_1 and B_5). However, it can be aperiodic such as in the intervals B_4 and B_6. An aperiodic ERP fluctuates with irregular patterns and gives rise to irregular price expectations. By means of interactions between price and demand, the irregularities are then delivered to a market. Unpredictable demand and volatile markets thus occur.

3.5.2 Border collision bifurcations

Fig. 3.3a shows the period diagram of the ERP as $\mathcal{B}$ is in the almost periodic window $B_1 = [0, 0.417)$. An irregular change occurs in the periodicity of a steady-state solution (Fig. 3.3a). The phenomenon is called a BCB [139, 181]. Figs. 3.3b and 3.3c have a common pattern in the periodicity ($y-$axis). Along the $x-$axis the periodicity of some point satisfies that it equals to the addition of the periodicities of its neighboring points. The phenomenon is coined to the period adding bifurcations [17, 139, 148, 357].

Figs. 3.3b and 3.3c show different structures of a period diagram. Fig. 3.3b shows overlapping structures with increasing increments dominated, which resembles those of

an incomplete Farey tree in [148]. Overlapping structures are due to discontinuous rotation number [148]. On the other hand, Fig. 3.3c shows evidently decreasing and increasing increments, which resembles those of a complete Fare tree in [148]. Obvious patterns in both decreasing and increasing increments are due to continuous variations in rotation number [148].

Fig. 3.3d shows a new pattern. The periodicity oscillates among the set $\{2,4,6,8\}$. Period-2 and period-4 solutions are the two dominating ones. In Fig. 3.3d, $\mathcal{B} \in B_1$ is in an interval that contains a doubling behavior in the bifurcation diagram (Fig. 3.2a. However, an occurrence of period-6 and period-8 solutions indicates that a BCB influences the doubling behavior. The influence is not as strong as that in Figs. 3.3b and 3.3c.

More complex dynamics may develop near the point $\mathcal{B} = \mathcal{B}_1 \approx 0.2772$ where period doubling bifurcations and a BCB simultaneously occur (Figs. 3.2a and 3.3a). The point ($\mathcal{B}_1$) is referred to as the so-called codimension-2 point [337]. It sits at the intersection of lines with different topological structures [17]. A small variation of the bifurcation parameter $\mathcal{B}$ thus leads to the evolution of different dynamics [17]. Moreover, quasi-periodic solutions are expected in the vicinity of the codimension-2 points [337], which may explain the jumps at the codimension-2 points shown in Figs. 3.2b and 3.2c.

We calculate a time series (Figs. $3.4a_1$ to $3.4c_1$), a phase space (Figs. $3.4a_2$ to $3.4c_2$), and the power spectral density* (Figs. $3.4a_3$ to $3.4c_3$), and benchmark the dynamics at $\mathcal{B}_1$ with periodic and aperiodic dynamics. We observe a periodic-11 orbit at $\mathcal{B} = 0.2$ (Figs. $3.4a_1$ to $3.4a_3$) and aperiodic dynamics at $\mathcal{B} = 1$ (Figs. $3.4b_1$ to $3.4b_3$). The observations are as follows. (1) The time series presents different patterns. Fig. $3.4a_1$ shows a regular pattern at $\mathcal{B} = 0.2$, whereas Fig. $3.4b_1$ shows an irregular pattern at $\mathcal{B} = 1$. (2) A phase plot shows different patterns. At $\mathcal{B} = 0.2$, the phase space includes eleven scattered points (Fig. $3.4a_2$). At $\mathcal{B} = 1$, the phase space shows a self-similar structure between the original and the zoomed plots (Fig. $3.4b_2$). (3) The number of

*Matplotlib.mlab.psd is used [177, 247]. The sampling frequency is 1.

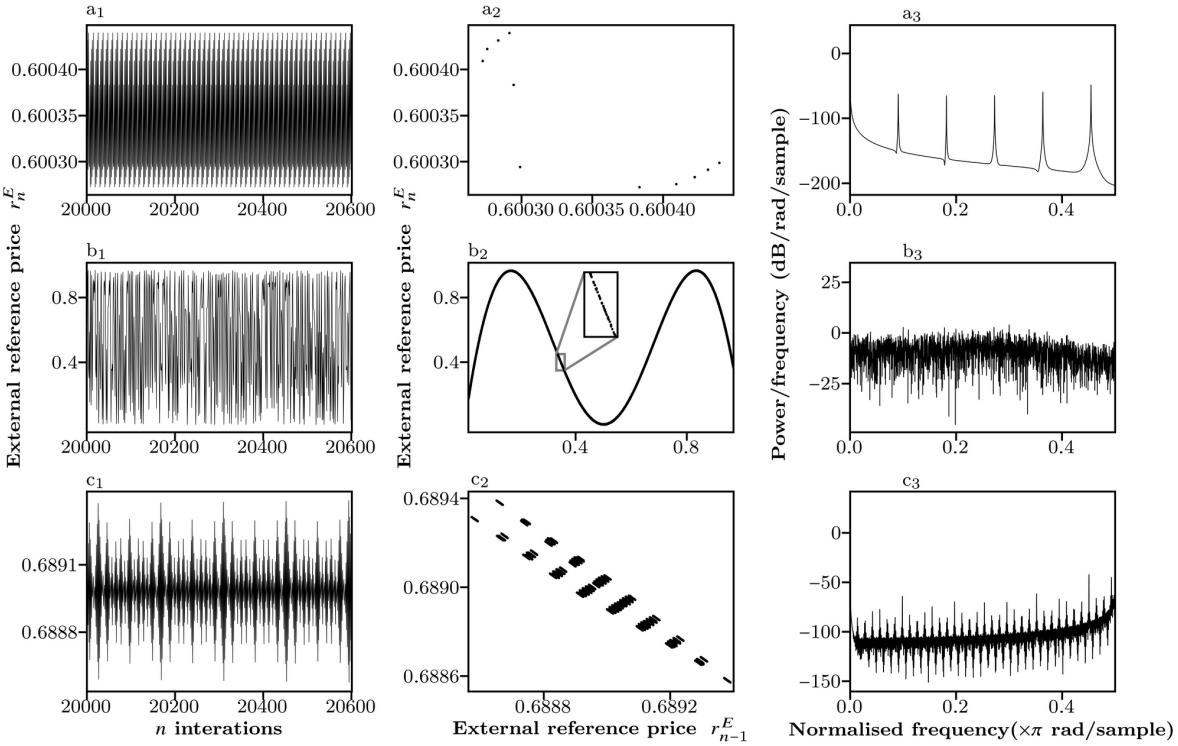

Figure 3.4 : Identifying the dynamics of a codimension-2 point at $\mathcal{B} = \mathcal{B}_1 \approx 0.2772$. Here, the initial condition corresponds to $(r_0^E, r_0^I) = (0.3, 0.3)$. ($a_1$ to c_1) A time series is plotted for the identification of dynamics. (a_2 to c_2) A phase space is plotted. (a_3 to c_3) Power spectrum density is calculated. (a_1 to a_3) At $\mathcal{B} = 0.2$, the patterns represent periodic dynamics. (b_1 to b_3) At $\mathcal{B} = 1$, the patterns represent aperiodic dynamics. (c_1 to c_3) At $\mathcal{B} = 0.2772$, the patterns are consistent with aperiodic dynamics shown at $\mathcal{B} = 1$.

bands are different in the power spectrums. Fig. 3.4a_3 shows a fixed number of bands at $\mathcal{B} = 0.2$, whereas Fig. 3.4b_3 shows broadband power spectrums at $\mathcal{B} = 1$. At $\mathcal{B} = \mathcal{B}_1$, (1) the time series is irregular (Fig. 3.4c_1). (2) A phase space exhibits self-similarity (Fig. 3.4c_2). (3) The power spectrums are of broadband (Fig. 3.4c_3). Those three observations are consistent with aperiodic dynamics shown at $\mathcal{B} = 1$ (Fig. 3.4b).

Another mechanism for volatility occurs in a period adding bifurcation and a non-periodic solution. The solution simultaneously undergoes a period doubling bifurcation and a period adding bifurcation. Here, the ERP fluctuates in a small range (Figs. 3.4c_1 and 3.4c_2), so a company is able to predict the ERP in a high accuracy. However, the

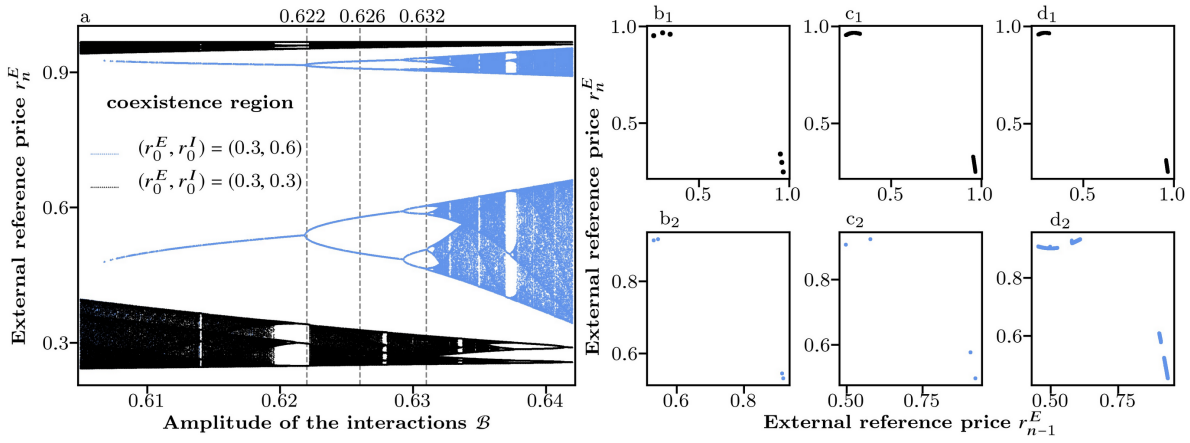

Figure 3.5 : Coexisting solutions and their phase space. (a) Different initial conditions lead to different structures in a bifurcation diagram. Here, $\mathcal{B} \in B_3$ (Fig. 3.2a). (b) At $\mathcal{B} = 0.622$, the dynamic pricing map (Eqs. 3.1, 3.3 and 3.9) reaches two different solutions. (b_1) A period-6 orbit is plotted in phase space. (b_2) A period-4 orbit is plotted. (c) At $\mathcal{B} = 0.626$, two coexisting solutions exist. (c_1) An aperiodic solution is plotted. (c_2) A period-4 orbit is plotted. (d) At $\mathcal{B} = 0.632$, two aperiodic solutions coexist (d_1 and d_2). (b_1 to d_1) The initial condition, $(r_0^E, r_0^I) = (0.3, 0.3)$, is taken for a solution. (b_2 to d_2) The initial condition, $(r_0^E, r_0^I) = (0.3, 0.6)$, is taken.

total number of elements that constitute steady-state solutions varies drastically as the market environment changes (Fig. 3.3). As a result, it becomes difficult to predict that total number, causing volatility.

3.5.3 Coexisting solutions

Here, we report the coexistence of solutions with different dynamics as $\mathcal{B}$ changes. The following cases are possible:

1. Two periodic solutions coexist. A period-4 solution (Fig. 3.5b_2) and a period-6 solution (Fig. 3.5b_1) are observed at $\mathcal{B} = 0.622$.

2. At $\mathcal{B} = 0.626$ a period-4 solution (Fig. 3.5c_2) and an aperiodic solution (Fig. 3.5c_1) coexist. Fig. 3.6 shows the basins of the two coexisting solutions. The basins exhibit a fractal structure. In addition, the basin of some solution is disconnected and separated by the basin of its counterpart (Fig. 3.6). A basin of a non-smooth

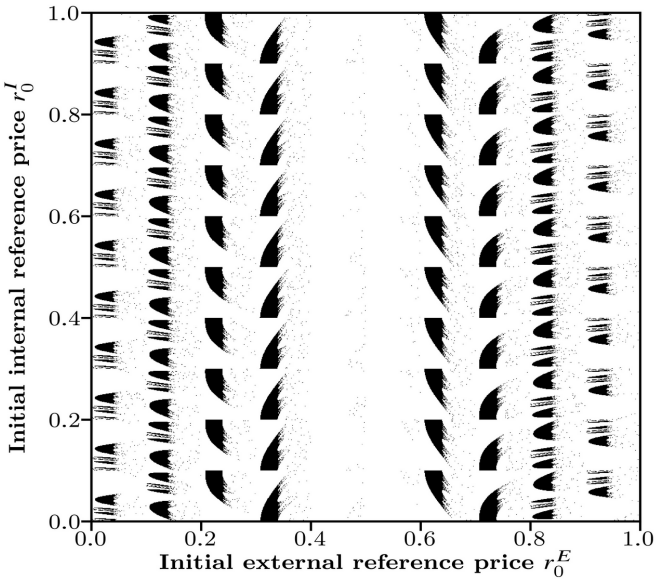

Figure 3.6 : Basins of coexisting solutions at $\mathcal{B} = 0.626$. Black blocks represent the basin of an aperiodic solution (Fig. 3.5c$_1$). The blank white areas represent the basin of a period-4 solution (Fig. 3.5c$_2$).

system is different from that of a smooth system. For a non-smooth system the borders and their preimages serve as repellers that separate the basins. A basin boundary thus shows up [308].

3. At $\mathcal{B} = 0.632$, two aperiodic solutions (Figs. 3.5d$_1$ and 3.5d$_2$) show up.

An initial IRP r_0^I and an initial ERP r_0^E are inextricably associated with a company. In particular, r_0^E may heavily reply on the initial behavior of a company [203, 255, 364]. Coexisting solutions contribute to a third type of volatility, which is related to a market manipulation. While implementing dynamic pricing strategies, a company can make consumer expectations develop in different directions, such as a period-4 solution or an aperiodic solution (Fig. 3.6). On the one hand, coexisting solutions indicate that a company should be forward-looking, so that a potentially volatile market could be avoided. On the other hand, regulators could discourage a manipulation and abusive pricing by means of an identification of the critical parameters. For example, the bifurcation parameter $\mathcal{B}$ runs into the intervals B_3 where coexisting solutions occur (Figs. 3.2, 3.5a, and 3.6).

3.6 Optimal actions

We have presented three mechanisms to volatility. A change of the parameter $\mathcal{B}$ (Eq. 3.3) has been used to model a change of market environments. The dynamics of the ERP has been presented. Results show that a rational route to apparent randomness can explain volatility of dynamic pricing problems from dynamical systems' perspective (Figs. 3.2, 3.3, and 3.6). We then point out the actions that participants should take as apparent randomness emerges from a rational route.

3.6.1 Optimal price choice

Fig. (3.1) shows a symbolic representation (Eq. 3.11) of optimal price choices. Four symbols are evident. This suggests that while considering an internal and an external reference effects, a company can take four actions to adjust the price for optimal revenue.

1. In Fig. 3.1, the area being labeled with $\mathcal{L}$ corresponds to a high IRP and a high ERP. The symbol $\mathcal{L}$ represents that an optimal price should be lower than both the ERP and the IRP (Eq. 3.11). If consumers have a high IRP and a high ERP, then a company's optimal action is to set the sales price at which consumers perceive gains from both the internal and the external reference effects.

2. In Fig. 3.1, the area being labeled with $\mathcal{R}$ corresponds to a low IRP and a low ERP. The symbol $\mathcal{R}$ represents that an optimal price should be higher than both the ERP and the IRP (Eq. 3.11). If consumers have a low IRP and a low ERP, then a company's optimal action makes consumers perceive losses from both the internal and the external reference effects.

3. The area with a low ERP, however, a high IRP is labeled with $\mathcal{M}^I$ (Fig. 3.1). The symbol $\mathcal{M}^I$ represents that an optimal price choice is larger than the ERP but lower than the IRP. Consumers, therefore, perceive gains from internal reference effects, however, losses from external reference effects. This indicates that for a large gap between the ERP and the IRP, a company should balance multiple attributes that affect consumer purchase decisions.

4. In the area being labeled with $\mathcal{M}^E$, an optimal price is larger than the IRP yet lower than the ERP (Fig. 3.1). Consumers, therefore, perceive gains from external reference effects however losses from internal reference effects. This further highlights the importance of the above-mentioned balance for a company.

Two peculiarities in Fig. 3.1 should be noted. The symbol $\mathcal{M}$ misses. Also, The borders between symbols are not smooth, but in the form of a stepwise curve. The absence of $\mathcal{M}$ indicates either (1) the map defined by Eq. (3.1) has no fixed point, or (2) the approximations of an optimal price or that of the (r_n^E, r_n^I)-plane make us skip fixed points. Eq. (3.9) yields a solution that approximate and reaches a small neighborhood of the optimum. However, the exact optimum cannot be derived from Eq. (3.9). Jumps thus occur in approximations, causing the borders of the map non-smooth.

3.6.2 Optimal pricing strategy

An optimal price choice gives an indication of how to set the exact value of a price (the variable p) under a specific pair of an ERP and an IRP (Fig. 3.1). Normative implications that can guide a pricing decision are as important as the indication of the exact value of a price [297]. A normative implication is concerned with how to choose an optimal pricing strategy (a function f) that improves a pricing decision. In Fig. 3.7, we observe four types of first return iterations, calculate the power spectrum density, and reveal four types of optimal pricing strategies.

1. At $\mathcal{B} = 0.622$, the pricing path has six different elements (Fig. 3.5b$_1$). Each element recurs after 6 iterations.

   Here, the time series of the first return iteration constitutes a horizontal line (Fig. 3.7a$_1$). Individual price choices that are elements of a price path, have an identical recurrent behavior. The frequency of the recurrences is identical for all elements (Fig. 3.7a$_2$). The number of optimal price choices is thus equal to the period of the map. In this setting, it is optimal to implement a regular pricing strategy that includes different price choices.

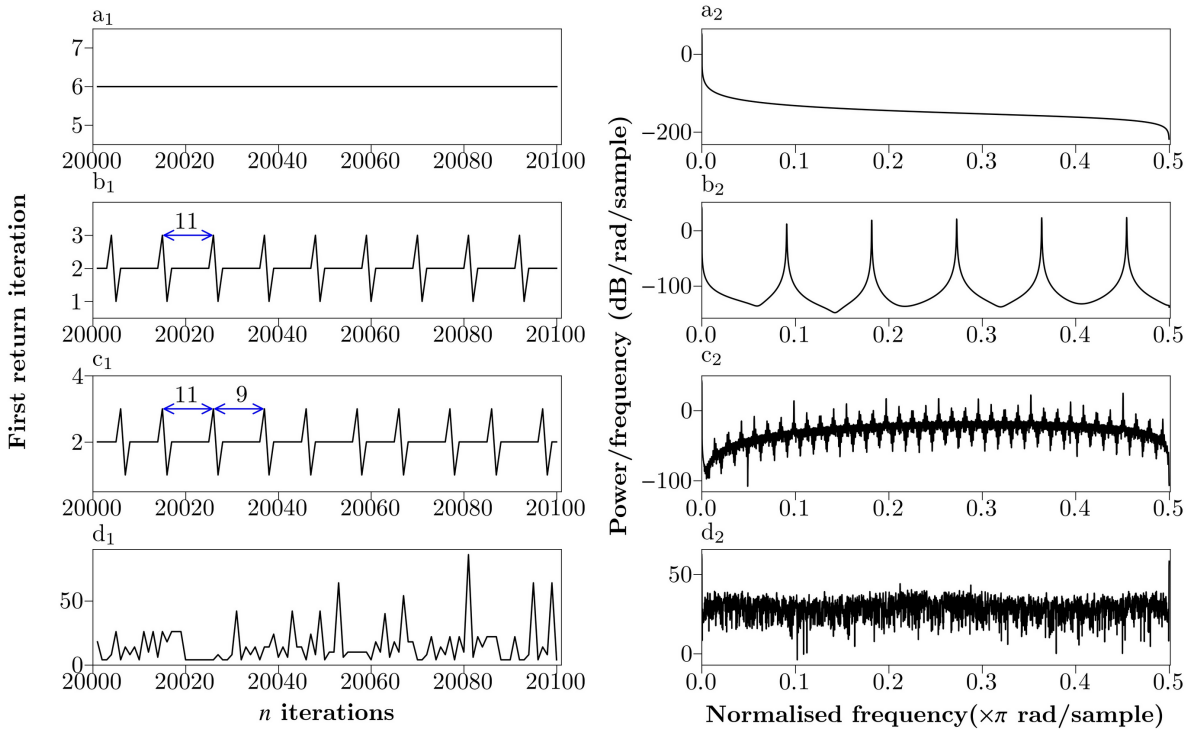

Figure 3.7 : Four types of optimal pricing strategies. (a_1 to d_1) The time series of a first return iteration is plotted. (a_2 to d_2) The power spectrum density of the corresponding first return iteration is calculated. (a) At $\mathcal{B} = 0.622$, a regular pricing strategy is optimal. The first return iteration contains only one constant (6). (b) At $\mathcal{B} = 0.2$, a regular pricing strategy is optimal. The first return iteration contains three constants (1, 2, 3), which contribute to a period-11 orbit (Eq. 3.10). (c) At $\mathcal{B} = 0.2772$, an irregular pricing strategy is optimal. The first return iteration contains three constants (1, 2, 3). However, two frequencies (9, 11) are set-wise co-prime as those constants repeat. (d) At $\mathcal{B} = 1$, an irregular pricing strategy is optimal. The first return iteration contains many elements. Irregular patterns are observed from both the time series (d_1) and the power spectrum density (d_2). (a to d) The initial condition, $(r_0^E, r_0^I) = (0.3, 0.3)$, is taken for a solution.

2. At $\mathcal{B} = 0.2$, Eq. (3.10) gives a pricing path, which is a period-11 orbit having two different elements.

   Here, the time series of the first return iteration forms a regular curve with a unique frequency, cf. Fig. 3.7b_1. The first return iteration is periodic, cf. Fig. 3.7b_2. In this scenario, a regular pricing strategy is optimal. The optimal price choices repeat, and the repetitions have a unique frequency. For example, at $\mathcal{B} = 0.2$, the

optimal pricing strategy is to implement the price path that Eq. (3.10) defines. The path has two price choices, a low price 0.276 and a high price 0.337. The sequence is to initiate a low price, and then repeat a low-high pricing pattern five times, finally return to the low price (Eq. 3.10).

3. At $\mathcal{B} = 0.2772$, the pricing path has two elements (Fig. 3.7c$_1$), 0.366 and 0.3. However, the first return iteration is aperiodic, suggested by the broadband power spectrums (Fig. 3.7c$_2$).

   Here, the time series of the first return iteration forms a regular curve with more than two recurrent patterns. The frequencies of recurrent patterns cannot be divided by each other, cf. Fig. 3.7c$_1$. An aperiodic first return iteration emerges from the step-wise co-prime frequencies. An irregular pricing strategy is thus optimal. However, the time series of the first return iteration is seemingly regular, cf. Fig. 3.7c$_1$. Consumers may perceive a seemingly regular pricing pattern.

4. At $\mathcal{B} = 1$, the time series of the first return iterations is irregular (Fig. 3.7d_1). An irregular pricing strategy is optimal, which makes consumer perceive irregular pricing pattern.

   We have presented two types of irregular pricing strategies at $\mathcal{B} = 0.2772$ and $\mathcal{B} = 1$. However, the irregularities are different in those two cases. At $\mathcal{B} = 0.2772$, the irregularity remains in the irregular recurrence of fixed price choices (Fig. 3.7c). At $\mathcal{B} = 1$, the irregularity remains in varied price choices and their irregular recurrence (Fig. 3.7d).

3.7 Conclusions

We have proposed a hypothetical model that applies a rational route to describe a dynamic pricing process. Deterministic chaos has explained a random-like and volatile phenomenon of a dynamic pricing problem. Our model has entailed two sources of nonlinearity. The one is concerned with a non-smooth demand function and with discontinuity in optimizations. The other one is concerned with an external reference price

(ERP), which models consumers' adaptions of expectations.

The entangled sources of nonlinearity allow us to unveil three possible mechanisms to a volatile phenomenon from dynamical systems' perspective. (1) An aperiodic ERP exhibits a large variation in amplitude (Fig. 3.2), thus delivering irregularities to markets. (2) A period adding bifurcation causes a complex change in the periodicity of consumer expectations (Fig. 3.3), thus giving irregularities to the periodicity of a pricing path. (3) Coexisting solutions offer changeable structures of consumer expectations (Figs 3.5 and 3.6). The results highlight that a rational route is capable of modeling a volatile phenomenon for a dynamic pricing problem. Since nonlinearity is ubiquitous in reality, the finding emphasizes the importance of considering a rational route in a hypothetical model and in the practical modeling of a real-life dynamic pricing problem.

As deterministic chaos occurs, optimal actions that participants should take is proposed. For companies, an optimal pricing strategy should agree with the dynamics of consumer behaviors. Facing with the volatility emerging from aperiodic price expectations, companies should choose an irregular pricing strategy. To implement an irregular pricing strategy, a company can make price choices irregular. A company also can take finite price choices but make the first return iterations irregular. For price regulators, coexisting solutions provide new ideas to detect consumer manipulation by an identification of critical parameters. Therefore, identifying nonlinear dynamics that a market underlies could be essential to a company for avoiding potential revenue losses and to a regulators for recognizing market mechanisms that consumers and companies should respond to.

We have proposed a rational route to apparent random demand, which theoretically justifies dynamic pricing. The dynamic pricing map (Eq. 3.1) is, however, built without a consideration of noise. For practical applications, noise is a constituent part of uncertain demand. It would be interesting to allow the dynamic pricing map contaminated by noise. The effect of noise on the dynamics of the map would then be investigated. Besides, the rational route has thrown up some questions in the model-

ing of uncertain demand. An identification of underlying dynamics is needed instead of directly assuming stochasticity. Recently, we apply order patterns to disambiguate between deterministic and stochastic dynamics [234]. A combination of the SINDy [53] algorithm and the Koopman operator [201, 259, 375] show a potential for deterministic and stochastic-driven system identifications [197]. Recurrence plots and recurrence quantification measures are capable of identifying the dynamics of Earth's climate system [397], daily S&P 500 returns [384], and the brake squeal [277]. In addition, recurrence quantification measures can be continuously calculated by sliding windowed recurrence plots. For streaming data, a sliding windowed recurrence analysis could be a promising tool to disambiguate between deterministic and stochastic dynamics. For example, a sliding windowed recurrence analysis identifies friction-induced vibrations [350] and an abrupt transition of dynamics in the EI Niño-Southern Oscillation [146]. In the next chapter, we will also conduct a sliding windowed recurrence analysis for identifying the dynamics of real-life demand.

Chapter 4

Recurrence-based reconstruction of on-demand attractor for dynamic pricing

Abstract

Price, demand, and supply are the fundamentals of a market. Dynamic pricing utilizes demand information to adjust price for an optimal revenue. In the modeling of uncertain demand, stochastic demand is widely assumed. However, demand dynamics remains yet to be identified when it comes to uncertain demand in a real-life dynamic pricing setting. We propose a recurrence-based reconstruction to identify real-life demand dynamics from a univariate time series. The reconstruction uses sliding windowed recurrence plots and a Pareto optimization to address an optimal parameter set, the embedding and the time delay dimensions. The optimization is to find an optimal parameter set under which recurrence plots yield the most robust results. Two recurrence quantification measures, the determinism and the trapping time, quantify the robustness. We also provide a decision matrix for identifying demand dynamics. The matrix covers the features that the Pareto front, optimal recurrence plots, recurrence quantification measures, and reconstructed attractors exhibit.

An on-demand attractor is extracted from empirical data. The data are from RideAustin, a company providing ride share service in the city of Austin, Texas, the United States. The attractor exhibits period-7 limit cycle oscillations and a slow and a fast dynamics that explains the well-known off-peak and on-peak patterns in an on-demand market. The results suggest that a stochastic demand may be incapable of describing a phenomenon of uncertainty. Our findings emphasize the need for identifying demand dynamics prior to an assumption of stochasticity. An attractor-based model would be further needed in the modeling of uncertain demand. Besides, a use of Pareto optimality that aims for an optimal parameter set opens a new door to reconstruct an attractor from observations in a practical signal with noise and non-stationarity.

4.1 Introduction

Dynamic pricing is a strategy in which a price is adjusted according to demand-based knowledge by optimizations [18, 232, 297, 361]. An optimal price is addressed by modeling a relationship between price and demand [70, 100]. A challenge comes from uncertain demand, since uncertainty affects consumers [232], industries [70], and regulators of governments [84].

Studies in operation research often assume a stochastic demand in the modeling of uncertain demand [18, 21, 35, 38, 40, 58, 82, 83, 144, 191, 192, 287, 321, 386, 389]. Reviews in [45, 70, 100, 119] summarize the modeling of a stochastic demand for dynamic pricing problems. The theory is that limited variables in a low dimensional system is incapable of describing some phenomenon of uncertainty, so an external force being random is introduced in the modeling of uncertainty [368]. Based on the assumption, either the quantity demanded [44, 111, 127, 261] or the time when a demand is realized is regarded as a stochastic variable [18, 35, 140, 287].

Nonlinear interactions between limited variables, however, are a critical mechanism to uncertainty. The theory is related to deterministic chaos [143, 333, 343, 353, 398].

In the modeling of dynamic pricing problems, a rational route has rarely been studied. Rump and Stidham [319] show that consumers' adaptions of expectations contribute to a rational route, which explains uncertainty in consumers' arrivals. Lu et al. [232] and Hu et al. [175] introduce discontinuous demand, which explains a phenomenon of uncertainty in the periodicity of periodic expectations [175, 232].

Identifying the dynamics that a real-life demand underlies is as important as proposing a hypothetical model that explains a phenomenon of uncertainty. It remains a debate whether the dynamics of equilibrium prices is deterministic or stochastic [384]. Increasing attention has been paid to contribute to the debate [24, 26, 176, 405]. Recently, Vogl and Rötzel [384] observe an attractor from the S&P 500 returns (2000–2020) in which equilibrium prices are considered.

However, it remains to be seen whether deterministic dynamics occurs in a real-life dynamic pricing setting. A lack of this knowledge casts doubt on the modeling of uncertainty and hinders an improvement of revenue. A hypothetical model, either building on a stochastic demand [18, 35, 140, 287] or a rational route [175, 232, 319], is challenged by a lack of empirical evidence for the modeling.

Dynamic pricing is different from equilibrium prices [232]. Dynamic pricing is an operational problem and uses demand-based knowledge for improving revenue [297, 361]. As supply is unadjustable in some decision window, dynamic pricing is concerned with a strategy that is profitable for consumers [348] or a seller [130]. As demand and supply are instantaneously adjustable, an equilibrium price is concerned with a price at which adopting any strategy is nonprofitable for any agents in the market. However, capturing the dynamics of uncertainty is the common challenge in the modeling of both dynamic pricing and equilibrium prices.

We therefore focus on identifying demand dynamics in a real-life dynamic pricing setting. Recurrence plots and Pareto optimality are introduced to find an optimal embedding and an optimal time delay dimensions for an attractor reconstruction. We then apply the recurrence-based attractor reconstruction to empirical data [310] from

RideAustin, a company providing ride share service in the city of Austin, Texas, the United States. We show the dynamic of demand by benchmarking against well-studied deterministic and stochastic systems and by conducting three types of surrogate tests. They are shuffle-based, Fourier-based, and truncated amplitude adjusted Fourier transform surrogates.

4.1.1 Ride-sharing market

A dataset [310] that records individual transactions in a ride-sharing market is taken as an example for an identification of demand dynamics. A description of the dataset will be given in section 4.2.3. A ride-sharing market is a representative case of the growing on-demand economics [332]. The market is exemplified for three reasons. Firstly, non-equilibrium prices occur [332]. Implementing a dynamic pricing strategy is profitable for both consumers and a driver (seller) [332]. Dynamic pricing becomes the main tool to match demand and supply in a ride-sharing market [18, 21, 58, 144, 287, 402]. Lyft and Uber [42, 44], for example, have implemented dynamic pricing models.

Secondly, strong interactions between demand and supply occur. In a ride-sharing market, the three variables, price, demand, and supply, highly interact in time and also in space [44]. This contributes to temporal and spatial demand fluctuations. Under a strong interaction, demand and supply become a dynamical variable of an identical system, rather than different systems being coupled by price. In this setting, deterministic chaos of a dynamical system [116, 143, 150, 333, 343, 353, 360, 398] is more suitable than synchronizations [13, 298] of different systems. Takens' embedding theorem [324, 360] is thus applicable for the study of demand dynamics. Also, demand can be a representative variable of the market dynamics, including that of either price or supply.

Thirdly, a ride-sharing market provides a testing ground for nonlinear time series analysis. On-peak and off-peak patterns are important features in a traÿc system [14, 198, 322]. The ride-sharing dataset [310] records the traÿc flow every second, leading to an even sampling time series. The dataset thus provides a new real-life scenario where different patterns are observed in a time series. For nonlinear time series analysis,

a system with a transition between different patterns remains to be understood [49]. Demand in a ride-sharing market has heterogeneous patters, non-stationarity, and a contamination of noise. A study of the dynamics of a ride-sharing market thus will provide new insights into nonlinear time series analysis.

4.1.2 Recurrence plots

The dynamics that a time series underlies can be visualized and analyzed by a recurrence plot [117, 246]. The analysis is based on a binary matrix, which is associated with the recurrence of underlying dynamics in phase space [246]. Many recurrence quantification measures exist such as the determinism and the trapping time to quantify the dynamics. Diagonal lines of a recurrence plot quantify the determinism [246]. Vertical lines quantify the trapping time [246]. Mathematical definitions will be given in section 4.2.2.

Recurrence plots being applied for a detection of different patterns in complex dynamics have attracted increasing attention [49, 146, 189, 350]. In thermo-acoustics, a change in recurrence quantification measures is consistent with a change in the slow and the fast dynamics [49, 189]. Recurrence analysis identifies an abrupt change in the EI Niño-Southern Oscillation [146]. Besides, recurrence plots allow an extraction of an attractor from friction-excited vibrations with multi-scale dynamics [350].

Our focus is on a real-life dynamic pricing setting where on-peak and off-peak patterns are evident. We aim to (1) identify the dynamics of demand and extract an on-demand attractor by recurrence plots and (2) utilize dynamic pricing scenario to complement recurrence analysis. Demand dynamics is benchmarked against deterministic and stochastic dynamics. The Rössler system and the Duÿng oscillation represent deterministic dynamics by showing periodic and chaotic states. The non-auto Fitzhugh-Nagumo model and a stochastic resonance in Duÿng oscillator represent deterministic dynamics contaminated by different levels of noise. An AR(2) process, multi-fractional Gaussian noise, and a Poisson process represent stochastic dynamics.

To complement the recurrence analysis, we apply Pareto optimality on the statis-

Table 4.1 : Deterministic and stochastic systems as the benchmarking dynamics.

System	Equations		Parameters and dynamics
Rössler	$\begin{cases} \dot{x} = -y - z \\ \dot{y} = x + ay \\ \dot{z} = b + z(x - c) \end{cases}$	(E1)	$a = 0.1, b = 0.2, c = 3$. Periodic $a = 0.1, b = 0.2, c = 14$. Chaotic
Duÿng	$\ddot{x} + \delta\dot{x} + \alpha x + \beta x^3 = A cos(\omega t)$	(E2)	$\delta = 0.3, \alpha = -1, \beta = 1, A = 0.37, \omega = 1.2$ Periodic $\delta = 0.05, \alpha = -1, \beta = 1, A = 0.33, \omega = 1.3$ Chaotic
SR	$\ddot{x} + \delta\dot{x} + \alpha x + \beta x^3 = A sin(\omega t) + D\xi(t)$	(E3)	$\delta = 0.5, \alpha = -1, \beta = 0.5, \omega = 0.09,$ $A = 0.38, D = 1, \xi(t)$: Gaussian noise Stochastic driven, $SNR = 26.85 dB$
nFHN	$\begin{cases} \dot{v} = v - v^3 - w + I_{\text{ext}}(t) \\ \dot{w} = v - a - bw \end{cases}$	(E4)	$a = -0.3, b = 1.4, \tau = 20$ I_{ext} : Gaussian noise $\mathcal{N}(0, 0.5)$ Stochastic driven, $SNR = 8.14 dB$
mfG	-		Stochastic
AR(2)	$x_t = a + bx_{t-1} + cx_{t-2} + \epsilon_t$	(E5)	$a = 1, b = -1, c = 0.5, \epsilon_t$: Noise Stochastic

tics of two recurrence quantification measures, the determinism and the trapping time. The optimization aims for an optimal parameter set, the embedding and the time delay dimensions. Our results will provide new insights into the modeling of uncertain demand and into the disambiguation between deterministic and stochastic dynamics by recurrence analysis and surrogate data.

4.2 Models, methods, and data

Five steps are involved to identify demand dynamics. (1) We propose a recurrence-based attractor reconstruction. (2) Raw data from RideAustin is converted into a time series

of demand. (3) Surrogate data of demand are generated. (4) We apply the recurrence-based attractor reconstruction on well-studied deterministic and stochastic systems, a time series of demand, and its surrogate data. (5) Demand dynamics is identified by comparing with the dynamics of the well-studied deterministic and stochastic systems, the surrogate data, and the widely assumed Poisson process. We develop a decision matrix to show the dynamics that a time series underlies.

We will introduce the well-studied deterministic and stochastic systems in section 4.2.1. The reconstruction-based attractor reconstruction will be described in section 4.2.2. A method of processing raw data will be given in section 4.2.3. A method of yielding a Poisson process to model raw data will be given in section 4.2.4. Surrogate data methods will be described in section 4.2.5.

4.2.1 Benchmarking systems

We utilize six well-studied systems to benchmark demand dynamics. The systems exhibit either deterministic dynamics being periodic or chaotic, stochastic dynamics, or deterministic dynamics contaminated by different levels of noise. Considering the on-peak and off-peak patterns of a ride-sharing market, we mainly choose the systems that present an obvious change in the time series. Tab. 4.1 gives the parameters and the equations of individual systems and indicates the corresponding dynamics.

The Rössler system (Rössler) [314] can exhibit periodic and chaotic dynamics, depending on the value of the parameters (Tab. 4.1). The system has suddenly bursting behaviors in $z-$component [143]. Generally, the dynamics of the Rössler system is studied on $x-$component, $y-$component, or its three components together [49, 246]. However, our focus is on a univariate time series with different patterns in dynamics, so our experiment is conducted on $z-$component.

The forced damped double-well Duÿng oscillator (Duÿng) [207] can also exhibit periodic and chaotic dynamics. The system has been used to model the damped and forced vibrations in many engineered systems [143, 207]. Under the parameters we

choose, the system oscillates between two symmetric potential wells and exhibits a cross-well behavior. The oscillation presents different time scales in dynamics [207]. The one is a slow dynamics associated with the decaying oscillations in a slow time scale [207]. The other one is a fast dynamics associated with the damped natural frequency in a fast time scale [207].

Non-auto FitzHugh-Nagumo model (nFHN) [131] and stochastic resonance (SR) [32, 136] have deterministic components, however, the driven force is Gaussian noise (Tab. 4.1). Stochastic resonance is a phenomenon taking place when a nonlinear signal is amplified and optimized by the presence of noise [32, 136]. The system (Eq. E3*) has been applied to model climate changes [33]. For a given strength A (Eq. E3) of a periodic force (periodic Duÿng oscillator), an optimal intensity D of noise (Eq. E3) exists [32, 136], resulting in an SR. Eq. (E4) describes an excitable system, such as the brain dynamics [420]. An nFHN model (Eq. E4) exhibits the slow and the fast dynamics [189]. An SR and an nFHN models combine deterministic with stochastic dynamics and represent stochastic-driven dynamics. Signal-to-noise ratio (SNR) measures the degree of deterministic dynamics in a system. The higher SNR is, the higher level of determinism a system contains.

For stochastic dynamics, we look at the multi-fractional Gaussian noise (mfG) and an AR(2) process. Being consistent with Braun et al. [49], the Hurst exponent of mfG is of time dependent, and sinusoidally changes from 0.25 to 0.75. Eq. (E5) defines an AR(2) process. The mfG and an AR(2) process are representative systems that show the feature of a recurrence plot related to stochastic dynamics [49]. In addition, a periodic modulation exists in both the mfG and an SR. We thus use mfG to benchmark against an SR for identifying a difference between stochastic dynamics and deterministic dynamics contaminated by an optimal level of noise.

*"E" is used to label equations related to benchmarking systems.

4.2.2 Methods

A recurrence-based reconstruction is to find an optimal embedding and an optimal time delay dimensions for reconstructing an attractor from a time series. To achieve that, we apply Pareto optimality on recurrence plots and allow the embedding and the time delay dimensions to travel through a feasible set. Pareto optimality is an optimization with more than two objectives [199, 241]. A solution is Pareto optimal if and only if any of its objectives cannot be improved without a deterioration in at least one objective [199, 241]. A Pareto front is a set of Pareto optimal solutions. In an objective space, the optimum of the corresponding objectives delineate a Pareto front.

Recurrence plot is a plot that visualizes and quantifies nonlinear dynamics based on a binary matrix [246]. The matrix is called a recurrence matrix and satisfies

$$R_{i,j} = \begin{cases} 1 & ||\boldsymbol{x}_i - \boldsymbol{x}_j|| \leq \epsilon \\ 0 & ||\boldsymbol{x}_i - \boldsymbol{x}_j|| > \epsilon \end{cases} \tag{4.1}$$

where $R_{i,j}$ is an entry of the matrix, and $i, j \in \left\{1, 2, \cdots, N_S\right\}$. Here, $\boldsymbol{x}_i$ and $\boldsymbol{x}_j$ are a state in phase space, N_S is the total number of states, ϵ is a threshold, and $||\bullet||$ is a distance measure. Euclidean distance $||\bullet||_2$ is used in our calculation. Despite a use of Euclidean distance in Eq. (4.1), one can customize the definition of a recurrence to construct a recurrence matrix. For point process data or an event series, for example, Hirata and Aihara [172] show that timing contains critical information. Suzuki et al. [358] thus propose a customized distance matrix to capture the timing of point process data.

An attractor reconstruction affects the quality of recurrence plots [246]. Takens' embedding theorem [324, 360] ensures the existence of a reconstruction that embeds an original attractor. Also, the reconstruction preserves the dynamics of the original attractor by

$$\boldsymbol{x}_i = (x_i, x_{i+\tau}, \cdots, x_{i+(m-1)\tau}) \tag{4.2}$$

where m is the embedding dimension, τ is the time delay dimension, and x_i is a scalar of a

dynamical system. Eq. (4.2) describes an attractor reconstruction from a univariate time series. The parameters, m and τ (Eq. 4.2), and a threshold, ϵ (Eq. 4.1), are adjustable parameters. The value of m, τ and ϵ should be chosen with caution for avoiding pitfalls of recurrence plots [243].

We use a fixed recurrence rate, which leads to an adaptive ϵ [246]. Recurrence rate is a recurrence quantification measure that quantifies the density of recurrence points in a recurrence matrix (Eq. 4.1) [246]. The definition follows

$$RR = \frac{1}{N^2} \sum_{i,j=1}^{N} R_{i,j}$$

In our experiments, $RR = 0.1$. Two reasons exist to use a fixed recurrence rate. Fixing RR yields more reliable results than its counterparts as m changes [208]. In addition, results are more comparable than its counterparts as m and τ simultaneously change. Under a fixed ϵ, an increase of m and τ leads a recurrence plot to be zero almost everywhere regardless of the underlying dynamics. Recurrence quantification measures thus suffer a disadvantage in disambiguating between stochastic and deterministic dynamics. A fixed recurrence rate takes an adaptive ϵ [243], thus avoiding the disadvantage.

The parameters, m and τ, are often derived from mutual information and the false nearest neighbors (FNN) [49, 60, 208, 278, 295], cf. section 1.4.3. For τ, the one under which mutual information reaches the first local minimum is chosen. For m, the one under which FNN goes below a threshold is chosen.

However, we do a reverse thinking to find an optimal m and an optimal τ. The experimental thought is as follows. Let (m, τ) be adjustable and travel through all feasible choices, then we apply an optimization to find an optimal parameter set (m^*, τ^*). An attractor is reconstructed at (m^*, τ^*) according to Eq. (4.2). Because our data coming from a ride-sharing market have obvious on-peak and off-peak patterns, we apply Pareto optimality to find (m^*, τ^*) under which recurrence plots yield the most robust results. The diagonal and the vertical lines of a recurrence matrix (Eq. 4.1) together quantify the robustness of recurrence plots.

Among recurrence quantification measures, the determinism DET quantifies the dynamics of a system by diagonal lines of a recurrence matrix. The trapping time TT quantifies the dynamics of a system by vertical lines. Here, DET and TT are calculated via

$$DET = \frac{\sum_{l=l_{min}}^{N} lP(l)}{\sum_{l=1}^{N} lP(l)} \tag{4.3}$$

$$TT = \frac{\sum_{v=v_{min}}^{N} vP(v)}{\sum_{v=v_{min}}^{N} P(v)} \tag{4.4}$$

At a given length l, $P(l)$ is a histogram of diagonal lines of which the length is equal to l in a recurrence matrix (Eq. 4.1). At a given length v, $P(v)$ is a histogram of vertical lines of which the length is equal to v. Also, l_{min} and v_{min} represent the minimal length for a calculation. A diagonal line of length l is closely related to the divergence of a trajectory segment [246]. During l time steps, the trajectory segment of length l is close under the time evolution. A vertical line of length v implies that the consecutive l points are close [246], thus being trapped in an identical state. Without explicit mentions, we let $l_{min} = 2$ and $v_{min} = 2$.

For reconstructing an attractor, two steps are involved. The first step is to obtain a time series $\{DET_t\}$ of the determinism and that $\{TT_t\}$ of the trapping time along sliding windows (Figs. 4.1A to 4.1E). The second step is to choose (m^*, τ^*) from Pareto optimal solutions (Figs. 4.1F and 4.1G). Those two steps are defined by

$$\begin{aligned}
\min_{(m,\tau)} \quad & \Big(\mathrm{SD}_{DET}(m,\tau),\, \mathrm{SD}_{TT}(m,\tau)\Big) \\
& \mathrm{SD}_{DET}(m,\tau) = \sqrt{\frac{1}{N-1}\sum_{t=1}^{N}(DET_t - \mu_{DET})^2} \\
& \mathrm{SD}_{TT}(m,\tau) = \sqrt{\frac{1}{N-1}\sum_{t=1}^{N}(TT_t - \mu_{TT})^2} \\
& \mu_{DET} = \frac{1}{N}\sum_{t=1}^{N} DET_t(m,\tau),\ \mu_{TT} = \frac{1}{N}\sum_{t=1}^{N} TT_t(m,\tau) \\
& DET_t = DET_t(m,\tau),\ TT_t = TT_t(m,\tau) \\
& m \in \Big\{2,3,\cdots,20\Big\},\ \tau \in \Big\{2,3,\cdots,20\Big\}
\end{aligned} \tag{4.5}$$

where N represents the total number of sliding windows, and DET_t is the determinism

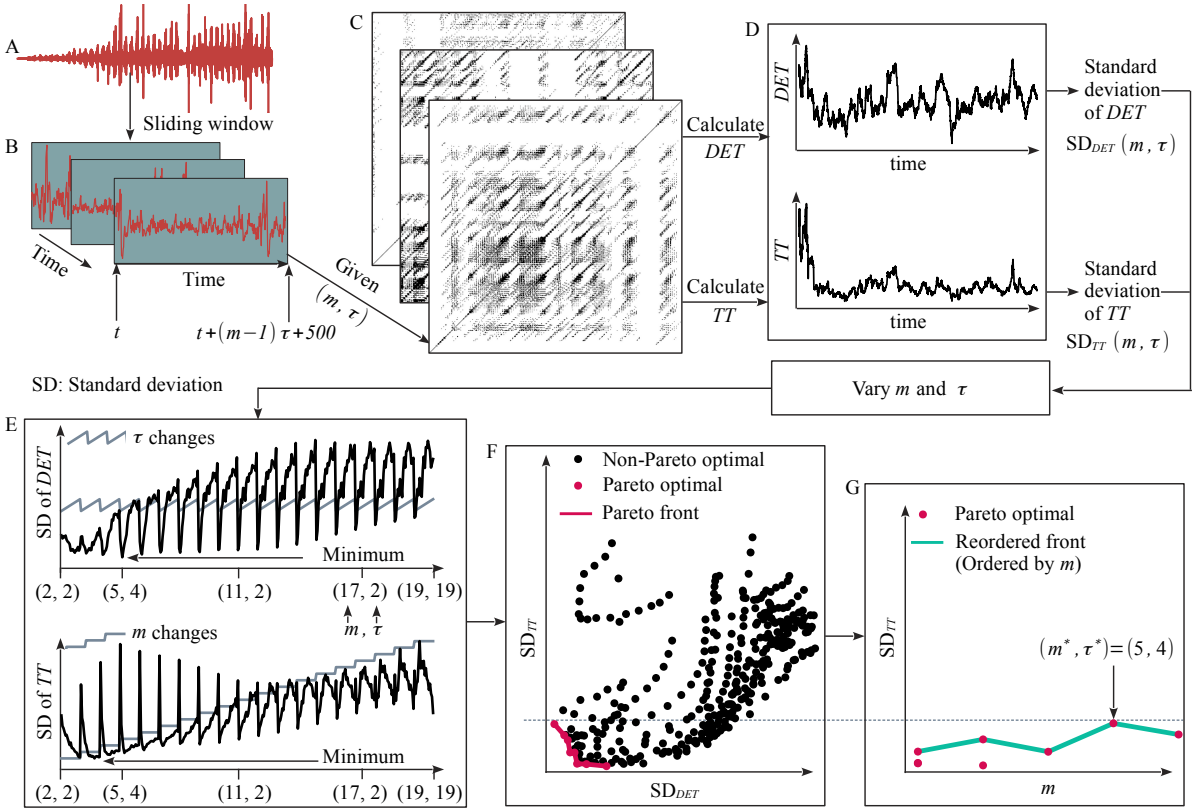

Figure 4.1 : A workflow of recurrence-based attractor reconstruction. A. The reconstruction is based on a univariate time series. B. At time t and a given parameter set (m,τ), Eq. (4.2) leads a $t-$th window that includes $(m-1)\tau+S$ consecutive points to S states in phase space. C. Eq. (4.1) is applied on those S states, yielding a recurrence plot. From Eq. (4.3), $DET_t(m,\tau)$ is calculated. From Eq. (4.4), $TT_t(m,\tau)$ is calculated. As t increases, sliding windowed recurrence plots are yielded. D. As t increases, a time series $\{DET_t\}$ of DET and that $\{TT_t\}$ of TT are saved. At a given (m,τ), the standard deviation SD_{DET} of $\{DET_t\}$ and that SD_{TT} of $\{TT_t\}$ are calculated. E. As (m,τ) changes, SD_{DET} and SD_{TT} fluctuate. F. Minimizing SD_{DET} and SD_{TT} together results in a Pareto optimization (Eq. 4.5). All Pareto optima outline a front. G. An optimal parameter set (m^*,τ^*) is then chosen by comparing between the maximum of local maxima and the global maximum in the $(m,\ \mathrm{SD}_{TT})$-plane as the front (F) is reordered by an increase of m.

that is calculated by Eq. (4.3) at a given (m,τ) and a given $t-$th window (Figs. 4.1A to 4.1C). Similarly, TT_t is the trapping time calculated by Eq. (4.4) at a given (m,τ) and a given window. An increase of t leads to $\{DET_t\}$ and $\{TT_t\}$ (Fig. 4.1D). Also, μ_{DET} and SD_{DET} correspond to the mean and the standard deviation of $\{DET_t\}_{t=1}^{N}$ (Fig. 4.1D),

respectively. Similarly, μ_{TT} and SD_{TT} correspond to that of $\{TT_t\}_{t=1}^{N}$, respectively.

To obtain a sliding window, we let $S = 500$ (Fig. 4.1B). In our experiments for ride-sharing demand, 500 states are enough for a sliding window to cover the dynamics of one day. For the benchmarking systems (Tab. 4.1), 500 states are enough to allow a window presenting the slow and the fast oscillations twice. However, the value of S should be application dependent and ensure a sliding window covering the dynamics that matters.

Eq. (4.5) has two objectives, $\mathrm{SD}_{DET}(m,\tau)$ and $\mathrm{SD}_{TT}(m,\tau)$. At a given (m,τ), $\mathrm{SD}_{DET}(m,\tau)$ and $\mathrm{SD}_{TT}(m,\tau)$ are derived from $\{DET_t\}$ and $\{TT_t\}$, respectively. Varying (m,τ) results in a fluctuation of $\mathrm{SD}_{DET}(m,\tau)$ and that of $\mathrm{SD}_{TT}(m,\tau)$ (Fig. 4.1F). This forms the objectives of Eq. (4.5). Here, m and τ are varied in this way.
(1) At a given m, we let τ change from 2 to 20.
(2) We then let m change from 2 to 20, and for a given m we do the procedure (1).
Here, m and τ start from 2, rather than 1. The reason is that the study is on a system with heterogenous patterns in a time series (Fig. 4.1A). The patterns are often observed in a phase space more than two dimensions. Varying m and τ makes m exhibit a step-wise pattern (Fig. 4.1E), however, makes τ exhibit a zigzag pattern (Fig. 4.1E).

A use of DET and TT in Eq. (4.5) is due to two reasons. Firstly, DET shows the ability to disambiguate between stochastic and deterministic dynamics [171, 244, 397]. The degree of determinism (predictability) of a system can be quantified by DET [246, 264]. A use of DET is thus consistent with our goal to identify a determinism from a real-life signal. Secondly, TT shows the ability to identify a change in dynamical patterns from a recurrence plot [277]. That how long a system is trapped in a specific state can be quantified by TT [246]. A use of TT is thus consistent with the feature of a ride-sharing market, which has two different (on-peak and off-peak) patterns. However, the objectives in Eq. (4.5) should be application dependent. The choices for the number and the type of recurrence quantification measures should agree with the goal of the study and reflect the dynamics that one cares about.

It is often the case that Pareto optimality leads to more than one solution. However,

an attractor reconstruction needs only one set of parameters (m,τ). We, therefore, choose the optimal parameters (m^*,τ^*) according to this rule: (m^*,τ^*) should yield a large SD_{TT} at the cost of a small m. A Pareto front and a reordered front are important for us to choose (m^*,τ^*). One plots SD_{DET} ($x-$axis) against SD_{TT} ($y-$axis), resulting in the (SD_{DET}, SD_{TT})-plane (Fig. 4.1F). Similarly, Plotting m ($x-$axis) against SD_{TT} ($y-$axis) results in the (m, SD_{TT})-plane (Fig. 4.1G). In the (SD_{DET}, SD_{TT})-plane, all feasible solutions, which can not be dominated by each other, outline a frontier. The frontier is the Pareto front (Fig. 4.1F). A reordered front is all feasible solutions plotted in (m, SD_{TT})-plane (Fig. 4.1G). A Pareto front is ordered by an increase of SD_{TT} (Fig. 4.1F), whereas a reordered front is ordered by an increase of m (Fig. 4.1G). Five procedures are taken for finding the (m^*,τ^*).

1. All feasible solutions to Eq. (4.5) outline a Pareto front and a reordered front. If more than two Pareto optimal solutions exist at some m, then the largest SD_{TT} is chosen as the point to outline a reordered front (Fig. 4.1G).
2. Does the reordered front has a local maximum? If none of maxima is observed, then (m^*,τ^*) is chosen case by case.
3. If a local maximum is observed, then a balance is made between a large SD_{TT} and a small m. If the local maximum corresponds to the global maximum, then the corresponding (m,τ) is chosen as (m^*,τ^*). If none of local maxima correspond to a global maximum, then two cases are possible.
4. (1) If the maximum of local maxima is close to the global maximum, then (m,τ) corresponding to the maximum of local maxima is chosen as (m^*,τ^*) (Fig. 4.9C_2).
5. (2) If the maximum of local maxima is distant from the global maximum, then a balance is made between the maximum of local maxima and the global maximum.

As it is diÿcult to tell the closeness between the global maximum and the maximum of local maxima, recurrence plots should be generated to make the balance. By looking at recurrence plots under different Pareto optimal choices of (m,τ), the one that reflects a desired dynamics is chosen as (m^*,τ^*). In our experiments, if a local maximum being a global maximum is observed, then Procedure (3) is applied for (m^*,τ^*). If none of

local maxima is observed, then (m, τ) that corresponds to a global maximum is chosen (Figs. 4.3H$_2$, 4.9A$_2$). If the maximum of local maxima is distant from a global maximum, then the smallest of m that leads SD$_{TT}$ being close to the global maximum is chosen (Figs. 4.3E$_2$ and 4.3F$_2$).

The rule to choose (m^*, τ^*) is based on a large SD$_{TT}$, because our desired dynamics is heterogenous patterns in a time series. A large SD$_{TT}$ indicates that along the sliding windows recurrence plots yield results with a large deviation. This is consistent with observations that the time series underlies heterogeneity. Eq. (4.5) is to find recurrence plots with the robustest results. A choose of (m^*, τ^*) is to find the recurrence plots with the best reflections of the heterogenous patterns from Pareto optimal solutions. Again, the rule to choose (m^*, τ^*) should depend on individual applications. It is worth mentioning that Eq. (4.5) does not lead to a recurrence plot with the maximal or the minimal DET or TT, since Eq. (4.5) minimizes the standard deviations.

4.2.3 Data

We look at demand that is processed from a real-life dataset [310]. The dataset was released by RideAustin [310]. It is a nonprofit company and provides transportation services in the greater Austin region, Texas, the United States [198], for one third of the local market share [217]. The dataset disclosures information of every transaction from 4 June 2016 to 13 April 2017 and aims to promote research in data analysis and transparent transportations [18, 198, 394].

The dataset [310] has $1,494,125$ transactions (Fig. 4.2A). Each transaction includes the time when it starts, creates, and completes and the latitude and the longitude where it starts and ends. Information related to prices such as base fares and total fares is included as well. More information about the dataset can be found in [310]. Raw data [310] are processed by aggregating a time series of transactions and and finding an optimal parameter p^*. Four procedures are involved in processing raw data.

(1) Aggregate transactions every p minutes. Here, p is related to the sampling rate and determines the frequency of aggregations of the transactions. We count the

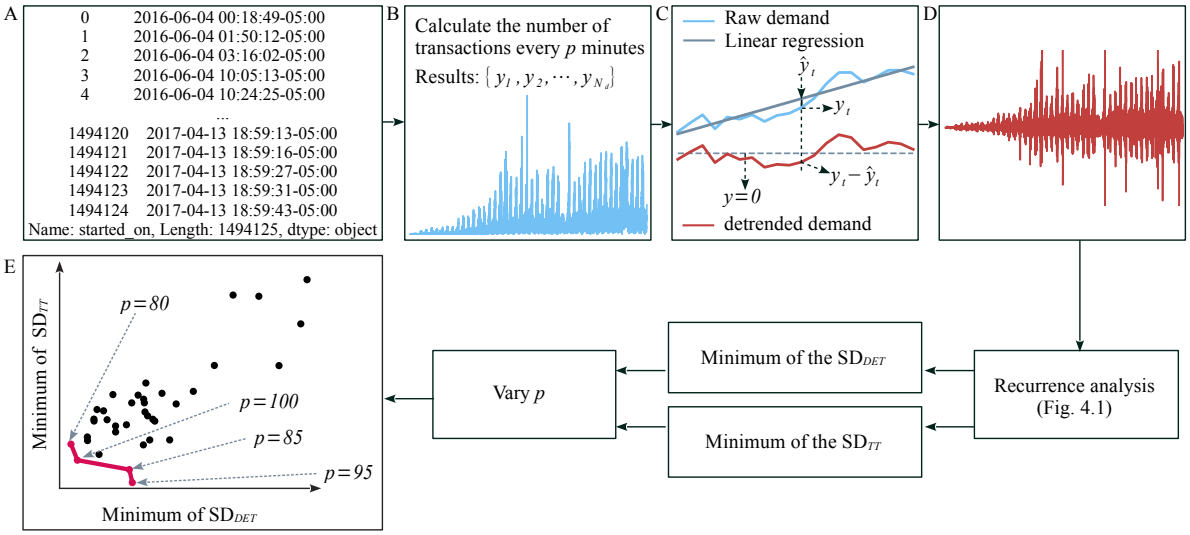

Figure 4.2 : Data preparation for an optimal parameter p^* to aggregate ride-sharing demand from transactions. A. The dataset [310] records the arrival time of each transaction. B. Raw demand is calculated by aggregating the number of transactions every p minutes. C. Linear regression is fitted in raw demand for removing the trends. At time t, the minus between the raw demand y_t and its linear fit $\hat{y}_t$ leads to detrended demand. (D) The object of recurrence analysis is the time series of detrended demand. At a given p, varying (m,τ) produces a time series of $\mathrm{SD}_{DET}(m,\tau,p)$ and that of $\mathrm{SD}_{TT}(m,\tau,p)$ (Fig. 4.1), and one can calculate the minimum of those SD_{DET} and that of those SD_{TT} (Fig. 4.1F). (E) Let $p \in \{5,10,\cdots,200\}$, then the optimal parameter p^* is chosen from Pareto optimal solutions to Eq. (4.6) that minimizes either the minimum of the SD_{DET} or that of the SD_{TT}.

number of transactions according to the time when the transaction starts, which corresponds to the field "started_on" (Fig. 4.2A) in the original dataset [310]. The field "started_on" records the arrival of consumers between 2016/06/04T00:18:49Z† and 2017/04/13T18:59:43Z. For example, at $p = 20$ (Fig. 4.2B), we count the number (y_1) of transactions from 2016/06/04T00:00:00Z to 2016/06/04T00:20:00Z, and the number (y_2) of transactions from 2016/06/04T00:20:00Z to 2016/06/04T00:40:00Z, and so on.

(2) Obtain a raw demand. At p, an aggregation yields a time series $\{y_1, y_2, \cdots, y_{N_d}\}$ of

†"-05:00" in Fig. 4.2A indicates an adjustment to UTC-5 (Eastern Time in the United States), which is different from the visualization in the original dataset [310].

raw demand (Fig. 4.2B). Here, y_{N_d} depends on p and represents the total length of the time series of raw demand. At $p = 20$, $y_{N_d} = 22,593$. At $p = 100$, $y_{N_d} = 4,518$.

(3) Apply a linear regression for a detrended demand. At time t, we make a linear regression on a point set $\left\{y_{t-10}, y_{t-9}, \cdots, y_t, y_1, \cdots, y_{t+10}\right\}$ and then find the linear fitting value $\hat{y}_t$ that fits the point y_t (Fig. 4.2C). A detrended demand represents the time series, $\left\{y_t - \hat{y}_t\right\}$. Algorithm 4.1 describes the regression and the procedures to detrend a raw demand.

(4) Apply Pareto optimality for an optimal parameter p^*. We let $p \in \{20, 25, \cdots, 200\}$. At an individual p, procedures (1) to (3) are applied, yielding 37 time series of detrended demand. At a given p and the corresponding detrended demand, we follow the workflow of conducting sliding windowed recurrence analysis (Figs. 4.1A to 4.1E). At a given p, the minimum of SD_{DET} and that of SD_{TT} are saved (Fig. 4.1E). Varying the parameter p yields two sets that contain the minimum of SD_{DET} and that of SD_{TT}, respectively. Pareto optimality is applied on those SD_{DET} and SD_{TT} for an optimal parameter p^*. At p^*, the corresponding detrended demand represents ride-sharing demand, thus being the subject of our empirical demand identification.

Algorithm 4.1: Algorithm for detrending a time series (Fig. 4.2C)

Result: Detrended demand

Input: A time series of raw demand $\{y_1, , y_2, \cdots, y_{N_d}\}$, where N_d is the total length;

for $t \in \{11, 12, y_{N_d} - 11\}$ **do**

  Make a linear regression of the data $\{(0, y_{t-10}), (1, y_{t-9}), \cdots, (10, y_t), \cdots, (20, y_{t+10})\}$;

  Fit the linear regression and calculate the prediction at the point $(10, y_t)$, which results in a linear fit $(10, \hat{y}_t)$;

  Return $y_t - \hat{y}_t$;

end

Yield a time series $\{y_t - \hat{y}_t\}_{t=11}^{N_d-11}$ of detrended demand;

Procedure (4) can be described by

$$
\begin{aligned}
\min_{p} \quad & \Big(\min_{m,\tau} \mathrm{S}_{DET}(m,\tau,p),\ \min_{m,\tau} \mathrm{S}_{TT}(m,\tau,p)\Big) \\
& \mathrm{SD}_{DET}(m,\tau,p) = \sqrt{\frac{1}{N-1}\sum_{t=1}^{N}(DET_t - \mu_{DET})^2} \\
& \mathrm{SD}_{TT}(m,\tau,p) = \sqrt{\frac{1}{N-1}\sum_{t=1}^{N}(TT_t - \mu_{TT})^2} \\
& \mu_{DET} = \frac{1}{N}\sum_{t=1}^{N} DET_t(m,\tau,p),\ \mu_{TT} = \frac{1}{N}\sum_{t=1}^{N} TT_t(m,\tau,p) \\
& DET_t = DET_t(m,\tau,p),\ TT_t = TT_t(m,\tau,p) \\
& m \in \Big\{2,3,\cdots,20\Big\},\ \tau \in \Big\{2,3,\cdots,20\Big\},\ p \in \Big\{20,25,\cdots,200\Big\}
\end{aligned}
\tag{4.6}
$$

Different from Eq. (4.5), DET_t and TT_t in Eq. (4.6) depend on (m,τ) and p. The reason is that Eq. (4.6) is applied on a detrended demand, which depends on the value of p (Figs. 4.2A to 4.2D). However, Eq. (4.5) is applied on a well-sampled time series. In addition, Eq. (4.5) is to find (m^*,τ^*) under which recurrence plots yields the smallest deviations in the diagonal and the vertical lines together. Eq. (4.6) is to find (m^*,τ^*) under which recurrence plots yields the smallest deviations either in the diagonal or in the vertical lines.

The rule that under a reasonable sampling rate recurrence plots yield a reliable dynamics is applied to define the objectives in Eq. (4.6). The reliability is quantified by the standard deviations of recurrence quantification measures as well. However, the dynamics can be represented by either diagonal or vertical lines. The reason to take the rule is that the diagonal and the vertical lines represent different types of dynamics [246]. The optimal sampling rate should lead to a time series with the reliable type of dynamics, which is unrelated to the choices over the diagonal or the vertical lines. Therefore, Eq. (4.6) aims for an optimal value of p^* under which the minimum between the minimum of SD_{DET} and that of SD_{TT} is chosen. The parameter set (m,τ) corresponding to the minimal SD_{DET} does not necessarily equal to that SD_{TT} (Eq. 4.6).

4.2.4 Poisson process

The dataset from RideAustin [310] is assumed to account to a Poisson process in the modeling of dynamic pricing problems [18]. We generate a new dataset to test the null hypothesis that demand extracted from the dataset follows a Poisson process. Here, the arrival of consumers represents demand. According to an existing assumption [18], the arrival rate of the Poisson process satisfies that five consumers randomly arrive per minute. We count the number of transactions every p^* minutes. Here, p^* is the optimal solution to Eq. (4.6) on which the dataset from RideAustin [310] is applied. A simulated demand is thus yielded from a Poisson process. The detrended algorithm (Algorithm 4.1) is applied to the simulated demand as well. We term the new dataset as a Poisson process, although it is the arrivals satisfying a Poisson process. An identical p^* is applied on the dataset from RideAustin [310] and the Poisson process.

4.2.5 Surrogate time series

A difference between stochastic and deterministic dynamics can be seen from a surrogate data method as well. The method constructs a surrogate that satisfies a null hypothesis and compares the dynamics between an original and a surrogated time series. From the comparisons, one can reject or accept the null hypothesis [188, 215, 331, 341, 367]. We use three surrogates to test the underlying dynamics of the ride-sharing demand from nonlinear time series analysis perspective. They are shuffle-based, Fourier-based, and truncated amplitude adjusted Fourier transform surrogates.

Shuffle-based surrogate The method randomly shuffles an original time series [215, 367]. The null hypothesis is that the time series underlies an independent and identically distributed process (IID) [215, 367]. We use a shuffle-based surrogate to test that whether the uncorrelated noise, such as Gaussian noise widely assumed for dynamic pricing models, is responsible for the dynamics of ride-sharing demand.

Fourier-based surrogate The method randomizes the Fourier components of an original time series [215, 367]. The null hypothesis is that the time series does not contain any nonlinearity [215, 367]. We use a Fourier-based surrogate to test that whether a stationary linear Gaussian process is responsible for the underlying dynamics.

Truncated amplitude adjusted Fourier transform (AAFT) The method preserves the amplitude distribution of an original time series, however, randomizes the Fourier components of an original time series. The null hypothesis is that the time series represents a rescaled linear Gaussian process [215, 267, 367]. We use a truncated AAFT to test that whether the irregularity is due to a stationary linear process [267].

Many surrogate data methods exist in testing a null hypothesis, such as a pseudo-periodic test [342] and a wavelet-based surrogate [193]. The reader may refer to a recent review about surrogate data in [215]. We use a package from Julia [43], TimeseriesSurrogate.jl [97, 370], to obtain the three types of surrogate data. The ride-sharing demand is regarded as the original time series for conducting the three types of surrogate data methods.

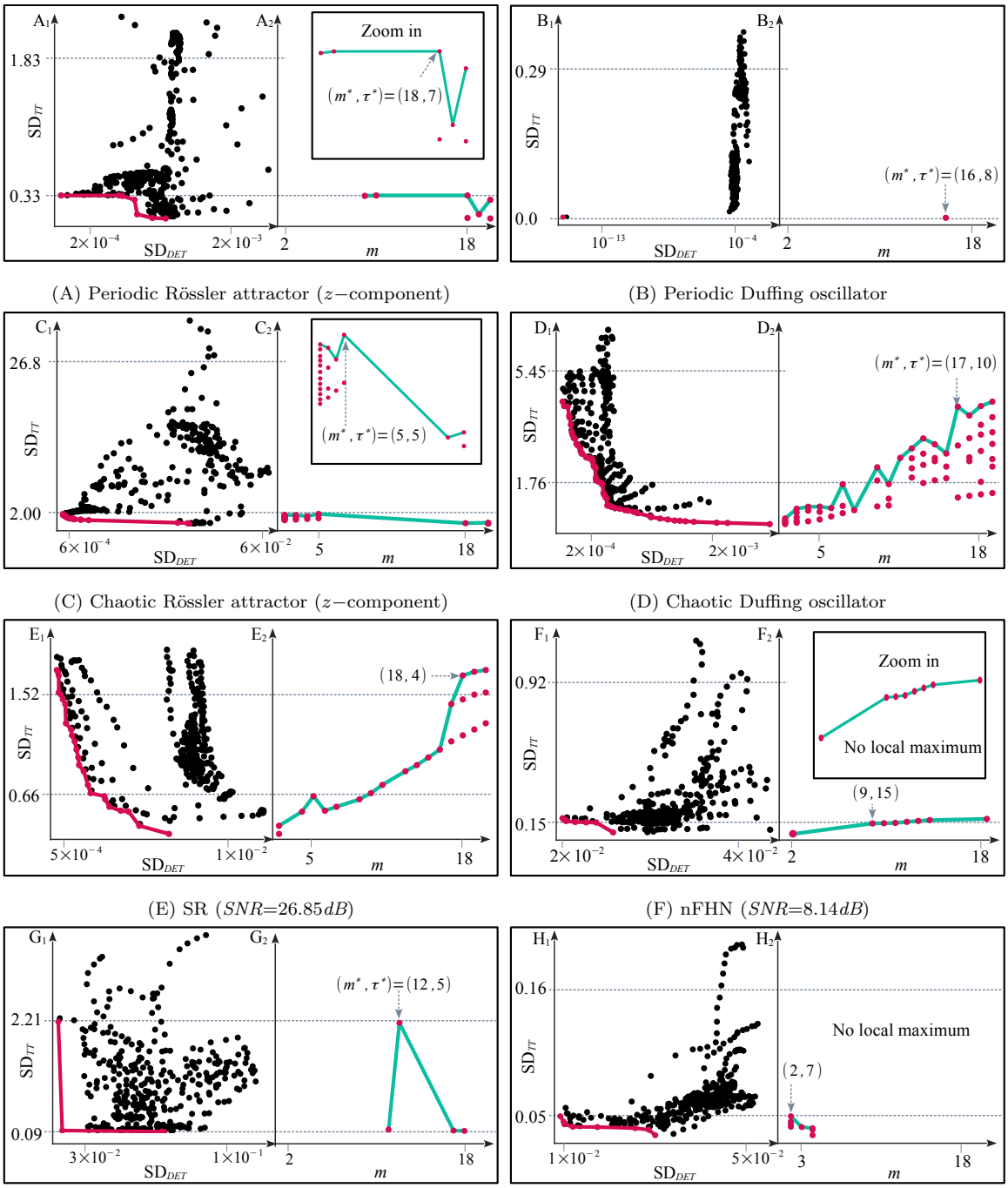

(A) Periodic Rössler attractor ($z-$component)

(B) Periodic Duffing oscillator

(C) Chaotic Rössler attractor ($z-$component)

(D) Chaotic Duffing oscillator

(E) SR (SNR=26.85dB)

(F) nFHN (SNR=8.14dB)

(G) mfG

(H) AR(2) process

Figure 4.3 : Pareto front and reordered front in the (m,SD_{TT})-plane for benchmarking dynamics. A and B: Periodic dynamics. C and D: Chaotic dynamics. E and F: Stochastic driven dynamics where noise drives the evolution of deterministic equations. G to H: Stochastic dynamics. A_1 to H_1: Pareto front is outlined by the corresponding optima to Eq. (4.5) in the $(\mathrm{SD}_{DET},\mathrm{SD}_{TT})$-plane. Here, the $x-$axis has a log scale. A_2 to H_2: The corresponding Pareto front of A_1 to H_1 is reordered in the (m,SD_{TT})-plane. The rule, a large SD_{TT} but a small m, is applied to find optimal parameters (m^*,τ^*). The global maximum and the maximum of local maxima are compared for finding (m^*,τ^*).

4.3 Results

Recurrence-based attractor reconstruction (Fig. 4.1) is applied to the benchmarking systems (Tab. 4.1), the ride-sharing demand (Fig. 4.2), the Poisson process (section 4.2.4), and the surrogate data (section 4.2.5). Results will be sequentially presented. The features of the benchmarking systems will be shown firstly. The ride-sharing demand will then be compared with the benchmarking systems, the Poisson process and the surrogate data. The features include an organization of the Pareto front and the reordered front, an observation of recurrence plot under (m^*, τ^*), a pattern of recurrence quantification measures, and an outline of attractor under (m^*, τ^*). A decision matrix will be developed for a summary of results as the ride-sharing demand is compared with those systems.

4.3.1 Benchmarking systems

As Eq. (4.5) is applied to the benchmarking systems (Tab. 4.1), differences between stochastic and deterministic dynamics can be seen from the Pareto front and the reordered front. Fig. 4.3 shows the feature of the Pareto front and the reordered front. The differences can be seen from three perspectives. They are (1) the feature of SD_{DET} in the $(\mathrm{SD}_{DET}, \mathrm{SD}_{TT})$-plane, (2) the feature of the Pareto front related to an identification of a plateau (Figs. 4.3A_1 to 4.3H_1), and (3) the feature of the reordered front in the (m, SD_{TT})-plane (Figs. 4.3A_2 to 4.3H_2).

The number of log scales in SD_{DET}. For deterministic dynamics (Figs. 4.3A_1 to 4.3D_1), SD_{DET} varies at least in two different scales (Figs. 4.3A_1 and 4.3B_1,Tab. 4.2). For stochastic driven dynamics, the number of log scales depends on the signal-to-noise ratio (*SNR*). For SR, its *SNR* is $26.85dB$. Its SD_{DET} covers from 10^{-4} to 10^{-2} (Fig. 4.3E_1) with maximum/minimum $= 43.18$ (Tab. 4.2) where maximum (minimum) is the maximum (minimum) of SD_{DET} over all possible choices of (m, τ). For nFHN, the *SNR* is $8.14dB$, and the maximum/minimum $= 2.25 < 10$ (Tab. 4.2). This indicates that only one log scale is enough to cover SD_{DET}.

For stochastic dynamics, the ratio of the maximum of SD_{DET} and the minimum of

Table 4.2 : Features of Pareto front in deterministic and stochastic dynamics with respect to the $x-$axis and $y-$axis of Figs. 4.3A$_1$ to 4.3H$_1$. For periodic and chaotic dynamics, SD$_{DET}$ covers at least two log scales, evidenced by maximum/minimum > 10. For stochastic driven dynamics, the feature of SD$_{DET}$ depends on *SNR*. The SR with $SNR = 26.85dB$ covers two log scales. However, the nFHN with $SNR = 8.14dB$ is unable to cover two log scales, evidenced by maximum/minimum < 10 (SD$_{DET}$). For stochastic dynamics, neither mfG nor AR(2) has SD$_{DET}$ that covers two log scales. For SR and AR(2), their $y-$axis fluctuates in one log scale, evidenced by maximum/minimum < 10 (SD$_{TT}$).

System	SD$_{DET}$ ($x-$axis)			SD$_{TT}$ ($y-$axis)		
	minimum	maximum	$\frac{\text{maximum}}{\text{minimum}}$	minimum	maximum	$\frac{\text{maximum}}{\text{minimum}}$
Periodic Rössler	1.2×10^{-4}	3.6×10^{-3}	30	7.3×10^{-2}	2.29	31.37
Periodic Duÿng	2.2×10^{-16}	8.5×10^{-4}	3.9×10^{12}	3.6×10^{-15}	3.6×10^{-1}	10^{14}
Chaotic Rössler	5.3×10^{-4}	7×10^{-2}	132.08	3.8×10^{-1}	3.4×10^{1}	89.47
Chaotic Duÿng	1.1×10^{-4}	6×10^{-3}	54.55	4.5×10^{-1}	6.82	15.16
SR	4.4×10^{-4}	1.9×10^{-2}	43.18	3.4×10^{-1}	1.9	5.59
nFHN	2×10^{-2}	4.5×10^{-2}	2.25	9.4×10^{-2}	1.14	12.13
mfG	2.4×10^{-2}	1.3×10^{-1}	5.42	9×10^{-2}	3.87	43
AR(2)	9.6×10^{-3}	5.5×10^{-2}	5.73	3.4×10^{-2}	2×10^{-1}	5.88

SD$_{DET}$ is less than 10 (Tab. 4.2). This indicates that it is diÿcult to reduce SD$_{DET}$ by a factor of 10 as different possible choices for (m,τ) are applied (Figs. 4.3G$_1$ and 4.3H$_1$). The $x-$axis in Fig. 4.3G$_1$ has two different log scales, 10^{-3} and 10^{-2}. However, the maximum/minimum $= 5.42$ (Tab. 4.2), which indicates that one log scale exists to cover all the variations in SD$_{DET}$ by rescaling SD$_{DET}$.

A plateau in Pareto front. For deterministic dynamics, its Pareto front shows one of the two phenomena. (1) Pareto optimality (Eq. 4.5) has a unique optimal solution under which the minimal SD$_{DET}$ and the minimal SD$_{TT}$ are simultaneously achieved. For example, for the periodic Duÿng oscillator, Fig. 4.3B$_1$ shows that the optimization (Eq. 4.5) yields a unique optimal parameter $(m^*,\tau^*) = (16,8)$. Under (m^*,τ^*), both SD$_{DET}$ and SD$_{TT}$ are the minimum. (2) The Pareto front shows an obvious plateau. A

plateau is a flat area of a Pareto front satisfying the following two properties. (A) SD_{DET} covers strictly more than one log scales ($x-$axis); and, (B) the points that sit around the plateau have a relative small variation in the $y-$axis. For example, Fig. 4.3A_1 presents a plateau at the beginning part of the Pareto front. The reasons are (A) SD_{DET} covers two log scales, 10^{-4} and 10^{-3} (Fig. 4.3A_1) with maximum/minimum $= 30$ (Tab. 4.2), and (B) the $y-$axis of the plateau is around 0.33 (Fig. 4.3A_1). Similarly, Figs. 4.3C_1 and 4.3D_1 also present a plateau.

For stochastic driven dynamics and stochastic dynamics, no obvious plateau exists. In Fig. 4.3E_1, the $y-$axis changes drastically, causing a lack of an area with a small variation in SD_{TT}. In Figs. 4.3F_1 to 4.3G_1, the $x-$axis is unable to cover two different log scales, which is evidenced by maximum/minimum < 10 in SD_{DET} (Tab. 4.2).

Local maxima in the reordered front. The number of local maxima in the (m, SD_{TT})-plane shows a difference between deterministic and stochastic dynamics. For deterministic dynamics, either at least one local maximum exists (Figs. 4.3A_2, 4.3C_2, 4.3D_2) or a unique optimal solution exists (Fig. 4.3B_2). For stochastic driven dynamics and stochastic dynamics, at most one local maximum exists (Figs. 4.3E_2 to H_2). In addition, for stochastic dynamics the Pareto optimal m clusters around some value (Figs. 4.3G_2 and 4.3H_2). Fig. 4.3G_2 presents that mfG has no Pareto optimal m that is less than 11. Also, the AR(2) process has no Pareto optimal m that is strictly larger than 5 (Fig. 4.3H_2).

Furthermore, the maximum of local maxima equaling or approaching a global maximum is a feature to differ between deterministic dynamics and stochastic driven dynamics. For deterministic dynamics, the maximum of local maxima is either a global maximum (Figs. 4.3A_2 to 4.3C_2) or close to it (Fig. 4.3D_2). For the periodic and the chaotic Rössler attractors, the unique local maximal of SD_{TT} is the global maximal of SD_{TT} over all possible Pareto optimal m (Figs. 4.3A_2 and 4.3C_2). For SR, a unique local maximum exists (Fig. 4.3E_2). However, SR has different patterns while compared with deterministic dynamics (chaotic Duÿng oscillation). The SD_{TT} of SR monotonically in-

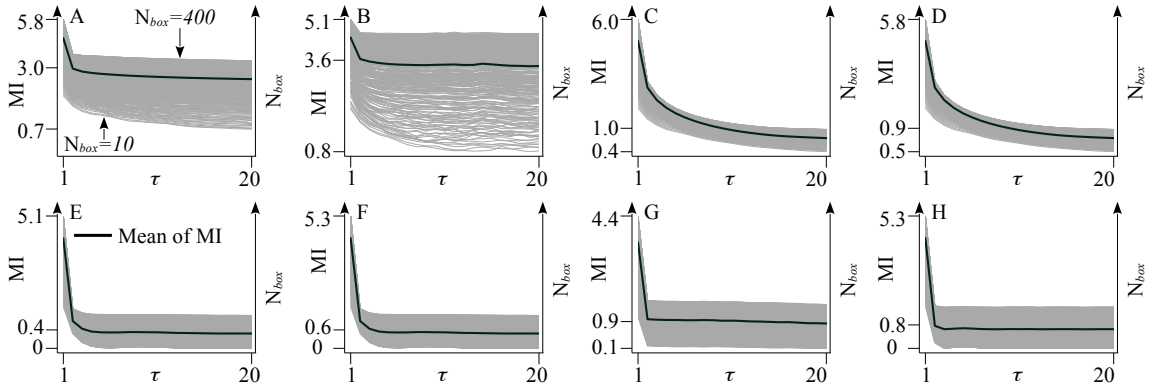

Figure 4.4 : Evident oscillations in averaged mutual information (MI) do not exist in locating the time delay τ. A. Periodic Rössler attractor. B. Periodic Duÿng oscillator. C. Chaotic Rössler attractor. D. Chaotic Duÿng oscillator. E. SR. F. nFHN. G. mfG. H. An AR(2) process. Here, MI is calculated by calling the TISEAN package [168], where the number of boxes (N_{box}) increases from 10 to 400. The mean of MI is the mean of MI over all boxes.

creases as m increases from 6 to 20 (Fig. 4.3E$_2$), whereas the SD_{TT} of the chaotic Duÿng oscillation presents multiple local maxima as m increases from 8 to 20 (Fig. 4.3D$_2$).

The reordered front show obvious ups and downs (Fig. 4.4), which clears the way for finding (m^*, τ^*). However, the method based on mutual information and FNN (section 1.4.3) is diÿcult to locate m and τ when it comes to the time series we study (Fig. 4.4). The periodic (Fig. 4.4B) and the chaotic (Fig. 4.4D) Duÿng oscillators have the first local minimum at $\tau = 9$ and $\tau = 12$, respectively. Also, SR (Fig. 4.4E), nFHN (Fig. 4.4F), and AR(2) (Fig. 4.4H) have the first local minimum at $\tau = 15$, $\tau = 6$, and $\tau = 8$, respectively. However, obvious oscillations, which are shown by multiple local maxima and minima [350], cannot be observed as mutual information is plotted against an increase of τ (Fig. 4.4). It is thus diÿcult to claim that τ at the first local minimum is suitable for recurrence plots. Pareto front and the reordered front present obvious features that lead to an optimal parameter set (m^*, τ^*). We then look at the feature of a recurrence plot under (m^*, τ^*).

Differences in recurrence plots. Fig. 4.5 shows recurrence plots of benchmarking

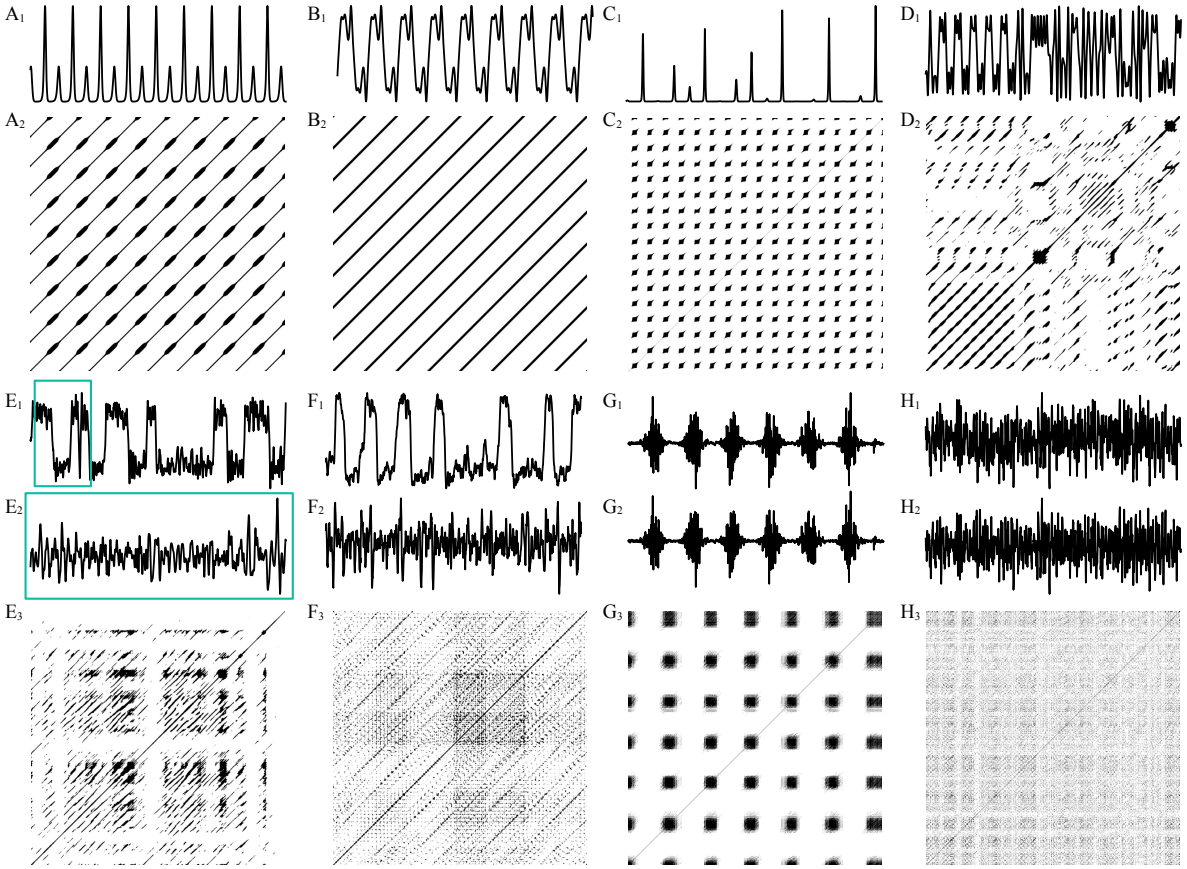

Figure 4.5 : Time series and recurrence plots of benchmarking dynamics under a Pareto optimal parameter set (m^*, τ^*). A_1 to D_1 are the time series. A_2 to D_2 are corresponding recurrence plots. E_1 to H_1 are an original time series. E_2 to H_2 are corresponding detrended time series. E_3 to H_3 are a recurrence plot of corresponding detrended time series. A shows the dynamics of the periodic Rössler attractor under $(m^*, \tau^*) = (18, 7)$, B shows the dynamics of periodic Duÿng oscillator under $(m^*, \tau^*) = (16, 8)$, C shows the dynamics of the chaotic Rössler attractor under $(m^*, \tau^*) = (5, 5)$, D shows the dynamics of the chaotic Duÿng oscillator under $(m^*, \tau^*) = (17, 10)$, E shows the dynamics of the SR under $(m^*, \tau^*) = (18, 4)$, F shows the dynamics of the nFHN under $(m^*, \tau^*) = (9, 15)$, G shows the dynamics of the mfG under $(m^*, \tau^*) = (12, 5)$, and H shows the dynamics of the AR(2) process under $(m^*, \tau^*) = (2, 7)$. Fig. 4.3 provides the calculations of corresponding (m^*, τ^*)

dynamics under (m^*, τ^*). For periodic dynamics (Figs. 4.5A_2 and 4.5B_2), recurrence plots exhibit non-interrupted diagonal lines [246], and the distance between diagonal lines is related to the periodicity of a signal [246]. For chaotic Rössler attractor, the recurrence

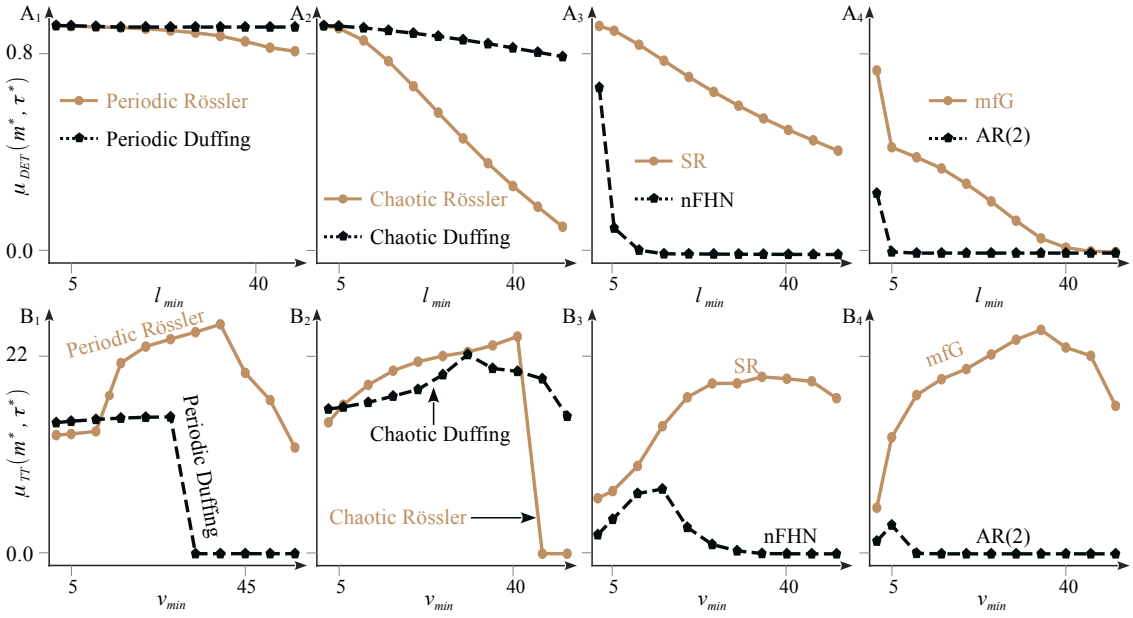

Figure 4.6 : Patterns of DET (Eq. 4.3) and TT (Eq. 4.4) as l_{min} and v_{min} are varied. A_1 to A_4 are the patterns of μ_{DET} as l_{min} is varied. Here, μ_{DET} is the mean of DET along all sliding windows, cf. Eq. 4.5. B_1 to B_4 are the patterns of μ_{TT} as v_{min} is varied. Here, μ_{TT} is the mean of TT along all sliding windows, cf. Eq. 4.5. A_1 and B_1 exemplify periodic dynamics. A_2 and B_2 exemplify chaotic dynamics. A_3 and B_3 exemplify stochastic driven dynamics. A_4 and B_4 exemplify stochastic dynamics.

plot exhibits a switch between clusters of points and blank white areas (Fig. 4.5C_2), indicating a heterogeneity in dynamics. For chaotic Duÿng oscillator, its recurrence plot contains long diagonal lines (Fig. 4.5D_2). However, those lines are interrupted by different patterns. For example, on the lower left in Fig. 4.5D_2, there is a patch of non-interrupted diagonal lines similar to that of Fig. 4.5A_2. The different patterns correspond to the cross-well behavior of chaotic Duÿng oscillator [207].

For stochastic driven dynamics, long diagonal lines in SR indicate that determinisms exist (Fig. 4.5E_3). However, an increase of noise level can destroy the diagonal lines. In nFHN blocks thus scatter along the diagonal lines (Fig. 4.5F_3). For stochastic dynamics, an AR(2) process presents many isolated black points (Fig. 4.5H_3), whereas the mfG exhibits a switch between clusters and blank white areas (Fig. 4.5G_3). Fig. 4.5E_1 shows

the cross-well behavior of an SR, which is consistent with the study of an SR in [49]. It is worth mentioning that Fig. 4.5E$_2$ corresponds to a segment of the detrended time series. Fig. 4.5E$_3$ is the recurrence plot of that segment, which is different from the plot shown in [49].

Variations in l_{min} and v_{min}. Fig. 4.6 depicts how μ_{DET} and μ_{TT} change as l_{min} and v_{min} change, respectively. While μ_{DET} (Eq. 4.5) monotonically decreases as l_{min} increases (Figs. 4.6A$_1$ to 4.6A$_4$), μ_{TT} firstly increases and then decreases as v_{min} increases (Figs. 4.6B$_1$ to 4.6B$_4$). The phenomenon is due to different definitions of DET and TT. The value of l_{min} only affects the numerator of DET (Eq. 4.3). However, the value of v_{min} affects both the numerator and the denominator of TT (Eq. 4.4).

For periodic dynamics, the change in l_{min} has a relative small influence on μ_{DET}. The periodic Rössler attractor and periodic Duÿng oscillator have μ_{DET} being larger than 0.8 at $l_{min} = 50$ (Figs. 4.6A$_1$). For chaotic dynamics, μ_{DET} presents two features. (1) At $l_{min} = 50$, μ_{DET} does not approach to zero (Fig. 4.6A$_2$). However, (2) the slope of the curve depends on individual systems. Fig. 4.6A$_2$ shows that the chaotic Rössler attractor decreases faster than the chaotic Duÿng oscillator. The reason is that the chaotic Rössler attractor has clusters in recurrence plots (Fig. 4.5C$_2$), rather than long diagonal lines shown in Fig. 4.5D$_2$. The length of most clusters in the chaotic Rössler attractor varies between 2 to 50. This causes a quick decrease as l_{min} increases. However, for chaotic Duÿng oscillator (Fig. 4.6A$_2$), most of long diagonal lines have a length larger than 50. An increases of l_{min} thus does not lead to a so quick decrease of μ_{DET} while compared with the chaotic Rössler attractor (Fig. 4.6A$_2$).

For stochastic driven dynamics, the feature of μ_{DET} depends on *SNR*. The SR with $\mu_{DET} = 26.85dB$ contains a high level of determinisms, and μ_{DET} shows a similar pattern (Fig. 4.6A$_3$) as the chaotic dynamics (Fig. 4.6A$_2$). Nevertheless, for the nFHN, its μ_{DET} approaches zero at $l_{min} = 10$. For stochastic dynamics, both the mfG and the AR(2) process approach zero (Fig. 4.6A$_4$). Also, the AR(2) shows a quicker way to approach zero than mfG. Furthermore, as l_{min} increases from 2 to 5, μ_{DET} shows an

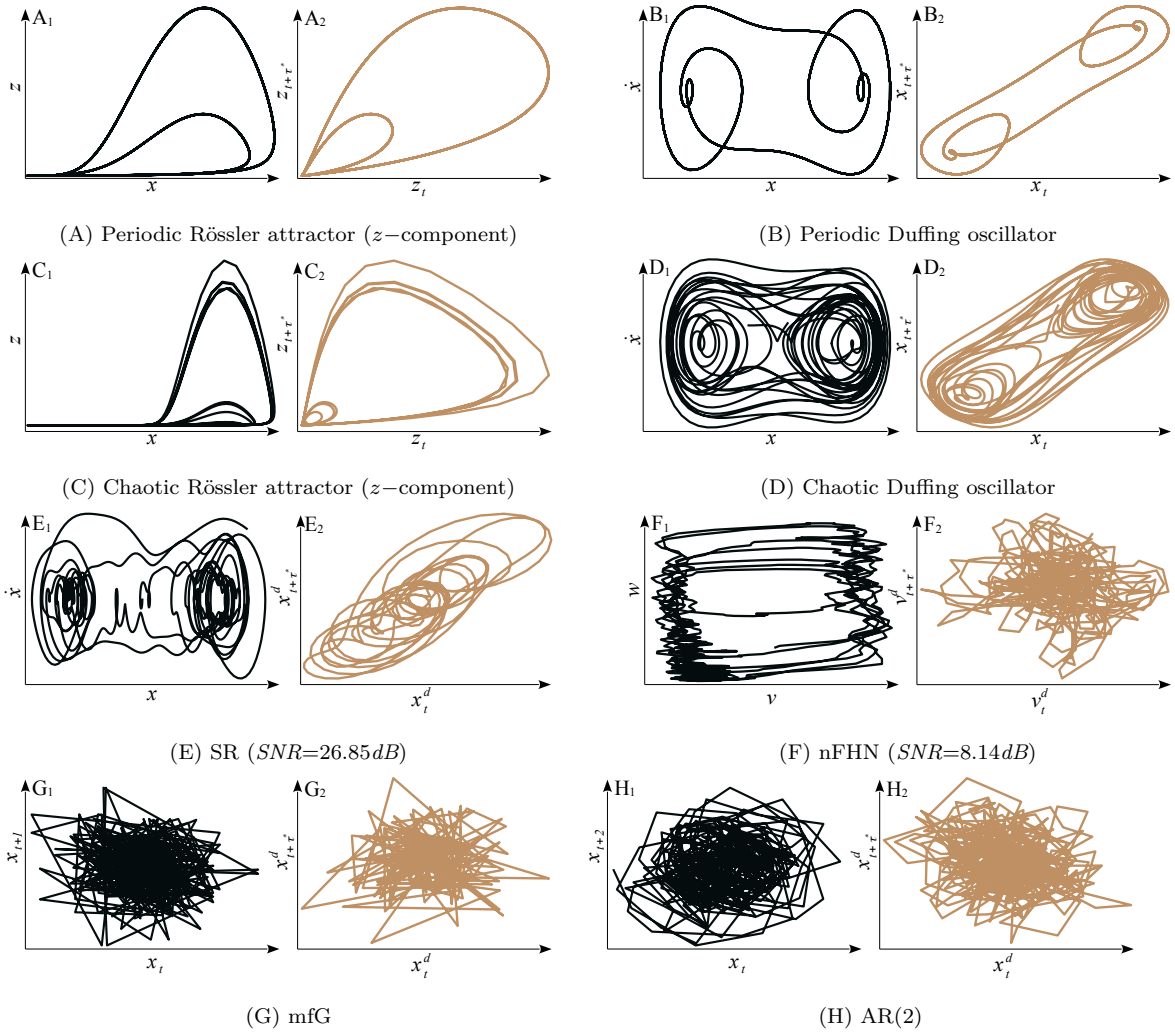

(A) Periodic Rössler attractor ($z-$component)

(B) Periodic Duffing oscillator

(C) Chaotic Rössler attractor ($z-$component)

(D) Chaotic Duffing oscillator

(E) SR (SNR=26.85dB)

(F) nFHN (SNR=8.14dB)

(G) mfG

(H) AR(2)

Figure 4.7 : Original and recurrence-based reconstructed attractors for benchmarking systems. A_1 to H_1: An original attractor is shown in a phase space. A_2 to H_2: Under (m^*, τ^*) reconstructed attractor is shown in a phase space. A_2 to D_2 are reconstructed from the corresponding original time series shown in Figs. 4.5A_1 to 4.5D_1, respectively. E_2 to H_2 are reconstructed from the corresponding detrended time series shown in Figs. 4.5E_2 to 4.5H_2, respectively, thus marking with the superscript ^{d}.

abrupt decrease for nFHN, mfG, and AR(2) (Fig. 4.6A_3 and 4.6A_4).

Fig. 4.6B shows the patterns of μ_{TT}. For periodic dynamics, μ_{TT} has a plateau at the beginning (Fig. 4.6B_1). For chaotic Rössoler attractor and chaotic Duÿng oscillator (Figs. 4.6B_2), μ_{TT} increases firstly and then abruptly decreases as v_{min} increases. The amplitude of the increase is relatively small. For stochastic driven dynamics (SR and

nFHN), a common feature is that a plateau exists in the middle (Fig. 4.6B_3), despite a short length for nFHN. For stochastic dynamics, both mfG and AR(2) present a downward "V".

Reconstructed attractor. Fig. 4.7 shows a phase plot an original attractor and that of the reconstructed attractor under (m^*, τ^*). For deterministic dynamics (Figs. 4.7A to 4.7D), the reconstructed attractors preserve the topological structures of corresponding original attractors. For example, the Duÿng oscillator (Figs. 4.7B_1 and 4.7D_1) exhibits double occurrences of the scroll-and-squeeze phenomenon [143]. The reconstructed attractors (Figs. 4.7B_2 and 4.7D_2) preserver that phenomenon. For stochastic driven dynamics, the SR is with high determinism, the reconstructed attractor shows deterministic structures (Fig. 4.7E_2). However, the double wells of SR are destroyed (Fig. 4.5E). The reconstructed attractor of nFHN is incapable of preserving the structure of the original attractor in phase plot (Fig. 4.5F). This is caused either by detrending the time series or by noise. For stochastic dynamics, the reconstruction does neither preserve nor distort the original phase plot (Figs. 4.5G and 4.5H).

4.3.2 Demand dynamics

The four features related to Pareto and reordered fronts, recurrence plots, recurrence quantification measures, and reconstructed attractors, have shown the ability to differ between deterministic and stochastic dynamics. We therefore benchmark the feature of ride-sharing demand dynamics with the benchmarking dynamics, the Poisson process and the surrogate data to test the corresponding null hypotheses.

Prior to show demand dynamics, we conclude the optimal sampling rate for processing the raw data from RideAustin [310]. Fig. 4.2E shows the four Pareto optimal solutions to Eq. (4.6). The solutions are $p = 80$, 85, 95, and 100. At $p = 100$, the minimum of SD_{DET} is the second smallest, and the minimum of SD_{TT} is the third smallest (Fig. 4.2E). The performances are reasonable for both SD_{DET} and SD_{TT}. We thus aggregate transactions every $p^* = 100$ minutes and then obtain ride-sharing demand from Algorithm 4.1.

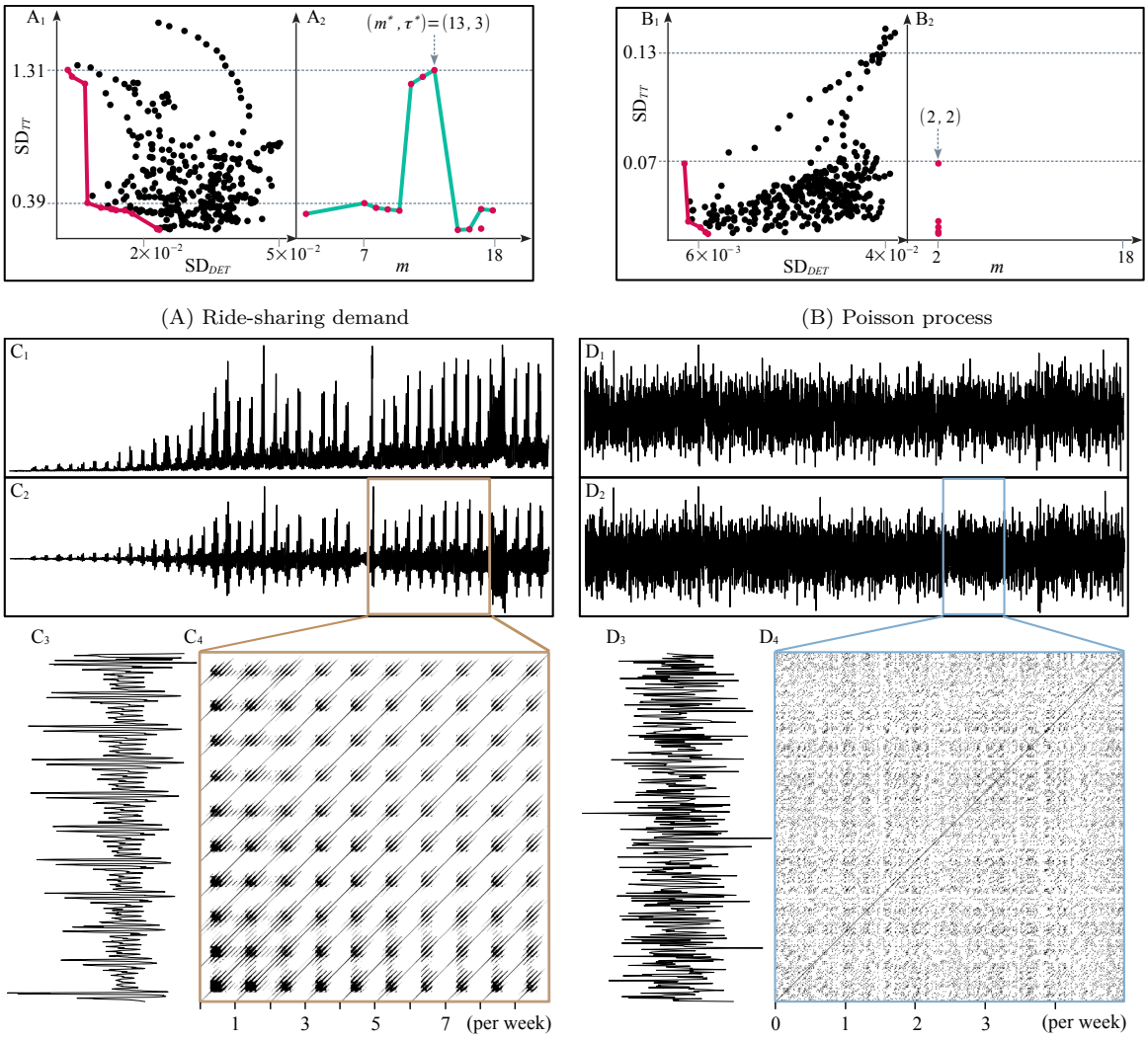

(A) Ride-sharing demand

(B) Poisson process

(C) Time series and recurrence plot (ride-sharing demand)

(D) Time series and recurrence plot (Poisson process)

Figure 4.8 : Dynamics of ride-sharing demand and the Poisson process at $p^* = 100$. A_1 and B_1 show the feature of a Pareto front. A_2 and B_2 show the the feature of a reordered front in the $(m, \mathrm{SD}_{TT})-$plane. C_1 and D_1 are an original time series. C_2 and D_2 are the corresponding detrended time series. C_3 and D_3 are a zoomed plot of the time series where recurrence plots are calculated. C_4 and D_4 are the corresponding recurrence plots.

Recurrence-based attractor reconstruction is conducted at $p^* = 100$, cf. Fig. 4.1. The features of ride-sharing demand is summarized in a decision matrix (Tab. 4.3). A score, ranging from 0 to 1, indicates the confidence in concluding ride-sharing demand dynamics. A score "S" (0) represents that a feature is consistent with that of stochastic

Table 4.3 : Identifications of ride-sharing demand dynamics. A decision matrix is developed for identifying demand dynamics based on four features. They are related to Pareto and reordered fronts (compared Fig. 4.8 with Fig. 4.3), recurrence plots (compared Fig. 4.8 with Figs. 4.5), the patterns as l_{min} and v_{min} increase (compared Fig. 4.10 with Figs. 4.6), and a phase plot of a reconstructed attractor (compared Fig. 4.11 with Fig. 4.7).

Features	Pareto and reordered fronts			Recurrence plots	Patterns[d]		Phase plot	Dynamics
	Number[a]	Plateau[b]	Maxima[c]		l_{min}	v_{min}		
Demand[e]			D	D	D	D	D	D
	S	S						
Poisson								
	S	S	S	S	S	S	S	S

[a] The number of log scales in SD_{DET}. [b] A plateau in Pareto front. [c] Local maxima that a reordered front presents. [d] Patterns in the changing of the minimal diagonal lines and the minimal vertical lines. [e] Ride-sharing demand.

D : The score is 1, showing a high confidence in concluding deterministic dynamics.

S : The score is 0, showing a high confidence in concluding stochastic dynamics.

: The confidence in concluding the corresponding dynamics is infinitesimally small.

dynamics. A score "D" (1) represents that a feature is consistent with deterministic dynamics. For example, when scoring the feature, the number of log scales in SD_{DET} (Tab. 4.3), we compare the patterns between ride-sharing demand and the benchmarking dynamics. The comparison is based on the $x-$axis of Fig. 4.8A_1 and that of Figs. 4.3A_1 to 4.3H_1. The maximum and the minimum of SD_{DET} in ride-sharing demand are 0.051, 0.012 (Fig. 4.8A_1), respectively. Also, the maximum/minimum equals to 4.25 that is less than 10. The feature is consistent with that of stochastic dynamics, as shown in Fig. 4.3E_1, 4.3G_1, 4.3H_1, and Tab. 4.2. Besides, a plateau is not observed in Fig. 4.8A_1. We thus score "S" to the two features, the number of log scales in SD_{DET} and a plateau in Pareto front (Tab. 4.3).

However, the feature related to the local maxima in the (m, SD_{DET})-plane indicates a more likely conclusion of deterministic dynamics (Fig. 4.8A_2). Two observations support the scoring of "D". Three local maxima are observed in Fig. 4.8A_2, and m spans from 2 to 18 (Fig. 4.8A_2). Also, the maximum of local maxima is equal to a global maximum. Those features are consistent with deterministic dynamics (Figs. 4.3A_1 to 4.3D_1).

Fig. 4.8C_4 further indicates a high confidence in concluding deterministic dynamics of ride-sharing demand. "D" is thus given to the feature related to recurrence plots in Tab 4.3. The observations include (1) non-interrupted diagonal lines (Fig. 4.8C_4), similar to the pattern in periodic Rössler attractor (Fig. 4.5A_2) and in periodic Duÿng oscillator (Fig. 4.5B_2); and, (2) recurring long diagonal lines (Fig. 4.8C_4), similar to that in chaotic Duÿng oscillator (Fig. 4.5D_2).

Apart from the benchmarking dynamics, ride-sharing demand is benchmarked against the Poisson process (Figs. 4.8B and 4.8D) and the three types of surrogate data (Fig. 4.9). Differences are observed from the comparisons. In the (m, SD_{DET})-space, all Pareto optimal solutions occur at $m = 2$ for the Poisson process (Fig. 4.8B_2). However, the Pareto optimal solutions occur at m that ranges from 2 to 18 for ride-sharing demand (Fig. 4.8A_2). In a recurrence plot, isolated dots are evident for the Poisson process (Fig. 4.8D_4). However, ride-sharing demand shows non-interrupted diagonal lines (Fig. 4.8C_4). Those observations reject the null hypothesis that ride-sharing demand satisfies a Poisson process [18] of which the arrival rate is five consumers per minute. We then compare ride-sharing demand with its surrogates.

For the shuffle-based surrogate, its feature is consistent with that of a Poisson process, instead of ride-sharing demand (Fig. 4.8A_2 and 4.8C_4). (1) In the (m, SD_{TT})-plane, a local maximum does not exists (Figs. 4.9A_2 and 4.8B_2). (2) Recurrence plot exhibits isolated dots (Figs. 4.9C_5 and 4.8D_4). Those two observations are different from the features that ride-sharing demand exhibits, thus rejecting the null hypothesis that uncorrelated noise is responsible for the ride-sharing demand.

For the Fourier-based surrogate, the features that are based on the Pareto and the re-

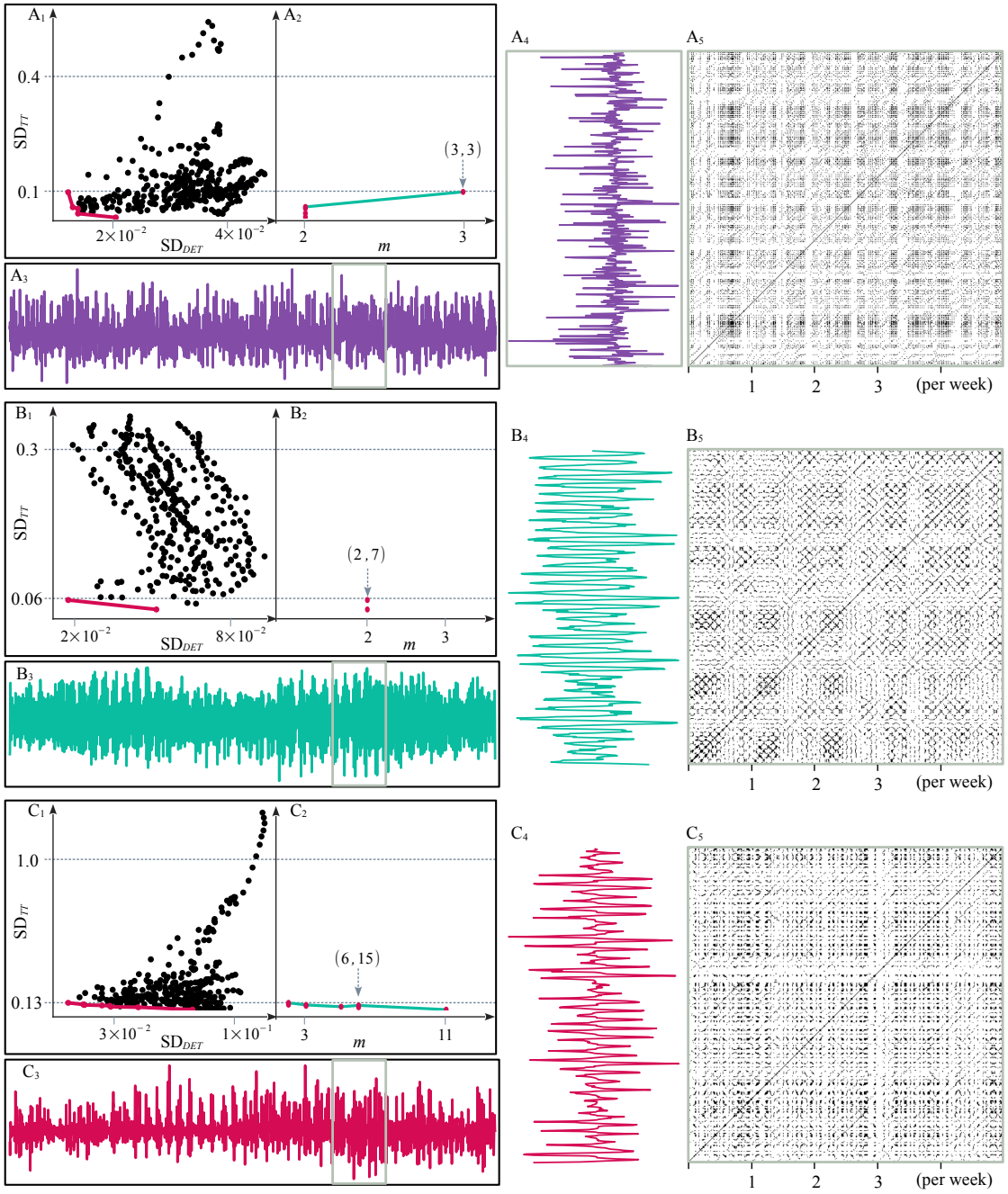

Figure 4.9 : Features in the surrogate data of ride-sharing demand. A. Shuffle-based surrogate shows a feature being consistent with the Poisson process (Fig. 4.8D). B. Fourier-based surrogate has Pareto optimal solution m^* clustering at $m^* = 2$ and presents sword-like patterns in a recurrence plot [189]. C. Truncated AAFT surrogate has a feature being consistent with nFHN ($4.3\mathrm{F}_1$, and $4.3\mathrm{F}_2$) and sword-like patterns in a recurrence plot. A_1 to C_1 are the Pareto front. A_2 to C_2 are the reordered front in the (m, SD_{TT})-plane. A_3 to C_3 are a time series. A_4 to C_4 are a zoomed plot of a segment of A_3 to C_3, respectively. A_5 to C_5 are a recurrence plot of the time series shown in A_4 to C_4, respectively.

ordered fronts are similar to that of a Poisson process (Figs. 4.9B$_1$, 4.9B$_2$, 4.8B$_1$, 4.8B$_2$). For the truncated AAFT, the features that are based on the Pareto and the reordered fronts are similar to that of nFHN (Figs. 4.9C$_1$, 4.9C$_2$, 4.3F$_1$, and 4.3F$_2$). Under Pareto optimal solutions, the change of SD_{TT} is relative small. Although $(m^*, \tau^*) = (6, 15)$ is a local maximum, SD_{TT} has no obvious increase when compared with points in the nearest left and right sides (Fig. 4.9C$_2$). Moreover, the recurrence plots of the Fourier-based and the truncated AAFT surrogates exhibit sword-like patterns along the diagonal line (Figs. 4.9B$_5$ and 4.9C$_5$). The phenomenon is related to the slow and the fast dynamics that a time series underlies [189]. Figs. 4.9B$_3$, 4.9B$_4$, 4.9C$_3$, and 4.9C$_4$ further show a heterogeneity in the corresponding surrogate. However, neither the Fourier-based nor the truncated AAFT shows the recurring long diagonal lines that ride-sharing demand presents (Figs. 4.9B$_5$, 4.9C$_5$, 4.8C$_4$). The different features between ride-sharing demand and the surrogate data (Fourier-based and truncated AADT) reject the corresponding hypothesis. This suggests that nonlinearity is responsible for the dynamics of ride-sharing demand, instead of stochasticity.

As l_{min} and v_{min} increase (Fig. 4.10), the changing patterns of μ_{DET} and μ_{TT} also indicate that ride-sharing demand is consistent with the dynamics of a deterministic system. (1) At $l_{min} = 50$, ride-sharing demand presents a non-zero μ_{DET} (Fig. 4.10A). (2) A linear correlation exists between l_{min} and μ_{DET}, which is consistent with the feature of chaotic Rössler attractor (Fig. 4.6A$_2$) and SR (Fig. 4.6A$_3$). (3) A plateau in μ_{TT} is observed in the middle as v_{min} increases (Fig. 4.10B), which is similar to the feature of SR (Fig. 4.6B$_3$).

The hypotheses to which the surrogate date methods correspond (section 4.2.5) are further rejected by statistical tests of DET (Fig. 4.10A) and TT (Fig. 4.10B). For either the 95% or the 5% percentile of DET, there is no overlapping between ride-sharing demand and the three types of surrogate data (Fig. 4.10A). This indicates a statistically significant difference between ride-sharing demand and its surrogate data. For DET, the 5% percentile of ride-sharing demand goes to zero (Fig. 4.10A). The observation indicates a contamination of noise. For the three types of surrogate data, μ_{TT} goes to

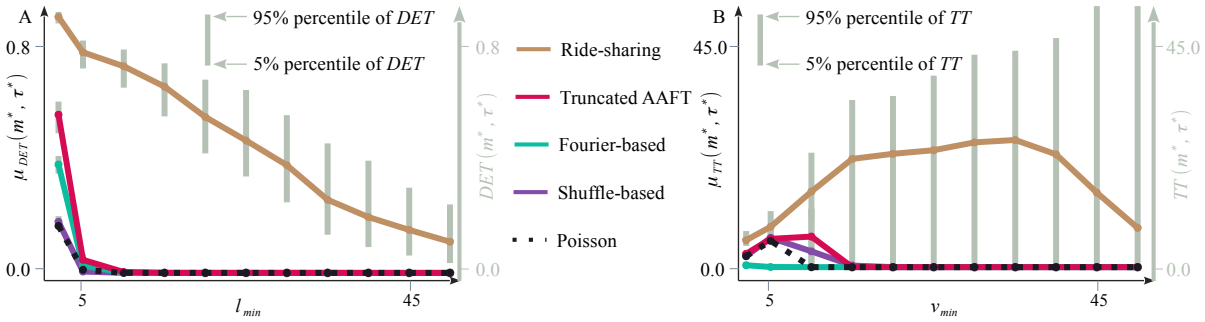

Figure 4.10 : Patterns and statistics of μ_{DET} and μ_{TT} in ride-sharing demand as l_{min} and v_{min} are varied. Ride-sharing demand is benchmarked with the shuffle-based, the Fourier-based and the truncated AAFT surrogates and the Poisson process. A. For ride-sharing demand, μ_{DET} decreases in a similar manner as the chaotic Rössler attractor and the SR (Figs. 4.6A$_2$ and 4.6A$_3$). The 95% and the 5% percentiles of DET have no overlapping with that of the three surrogates. B. For ride-sharing demand, μ_{TT} has a plateau in the middle. The pattern is consistent with that of the SR (Fig. 4.6B$_3$), showing an obvious difference with that of the three surrogates and the Poisson process. The error bars of μ_{DET} and μ_{TT} are too small to be seen. In A and B, the bars correspond to the 95% and the 5% percentiles of the DET and the TT among all sliding windows, respectively.

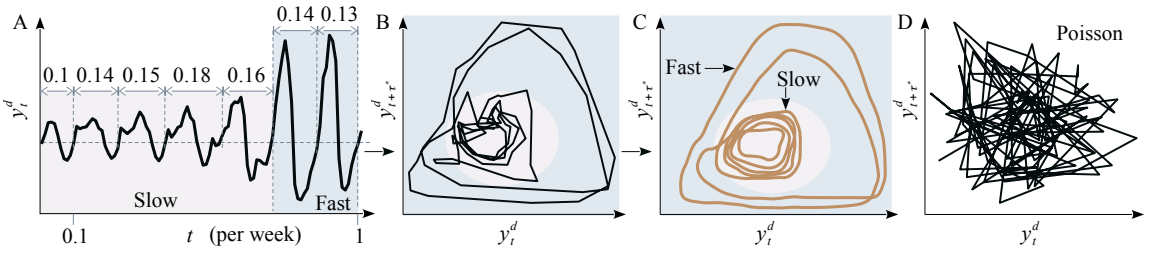

Figure 4.11 : On-demand attractor and a Poisson process. A. A time series covers one week of ride-sharing demand. It exhibits the slow and the fast dynamics. B. On-demand attractor is reconstructed from the time series. C. An outline of the on-demand attractor further indicates the slow and the fast dynamics and the period-7 limit cycle oscillations. D.The Poisson process is reconstructed to show a difference between a practical on-demand attractor and an assumed stochastic demand in describing the empirical data [310].

zero at $v_{min} = 15$ (Fig. 4.10B). For ride-sharing demand, however, μ_{TT} does not goes to zero (Fig. 4.10B). This further rejects the corresponding hypotheses.

Finally, a reconstructed attractor further confirms that ride-sharing demand is consistent with deterministic dynamics (Figs. 4.11B and 4.11C). The attractor is reconstructed under $(m^*, \tau^*) = (13, 3)$, which is calculated by the recurrence-base reconstruction (Fig. 4.1) and Fig. 4.8A_2. Fig. 4.8C_4 further indicates that the periodicity of the attractor is around one week. Fig. 4.11A thus shows a time series that covers one week. Fig. 4.11B shows the attractor that is reconstructed from the exemplified time series (Fig. 4.11A). Fig. 4.11C is an outline of the reconstructed attractor for showing a switch behavior. The following features are evident.

(1) The system switches between the slow and the fast dynamics (Figs. 4.11A to 4.11C).

(2) The slow dynamics takes the five inner circles (Figs. 4.11A to 4.11C), whereas the fast dynamics takes the two outer circles (Figs. 4.11A to 4.11C). The oscillations produce a periodic-7 limit cycle. Here, a circle is not closed, cf. Lu et al. [232].

(3) However, the oscillations take different time to complete an individual circle. For the time series we present, the seven circles take 0.1, 0.14, 0.15, 0.18, 0.16, 0.14, and 0.13 weeks (Fig. 4.11A), respectively.

Nevertheless, the Poisson process fails to preserve either periodic oscillations (Fig. 4.8D_4) or the slow and the fast dynamics (Fig. 4.11D). The comparison further confirms that the Poisson process is incapable of capturing the dynamics of ride-sharing demand.

In summary, Tab. 4.3 shows the scores of ride-sharing demand and that of the Poisson process. The Poisson process are scored with "S" from seven features. We have a high confidence in concluding that the Poisson process underlies stochastic dynamics, indicating the eÿciency of recurrence-based attractor reconstruction. Ride-sharing demand is scored with "S" in two features and "D" in five features. In addition, ride-sharing demand shows statistically significant differences with shuffle-based, Fourier-based, and truncated AAFT surrogate data (Figs. 4.8, 4.9, and 4.6).

4.4 Discussions

Demand information is critical for online and traditional marketplaces to increase revenue by dynamic pricing [69, 70, 232, 330]. Governing equations that describe the interactions between price, demand, and supply are absent. This motivates various models for addressing dynamic pricing problems. A stochastic demand is a widespread assumption in those models [18, 35, 40, 111, 140, 191, 261, 287, 389]. However, the assumption is made without an identification of demand dynamics [232]. A lack of that knowledge makes the assumption open to being challenged.

Nonlinear time series analysis [333] such as recurrence plot [246] provides a tool that studies the dynamics of a system without any prior knowledge of governing equations. The embedding m and the time delay τ dimensions are the critical parameters that affect the eÿciency of nonlinear time series analysis [243, 333]. We propose a recurrence-based method that applies recurrence plots and Pareto optimality to find an optimal embedding m^* and an optimal time delay τ^* dimensions. The idea is to let m and τ travel through feasible choices and then let Pareto optimality find m^* and τ^*. Sliding windowed recurrence plots yield a time series of the determinism DET (Eq. 4.3) and that of the trapping time TT (Eq. 4.4). A statistics of DET and that of TT constitute the two objectives of an optimization (Eq. 4.5).

A recurrence-based reconstruction has four features that disambiguate between deterministic and stochastic dynamics. The features consider Pareto and reordered fronts, recurrence plots under (m^*, τ^*), μ_{DET} and μ_{TT}, and the reconstructed attractor. Among benchmarking systems (Tab. 4.1), those features differ deterministic (Rössler and Duffing), stochastic (mfG and AR(2)), and stochastic driven (SR and nFHN) dynamics. Results show that ride-sharing demand exhibits patterns being consistent with deterministic dynamics. The patterns also have a statistically significant difference with that of the Poisson process and that of the shuffle-based, Fourier-based, and truncated AAFT surrogates. The results indicate the eÿciency of a recurrence-based reconstruction. Those four features show the ability to identify the dynamics of a real-life signal

with noise and non-stationarity. The comparisons with benchmarking systems and surrogate data confirm that ride-sharing demand underlies deterministic dynamics. The assumption of a stochastic demand is thus rejected. The findings emphasize the importance of identifying demand dynamics prior to an assumption of stochasticity [232].

4.4.1 Recurrence-based attractor reconstruction

The diagonal and the vertical lines of recurrence plots lead to many quantification measures [246]. Those measures are closely related to the dynamics of a system, such as the positive Lyapunov [117, 246], transitions [246], and unstable periodic orbits [284]. A traditional thinking is to reconstruct an attractor firstly, and then obtain m and τ for recurrence plots [49, 60, 208, 243, 278, 284, 295]. However, our reverse thinking lets sliding windowed recurrence plots search over a mesh grid that m and τ define. Pareto optimality is then applied to find (m^*,τ^*) under which recurrence plots yield the most robust results. The robustness is quantified by DET and TT (Eq. 4.5), which connects with the diagonal (Eq. 4.3) and the vertical (Eq. 4.4) lines, respectively. Finally, under (m^*,τ^*), an on-demand attractor is reconstructed (Figs. 4.11B and 4.11C).

Observations show that τ^* being found in a deterministic system is relative small (Figs. 4.3A to 4.3D and Fig. 4.8A). This finding is consistent with the observation that the method based on auto-correlation or mutual information causes an overestimation of τ [243]. In a system that exhibits the slow and the fast dynamics, it is diÿcult to locate an appropriate τ for attractor reconstruction (Fig. 4.4) by the traditional method (section 1.4.3) such as averaged mutual information. For example, the problem happens to the $z-$component of the Rössler attractor (Fig. 4.4B) and the Duÿng oscillator (Fig. 4.4D).

Moreover, a recurrence-based reconstruction provides a tool for identifying dynamics that a time series underlies from evidence of multiple sources. Clusters are observed in a recurrence plot of chaotic Rössler attractor ($z-$component) (Fig. 4.5B_2) and that of mfG(Fig. 4.5H_3). However, under corresponding (m^*,τ^*) (Figs. 4.3B and 4.3H), the reconstructed attractor of chaotic Rössler attractor and that of mfG are completely dif-

ferent (Figs. 4.7B_2 and 4.7H_2). The findings confirm a necessity to cross-check recurrence quantification measures for illustrating nonlinear dynamics [171, 243].

Furthermore, a recurrence-based reconstruction utilizes multiple recurrence quantification measures and Pareto optimality together (Eq. 4.5) for (m^*, τ^*). There are several interesting topics that are needed to be further explored. It could be interesting to compare (m^*, τ^*) derived from Eq. (4.5) with that from a traditional method. The systems, which have no obvious heterogeneous dynamics, such as the Lorenz attractor and the $x-$ or $y-$component of Rössler attractor, are of particular interest. Also, It could be interesting to investigate the influence of a change of the objective functions (Eq. 4.5) of Pareto optimality on (m^*, τ^*). For example, Eq. (4.5) could use three or more recurrence quantification measures, or replaces DET and TT with other measures.

4.4.2 Nonlinearity of low-dimensional versus linearity of infinite-dimensional

The null hypothesis that ride-sharing demand is as a result of uncorrelated noise or a linear process is rejected by the shuffle-based, Fourier-based and truncated AAFT surrogate data (Fig. 4.9). Those types of surrogate data reject a stochastic or a linear process from nonlinear time series analysis' perspective [188, 341]. However, an alternative perspective stems from Koopman operator theory for showing the dynamics that a time series underlies. The theory introduces an operator of infinite-dimensional to represent nonlinear systems in a linear way [48, 54, 201, 259, 260]. A chaotic system becomes "an intermittently forced linear system" [54].

Koopman operator is found from a Hankel matrix in a recent study [54]. A Hankel matrix is a matrix whose columns and rows are in the form of a time-delayed coordinate (Eq. 4.2). Linear algebra, such as singular value decomposition, and contemporary regressions are applied on the Hankel matrix [54]. The eigenvalues and eigenvectors are then calculated for an analysis of the Koopman operator [54]. This is called a Hankel alternative view of Koopman (HAVOK) analysis.

Many interesting directions to be investigated have been identified. A new surrogate

data should be proposed to test the null hypothesis that the underlying dynamics is "an intermittently forced linear system" [54] where stochasticity is a forced term. As Mezić [259] argued, a system that satisfies the superposition theorem may represent the nonlinearity of low-dimensional in the sense of preserving the spectrum of the Koopman operator by involving of a stochastic term. The recurrence-based reconstruction can be applied on the nonlinearity of low-dimensional and the linearity of infinite-dimensional for testing the null hypothesis. Moreover, the HAVOK analysis will also improve our understanding of ride-sharing demand. Singular spectrum analysis of the Hankel matrix is related to Fourier analysis of a time series [48]. It would be interesting to look at the dimensionality of ride-sharing demand from HAVOK or Fourier analysis. Finally, the "relationships between the number of delays included in the Hankel matrix and the geometry of the resulting embedded attractor" [54] should be explored in more details by means of recurrence plots and contemporary optimizations.

4.4.3 On-demand attractor

The slow and the fast dynamics explain on-peak and off-peak patterns. The patterns are observed in traÿc dynamics [14, 198, 322] and in on-demand markets [332, 352]. We observe that as the on-demand attractor goes through the slow dynamics (Figs. 4.11B and 4.11C), the time series shows off-peak patterns (Fig. 4.11A). As the attractor goes through the fast dynamics (Figs. 4.11B and 4.11C), the time series shows on-peak patterns (Figs. 4.11A). Figs. 4.8C_4, 4.11A to 4.11C further indicate that ride-sharing demand satisfies period-7 limit cycle oscillations.

Figs. 4.11B and 4.11C exemplify the oscillation of an on-demand attractor. A complete oscillation takes about 7 days (Figs. 4.11B and 4.11C). The result supports the method that studies traÿc dynamics by day of the week [198]. Within one week, demand goes through seven circles. The inner and outer circles exhibit two different types of dynamics. The inner area is with five circles (Figs. 4.11B and 4.11C), whereas the outer area is with two circles (Figs. 4.11B and 4.11C). As the attractor moves along the five inner circles (Figs. 4.11B and 4.11C), the amplitude of demand changes in a small

scale (Fig. 4.11A). A slow dynamics occurs, and the off-peak patterns are observed (Figs. 4.8C_1 to 4.8C_3). However, as the attractor moves along the two outer circles (Figs. 4.11B and 4.11C), the amplitude of demand changes in a large scale (Fig. 4.11A). A fast dynamics occurs, and the on-peak patterns are observed (Figs. 4.8C_1 to 4.8C_3).

The slow and the fast dynamics are further shown in recurrence plots (Fig. 4.8C_4). Along the main diagonal lines, recurrence plot presents a switch between a block of long diagonal lines and a block of blank white areas. The former corresponds to the slow dynamics. The latter corresponds to the fast dynamics. A common understanding of traÿc dynamics is that the on-peak pattern occurs on weekend (Friday to Sunday, three days), and the off-peak pattern occurs on other days (four days) [198]. The ratio we observed between the slow and the fast dynamics is 5:2, rather than 4:3. The difference comes from the fifth circle (ordered from the inner to the outer). The circle represents a transient between the slow and the fast dynamics (Fig. 4.8B). Its amplitude is larger than the inner four circles (Figs. 4.8A and 4.8B), however, smaller than the outer two circles (Figs. 4.8A and 4.8B). In our experiments, the fifth circle sometimes exhibits slow dynamics, but sometimes exhibits fast dynamics. The dynamics depends on individual weeks. We use the time series of Fig. 4.11A to illustrate the transient behavior, and categorize it into the slow dynamics. It is owing to that the exemplified fifth circle is closer to the inner four circles than the outer two circles (Fig. 4.11A).

Our results support that ride-sharing demand underlies deterministic dynamics, explaining the success of the application of nonlinear dynamics in a traÿc system. For example, the susceptible-infected-recovered (SIR) model fits well in Melbourne traÿc systems [322]. A linear decomposition of nonlinear dynamics (Koopman mode decomposition) well reconstructs the dynamics of the US-101 highway [14]. Also, the on-demand attractor complements an existing study [332]. Schröder et al. [332] introduce game theory and propose a theoretical model for identifying the dynamics that a time series of prices underlies in on-demand markets of different countries. We reconstruct the on-demand attractor, further supporting the eÿciency of the method [332] that separates price changes into a slow and a fast time scales for dynamic pricing problems.

Despite an observation of period-7 limit cycle oscillations (Fig. 4.8C_4), Fig. 4.11A indicates that irregularity occurs in the periodicity among individual circles. For the exemplified time series (Fig. 4.11A), one week is separated into 0.1, 0.14, 0.15, 0.18, 0.16, 0.14, and 0.13 weeks by those 7 circles. One day is around 0.14 weeks. Within a limit cycle oscillation (a week), the time that a circle takes is uneven and not necessarily to be one day. The finding indicates irregular demand. In addition, Fig. 4.8C_4 shows that within each week, the location where blocks of long diagonal lines and the length of the long diagonal lines are different. The observation confirms that the irregularities exist in the length of each circle for individual weeks as well. The result is consistent with border collision bifurcations we observe in [232]. It could be due to either a discontinuity in optimizations for dynamic pricing problems [232] or consumers' discontinuous adoption of the ride-sharing services [352].

Finally, our results confirm that a Poisson process fails to reflect the dynamics that a ride-sharing market underlies. In a ride-sharing market consumers' demand is inelastic because of fixed daily routines [332]. The findings demonstrate that a careful identification of demand dynamics becomes necessary for dynamic pricing problems before assuming a stochastic demand. The matrix that summaries the features of a recurrence-based reconstruction could be a promising tool for identifying demand dynamics. As an on-demand attractor has been extracted, a future study that utilizes deterministic chaotic information [53, 293, 359] as opposed to assuming a stochastic demand becomes critical for dynamic pricing problems. Applying the theory that studies a dynamical system to a dynamic pricing problem would be needed for better understanding and predicting the behavior of demand and prices.

Chapter 5

Inherent signatures of machine behaviors to analyze artificial chaos in complex dynamics

Abstract

Machine learning is increasingly used to analyze complex dynamics, which can solve some qualitative and quantitative issues of individual chaotic trajectories well. However, this does not guarantee an equivalence between an original and an artificial systems. To illustrate this, we apply nonlinear time series analysis to examine machine behaviors, the behaviors of an artificial system that mimics a chaotic system as initial conditions are varied. The originally chaotic trajectories are from the coexisting Rössler attractors, the Lorenz attractor with an unbounded basin, and the Hénon map with fractal basins. The reservoir computing paradigm is employed as the artificial system to mimic those trajectories, respectively. Initial conditions of an artificial system are identified. Varying initial conditions allows an artificial system to yield a series of outputs. The sensitive dependence on initial conditions are compared between the original trajectories and the outputs. Our results show that machine behaviors coincide chaotic trajectories, however, may fail to capture the sensitive dependence on initial conditions that an original system possesses. For example, machine learning basins could alter the basins of

the Hénon map, although the artificial system synthesizes a map that coincides the Hénon map. Garbled symbolic dynamics further indicates that a coincidence of a single chaotic trajectory could mislead conclusions. Besides, a common way to deviate from an originally chaotic trajectory is observed under varying initial conditions, which forms the signature of machine behaviors. The findings emphasize the importance of revealing the sensitive dependence on initial conditions to machine learning methods. Machine behaviors being applied with nonlinear time series analysis could provide a potential tool for revealing the sensitivity.

5.1 Introduction

Complex dynamics is ubiquitous in nature and society [246, 387], owing to omnipresent nonlinearity. Its analysis is challenging, especially as an original system runs into deterministic chaotic regimes [333]. Researchers who analyze complex dynamics are facing twofold challenges: (a) for many real-life systems, explicit and mathematical formulations and their solutions remain elusive [53, 351]. The lack of knowledge often prohibits a mode-based analysis of a complex system. (b) For deterministic chaos, the sensitive dependence on initial conditions leads not only to different trajectories [398] but also to multi-stability with scenario-dependent invariant sets (attractors) [232, 258, 299].

Machine learning methods show a potential to realize a model-free analysis of deterministic chaos [293], thanks to abundant time-series data available from measurements [351]. Related to machine learning methods, we have introduced the terms, *artificial systems*, *artificial chaos*, *mimetic trajectory*, and *ML-mimetic attractor* in section 1.4.2 and will give the mathematical definitions in section 5.1.1. An artificial system is an artificial intelligence system that is designed for mimicking deterministic chaos with two special purposes. The first one is for mimicking trajectory-level dynamics of deterministic chaos, such as the correlation dimension [248] and the Lyapunov exponent [292]. The second one is for mimicking system-level dynamics of deterministic chaos. The examples include a prediction of tipping points [200], a reconstruction of attractors [235, 266],

and a detection of unstable periodic orbits as part of an attractor [421]. An especially appealing prospect of artificial chaos is that it has the potential to mimic the long-term evolution of a chaotic system for chaos predictions [64, 179, 293, 383, 423].

Among these applications an artificial system generally works in a sequential manner. The system is fed with chaotic trajectories (input). It then produces an optimal mimetic trajectory (output) for mimicking deterministic chaos that the input possesses. The optimization can be based on the distance of natural or embedded coordinates [383, 423], the duration of trajectories overlap in phase space [200, 293], vector field discrepancies [303, 318], or a combination of the above [237]. An artificial system can behave either like a universal function *generator* [53, 288, 378] or like a universal function *approximator* [95, 155, 194, 387]. The former delivers explicitly mathematical formulations that approximate an original system. The latter allows an artificial system directly resembling an original system.

However, deterministic chaos has a diÿcult y in high-fidelity and reliable predictions [277, 333]. The diÿcult is due to the sensitive dependence on initial conditions [277, 333]. In a chaotic system, an arbitrarily small variation in initial conditions grows exponentially with time [333, 398]. This property causes qualitatively and quantitatively different trajectories or a system with multistability. Nonlinear dynamics under varying initial conditions thus becomes critical for deterministic chaos [232, 333, 398].

Artificial chaos represents the dynamics of an artificial system that mimics the behavior of a chaotic system. For an artificial system, however, its sensitive dependence on initial conditions remains to be elucidated. Under varying initial conditions, the behavior of an artificial system remains unclear. Three questions are thus raised. (Q.A) How does artificial chaos recur as a coincidence is observed between an original and a mimetic trajectories? (Q.B) Does an artificial system produce signatures in mimicking deterministic chaos? (Q.C) What could lead an original system to success in preserving deterministic chaos that an original system possesses?

Machine behaviors study the patterns of an artificial intelligence system under vary-

ing settings [304]. The study is to mitigate unfavorable affects and harvest the benefits of machine learning methods [304]. Our focus is therefore on studing machine behaviors of artificial systems for providing insights into those three questions (Q.A to Q.C). A mathematical definition of machine behaviors will be given in the next section. An artificial system often works as a black box [218]. Analytical formulas that describe the evolution of artificial chaos are thus often absent.

Nonlinear time series analysis is a model-free tool that analyzes nonlinear dynamics without prior knowledge of the governing equations of a system [188]. Trajectory-level and system-level methods exist in quantifying nonlinear dynamics [257]. Trajectory-level methods are based on a unique trajectory. From a time series the correlation dimension, for example, can be estimated over a change of the size of an $\epsilon-$neighborhood [168]. The estimations provide information about the fractal property of an individual trajectory under a perturbation of the size of $\epsilon-$neighborhoods. By contrast, system-level methods are based on a series of trajectories yielded from variations of initial conditions. For example, basins of attraction provide a global view of the behavior of a system with respect to a perturbation of its initial conditions [3, 257, 258]. A basin of attraction is the largest open set of points in phase space [3, 353, 398], and the points taken as initial conditions lead to an identical asymptotic behavior [188].

Basins of attraction often have fractal basin boundaries [3]. A visualization of basins is feasible in a phase space of $n-$dimensional with $n = 1, 2$ [3]. The basins provide information about how a chaotic system recurs under variations in initial conditions. For a flow in phase space with dimension higher than three, it becomes diÿcult to visualize the basins [3]. However, a return map provides information about the recurrent behavior of a chaotic system [188, 333]. Besides, conducting a symbolic analysis provides a tool for identifying an equivalence between two different systems [143]. A symbolic analysis shifts a focus from phase space to a space of symbols [110, 312].

We introduce machine behaviors for identifying a gap between deterministic and artificial chaos. The Rössler system [313, 314], the Lorenz system [230], and the Hénon

map are employed as original systems for benchmarking machine behaviors. In the Rössler system, we calculate the return map of coexisting attractors and that of mimetic trajectories. In the Lorenz system, the return map and unbounded basin are introduced for an analysis. In the Hénon map, basins of an artificial system (machine learning basins) are calculated and benchmarked against original fractal basins. Besides, symbolic dynamics is conducted in the Hénon map. Those three systems are well studied, leading to full knowledge of corresponding behaviors under varying initial conditions. That an original system results in a new trait of machine behaviors is thus excluded.

We aim to identify a gap between deterministic chaos that an original system possesses and artificial chaos that an artificial system represents. Behavioral traits of artificial systems are analyzed by varying initial conditions. The focus is on artificial systems that satisfy the universality to approximate any underlying equations within arbitrarily small errors. Fractal properties of a return map and that of basins of attraction are compared between an original and an artificial systems. We hypothesize that an artificial system establishes a local connection with its input trajectory rather than a global relationship with its original system. We further hypothesize that an artificial system imprints its signature in machine behavior, thus changing the fractal properties of deterministic chaos. To testify the hypothesis, we apply nonlinear time series to study machine behavior. Our results will gain insights into the properties that lead artificial chaos to an equivalence with deterministic chaos.

5.1.1 Mathematical definitions

We consider a dynamical system[159, 333, 346] that is governed by a function $\boldsymbol{f}^{\omega}$ under fixed parameters via

$$\frac{d}{dt}\boldsymbol{\omega}(t) = \boldsymbol{f}^{\omega}(\boldsymbol{\omega}(t)) \tag{5.1}$$

where $\boldsymbol{\omega}(t) \in \mathbb{R}^m$ is a point in phase space and represents a state of the system at time t. Here, m is the dimension of the system, and $\boldsymbol{\omega}_0 = \boldsymbol{\omega}(0)$ is the initial point. Taken $\boldsymbol{\omega}_0$ as initial conditions, an original trajectory $\boldsymbol{\omega}$ is yielded (Fig. 5.1A). Two consequences are possible as $\boldsymbol{\omega}_0$ is varied. (1) Varying $\boldsymbol{\omega}_0$ leads to a new trajectory. (2) Also, a new

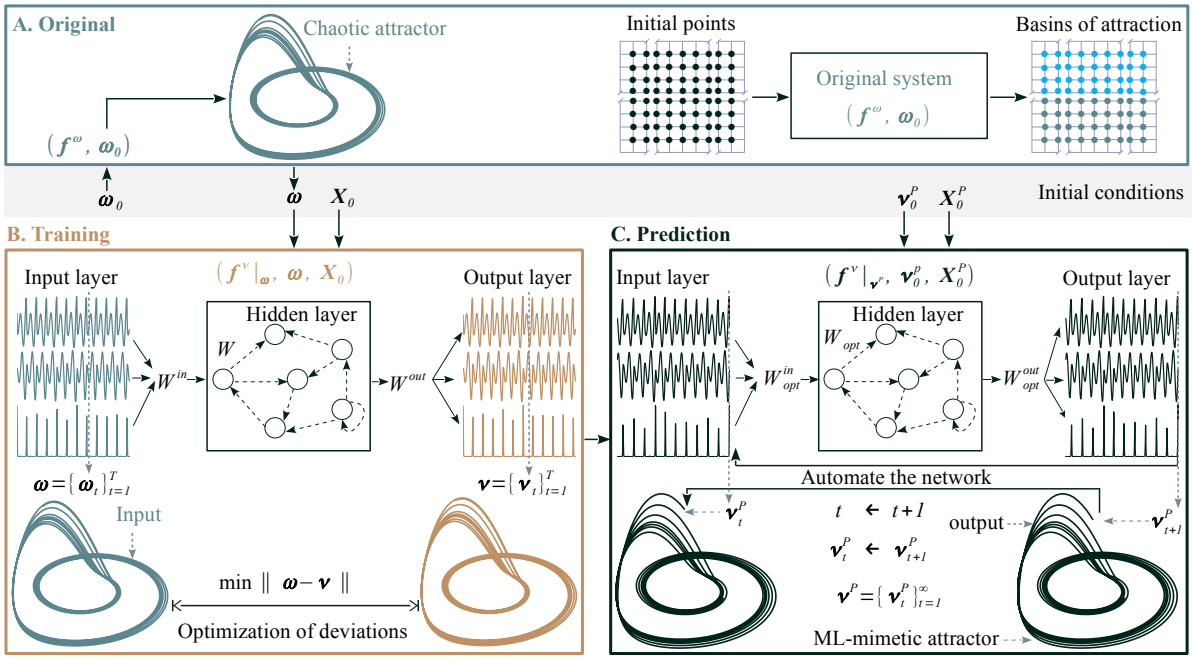

Figure 5.1 : A conceptual diagram of the behavior of an artificial system in mimicking deterministic chaos. Three types of initial conditions affect the system (Section 5.2). A. Type I initial condition is an original trajectory $\boldsymbol{\omega}$. An original system (Eq. 5.1) takes a point ($\boldsymbol{\omega}_0$) that sits in an original phase space as an initial point, thus yielding $\boldsymbol{\omega}$. B. An artificial system is fed with $\boldsymbol{\omega}$ in a training process (Eq. 5.2) that aims to optimize deviations between $\boldsymbol{\omega}$ and $\boldsymbol{\nu}$. Here, $\boldsymbol{\nu}$ is an output with a finite length T for mimicking $\boldsymbol{\omega}$. C. Type II initial condition is an initial point $\boldsymbol{\nu}_0^P$. The point sits in an original phase space and initializes a mimetic trajectory $\boldsymbol{\nu}^P$ in a prediction process (Eq. 5.2). Type III initial condition is initial network states ($\boldsymbol{X}_0$, or $\boldsymbol{X}_0^P$) in a training or a prediction process.

attractor may be produced, depending on where $\boldsymbol{\omega}_0$ sits in phase space. If a variation leads $\boldsymbol{\omega}_0$ crossing different basins, then the new trajectory approaches a new attractor. The system that yields a chaotic trajectory via Eq. (5.1) is called an *original system*.

We then consider a system that takes an input/output framework to mimic deterministic chaos

$$\begin{aligned} \text{Training: } \boldsymbol{\nu}_{t+1} &= \boldsymbol{f}^{\nu}|_{\boldsymbol{\omega}}(\boldsymbol{\omega}_t, \boldsymbol{X}_t, \theta) \\ \text{Prediction: } \boldsymbol{\nu}_{t+1}^P &= \boldsymbol{f}^{\nu}|_{\boldsymbol{\nu}}(\boldsymbol{\nu}_t^P, \boldsymbol{X}_t^P, \theta) \end{aligned} \tag{5.2}$$

where $\boldsymbol{\omega}_t$ is a state of an original system (Eq. 5.1), $\boldsymbol{\nu}_t \in \mathbb{R}^m$ and $\boldsymbol{\nu}_t^P \in \mathbb{R}^m$ are a state of the system in a training (Fig. 5.1B) and a prediction (Fig. 5.1C) processes, respectively.

Also, $\boldsymbol{X}_t \in \mathbb{R}^n$ and $\boldsymbol{X}_t^P \in \mathbb{R}^n$ are network states with n being the size of a network. Here, θ represents the hyperparameter that is fixed for setting up a network and other parameters that is derived from a training process [145, 178]. A chaotic trajectory $\boldsymbol{\omega} = \{\boldsymbol{\omega}_t\}_{t=1}^T$ with finite length T is an input of the system. A *mimetic trajectory* is an output that the system synthesizes in a prediction process, i.e. $\{\boldsymbol{\nu}_t^P\}_{t=0}$. An *ML-mimetic attractor* is the invariant set [398] that $\{\boldsymbol{\nu}_t^P\}_{t=0}$ approaches. Here, $\boldsymbol{f}^\nu|_{\boldsymbol{\omega}}$ maps an original trajectory to an output for mimicking $\boldsymbol{f}^\omega$ (Eq. 5.1) in a training process (Fig. 5.1B). However, $\boldsymbol{f}^\nu|_{\boldsymbol{\nu}}$ synthesizes a mimetic trajectory in a prediction process for mimicking an original trajectory that $\boldsymbol{f}^\omega$ yields from $\boldsymbol{\nu}_0^P$ via Eq. (5.1). The relationship between $\boldsymbol{f}^\nu|_{\boldsymbol{\omega}}$ and $\boldsymbol{f}^\nu|_{\boldsymbol{\nu}}$ will be discussed in section 5.2.4. The system that mimics the original system via Eq. (5.2) is called an *artificial system*.

Three types of initial conditions influence an artificial system (Eq. 5.2) when it synthesizes a mimetic trajectory. They are an original trajectory $\boldsymbol{\omega}$ (Fig. 5.1A), an initial point $\boldsymbol{\nu}_0^P$ (Fig. 5.1C), and initial network states $\boldsymbol{X}_0$ and $\boldsymbol{X}_0^P$ (Figs. 5.1B and 5.1C). We term them as *Type I*, *II*, and *III* initial conditions, respectively. Type I initial condition is the input $\boldsymbol{\omega} = \{\boldsymbol{\omega}_t\}_{t=1}^T$ that an artificial system is fed with in a training process (Eq. 5.2). Type II initial condition is a point $\boldsymbol{\nu}_0^P$ of $m-$dimensional space. The point also initializes a chaotic trajectory (supposed) in an original system via Eq. (5.1). Type III initial condition is an initial state that initializes a network. *Suppose behavior* of an artificial system is the behavior of $\boldsymbol{f}^\omega$ (Eq. 5.1) when it starts from $\boldsymbol{\nu}_0^P$. *Actual behavior* is the behavior of $\boldsymbol{f}^\nu|_{\boldsymbol{\nu}}$ (Eq. 5.2) when an artificial system starts from given initial conditions that is a fixed set of $\boldsymbol{\omega}$, $\boldsymbol{\nu}_0^P$, $\boldsymbol{X}_0$ and $\boldsymbol{X}_0^P$. *Machine behavior* is the behavior of $\boldsymbol{f}^\nu|_{\boldsymbol{\nu}}$ (Eq. 5.2) under varying type I, type II, or type III conditions. We only focus on the dynamics of $\boldsymbol{f}^\nu|_{\boldsymbol{\nu}}$ under varying type I or type II initial conditions.

5.1.2 Differences with existing studies

We apply nonlinear time series analysis for a study of machine behaviors. Our study is different from a statistical analysis of ML-mimetic attractors [80, 383] and a study of a network to possess the ability of arbitrarily small approximation errors [154, 163, 164,

238, 323]. Firstly, we study how an artificial system behaves under varying initial conditions. The statistical analysis of ML-mimetic attractors averages out the outliers that do not follow the distribution of target trajectories. An underlying assumption is that an original system approaches a unique attractor. Otherwise, an occurrence of outliers has two implications. (1) An outlier indicates a divergence from a target trajectory, which implies a bad performance in mimicking the supposed behavior. (2) An outlier indicates a convergence to an original trajectory that is different from the target trajectory. In this setting, $\boldsymbol{f}^{\omega}$ has two coexisting attractors, and $\boldsymbol{f}^{\nu}|_{\boldsymbol{\nu}}$ well mimics one attractor. However, the other attractor is the target one. An outlier thus implies a good performance in mimicking an original system. A statistics of ML-mimetic attractors becomes ambiguous to tell the implication of errors or outliers. For example, the correlation analysis of ML-mimetic attractors [80, 383] gives information about the closeness between an original and an ML-mimetic attractors [383]. However, the closeness is incapable of indicating the dynamics of an artificial system under varying conditions.

Secondly, machine behavior examines the relationship between an original $\boldsymbol{f}^{\omega}$ (Eq. 5.1) and an artificial systems $\boldsymbol{f}^{\nu}|_{\boldsymbol{\nu}}$ (Eq. 5.2). Recently, the attention has been paid on the closeness of trajectories as Type III initial condition changes [154, 163, 164, 323]. The focus is on network architectures [163, 323] or network properties [154, 164] that improve the performance in a coincidence between an original and a mimetic trajectories. Those studies give information about what properties an artificial system should have to achieve the consistency of an ML-mimetic attractor [238]. Most of artificial systems we use satisfy an insensitivity to Type III initial condition. The coincidence can be satisfied in experiments related to the Hénon map and the Lorenz system. Therefore, network architectures and network properties are not the focus of this chapter.

Thirdly, our study of machine behavior does neither intend for "applying complex system techniques to leverage the performance of machine learning techniques with high-eÿciency" [363] nor for reproducing long-term behavior of complex systems by machine learning methods [293, 363]. In particular, the reservoir computing paradigm we employ has attracted a focus issue to facilitate the research field "When machine learning

meets complex systems" [363]. We employ the reservoir computing paradigm only for exemplifying a gap between $\boldsymbol{f}^{\omega}$ (Eq. 5.1) and $\boldsymbol{f}^{\nu}|_{\boldsymbol{\nu}}$ (Eq. 5.2). We will provide an insight into the question "When machine learning induces an arbitrarily small error, what does the error mean?"

Indeed, "even with an infinite amount of data the optimal least squares solution is simply incorrect" [254]. It is thus diÿcult to erase errors between $\boldsymbol{f}^{\omega}$ (Eq. 5.1) and $\boldsymbol{f}^{\nu}|_{\boldsymbol{\nu}}$ (Eq. 5.2). Machine behaviors aim to investigate how the errors evolve under varying initial conditions. We introduce machine behavior to disambiguate between the sensitivity of $\boldsymbol{f}^{\omega}$ to errors of initial conditions and new dynamics developed by the errors that diverge $\boldsymbol{f}^{\nu}|_{\boldsymbol{\nu}}$ from $\boldsymbol{f}^{\omega}$.

In the research field of nonlinear time series analysis, a solution exists in reducing an error that the modeling of a dynamical system induces. Kantz and Jaeger [187] introduce total least squares and more step errors to minimize errors of fittings. McSharry and Smith [254] utilize a maximum likelihood estimation to reduce the error. Kilminster [195] builds behavior criteria to balance between short-term predictions and long-term behavior matches for modeling complex dynamics. Shadowing theorem [47, 152] ensures that the error resulting from measurements such as computers and sensors is bounded. The theorem illustrates "the existence of an uncountable number of true trajectory" [152] that is close to a numerical trajectory with measurement errors. When it comes to "machine learning meets complex systems" [363], the shadowing of a mimetic trajectory by an original trajectory remains unclear as initial conditions are varied. A solution to reduce the error of machine learning methods thus remains understudied.

Fig. 5.2 schematizes our study of machine behaviors. In Section 5.2, the role of initial conditions on an artificial system is discussed (Fig. 5.2A). In Section 5.3, three original systems and seven artificial systems are provided (Fig. 5.2B). Under varying initial conditions (Figs. 5.2A and 5.2B), three experiments are conducted for collecting data that describe machine behavior (Figs. 5.2C and 5.2D). In Section 5.4.1, the trajectory-level machine behavior is collected from mimetic trajectories that mimic the coexisting

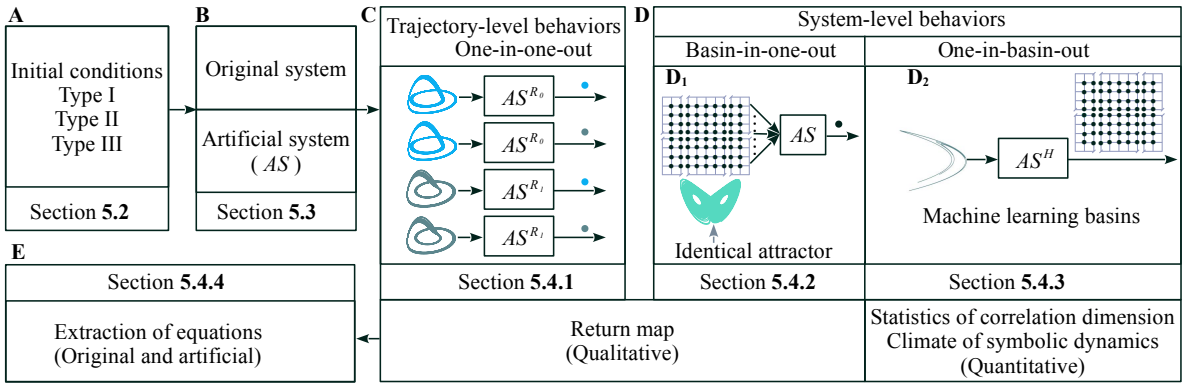

Figure 5.2 : A conceptual diagram of three experiments that collect machine behaviors. A. Section 5.2 describes the role of the three types of initial conditions on an artificial system. B. Section 5.3 describes three original systems and seven artificial systems. Supposed and actual behaviors are collected from the original and the artificial systems, respectively. C. Section 5.4.1 describes the experiment on the Rössler attractors and collects a unique mimetic trajectory from a unique initial condition. The experiment examines the behavior of an artificial system in mimicking two co-existing chaotic attractors. D. Section 5.4.2 describes the experiment on the Lorenz attractor and examines the behavior of an artificial system under varying original trajectories (inputs, Type I). The trajectories are from an identical basin. Section 5.4.3 describes the experiment on the Hénon map and examines the behavior of an artificial system under varying initial points (Type II). The points are from fractal basins. E. Section 5.4.4 describes a method that extracts governing equations from a time series. The extraction compares between supposed and actual behaviors in the sense of preserving mathematical formulas.

Rössler attractors (Fig. 5.2C). The analysis is on comparing the return map of original trajectories and that of mimetic trajectories (Fig. 5.2C). System-level machine behaviors are designed to mimic the Lorenz attractor (Fig. 5.2D$_1$) and the basins of the Hénon map (Fig. 5.2D$_2$), respectively. In Section 5.4.2, the experiment is conducted on the Lorenz attractor as Type I initial conditions are varied. The analysis is on the behavior of an artificial systems as a series of inputs that approach an identical attractor are varied. In Section 5.4.3, the experiments is conducted on the Hénon map as Type II initial conditions are varied. The analysis is on quantitative differences between an original and an artificial systems. Three quantifications are used (Fig. 5.2D$_2$), including (1) a comparison of the basins calculated from an original and an artificial systems, (2)

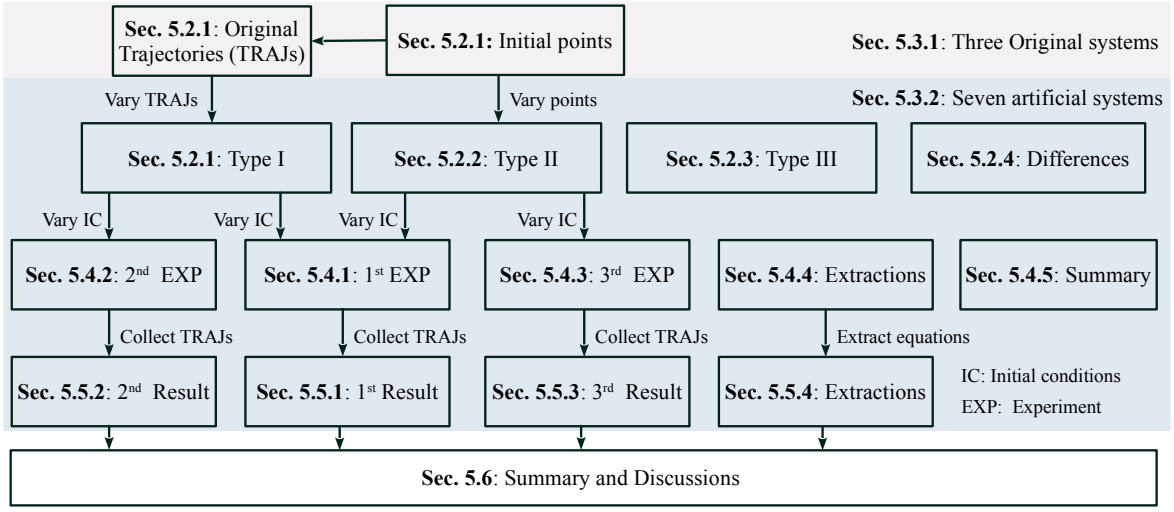

Figure 5.3 : An organization of Chapter 5. Section 5.2 introduces the role of initial condition on artificial systems. Section 5.3 describes the mathematical formulas of the original (Section 5.3.1) and the artificial systems (Section 5.3.2). Section 5.4 describes the three experiments that collect machine behaviors. Section 5.4.1 describes the first experiment on the Rössler system by varying Type I and Type II initial conditions. Section 5.4.2 describes the second experiment on the Lorenz system by varying Type I initial conditions. Section 5.4.3 describes the third experiment on the Hénon map by varying Type II initial conditions. Section 5.4.4 describes an extraction of governing equation from a time series. A summary is made in the final part of Section 5.4. Section 5.5 presents the experimental results. Section 5.6 discusses the three experiments and their corresponding results.

symbolic dynamics, and (3) the statistics of correlation dimension estimations. Finally, the governing equations of the three original systems and that of the seven artificial systems are extracted and compared in Section 5.4.4 (Fig. 5.2E).

Fig. 5.3 further indicates an organization of this chapter. Three experiments are conducted on three different original systems. In Section 5.2, the initial conditions are identified. In Section 5.3, the three original and the seven artificial systems are described. In Section 5.4, three experiments are introduced. In Section 5.5, results are shown. In Section 5.6, results are discussed.

5.2 Initial conditions of artificial chaos

We shall discuss the initial conditions that a mimetic trajectory depends on (Fig. 5.2A). There exist three types of initial conditions. Type I ($\boldsymbol{\omega}$) initial conditions can have an influence on a training process (Eq. 5.2). Type II ($\boldsymbol{\nu}_0^P$) initial conditions can have an influence on a prediction process (Eq. 5.2). Type III ($\boldsymbol{X}_0$ and $\boldsymbol{X}_0^P$) initial conditions can have an influence on both a training and a prediction processes.

5.2.1 Type I initial condition: original trajectory ($\boldsymbol{\omega}$)

Figs. 5.1A and 5.1B and Eq. (5.2) indicate how an artificial system depends on an original trajectory. A training process (Fig. 5.1B) is described by a function $\boldsymbol{f}^{\nu}|_{\boldsymbol{\omega}}$. An input that the system is fed with is an original trajectory of a finite length T (Eq. 5.2). The system synthesizes an output $\boldsymbol{\nu}$ as a network state $\boldsymbol{X}_0$ is initialized. In a training process the deviations between $\boldsymbol{\omega}$ and $\boldsymbol{\nu}$ are optimized for fixing the parameter θ (Eq. 5.2), rather than synthesizing a mimetic trajectory. We then shall discuss the role of an original trajectory on a mimetic trajectory in a prediction process.

5.2.2 Type II initial condition: initial point ($\boldsymbol{\nu}_0^P$)

Fig. 5.1C and Eq. (5.2) indicate how an artificial system depends on an initial point $\boldsymbol{\nu}_0^P$. A prediction process is described by a function $\boldsymbol{f}^{\nu}|_{\boldsymbol{\nu}^P}$. The system starts from $\boldsymbol{\nu}_0^P$ and $\boldsymbol{X}_0^P$ together to synthesize a mimetic trajectory. Type II initial condition $\boldsymbol{\nu}_0^P \in \mathbb{R}^m$ is a point in phase space of an original system (Eq. 5.1). Let assume that an artificial system (Eq. 5.2) is equivalent with its original system (Eq. 5.1). The supposed behavior of a mimetic trajectory then should be consistent with the dynamics of an original trajectory that is initialized from $\boldsymbol{\omega}_0 = \boldsymbol{\nu}_0^P$ via Eq. (5.1). Therefore, the role of $\boldsymbol{\nu}_0^P$ on an artificial system is supposed to be identical to the role of $\boldsymbol{\omega}_0$ on an original system. Varying $\boldsymbol{\nu}_0^P$ should have those two consequences mentioned in Section 5.1.1. For arbitrary two different initial points, the supposed behavior depends on where the points sit in an original system. (1) The two points are from an identical basin of an original system. The mimetic trajectories should approach an identical ML-mimetic attractor. (2) The

two points cross different basins of an original system. The mimetic trajectories should approach different ML-mimetic attractors.

The universality [95, 112, 155, 410] of machine learning methods ensures an existence of an artificial system satisfying that $\boldsymbol{f}^{\nu}|_{\boldsymbol{\nu}^P}$ approximates $\boldsymbol{f}^{\omega}$ within any small errors. This suggests that $\boldsymbol{f}^{\nu}|_{\boldsymbol{\nu}^P}$ should be insensitive to Type I initial conditions ($\boldsymbol{\omega}$), provided that different original trajectories $\boldsymbol{\omega}$ are yielded via identical equations (Eq. 5.1). Let assume that $\boldsymbol{f}^{\nu}|_{\boldsymbol{\nu}^P}$ is equivalent to $\boldsymbol{f}^{\omega}$. A mimetic trajectory that is synthesized via Eq. (5.2) should be consistent with the dynamics of a trajectory that is yielded via Eq. (5.1) at $\boldsymbol{\omega}_0 = \boldsymbol{\nu}_0^P$. The consistence is supposed to be free from the influence of $\boldsymbol{\omega}$.

5.2.3 Type III initial condition: initial network states (X_0, X_0^P)

Figs. 5.1B and 5.1C and Eq. (5.2) indicate how an artificial system depends on initial network states. A training process learns information related to an original system (Eq. 5.2). However, initial network states do not contain any information of an original system. Therefore, a critical property being imposed on an artificial system is that the system does not have sensitive dependence on initial network states. The insensitivity ensures that an artificial system has asymptotic convergence while synthesizing a mimetic trajectory [335, 403].

5.2.4 A training and a prediction processes ($\boldsymbol{f}^{\nu}|_{\boldsymbol{\omega}}$, $\boldsymbol{f}^{\nu}|_{\boldsymbol{\nu}}$)

A difference exists between a training and a prediction processes (Eq. 5.2). The equation $\boldsymbol{f}^{\nu}$ maps an inputted state to an outputted state, which is identical in those two processes. The difference comes from what a network is fed with. In a training process (Fig. 5.1B and Eq. 5.2), $\boldsymbol{f}^{\nu}$ maps an original trajectory to an output. In a prediction process (Fig. 5.1C and Eq. 5.2), $\boldsymbol{f}^{\nu}$ maps $\boldsymbol{\nu}_t^P$ to $\boldsymbol{\nu}_{t+1}^P$. Therefore, $\boldsymbol{f}^{\nu}$ is fed with $\boldsymbol{\omega}$ that exhibits the dynamics of an original attractor in a training process (Fig. 5.1B). However, $\boldsymbol{f}^{\nu}$ defines an automatic system by iterating previous states to current states in a prediction process (Fig. 5.1C), which leads to a time-delay dynamical system. Compared with the training process, the prediction process admits a state that deviates from an original

attractor. Therefore, $\boldsymbol{f}^{\nu}$ is restricted to $\boldsymbol{\omega}$ in a training process, and we mark it as $\boldsymbol{f}^{\nu}|_{\boldsymbol{\omega}}$. However, $\boldsymbol{f}^{\nu}$ is restricted to an ML-mimetic attractor that $\boldsymbol{\nu}^{P}$ approaches in a prediction process, and we mark it as $\boldsymbol{f}^{\nu}|_{\boldsymbol{\nu}^{P}}$.

Since $\boldsymbol{f}^{\nu}|_{\boldsymbol{\nu}^{P}}$ synthesizes an ML-mimetic attractor, our focus is thus on the differences between $\boldsymbol{f}^{\omega}$ and $\boldsymbol{f}^{\nu}|_{\boldsymbol{\nu}^{P}}$. *Machine behavior* is the behavior of $\boldsymbol{f}^{\nu}|_{\boldsymbol{\nu}^{P}}$ in mimicking $\boldsymbol{f}^{\omega}$ under varying $\boldsymbol{\omega}$, $\boldsymbol{\nu}_0^P$, $\boldsymbol{X}_0$, or $\boldsymbol{X}_0^P$ (Eq. 5.2). The supposed behavior of $\boldsymbol{f}^{\nu}|_{\boldsymbol{\nu}^{P}}$ is the behavior of $\boldsymbol{f}^{\omega}$ when $\boldsymbol{f}^{\nu}|_{\boldsymbol{\nu}^{P}}$ and $\boldsymbol{f}^{\omega}$ are applied with an identical initial point $\boldsymbol{\nu}_0^P$. *Deterministic chaos* represents the phenomenon that the trajectories being yielded via Eq (5.1) diverge as $\boldsymbol{\nu}_0^P$ is varied. *Artificial chaos* represents the phenomenon that mimetic trajectories being synthesized via Eq. (5.2) diverge or converge as $\boldsymbol{\omega}$, $\boldsymbol{\nu}_0^P$, $\boldsymbol{X}_0$, or $\boldsymbol{X}_0^P$ is varied.

5.3 Original and artificial systems

To study machine behaviors, we need to describe the original and the artificial systems that are responsible for the behaviors (Fig. 5.2B). Two elements are vital for machine behavior. They are an input yielded from an original system and an output synthesized from an artificial system. Fig. 5.1 schematizes how artificial chaos works in translating an input, a chaotic trajectory, into an output, a mimetic trajectory.

Our experiments are based on three original systems, the Rössler and the Lorenz systems and the Hénon map. To collect the data about machine behaviors, we use seven artificial systems to synthesize artificial chaos. Two artificial systems are used to mimic the coexisting Rössler attractors, respectively. One artificial system is used to mimic the Hénon map. Those three artificial systems follow an identical architecture, however, equip with different parameters. Four different artificial systems are used to mimic the Lorenz attractor.

5.3.1 Original systems

We separate the behaviors of artificial systems from that of original systems. The idea is to choose the original systems that are well studied as inputs, so any new behavioral traits if observed from outputs are caused by the artificial systems. In this way, the new traits

Table 5.1 : Equations and dynamical properties of original systems. Eqs. (F1) and (F2) describe a flow. Eq. (F3) describes a two-dimensional map. The python package, scipy.integrate.ode [302, 390], is applied to obtain a numerical trajectory from Eqs. (F1) and (F2). The integrator is "dopri5", an explicit Runge-Kutta method of orders four and five. The step-size control is set to be 0.02.

System	Equations		Parameters	Dynamical template	Basin boundary
Rössler	$\begin{cases} \dot{x} = -y - z \\ \dot{y} = x + ay \\ \dot{z} = b + z(x - c) \end{cases}$	(F1)	$a = 0.29, b = 0.14,$ and, $c = 4.52$	Stretching and folding [56]	Fractal
Lorenz	$\begin{cases} \dot{x} = \sigma_L(y - x) \\ \dot{y} = x(\rho_L - z) - y \\ \dot{z} = xy - \beta_L z \end{cases}$	(F2)	$\sigma_L = 10, \beta_L = 8/3,$ and, $\rho_L = 28$	Stretching and tearing [56]	Unbounded
Hénon	$\begin{cases} x_{n+1} = a - x_n^2 + by_n \\ \\ y_{n+1} = x_n \end{cases}$	(F3)	$a = 1.4, b = 0.3.$	Stretching and folding [143]	Fractal

reflect the nonlinear dynamics of artificial chaos, instead of that of original deterministic chaos. We therefore choose the Rössler system [314], the Lorenz system [230], and the Hénon map [169] as the original systems. Tab. 5.1 summarizes the equations, the parameters and well-established nonlinear dynamical properties of the three original systems.

Rössler system. Rössler [314] proposed an equation with only one nonlinear term in its $z-$component, cf. Eq. (F1*) in Tab. 5.1, to study deterministic chaos. The Rössler attractor is with a single-scroll mechanism in a three-dimensional phase space [221]. Multistability is a crucial phenomenon for the Rössler attractor. If a nonlinear dynamical system has coexisting attractors under given parameters, [128], then multistability occurs. For a system with multistability, its initial conditions determine final states

*We use "F" to label equations related to original systems or extracted equations.

[221, 299]. Under the parameters we study (Tab. 5.1), the Rössler system approaches two co-existing chaotic attractors [313], marked as R_0 and R_1, respectively. The initial point $\boldsymbol{\omega}_0^{R_0} = (-1.25, -0.72, -0.1)$ approaches R_0, whereas $\boldsymbol{\omega}_0^{R_1} = (0.72, -1.28, 0.21)$ approaches R_1.

Lorenz system. Lorenz [230] proposed an equation, cf. Eq. (F2) in Tab. 5.1, to truncate the Navier-Stokes equation for a study of fluid dynamics. The equation contributes to the first study of deterministic chaos [143]. Lorenz attractor have two fundamental differences with Rössler attractor. Firstly, the dynamical template is different. A template is a branched manifold that describes how unstable periodic orbits topologically organize in a phase space [143]. It also represents the signature of chaotic attractors [143, 376]. The responsible mechanism of Rössler attractor is the stretching and the folding [56, 143], resulting in a single scroll. However, the responsible mechanism of Lorenz attractor under the parameters we study (Tab. 5.1) is the stretching and the tearing [56], evidenced by a discontinuity in return map [56]. The second fundamental difference lies in the fractality of basins of attraction. The Rössler system has co-existing attractors. Fractal basin boundaries separate the basins of the two coexisting attractors [3]. However, the basin of the Lorenz attractor is the whole phase space, $\mathbb{R}^3$, so basin boundary does not exist. A basin of attraction of an attractor includes the domain of the attractor [398], thus being an open set in phase space [3, 353, 398].

It is worth mentioning that the Lorenz system defined by Eq. (F2) (Tab. 5.1) has three fixed point, $(0, 0, 0)$, $F_L = (-\sqrt{72}, -\sqrt{72}, 27)$, and $F_R = (\sqrt{72}, \sqrt{72}, 27)$ [398]. The three fixed points have corresponding manifolds. Along the manifolds the Lorenz system approaches corresponding fixed points. In phase space, however, any deviations from the manifolds cause the Lorenz system approaching the chaotic attractor. This suggests that any point from the manifolds exists and only exists one direction along which its final state is one of the fixed points. A neighborhood of a point is defined over an arbitrary direction [273]. Therefore, for a point that lies in the manifolds, its neighborhood that is capable of reaching its corresponding fixed point does not exist in $\mathbb{R}^3$. A basin of attraction of an attractor is well defined if and only if a neighborhood exists [3, 353, 398].

The definition of a basin of attraction thus excludes the manifolds of those three fixed points. Therefore, the basin of the chaotic Lorenz attractor is unbounded in $\mathbb{R}^3$.

Hénon map. Hénon [169] proposed a simple two-dimensional map, cf. Eq. (F3) in Tab. 5.1, to show deterministic chaos. The Hénon map serves as a testing ground for deterministic chaos in real-life dynamical systems [151, 278, 284]. It has become the most widely studied once-folding map in a two-dimensional phase space [143]. Symbolic dynamics [143, 151] and basins of attraction [344] enable the analysis of the nonlinear dynamics of the Hénon map. Symbolic dynamics is concerned with an invariant set and translates it into an infinite sequence of symbols by a one-to-one shifting map [143, 398]. Under the map, the analysis is shifted from a phase space to a space of symbols.

Grassberger, Kantz, and Moenig [151] develop algorithms to locate critical points of the Hénon map. Critical points are points in phase space and define a shifting map under which symbolic dynamics in a space of symbols is equivalent to the dynamics of an original system in phase space (Eq. 5.1) [143]. Forbidden words emerge from symbolic dynamics. A forbidden word is related to a grammar of deterministic chaos, alike a forbidden grammar of a language [110, 312]. The word is prohibitive due to nonlinear operations of deterministic chaos [143], for example, the once-folding operation in Hénon map [143]. On the other hand, the basins of attraction provide information of future behavior of a dynamical system [3]. For the Hénon map, its basins of attraction present two different types of behaviors. In one area of a two-dimensional phase space, the points attract to infinity [344]. However, in the other area, the points attract to the Hénon map [344]. Fractal basin boundaries separate the two different areas [3]. Moreover, the Hénon map has a similar mechanism as the Rössler attractors [143]. The responsible mechanism for deterministic chaos is the stretching and the folding as well [143].

5.3.2 Artificial systems

We have presented the three original systems that exhibit deterministic chaos. We then need to describe the seven artificial systems that produce artificial chaos for mimicking deterministic chaos. Here, we apply the reservoir computing paradigm [179] to study

machine behaviors. Reservoir computing is a recurrent neural network [179] and takes an input/output framework (Eq. 5.2).

Fig. 5.1 schematizes the input/output framework. The matrix W^{in} maps an input $\boldsymbol{\omega}$ to network states $\boldsymbol{X}_t$ (Figs. 5.1B and 5.1C). The matrix W maps previous network states $\boldsymbol{X}_{t-1}$ to new network states $\boldsymbol{X}_t$ (Figs. 5.1B and 5.1C). The matrix W^{out} maps network states to an output (Figs. 5.1B and 5.1C). While the matrices W^{in} and W are randomly set up, the matrix W^{out} is optimized by minimizing deviations between an input and an output (Fig. 5.1B).

Four reasons exist in using the reservoir computing paradigm. Firstly, echo state property ensures that the output has asymptotically convergent behavior [335, 403]. An echo state property is a condition that is imposed on either W or W^{in} [403]. As echo state property is satisfied, $\boldsymbol{\nu}$ and $\boldsymbol{\nu}^P$ are asymptotically convergent. Here, $\boldsymbol{\nu}$ is an output in a training process (Eq. 5.2), whereas $\boldsymbol{\nu}^P$ is a mimetic trajectory that an artificial system synthesizes in a prediction process (Eq. 5.2). Secondly, a convergence of an output effectively mitigates the gradient problems of machine learning methods [166, 291]. The problems are widely observed in recurrent neural networks and cause an output to diverge or have a diÿcult y in connecting with an input in a training process [291]. However, reservoir computing utilizes random setups for W and W^{in} by imposing echo state property. Thirdly, artificial chaos is widely studied on reservoir computing [80, 266, 293, 393, 423]. Importantly, memristor-based reservoir computing is attracting attention for mimicking deterministic chaos through physical devices [362, 419]. Our study on reservoir computing will provide insights for the memristor-based analysis of deterministic chaos. Lastly, although deep neural networks [237] and long short term memory networks [64, 323] are applied to study deterministic chaos, reservoir computing runs the fastest among its counterparts. Our study of machine behaviors is based on enormous runnings of artificial systems, for example, 4×10^6 runnings to calculate a basin. The use of reservoir computing saves time. Other machine learning frameworks take hours to conduct one running, which makes one experiment diÿcult to finish in one year. However, reservoir computing conducts one experiment less than one week.

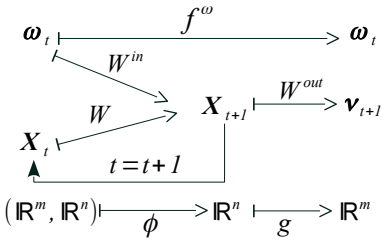

(A) A training process (Fig. 5.1B) where g is without delay items

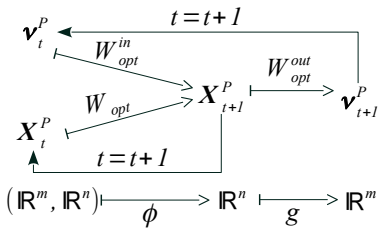

(B) A prediction process (Fig. 5.1C) where g is without delay items

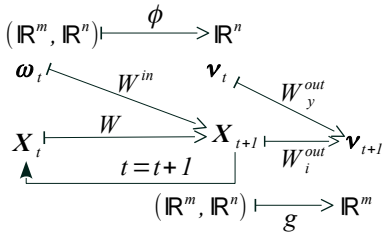

(C) A training process (Fig. 5.1B) where g is with delay items

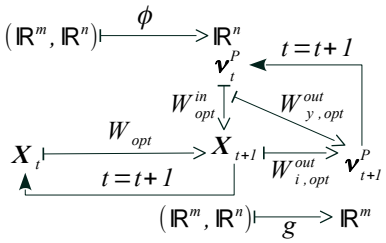

(D) A prediction process (Fig. 5.1C) where g is with delay items

Figure 5.4 : Architectures of artificial systems in a training and a prediction processes (Fig. 5.2B). A and B: The classical reservoir computing paradigm directly synthesizes an output from network states via $\boldsymbol{\nu}_t = g(\boldsymbol{X}_t)$ in a training process (A) and $\boldsymbol{\nu}^P_t = g(\boldsymbol{X}^P_t)$ in a prediction process (B). C and D: A new reservoir computing paradigm synthesizes an output from network states and a previous outputted state via $\boldsymbol{\nu}_t = g(\boldsymbol{X}_t, \boldsymbol{\nu}_{t-1})$ in a training process (C) and $\boldsymbol{\nu}^P_t = g(\boldsymbol{X}^P_t, \boldsymbol{\nu}^P_{t-1})$ in a prediction process (D).

According to the nonlinearity of the output layer (Figs. 5.1B and 5.1C), we use a linear and a nonlinear readouts to synthesize a mimetic trajectory. Fig. 5.4 outlines the architecture of different readouts in a training and a prediction processes. Classical reservoir computing paradigm synthesizes $\boldsymbol{\nu}^P_t$ solely from $\boldsymbol{X}_t$ via $\boldsymbol{\nu}^P_t = g(\boldsymbol{X}_t)$, cf., Fig. 5.4B. Here, $\boldsymbol{\nu}^P_t$ is a state of a mimetic trajectory, and g is a function that reads out network states at time t. We term the classical reservoir computing architecture as a linear readout (Figs. 5.4A and 5.4B). However, we propose a new reservoir computing paradigm, which synthesizes $\boldsymbol{\nu}^P_t$ from $\boldsymbol{X}_t$ and $\boldsymbol{\nu}^P_{t-1}$ together via $\boldsymbol{\nu}^P_t = g(\boldsymbol{X}_t, \boldsymbol{\nu}^P_{t-1})$, cf., Fig. 5.4D. We term the new paradigm as a nonlinear readout (Figs. 5.4C and 5.4D). In a nonlinear readout, the function g acts on network states $\boldsymbol{X}_t$ and the last state $\boldsymbol{\nu}^P_{t-1}$ of a mimetic trajectory.

We propose the nonlinear readout for two reasons. According to Takens' embedding theorem [324, 360], time delays are crucial for an attractor reconstruction. Time delay terms capture information associated with the time derivative of an original system. Besides, the original systems we use have time delay terms. The Hénon map, cf. Eq. (F3), is described by a time delay term. Rössler attractor (Eq. F1) and Lorenz attractor (Eq. F2) can be discretized by incorporating a time delay term. The well-known Runge–Kutta method, for example, utilizes time delay terms to obtain a numerical solution of a flow.

We then need to describe the mathematical formulas that define the architectures. An original system is described by $\boldsymbol{f}^{\omega}$ via Eq. (5.1), cf. Tab. 5.1. A training process (Figs. 5.4A and 5.4C) is described by $\boldsymbol{f}^{\nu}|_{\omega} = g \circ \phi(\boldsymbol{\omega}_t, \boldsymbol{X}_t)$. Here, $\boldsymbol{\omega}_t \in \mathbb{R}^m$ is a state of an original system with m equaling to the dimension of an original system, and ϕ is an activation function. For example, $m = 2$ for the Hénon map. A prediction process (Figs. 5.4B and 5.4D) is described by $\boldsymbol{f}^{\nu}|_{\nu^P} = g \circ \phi(\boldsymbol{\nu}_t^P, \boldsymbol{X}_t^P)$. Here, ϕ acts on a $\mathbb{R}^m \times \mathbb{R}^n$ space where n is the total number of network states and represents the size of a network. A linear and a nonlinear readouts are different due to the definition of g. For a linear readout, g solely acts on $\mathbb{R}^n$ (Figs. 5.4A and 5.4B). However, g acts on a $\mathbb{R}^m \times \mathbb{R}^n$ space for a nonlinear readout.

Before defining the formulas of $\boldsymbol{f}^{\nu}|_{\omega}$ and $\boldsymbol{f}^{\nu}|_{\nu^P}$, we elaborate how to set up the matrices, W and W^{in}. A construction of W is based on an adjacent matrix of a random Erdös-Rényi network. The average degree of the network is d, and the size of the network is n. We then follow Pathak et al. [292] to rescale the adjacent matrix.

(1) An arbitrarily non-zero entry of the adjacent matrix is reset to a random number that is independently and uniformly drawn from the interval $[-a, a]$. In our experiment $a = 1$.
(2) We let the adjacent matrix derived from (1) be a matrix $W^{(1)}$.
(3) Assuming $\rho_0 = ||W^{(1)}||_2$, we apply $W = W^{(1)} * \rho/\rho_0$. Here, $\rho = ||W||_2$ is the Euclidean norm of W, and its value is related to the echo state property.

To construct W^{in}, we randomly set up an $n \times m$ matrix whose non-zero elements are independently and uniformly drawn from the interval $[-\delta, \delta]$, where $\delta > 0$.

The echo state property is satisfied as $\rho < 1$ [166, 403], and $\rho > 1$ often leads to a network dissatisfying the echo state property. The expression $\rho < 1$ can be true or false, depending on the value of ρ. A choice between a linear and a nonlinear readouts and the value of ρ lead to four combinations for setting up an artificial system.

A linear readout and $\rho < 1$ are adopted for artificial systems that mimic the Rössler system and the Hénon map, respectively. A training process (Figs. 5.1B and 5.4A) is described via

$$\boldsymbol{f}^{\nu}|_{\omega} : \boldsymbol{X}_t = \phi(\boldsymbol{\omega}_{t-1}, \boldsymbol{X}_{t-1}) = \tanh(W^{\text{in}}\boldsymbol{\omega}_{t-1} + W\boldsymbol{X}_{t-1}),\ \boldsymbol{\nu}_t = g(\boldsymbol{X}_t) = W^{\text{out}}\boldsymbol{X}_t \quad (5.3)$$

where $\boldsymbol{X}_0 = \boldsymbol{0}$. We then let $W^{\text{in}}_{\text{opt}} = W^{\text{in}}$ and $W_{\text{opt}} = W$, and $W^{\text{out}}_{\text{opt}}$ is the solution to a least square regression problem

$$\min_{W^{\text{out}}} = \sum_{t=1}^{t=T}(||\boldsymbol{\omega}_t - \boldsymbol{\nu}_t||^2 + \beta||I||^2) = \sum_{t=1}^{t=T}(||\boldsymbol{\omega}_t - W^{\text{out}}\boldsymbol{X}_t||^2 + \beta||I||^2) \quad (5.4)$$

where I is an identity matrix, and T is the length of the input, representing the finiteness of a training process. Here, a Tikhonov regulation is to mitigate an overfitting [423], and β is the parameter that controls the regulation. We let $\beta = 0.0001$ in all experiments. A prediction process is then described via

$$\begin{aligned} \boldsymbol{f}^{\nu}|_{\nu^P} : \boldsymbol{X}^P_t &= \phi(\boldsymbol{\nu}^P_{t-1}, \boldsymbol{X}^P_{t-1}) = \tanh(W^{\text{in}}_{\text{opt}}\boldsymbol{\nu}^P_{t-1} + W_{\text{opt}}\boldsymbol{X}^P_{t-1}) \\ \boldsymbol{\nu}^P_t &= g(\boldsymbol{X}^P_t) = W^{\text{out}}_{\text{opt}}\boldsymbol{X}^P_t \end{aligned} \quad (5.5)$$

where $\boldsymbol{X}^P_0 = \boldsymbol{0}$, and $\boldsymbol{\nu}^P_0$ is an initial point that depends on applications. Two artificial systems, AS^{R_0} and AS^{R_1}, are employed for mimicking coexisting Rössler attractors, R_0 and R_1, respectively. One artificial system AS^H is employed for mimicking the Hénon map. Therefore, AS^{R_0}, AS^{R_1}, and AS^H follow Eq. (5.3) in a training process (Figs. 5.1B and 5.4A), and follow Eq. (5.5) in a prediction process (Figs. 5.1C and 5.4B).

For the Lorenz attractor, we allow $\rho < 1$ and $\rho > 1$. Also, both linear and nonlinear readouts are applied. The combinations of the choice of ρ and that of readouts give four different artificial systems, AS^A_L, AS^S_L, AS^A_N , and AS^S_N. They are marked with a superscript ^{A} as $\rho > 1$, a superscript ^{S} as $\rho < 1$, a subscript $_L$ for a linear readout, and

a subscript $_N$ for a nonlinear readout. With a linear readout, the artificial systems, M_L^A and M_L^S, satisfy the following formulas.

$$\begin{aligned} \boldsymbol{f}^{\nu}|_{\omega}: \ \boldsymbol{X}_t &= \phi(\boldsymbol{\omega}_{t-1}, \boldsymbol{X}_{t-1}) = \tanh(W^{\text{in}}\boldsymbol{\omega}_{t-1} + W\boldsymbol{X}_{t-1}) \\ \boldsymbol{\nu}_t &= g(\boldsymbol{X}_t) = [W_1^{\text{out}}\boldsymbol{X}_t, W_2^{\text{out}}\boldsymbol{X}_t, W_3^{\text{out}}\hat{\boldsymbol{X}}_t]^T \end{aligned} \tag{5.6}$$

Eq. (5.6) describes the training process of M_L^A and M_L^S. Here, $\left[\cdot\right]^T$ is a transpose of a matrix. The matrices W_1^{out}, W_2^{out}, and W_3^{out} map the network states to the $x-$, $y-$, and $z-$component of $\boldsymbol{\nu}$, respectively. Also, we let $W_{\text{out}} = \left[W_1^{\text{out}}, W_2^{\text{out}}, W_3^{\text{out}}\right]^T$, where $W_i^{\text{out}} \in R^{1\times n}$ with $i = 1, 2, 3$. In Eq. 5.6,

$$\hat{\boldsymbol{X}}_t = \begin{cases} \boldsymbol{X}_{i,t}, & \text{for } 0 \le i \le \lfloor n/2 \rfloor \\ \boldsymbol{X}_{i,t}^2, & \text{for } \lfloor n/2 \rfloor + 1 \le i < n \end{cases} \tag{5.7}$$

Eq. (5.7) is consistent with existing studies [292, 293]. Using square terms in network states is to improve artificial chaos when the original attractors are with symmetry. The Lorenz attractor is symmetric since Eq. (F2) is invariant under a transformation of $x \mapsto -x$ and $y \mapsto -y$. Optimal matrices, $W_{1,opt}^{\text{out}}$, $W_{2,opt}^{\text{out}}$ and $W_{3,opt}^{\text{out}}$, are derived from Eq. (5.4). A prediction process then satisfies

$$\begin{aligned} \boldsymbol{f}^{\nu}|_{\nu^P}: \boldsymbol{X}_t^P &= \phi(\boldsymbol{\nu}_{t-1}^P, \boldsymbol{X}_{t-1}^P) = \tanh(W_{\text{opt}}^{\text{in}}\boldsymbol{\nu}_{t-1}^P + W_{\text{opt}}\boldsymbol{X}_{t-1}^P) \\ \boldsymbol{\nu}_t^P &= g(\boldsymbol{X}_t^P) = \left[W_{1,\text{opt}}^{\text{out}}\boldsymbol{X}_t^P, W_{2,\text{opt}}^{\text{out}}\boldsymbol{X}_t^P, W_{3,\text{opt}}^{\text{out}}\hat{\boldsymbol{X}}_t^P\right]^T \end{aligned} \tag{5.8}$$

where $\boldsymbol{X}_0^P = \boldsymbol{0}$, and $\boldsymbol{\nu}_0^P$ depends on individual cases as well.

With a nonlinear readout, the artificial systems, M_N^A and N_S^S, satisfy the following formulas.

$$\begin{aligned} \boldsymbol{f}^{\nu}|_{\omega}: \boldsymbol{X}_t &= \phi(\boldsymbol{\omega}_{t-1}, \boldsymbol{X}_{t-1}) = \tanh(W^{\text{in}}\boldsymbol{\omega}_{t-1} + W\boldsymbol{X}_{t-1}) \\ \boldsymbol{\nu}_t &= g(\boldsymbol{X}_t, \boldsymbol{\nu}_{t-1}) = W_{\nu}^{\text{out}}\boldsymbol{\nu}_{t-1} + \left[W_1^{\text{out}}\boldsymbol{X}_t, W_2^{\text{out}}\boldsymbol{X}_t, W_3^{\text{out}}\hat{\boldsymbol{X}}_t\right]^T \end{aligned} \tag{5.9}$$

Eq. (5.9) describes the training process of M_N^A and M_N^S. Here, W_{ν}^{out} is a vector that defines the coeÿcien ts of the $x-$, $y-$, and $z-$component of $\boldsymbol{\nu}_{t-1}$, respectively. Those coeÿcien ts represent the parameters of the delay terms in a nonlinear readout (Figs. 5.4C

Table 5.2 : Parameters and equations of artificial systems (Fig. 5.2B). The artificial systems, AS^{R_0} and AS^{R_1}, use Eqs. 5.3 and 5.5 to mimic the coexisting Rössler attractors (Figs 5.4a and 5.4b), R_0 and R_1, respectively. The artificial systems, AS_L^S and AS_L^A, use Eqs. 5.6 and 5.8 to mimic the Lorenz attractor (Figs 5.4a and 5.4b). However, AS_N^S and AS_N^A, use Eqs. 5.9 and 5.10 to mimic the Lorenz attractor (Figs 5.4c and 5.4d). Also, AS^H uses Eqs. 5.3 and 5.5 to mimic the Hénon map (Figs 5.4a and 5.4b).

Original	Artificial	m	n	T	ρ	d	δ	Equations
Rössler	AS^{R_0}	3	300	2,000,000	0.91	8	0.09	Eqs. 5.3, 5.5
	AS^{R_1}	3	300	2,000,000	0.91	8	0.07	
Lorenz	AS_L^A	3	300	5,000	>1	6	-	Eqs. 5.6, 5.8
	AS_L^S	3	300	5,000	<1	6	-	
	AS_N^A	3	300	5,000	>1	6	-	Eqs. 5.9, 5.10
	AS_N^S	3	300	5,000	<1	6	-	
Hénon	AS^H	2	300	180,000	0.78	6	0.07	Eqs. 5.3, 5.5

and 5.4D). We let $W_{\text{out}} = \left[W_\nu^{\text{out}}, W_1^{\text{out}}, W_2^{\text{out}}, W_3^{\text{out}}\right]^T$. According to Eq. (5.4), a prediction process of M_N^S and N_L^A then follows

$$\begin{aligned} \boldsymbol{f}^\nu|_{\boldsymbol{\nu}^P} : \boldsymbol{X}_t^P &= \phi(\boldsymbol{\nu}_{t-1}^P, \boldsymbol{X}_{t-1}^P) = \tanh(W_{\text{opt}}^{\text{in}} \boldsymbol{\nu}_{t-1}^P + W_{\text{opt}} \boldsymbol{X}_{t-1}^P) \\ \boldsymbol{\nu}_t^P &= \boldsymbol{g}(\boldsymbol{X}_t^P) = W_{\nu,\text{opt}}^{\text{out}} \boldsymbol{\nu}_{t-1}^P + \left[W_{1,\text{opt}}^{\text{out}} \boldsymbol{X}_t^P, W_{2,\text{opt}}^{\text{out}} \boldsymbol{X}_t^P, W_{3,\text{opt}}^{\text{out}} \hat{\boldsymbol{X}}_t^P\right]^T \end{aligned} \tag{5.10}$$

where $W_{\nu,\text{opt}}^{\text{out}}$ and $W_{i,\text{opt}}^{\text{out}}$ with $i = 1, 2, 3$ are optimal solutions derived from Eq. (5.4). Tab. 5.2 summarizes the artificial systems in our experiments and their parameters.

5.4 Experiments

We have identified the different roles of initial conditions (Fig. 5.2A) and presented the three original and the seven artificial systems (Fig. 5.2B). Prior to study machine behaviors, we need to describe how experiments are conducted under varying initial conditions (Figs. 5.2C and 5.2D). We need to describe the methods for an analysis of the behaviors as well.

Machine behaviors are categorized into *trajectory-level* and *system-level* behaviors. Trajectory-level behaviors are concerned with the behavior of a unique mimetic trajectory that mimics an original chaotic trajectory. In this setting, an artificial system (Eq. 5.1) is fed with one input, and synthesizes one output (Fig. 5.2C). We term it as one-in-one-out mode. The experiment on the Rössler system follows a *one-in-one-out* mode (Fig. 5.2C). An individual artificial system is fed with only one original trajectory and initialized from two initial points for mimicking the coexisting attractors, R_0 and R_1, respectively. This allows one artificial system yielding two mimetic trajectories in case of two coexisting attractors.

System-level behaviors are concerned with the behaviors of an artificial system as either initial points $\boldsymbol{\nu}_0^P$ or original trajectories $\boldsymbol{\omega}$ are varied (Fig. 5.1 and Eq. 5.2). This corresponds to two modes. (1) Original trajectories $\boldsymbol{\omega}$ are varied (Eq. 5.2), however, the initial point $\boldsymbol{\nu}_0^P$ is fixed (Eq. 5.2). A series of mimetic trajectories are thus synthesized. In this setting, an artificial system is fed with enormous original trajectories, and synthesizes a series of mimetic trajectories (Fig. 5.2D_1). The number of mimetic trajectories is equal to the number of original trajectories, which are from an identical basin. We term the setting as *basin-in-one-out* mode. The experiments on the Lorenz attractor follows a basin-in-one-out mode (Fig. 5.2D_1). (2) Initial points $\boldsymbol{\nu}_0^P$ are varied (Eq. 5.2), however, the original trajectory $\boldsymbol{\omega}$ is fixed (Eq. 5.2). A series of mimetic trajectories are synthesized as well. In this setting, an artificial system is fed with a unique original trajectory, however, synthesizes enormous mimetic trajectories for mimicking the basin of an original attractor (Fig. 5.2D_1). The number of mimetic trajectories are equal to the number of initial points that is applied on an artificial system. We term is as *one-in-basin-out* mode. The experiments on the Hénon map follow a one-in-basin-out mode (Fig. 5.2D_2).

An intuitive difference between trajectory-level and system-level behaviors is what machine behaviors are benchmarked against with. Trajectory-level behaviors require a unique original and a unique mimetic trajectory. However, system-level behaviors require either a series of original trajectories or a series of initial points to synthesize

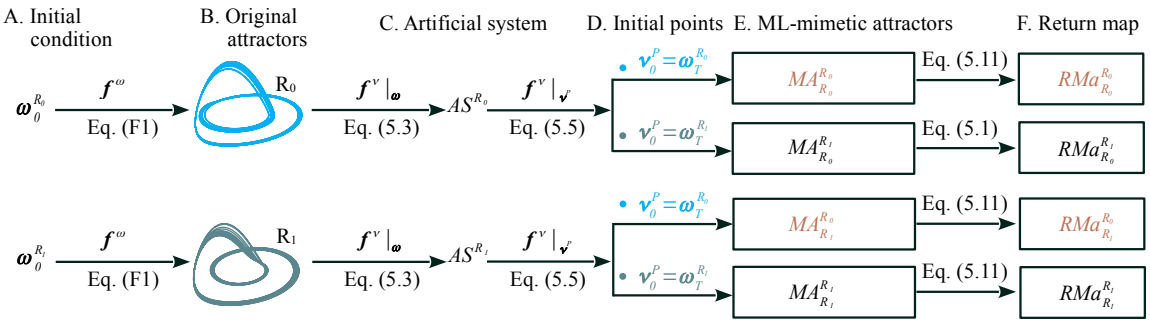

Figure 5.5 : One-in-one-out experiment that collects trajectory-level behaviors by fixing Type I and II initial conditions (Fig. 5.2C). A and B: The Rössler system yields two coexisting attractors, R_0 and R_1, under two different initial points. C. While AS^{R_0} is fed with R_0, AS^{R_1} is fed with R_1. D. Type II initial conditions, $\boldsymbol{\omega}_T^{R_0}$ and $\boldsymbol{\omega}_T^{R_1}$, are the $T-$th point of R_0 and R_1, respectively. E. Initialized from the two points, AS^{R_0} synthesizes two ML-mimetic attractors, $MA_{R_0}^{R_0}$ and $MA_{R_0}^{R_1}$, respectively. Similarly, AS^{R_1} synthesizes, $MA_{R_1}^{R_0}$ and $MA_{R_1}^{R_1}$. Supposed behavior of $MA_{R_0}^{R_0}$ and $MA_{R_1}^{R_0}$ should satisfy the dynamics of R_0. Supposed behavior of $MA_{R_0}^{R_1}$ and $MA_{R_1}^{R_1}$ should satisfy the dynamics of R_1. F. The qualitative analysis is based on return maps that Eq. (5.11) defines.

enormous mimetic trajectories. Therefore, trajectory-level experiments benchmark a mimetic trajectory with a unique trajectory of an original system. Nevertheless, system-level experiments benchmark an ML-mimetic attractor with an original attractor.

5.4.1 Trajectory-level behaviors: Return maps

The fist experiment compares trajectory-level behaviors between an original and an artificial systems (Fig. 5.2C). Mean square error is a well-know and a widely used measure to compare trajectory-level behaviors [50, 293]. However, a return map of a flow provides invariant topologies of deterministic chaos [219] and its signatures [56, 373]. A return map as an invariant set defines the recurrence of a chaotic system in a Poincaré section. We, therefore, benchmark the return map of mimetic trajectories against that of original trajectories for experiments related to the Rösser and the Lorenz systems.

Rössler attractors. The experiment on the Rössler system (Eq. F1) collects trajectory-level behaviors and follows a one-in-one-out mode. It is designed to find how an artificial system responds to varying original trajectories. Those trajectories are

governed by an identical equation, however, approach different chaotic attractors.

Fig. 5.5 outlines the procedures of conducting a one-in-one-out experiment. Two artificial systems AS^{R_0} and AS^{R_1} are introduced for examining the sensitive dependence on Type I initial condition (Fig. 5.1A). Here, AS^{R_0} is fed with R_0 (Fig. 5.5B), whereas AS^{R_1} is fed with R_1 (Fig. 5.5B). We then apply two different types of initial points to examine the sensitive dependence on Type II initial condition (Fig. 5.1C). Under two different original trajectories and two different initial points, four ML-mimetic attractors are synthesized (Fig. 5.5E). They are marked as $MA^{R_0}_{R_0}$, $MA^{R_1}_{R_0}$, $MA^{R_0}_{R_1}$, and $MA^{R_0}_{R_1}$. The subscript $_{R_0}$ represents that the ML-mimetic attractor is synthesized by AS^{R_0}, whereas the subscript $_{R_1}$ represents that the ML-mimetic attractor is synthesized by AS^{R_1}. The superscript ^{R_0} represents that the ML-mimetic attractor is designed to approach R_0; and, the superscript ^{R_1} represents that the ML-mimetic attractor is designed to approach R_1. Finally, we stay consistent with Rosalie [313] and apply the following Poincaré section $\mathcal{P}$ to calculate the return map of the two coexisting Rössler and the four ML-mimetic attractors

$$\begin{aligned} \mathcal{P}: \ & \Big\{(y_n, -z_n) \in \mathbb{R}^2 | -x_n = -x_-, -\dot{x} < 0, y < -7\Big\} \\ & \text{and } \Big\{M_n : M_n = \frac{\max - y_n}{\max - \min}, (y_n, -z_n) \in \mathcal{P}\Big\} \end{aligned} \tag{5.11}$$

where $x_- = 0.009$ being equal to the $x-$component of one of the fixed points of the Rössler system [313]. Here, x_n, y_n, and z_n are the $x-$, $y-$, and $z-$component of a point, respectively. The point represents the state as the attractor crosses the Poincaré section. Also, M_n is a normalization of y_n. Here, "max" and "min" represent the maximum and the minimum of a time series $\{y_n\}$, respectively.

The reason to normalize y_n is that trajectory-level behaviors are compared among the two Rössler attractors and the four ML-mimetic attractors, and their return maps. Eq. (5.11) gives a linear transformation. The normalization thus keeps the topological structures of a return map, and allows comparable results among different return maps. For example, Rosalie [313] uses an identical normalization to compare different return maps of the Rössler attractors as different parameters are applied on Eq. (F1).

5.4.2 System-level behaviors: Basin-in-one-out mode

We have described our first experiment that collects trajectory-level behaviors (Figs. 5.2C and 5.5). We then need to describe our second experiment related to system-level behaviors. A basin of attraction is an invariant measure to differ the behavior of a dynamical system under varying initial conditions [3, 353, 398]. A basin-in-one-out experiment lets an artificial system be fed with enormous original trajectories that are initialized from an identical basin (Fig. 5.2D$_1$).

Lorenz attractor. The experiment on the Lorenz system, cf. Eq. (F2), collects system-level behaviors and follows a basin-in-one-out mode. It is designed to find how an artificial system responds to individual chaotic trajectories. Those trajectories are described by identical equations and approach an identical attractor. We apply the following two return maps to both original and mimetic trajectories

$$\Big\{z_n : z_n \text{ is the local minimum of z-component}\Big\} \tag{5.12}$$

$$\Big\{Y_n : Y_n = y_n - \sqrt{72} \text{ if } x > 0 \text{ and } \dot{x} < 0;\ Y_n = y_n + \sqrt{72} \text{ if } x < 0 \text{ and } \dot{x} < 0\Big\} \tag{5.13}$$

Eq. (5.12) derives a return map from the minima of the $z-$component of the attractor. Eq. (5.13) derives a return map from disconnected segments of a Poincaré section where $\mathcal{P}_R = \Big\{(x, y, z) : x = \sqrt{72}, \dot{x} < 0\Big\}$ and $\mathcal{P}_L = \Big\{(x, y, z) : x = -\sqrt{72}, \dot{x} < 0\Big\}$. Here, Y_n is an oriented distance, which measures the distance between an interior point and the point that crosses the Poincaré section in the $(x, y)-$plane. If $x < 0$, the interior point is $(-\sqrt{72}, -\sqrt{72})$; otherwise, the interior point is $(\sqrt{72}, \sqrt{72})$. The selection of two disconnected segments is because of the Lorenz attractor, which is bounded by a genus-g (g=3) torus [56, 219, 373]. A Poincaré section with $g-1$ (two) disconnected segments well presents the topology of an attractor with a genus-g (g=3) torus [56, 219].

Fig. 5.6 outlines the procedures of conducting a basin-in-one-out experiment. We use four artificial systems $\mathcal{S} \in \Big\{AS_L^A, AS_L^S, AS_N^A, AS_N^S\Big\}$ to examine the sensitive dependence on Type I initial conditions (Fig. 5.1A). Here, $\mathcal{S}$ represents an individual artificial system. The experiment takes the following steps.

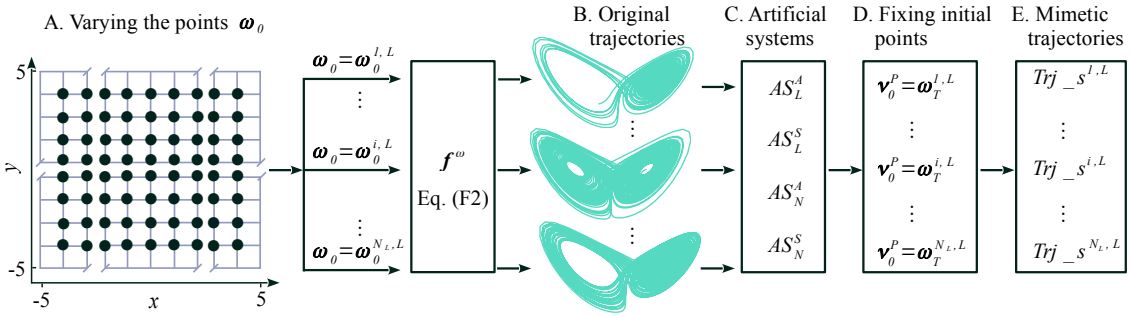

Figure 5.6 : Basin-in-one-out experiment that collects system-level behaviors under varying Type I initial conditions. A. The initial conditions of an original system (Fig. 5.1A) travel through a grid $\mathcal{B}_L$ that represents the basin of the Lorenz attractor. B. Original trajectories have an identical equation (Eq. F2) and approach an identical attractor. C. For an individual artificial system $\mathcal{S} \in \{AS_L^A, AS_L^S, AS_N^A, AS_N^S\}$, it is fed with those original trajectories. D and E: Initialized from a fixed point $\boldsymbol{\nu}_0^P = \boldsymbol{\omega}_T^{i,L}$, $\mathcal{S}$ synthesizes N_L mimetic trajectories, $Trj\_s^{i,L}$. Here, i is the index of trajectories, and N_L is the cardinality of $\mathcal{B}_L$. Supposed behavior of mimetic trajectories should satisfy the dynamics of the Lorenz attractor.

(1) We vary the points $\boldsymbol{\omega}_0$ and let it travel through a grid $\mathcal{B}_L$ (Fig. 5.6A). The definition satisfies $\boldsymbol{\omega}_0 \in \mathcal{B}_L = \left\{(x,y,z) : x = -5+10i_x/1000, y = -5+10i_y/1000, z = 27\right\}$ with $i_x = 0,\cdots,999$ and $i_y = 0,\cdots,999$. The cardinality of $\mathcal{B}_L$ is 10^6, and $\mathcal{B}_L$ represents a plane ($z = 27$) in a three-dimensional space.

(2) We obtain 10^6 original trajectories from the Lorenz system (Fig. 5.6B).

(3) For a given artificial system $\mathcal{S}$ (Tab. 5.2), we feed $\mathcal{S}$ with individual original trajectories (Figs. 5.6B and 5.6C).

(4) We fix the initial point $\boldsymbol{\nu}_0^P = \boldsymbol{\omega}_T^{i,L}$ (Fig. 5.6D). Here, $\boldsymbol{\omega}_T^{i,L}$ is the $T-$th point of the $i-$th original trajectory that $\mathcal{S}$ is fed with, and, $i = 1,\cdots,10^6$.

(5) The given $\mathcal{S}$ then synthesizes 10^6 mimetic trajectories (Fig. 5.6E).

(6) We calculate the return map of the mimetic trajectories according to Eq. (5.12).

(7) We choose a new $\mathcal{S} \in \left\{AS_L^A, AS_L^S, AS_N^A, AS_N^S\right\}$ and return to Procedure (3).

(8) In total, we obtain 4×10^6 mimetic trajectories and 4×10^6 return maps.

Enormous return maps are calculated from the experiment (Fig. 5.6), which are diÿcult to be visualized. We focus on seven cases to exemplify those results. Fig. 5.7

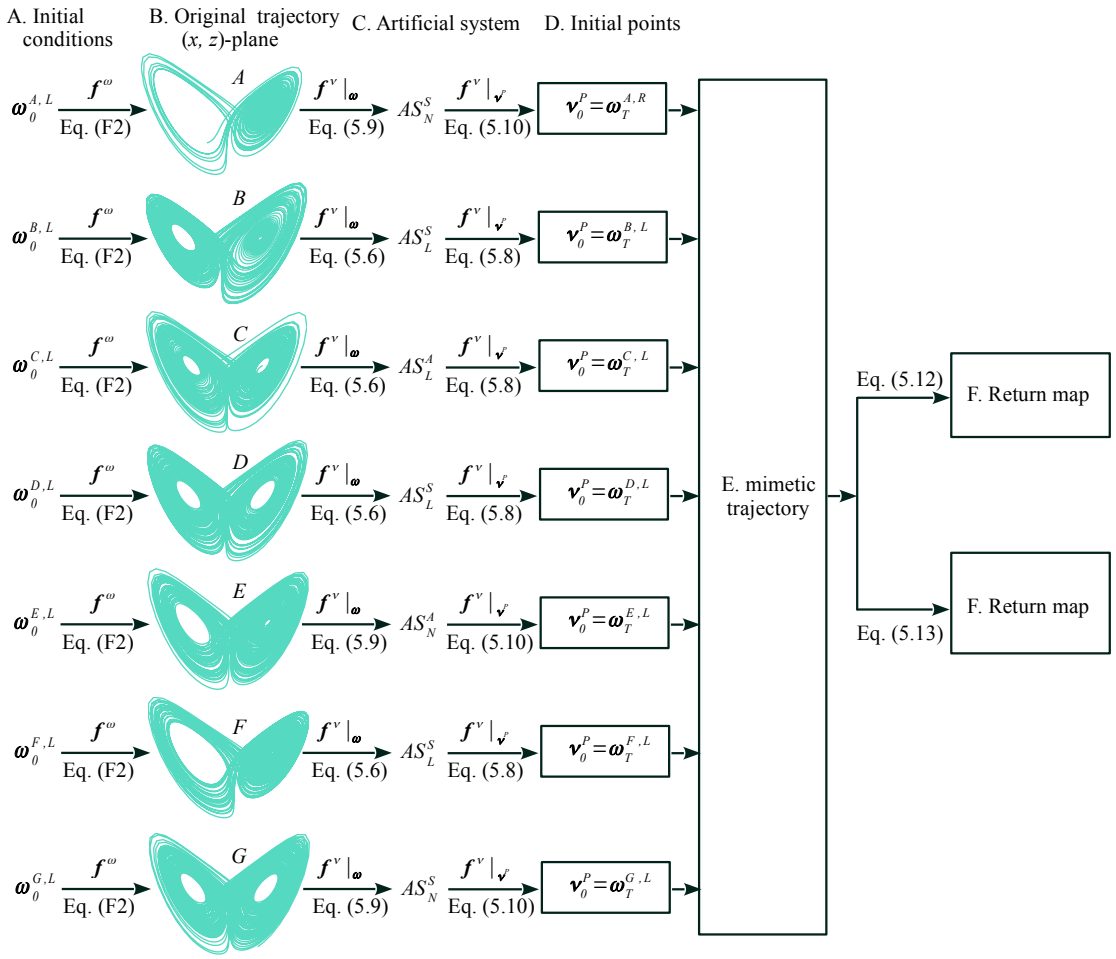

Figure 5.7 : Seven cases to exemplify system-level machine behaviors (Fig. 5.2D$_1$). Cases A to G are either widely observed patterns or patterns shown in existing literature [163, 292]. Procedures A to E follow the procedures that Fig. 5.6 outlines for collecting machine behaviors. Procedure F calculates two different return maps according to Eqs. (5.12) and (5.13).

presents how the seven cases are analyzed. Three reasons exist for us to use those seven cases A to G (Fig. 5.7). Firstly, some cases are widely observed in those 4×10^6 return maps. Here, we randomly choose 10^4 return maps among those 4×10^6 samples and manually find the patterns of the chosen return maps. Secondly, some cases are also observed in existing studies [163, 292]. The cases exemplify the prevalence of the corresponding patterns as "machine learning meets complex dynamics" [363].

A third reason is closely related to the goal of our experiments shown in Fig. 5.6. For

cases A and G, their artificial systems are identical. The only difference is the original trajectory that AS_N^S is fed with (Fig. 5.7). Similarly, cases B, D, and F only differ in their original trajectories that AS_L^S is fed with. The cases in Fig. 5.7 thus exemplify the behavior of AS_L^S or AS_N^S under varying $\boldsymbol{\omega}$ that underlies an identical $\boldsymbol{f}^{\omega}$ (Eq. 5.1) and approaches an identical attractor.

It is worth mentioning that Eq. (5.13) is applied solely to the seven cases that Fig. 5.7 exemplifies. The reasons are twofolds. One return map, Eq. (5.12), is enough to lead to the seven cases A to G. Also, calculating only one type of return map saves time.

5.4.3 System-level behaviors: One-in-basin-out mode

We have presented two experiments. The experiments collect trajectory-level behaviors in the Rössler system (Figs. 5.2C and 5.5) and collect system-level behaviors in the Lorenz system (Figs. 5.2D$_1$, 5.6 and 5.7). We then describe the third experiment on comparing system-level behaviors in the Hénon map. The experiment follows a one-in-basin-out mode (Fig. 5.2D$_2$). An original trajectory[†] is fixed (Figs. 5.8A and 5.8B). However, the initial points are varied and allowed traveling through a grid in phase space (Fig. 5.8D$_2$). The amount of mimetic trajectories that an artificial system synthesizes is equal to the amount of initial points.

The experiment on the Hénon map, cf. Eq. (F3), is designed to find how an artificial system responds to individual initial points. Taking the points as initial conditions, an original system approaches different attractors. Fig. 5.8 outlines the procedures of conducting a one-in-basin-out experiment. We use a unique artificial system AS^H to examine the sensitive dependence on Type II initial conditions (Fig. 5.1C). The experiment takes the following steps.

(1) The point $\boldsymbol{\omega}_0 = \boldsymbol{\omega}_0^H$ (Fig. 5.8A) is fixed. The Hénon map thus yields a unique chaotic trajectory (Fig. 5.8B).

[†]We use "trajectory" to make terms be consistent in a flow and a map, although the term "orbit" is suitable for a map.

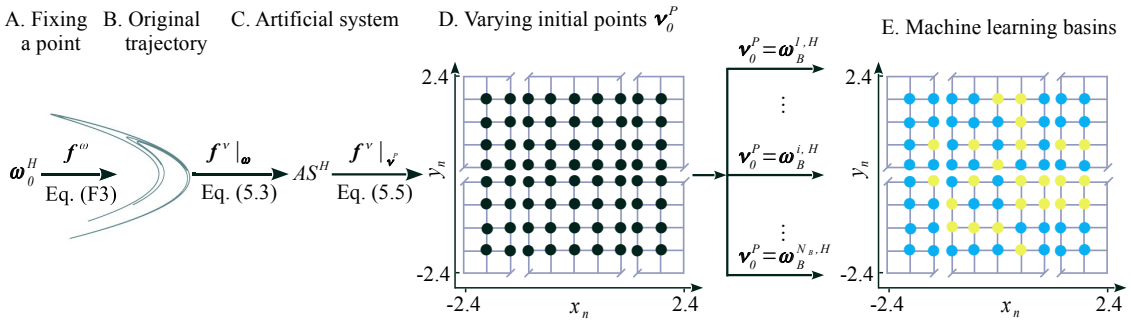

Figure 5.8 : One-in-basin-out experiment that collects system-level behaviors under varying Type II initial conditions (Fig. 5.2D$_2$). A. The initial condition of the Hénon map is fixed. B. A unique original trajectory is yielded. C. A unique artificial system, AS^H, is used. D. AS^H is fed with the unique original trajectory, however, its Type II initial conditions travel through a grid, $\mathcal{B}_H$. E. Machine learning basins present the different dynamics of mimetic trajectories in $\mathcal{B}_H$. Supposed behavior should satisfy the dynamics of the Hénon map and its basins. The quantitative analysis is based on the climate of symbolic dynamics and the statistics of correlation dimension estimations (Fig. 5.2D$_2$).

(2) The artificial system AS^H (Tab. 5.2) is fed with the unique trajectory (Fig. 5.8D).

(3) The initial points $\boldsymbol{\nu}_0^P$ are varied (Fig. 5.8D) and allowed traveling through basins of the Hénon map, $\mathcal{B}_H$. The artificial system then synthesizes a series of mimetic trajectories. Here, $\boldsymbol{\nu}_0^P \in \mathcal{B}_H = \left\{(x,y) : x = -2.4 + 4.8 i_x/2048, y = -2.4 + 4.8 i_y/2048\right\}$ with $i_x, i_y \in \{-, \cdots, 20-7\}$. The cardinality of $\mathcal{B}_H$ is 2048^2.

(4) In total, 2048^2 mimetic trajectories are collected. We translate those trajectories to symbolic sequences.

(5) The visualization of $\mathcal{B}_H$ is based on an appearance and a disappearance of forbidden words of mimetic trajectories (Fig. 5.8E).

We introduce three quantifications to analyze a gap between an original and an artificial systems. The three quantifications are machine learning basins, symbolic dynamics, and a statistics of correlation dimension (Fig. 5.2D$_2$). Machine learning basins are calculated from $\clubsuit_H$. Symbolic dynamics and the statistics of correlation dimension estimations are calculated from a subset of $\clubsuit_H$. The points in the subset approach an identical attractor.

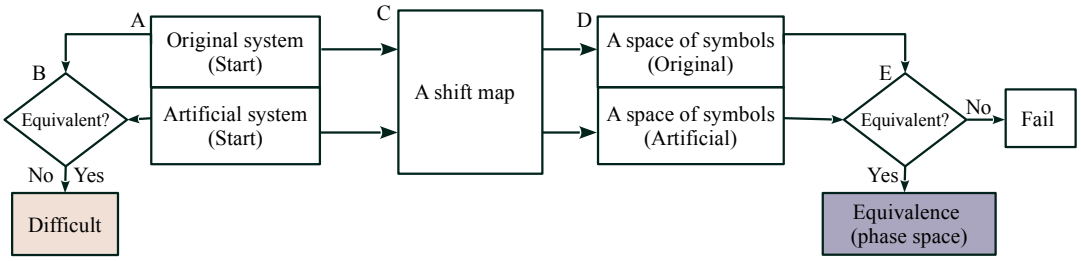

Figure 5.9 : A conceptual diagram of why (A and B) and how (C to E) to conduct a symbolic analysis (Figs. 5.2D$_2$ and 5.8). A. In phase space, a mimetic trajectory coincides with an original trajectory. B. The coincidence makes it difficult to spot a difference between an original and an artificial systems. C. A shift map encodes a time series into a sequence of symbols. Symbolic analysis is concerned with the dynamics of the time series in a space of symbols. D. A shift map, which allows an original system having an equivalence between the dynamics in phase space and that in a space of symbols, is applied to both the original and the mimetic trajectories. E. A comparison of symbolic dynamics between original and mimetic trajectories provides insights into a relationship between an original and an artificial systems.

5.4.3.1 Machine learning basins

The basin of the Hénon map is in a two-dimensional phase space, which can be visualized from the (x, y)-plane. As initial points ($\boldsymbol{\omega}_0$) of the Hénon map travel through $\mathcal{B}_H$, the dynamics of original trajectories defines *original basins* (Fig. 5.8D). As initial points ($\boldsymbol{\nu}_0^P$) travel through an identical phase space to which original basins correspond ($\mathcal{B}_H$), the dynamics of mimetic trajectories defines *machine learning basins* (Fig. 5.8E).

Since $\boldsymbol{\nu}_0^P$ is one of the three types of initial conditions of an artificial system (Fig. 5.1 and Eq. 5.2), a machine learning basin is a basin of a solution [143] or a state [257], rather than a basin of attraction [3, 353, 398]. A basin of a solution or a state is the set of initial conditions that approach an identical attractor [143, 257]. However, a basin of attraction is the largest open set of phase space whose points have a neighborhood approaching an identical attractor [3, 353, 398].

Our results will show that machine learning basins alter original ones. To find the reasons to the results, we conduct symbolic and statistical analysis on original and mimetic trajectories. To achieve it, we need to introduce methods related to symbolic

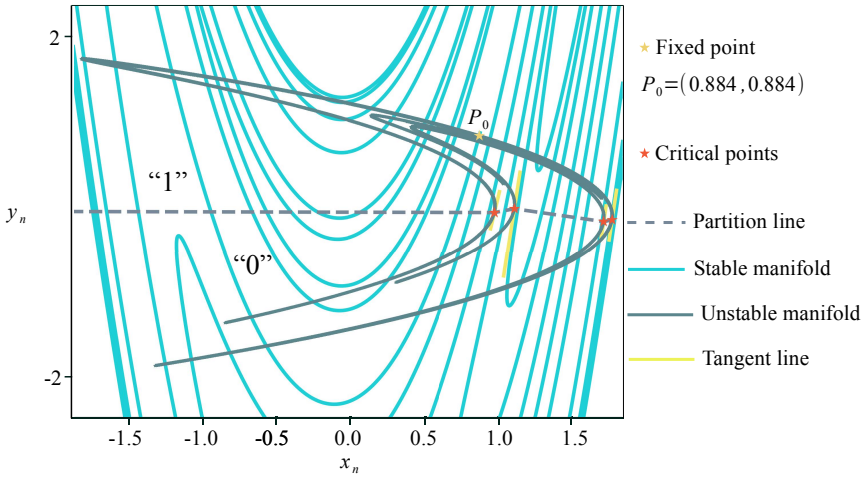

Figure 5.10 : Stable and unstable manifolds to locate the critical points of the Hénon map (Fig. 5.2D$_2$). Those points define a shift map that achieves an equivalence between the dynamics in phase space and that in a space of symbols (Fig. 5.9C). The "Segplot" algorithm [406] is used to draw the stable and the unstable manifolds of the fixed point $P_0 = (0.884, 0.884)$. The parabola-like curves (vertical) represent the stable manifold. The curves (horizontal) that looks like the Hénon map represent the unstable manifold. They coincide with the Hénon map in phase space. The tangencies between the stable and the unstable manifolds define four critical points. A line that connects those four points divides phase space into two segments being marked with "0" and "1", respectively.

and statistical analysis.

5.4.3.2 Climate of symbolic dynamics

Fig. 5.9 schematizes the idea of symbolic dynamics and how to translate a trajectory to its symbolic sequence. If an original system has analytical formulas, then a shift map that preserves nonlinear dynamics of the system can be derived by locating critical points. We then apply an identical shift map to mimetic trajectories.

When it comes to the Hénon map, You, Kostelich, and Yorke [406] utilize the tangencies between the stable and the unstable manifolds of a fixed poin–$P_0 \approx (0.884, 0.884)$ to locate the critical points. Those points define a shift map being one-to-one with the Hénon map [143, 406]. Fig. 5.10 outlines the stable and the unstable manifolds of P_0. The two manifolds segment a phase space into two parts, which are marked as "0"

and "1" in Fig. 5.10. Here, the partition line is defined by four critical points, which correspond to the tangencies between the stable and the unstable manifolds (Fig. 5.10). From the left to the right of the partition line (Fig. 5.10), those critical points are C_1, C_2, C_3,and C_4, respectively. Their values satisfy

$$C_1 = (C_1^x, C_1^y) \approx (0.986, -0.012), C_2 = (C_2^x, C_2^y) \approx (1.121, 0.032),$$
$$C_3 = (C_3^x, C_3^y) \approx (1.724, -0.118), C_4 = (C_4^x, C_4^y) \approx (1.780, -0.097).$$

where C_i^x is the $x-$coordinate of C_i with $i = 1, \cdots, 4$, and C_i^y is the $y-$coordinate of C_i. The partition line defines a shift map via

$$(x,y) = \delta^H(x,y) = \begin{cases} \text{“0”} \ \text{ if } x < C_1^x \text{ and } y < C_1^y \\ \text{“1”} \ \text{ if } x < C_1^x \text{ and } y \geq C_1^y \\ \text{“0”} \ \text{ if } C_i^x \leq x < C_{i+1}^x \text{ and } y < \frac{(x-C_i^x)(C_{i+1}^y - C_i^y)}{(C_{i+1}^x - C_i^x) + C_i^y} \\ \text{“1”} \ \text{ if } C_i^x \leq x < C_{i+1}^x \text{ and } y \geq \frac{(x-C_i^x)(C_{i+1}^y - C_i^y)}{(C_{i+1}^x - C_i^x) + C_i^y} \\ \text{“0”} \ \text{ if } x \geq C_4^x \text{ and } y < C_4^y \\ \text{“1”} \ \text{ if } x \geq C_4^x \text{ and } y \geq C_4^y \end{cases} \tag{5.14}$$

The point above the partition line is encoded with "1", otherwise, "0" is encoded. A trajectory $\left\{(x_n, y_n)\right\}$ is translated to a symbolic sequence $\left\{\delta^H(x_n, y_n)\right\}$ according to Eq. (5.14). For example, the symbolic sequence of a trajectory $(0,0) \to (1.4,0) \to (-0.56, 1.4) \to (1.5064, -0.56) \to (-1.1037, 1.5064)$ is "11101" since $\delta^H(0,0) = 1$, $\delta^H(1.4,0) = 1$, and so on.

We have introduced how to conduct symbolic analysis. We then need to introduce a new quantification based on symbolic dynamics. The quantification is the climate of symbolic dynamics, which is related to the statistics of $k-$words. A $k-$word is consecutive k words of a symbolic sequence. For example, the symbolic sequence "11101" has three different $2-$words, "11", "10", and "01". The climate of symbolic dynamics is based on a dataset that records symbolic sequences and their $k-$words.

Fig. 5.11 schematizes how a dataset is created for a calculation of the climate of symbolic dynamics. Initial points are chosen from a set $\left\{\boldsymbol{\nu}_0^P = \boldsymbol{\omega}^{i,H} \in \mathcal{B}_H\right\}_{i=1}^{N_S}$ (Fig. 5.11D).

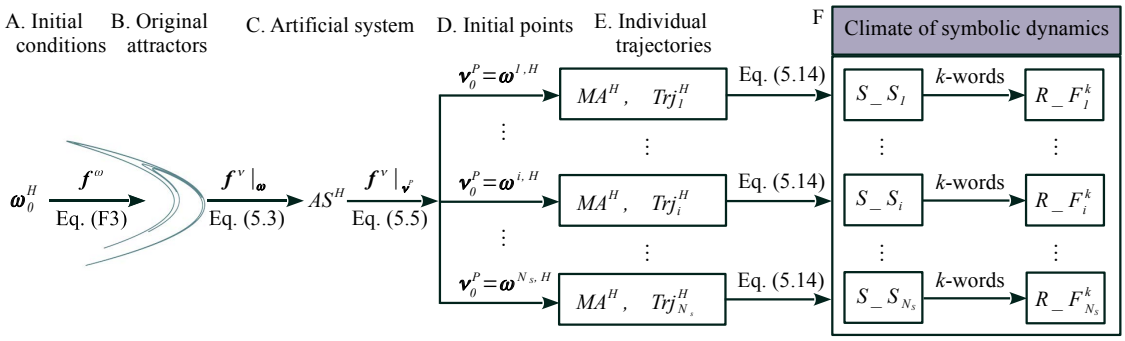

Figure 5.11 : A workflow of a calculation of the climate of symbolic dynamics (Figs. 5.2D$_2$ and 5.8). Procedures A to C are consistent with the procedures in Fig. 5.8 for collecting system-level behaviors. D. Taken an arbitrary point $\boldsymbol{\nu}_0^P = \boldsymbol{\omega}^{i,H}$ as initial conditions, the artificial system AS^H synthesizes a mimetic trajectory Trj_i^H. Here, $i = 1, 2, \cdots, N_S$ with $N_S = 1{,}000$, and represents the index of mimetic trajectories. E. The initial points are chosen in this way. Taken an arbitrary point $\boldsymbol{\nu}_0^P = \boldsymbol{\omega}^{i,H}$ as initial conditions, the original system (Eq. F3) approaches the Hénon map, and the artificial system AS^H approaches the ML-mimetic attractor MA^H. F. Eq. (5.14) translates an individual trajectory (Trj_i^H) to a symbolic sequence S_S_i. A dictionary, $R\_F_i^k$, saves an individual $k-$word as a key. The value of the key is the relative frequency of the corresponding $k-$word among S_S_i. As i increases from 1 to N_S, one can calculate the relative frequency of the value of a given $k-$word among $\left\{S\_S_i\right\}_{i=1}^{N_s}$. The climate of symbolic dynamics is concerned with the statistics of that relative frequency.

An artificial system then synthesizes N_S mimetic trajectories as $\boldsymbol{\nu}_0^P$ is varied (Fig. 5.11E). Here, $N_S = 1{,}000$ is the total amount of initial points for a calculation. The set $\left\{\boldsymbol{\nu}_0^P = \boldsymbol{\omega}^{i,H} \in \mathcal{B}_H\right\}_{i=1}^{N_S}$ satisfies two properties. An arbitrary point $\boldsymbol{\omega}^{i,H}$ in the set leads the original system (Eq. F3) to approach the Hénon map, and also leads the artificial system (AS^H) to approach an identical ML-mimetic attractor MA^H (Fig. 5.11E).

An individual mimetic trajectory Trj_i^H is then translated into a symbolic sequence S_S_i via Eq. (5.14). For each S_S_i, a dictionary $R\_F_i^k$ is created. The key of the dictionary is individual $k-$words, and the value is the relative frequency of the corresponding $k-$word. The subscript $_i$ represents the index of a mimetic trajectory. The superscript ^{k} represents the length of a $k-$word. For example, the dictionary of 2-words of the symbolic sequence "11101" is $\left\{\text{"11"} : \frac{2}{4}; \text{"10"} : \frac{1}{4}; \text{"01"} : \frac{1}{4}\right\}$. By varying initial points N_S symbolic sequences $\left\{S\_S_i\right\}_{i=1}^{N_S}$ and N_S dictionaries $\left\{R\_F_i^k\right\}_{i=1}^{N_S}$ are collected.

A two-dimensional dataset $\left\{R\_F_i^k\right\}_{i=1}^{N_S}$ is thus created. The first dimension saves information about the relative frequency of an individual $k-$word among all $k-$words for a given S_S_i. A given key of a given $R\_F_i^k$ represents the first dimension. For example, for "11101" , the relative frequency of "11" is $\frac{2}{4}$. As i changes from 1 to N_S, an individual $k-$word has N_S values by searching through $\left\{R\_F_i^k\right\}_{i=1}^{N_s}$. This contributes to a second dimension, which saves information about N_S corresponding relative frequencies of a given key ($k-$word). The climate of symbolic dynamics is concerned with a statistic of those N_S relative frequencies. For example, a second dimension can appear if we have N_S dictionaries, and each dictionary records the relative frequency of the $2-$word "11". A climate of symbolic dynamics is then about the statistics of those N_S relative frequencies of the $2-$word "11".

It is worth mentioning that we schematize the concept of the climate of symbolic dynamics in an ML-mimetic attractor. However, a calculation is based on a series of trajectories and their symbolic sequences (Fig. 5.11). A calculation of the climate of symbolic dynamics is thus not limited to an artificial system. For the Hénon map, we calculate its climate of symbolic dynamics to benchmark that of the ML-mimetic attractor MA^H. The calculations can be applied to other dynamical systems as well.

5.4.3.3 Forbidden words

We have collected a series of symbolic sequences (Fig. 5.11F). Forbidden words provide another perspective to understand the mechanism of deterministic chaos [143]. A forbidden word is a $k-$word that the topology of deterministic chaos precludes [143]. A forbidden word can be understood in the following way. An invariant topology is responsible for the organization of a chaotic attractor in phase space [143, 219]. A shift map divides a phase space into L segments. For example, Eq. (5.14) divides phase space of the Hénon map into two segments (Fig. 5.10). Under time evolution, redundant permutations of the L segments emerge. On the one hand, after p iterations, a phase space is divided into L^p segments since L words have L^p different permutations with repetition. On the other hand, an attractor is invariant under iterations and bounded

in a phase space by its topology. This suggests that if a phase space has a blank white area to which an attractor does not visit, then a redundant permutation appears at a suÿcien t large p. To be special, there exists a minimum p satisfying that a permutation of length p is well defined in the blank area, however, the attractor has no definition in the blank area. This results in a redundant permutation. The permutation is thus prohibitive in the symbolic sequences of the attractor, which is the so-called forbidden word [110, 143, 312]. For example, a 4-word "0000" is a forbidden word of the Hénon map [151]. The stretching and folding mechanism prohibits the Hénon map to stay at phase space that is marked with "0" for 4 consecutive iterations (Fig. 5.10). Therefore, a difference in the appearance and the disappearance of forbidden words indicates inequivalent topologies [143]. Besides, a forbidden word has the least length to appear in symbolic sequences, for it takes at least p iterations to allow the blank area being encoded with a redundant permutation. For example, the least length of forbidden words in the Hénon map is four [151].

The climate of symbolic dynamics provides information about forbidden words. The dataset $\left\{R\_F_i^k\right\}_{i=1}^{N_S}$ collects $k-$words that appear in symbolic sequences. Those $k-$words can be studied from two perspectives. (1) For arbitrary i and j, if two dictionaries, $R\_F_i^k$ and $R\_F_j^k$, have different keys, then $\mathrm{S\_S}_i$ and $\mathrm{S\_S}_j$ have different forbidden words. This suggests that AS^H yields different ML-mimetic attractors from different initial points $\boldsymbol{\nu}_0^P$. (2) If two dictionaries, $R\_F_i^k$ and $R\_F_j^k$, have identical keys, then we gather a new data set, dict_H=$\left\{R\_F_i^k : i \in \mathcal{K}_k\right\}$. Here, $\mathcal{K}_k$ is a set of indexes of those dictionaries that have identical keys of length k. A set $\left\{\mathrm{S\_S}_i^k : i \in \mathcal{K}_k\right\}$ collects the symbolic sequences that have identical keys. The sequences in the set thus have an identical appearance and an identical disappearance of forbidden words of length k. In our experiment, the climate of symbolic dynamics is conducted at $k = 11$. The reason is that the mimetic attractor MA^H firstly shows a difference with the Hénon map at $k = 11$.

5.4.3.4 Statistics of correlation dimension estimations

For an analysis of mimetic trajectories, a natural idea is to investigate the statistics of invariant measures. We therefore conduct a statistic of correlation dimension estimations on those N_S original and those N_S mimetic trajectories (Fig. 5.11). Finding a scaling regime is the key to correlation dimension estimations. We identify a scaling regime based on N_S original trajectories and take the following steps.

(1) For an individual trajectory, the "D2" algorithm is called from the TISEAN package [168]. We then save two pieces of information. They are the size (ϵ) of an $\epsilon-$neighborhood and the correlation dimension estimation $\mathrm{D}_2^i(\epsilon, m)$ under an ϵ. Here, i is the index of original trajectories (Fig. 5.11), and m is an embedding dimension. We change m from 1 to 20 and let the minimum size r and the maximum size R of $\epsilon-$neighborhoods be 10^{-5} and 2.2 respectively.

(2) For an ϵ, N_S estimations $\left\{\mathrm{D}_2^i(\epsilon, m)\right\}_{i=1}^{N_S}$ are thus collected at a given m.

(3) A statistic over each ϵ is conducted. At a given $\epsilon = \epsilon'$, we calculate the median of $\left\{\mathrm{D}_2^i(\epsilon', m)\right\}_{i=1}^{N_S}$. Here, ϵ' represents a given value of ϵ. As ϵ' increases from r to R, we connect the corresponding median of $\left\{\mathrm{D}_2^i(\epsilon', m)\right\}_{i=1}^{N_S}$, thus forming the median of correlation dimension estimations. A scaling regime $\epsilon \in [p_s, P_S]$ represents a plateau of the median of correlation dimension estimations. Here, p_s and P_S are the lower and the upper values of ϵ that the scaling regime corresponds to.

(4) A series of correlation dimension estimations $\mathrm{ED}_2 = \left\{\mathrm{D}_2^i(\epsilon, m) : \epsilon \in [p_s, P_S]\right\}_{i=1}^{N_S}$ are collected. The cardinality of ED_2 is N_{D2}, representing the sampling size of the statistics.

(5) A 99% confidence interval of the mean of ED_2 is calculated and interpreted as the estimations of the correlation dimension.

For the N_S mimetic trajectories (Fig. 5.11), procedures (1) and (2) lead to N_S correlation dimension estimations. The scaling regime is then fixed to $\epsilon \in [p_s, P_S]$, which is identified from the N_S original trajectories. Finally, following procedures (4) and (5) yields an estimation.

Existing studies [168, 278] have applied the "D2" algorithm [168] to calculate correlation dimension. However, our statistics are different. Hegger, Kantz, and Schreiber [168] utilize only one trajectory for the estimation. However, we utilize N_S different trajectories, which approach an identical attractor. In our experiment, N_S=1,000. Oberst and Lai [278] propose a statistical approach for correlation dimension estimations as well. However, the scaling regime is identified from only one trajectory. Besides, our approach to find the scaling regime is different from that in [278]. We let ϵ, m, and i increase for obtaining a statistical curve and then identify a plateau of the curve. For a given ϵ, we calculate the median of $\left\{\mathrm{D}_2^i(\epsilon, m)\right\}_{i=1}^{N_S}$. As ϵ increases, we then connect the corresponding median. The scaling regime corresponds to a plateau of the connected curve. Therefore, we conduct a statistic firstly, and then identify the scaling regime. Finally, we follow Oberst and Lai [278] and conduct a second statistics over the identified scaling regime $\epsilon \in [p_s, P_S]$ for an estimation.

The reasons for us to use N_S trajectories are twofolds. A use of N_S trajectories is for reliable and comparable estimations as nonlinear time series analysis is applied. No analytical formulas exist to describe how an artificial system works (Fig. 5.1 and Tab. 5.2). Optimizations in a training process (Fig. 5.1B) are often without analytical solutions [145, 218], which preclude analytical formulas in a prediction process (Fig. 5.1C, Eq. 5.2). Although analytical formulas exist in original systems (Tab. 5.1), we apply nonlinear time series analysis to both the original and the artificial systems for comparable results. The second reason is related to the way we find the scaling regime. From N_S trajectories, an alternative thought is to estimate the correlation dimension of individual trajectories and then apply a statistic on those final estimations. However, in our experiments, we observe that individual trajectories of an identical attractor have a difference in the scaling regime, although most of areas overlap. The observation will present in Fig. 5.16, which gives motivation for identifying the scaling regime firstly and then conducting a statistics.

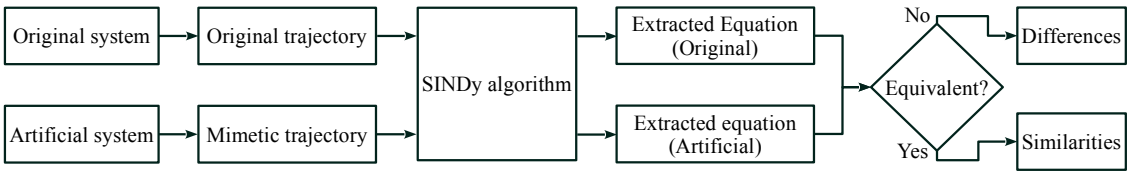

Figure 5.12 : An extraction of governing equations from a time series (Fig. 5.2E). The SINDy algorithm [53] is applied on a single trajectory and extracts governing equations by a sparse regression. Supposed and actual behaviors are compared in the sense of measuring a closeness in governing equations.

5.4.4 Extraction of equations

We have introduced nonlinear time series analysis for comparing between an original and an artificial systems (Figs. 5.2C and 5.2D). The comparison can also be based on an extraction of the equations that govern the systems (Figs. 5.2E). To achieve it, we need to introduce the methods of extracting governing equations from a trajectory (Figs. 5.2E).

Fig. 5.12 presents a use of the SINDy algorithm [53] to extract the governing equations of a time series. The SINDy algorithm [53] makes a sparse regression over a library of known equations. The regression allows identifying the parameters of equations. In our experiments, the library of equations includes the terms of individual original systems. For example, in experiments related to the Lorenz system, we allow the library including the terms of the original system, x, y, z, xy, xz, and yz.

Two reasons exist to compare an extracted equation of an artificial system $\boldsymbol{f}^{\nu}|_{\boldsymbol{\nu}}$ (Eq. 5.2) with that of an original system $\boldsymbol{f}^{\omega}$ (Eq. 5.1), rather than the ground truth (Tab. 5.1). The SINDy algorithm is a data-driven approximation of a dynamical system [303], which induces errors [63]. A comparison between extracted equations is to mitigate the error that the SINDy algorithm induces. In addition, the comparisons among trajectory-level behaviors, system-level behaviors, and approximations of governing equations together provide an insight into what matters for an artificial system in mimicking deterministic chaos. Universal approximation theorems tell that $\boldsymbol{f}^{\nu}|_{\boldsymbol{\nu}}$ is close to $\boldsymbol{f}^{\omega}$ within arbitrarily small errors. A comparison between extracted equations shows the closeness between $\boldsymbol{f}^{\nu}|_{\boldsymbol{\nu}}$ and $\boldsymbol{f}^{\omega}$ in the sense of governing equations.

Table 5.3 : Summary of experiments that collect machine behaviors with reference to Figs. 5.2C, 5.2D$_1$ and 5.2D$_2$. The experiments examine a gap between supposed and actual behaviors as the initial conditions of artificial systems are varied. The label • is related to Methods, and the label ⋄ is related to the hypothesis to be validated.

Original	Experiments	Descriptions
Rössler	Fig. 5.5	• The original system yields two chaotic trajectories that approach different attractors. • The artificial system is fed with the two chaotic trajectories, respectively, and takes two initial points to mimic the coexisting attractors that the original system approaches. ⋄ A coincidence in one of coexisting attractor is incapable of showing an equivalence between an original and an artificial systems.
Lorenz	Figs. 5.6 and 5.7	• The original system yields enormous chaotic trajectories that approach an identical basin. • Four types of artificial systems are fed with those chaotic trajectories (inputs), respectively, and take the $T-$th point of the input to synthesize equal amount of mimetic trajectories as inputs. ⋄ A coincidence in one types of return maps is incapable of showing an equivalence between an original and an artificial systems ⋄ Under the coincidence, an artificial system can develop trajectory-level behaviors.
Hénon	Figs. 5.8 to 5.11	• The original system yields one chaotic trajectory. • The artificial system is fed with the unique trajectory, and synthesizes mimetic trajectories from enormous initial points. Taken those points as initial conditions the original system has fractal basins. ⋄ A coincidence in chaotic trajectories is incapable of concluding a similar sensitive dependence on initial conditions.

5.4.5 Summary of experiments

Our experiments are conducted in the Rössler attractor, the Lorenz attractor, and the Hénon map for the study of the trajectory-level and system-level behaviors (Fig. 5.2).

Tab. 5.3 summarizes the methods and the hypotheses related to the three experiments.

For the Rössler system, Eq. (F1), the experiments use two artificial systems that satisfy the echo state property (Tab. 5.2) and adopt a classical reservoir computing paradigm (Figs. 5.4A and 5.4B). The main purpose is to investigate how an artificial system (Eq. 5.2) behaves as its mimicked system has co-existing chaotic attractors (Tab. 5.3). Here, our focus is on the trajectory-level behaviors. The results will provide insights into the following problem. Let assume that an original system has two coexisting chaotic attractors. If we feed an artificial system with one of the attractors, then which of the two original attractors does a mimetic trajectory approach (Tab. 5.3)?

For the Lorenz system, Eq. (F2), the experiments use four artificial systems. They represent a satisfaction and a dissatisfaction of the echo state property and an adoption of a classical reservoir computing paradigm and an adoption of our newly proposed paradigm with a time delay term (Fig. 5.4 and Tab. 5.2). The main purpose is to investigate how artificial systems behave under varying inputted trajectories, Type I initial conditions. The trajectories have an identical governing equations and approach an identical attractor, thus sitting in an identical basin. Here, our focus is on the system-level behaviors responding to a variation in original trajectories (Fig. 5.6). The results will provide insight into the problem. Which does matter for artificial chaos, a fitting of a chaotic trajectory, the approaching of a chaotic attractor, or an approximation of the underlying equations (Tab. 5.3)?

For the Hénon map, Eq. (F3), the experiments use one artificial system, which satisfies the echo state property (Tab. 5.2) and adopts a classical reservoir computing paradigm (Figs. 5.4A and 5.4B). The main purpose is to investigate how an artificial system behaves under varying initial points, Type II initial conditions. Here, our focus is on the basin boundaries and the climate of symbolic dynamics. The results will provide insight into the problem. What properties that an artificial system preserve do lead to an equivalence between an original and an ML-mimetic attractors (Tab. 5.3)?

5.5 Experimental results

We have described three experiments that collect the data about machine behavior (Fig. 5.2B). The three experiments are conducted on the Rössler and the Lorenz systems and the Hénon map (Fig. 5.2A), respectively. Three types of initial conditions have been identified (Fig. 5.1). In theory, an artificial system is supposed to be sensitive to Type II initial condition (initial point, $\boldsymbol{\nu}_0^P$), however, be insensitive to Type I (original trajectory, $\boldsymbol{\omega}$) and Type III (initial network states, $\boldsymbol{X}_0$ and $\boldsymbol{X}_0^P$) initial conditions (Eq. 5.2). In practice, machine behaviors, related to the behaviors of an artificial system under varying initial condition, need to be investigated.

A behavior that an artificial system presents has two intrinsic properties. The one is supposed behavior which relies on an original system. The other one is actual behavior. Our narratives thus include two parts. The first part presents supposed behavior that we observe from an original system. The second part presents actual behavior that we observe from an artificial system. A summary is then followed. Finally, supposed and actual behaviors are compared.

5.5.1 Trajectory-level machine behaviors

The first experiment is conducted on the co-existing chaotic Rössler attractors. Fig. 5.13 shows the supposed and the actual behaviors.

Supposed behaviors. The Rössler system approaches two attractors (Fig. 5.13A), R_0 and R_1. The return map RMo^{R_0} of R_0 and that RMo^{R_1} of R_1 are topologically equivalent and symmetric [313] (Fig. 5.13E). The symmetry is in a sense that reversing the branch order of RMo^{R_0} leads to RMo^{R_1}. The maximum is the critical point of RMo^{R_0} (Fig. 5.13E). The point segments the return map to a left and a right branches. The left side of the maximum corresponds to a left branch, and the right side of that corresponds to a right branch. The order of branches represents the topological structure. Also, the left branch is shorter than the right one. However, RMo^{R_1} is a symmetrically

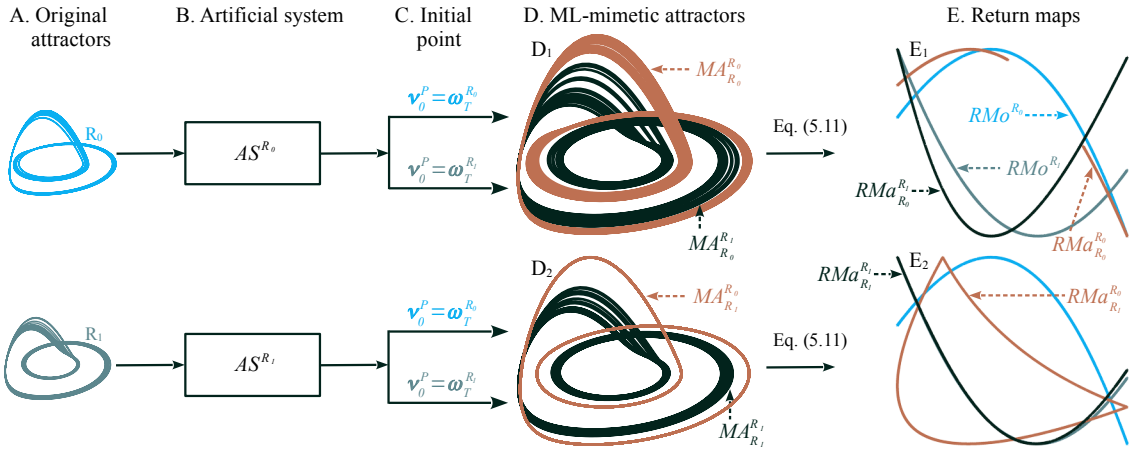

Figure 5.13 : Trajectory-level machine behaviors in mimicking the coexisting Rössler attractors. Procedures A to C are consistent with the procedures that conduct trajectory-level experiments (Fig. 5.5). D. A phase plot of attractors is used to visualize a difference between an original and an ML-mimetic attractors. D_1 is a phase plot of $MA^{R_0}_{R_0}$ and $MA^{R_1}_{R_0}$. D_2 is a phase plot of $MA^{R_0}_{R_1}$ and $MA^{R_1}_{R_1}$. E. Return maps are calculated. E_1 outlines the return maps of $MA^{R_0}_{R_0}$ and $MA^{R_1}_{R_0}$, marked as $RMa^{R_0}_{R_0}$ and $MA^{R_1}_{R_0}$, respectively. E_2 outlines the return maps of $MA^{R_0}_{R_1}$ and $MA^{R_1}_{R_1}$, marked as $RMa^{R_0}_{R_1}$ and $RMa^{R_1}_{R_1}$, respectively. Here, RMo^{R_0} and RMo^{R_1} are return maps of R_0 and R_1, respectively.

reversed organization. Its critical point is the minimum (Fig. 5.13E). The left side of the minimum corresponds to a left branch, and the right side of that corresponds to a right branch. Reversing the left branch of RMo^{R_1} leads to the righ branch of RMo^{R_0}. Similarly, the right branch of RMo^{R_1} is a reversed left branch of RMo^{R_0}.

Actual behaviors. The artificial system AS^{R_0} synthesizes two ML-mimetic attractors (Fig. 5.13D_1), $MA^{R_0}_{R_0}$ and $MA^{R_1}_{R_0}$, to mimic R_0 and R_1, respectively. Similarly, AS^{R_1} synthesizes two ML-mimetic attractors (Fig. 5.13D_2), $MA^{R_0}_{R_1}$ and $MA^{R_1}_{R_1}$, to mimic R_0 and R_1, respectively. The return map of $MA^{R_0}_{R_0}$ and that of $MA^{R_1}_{R_0}$ are $RMa^{R_0}_{R_0}$ and $RMa^{R_1}_{R_0}$ (Fig. 5.13E_1), respectively. The return map of $MA^{R_0}_{R_1}$ and that of $MA^{R_1}_{R_1}$ are $RMa^{R_0}_{R_1}$ and $RMa^{R_1}_{R_1}$ (Fig. 5.13E_2), respectively.

The two artificial systems, AS^{R_0} and AS^{R_1} (Tab. 5.2), fail to preserve the supposed behaviors (Fig. 5.13E). Neither AS^{R_0} nor AS^{R_1} is capable of preserving the symmetric

structure of RMo^{R_0} and RMo^{R_1} (Fig. 5.13E). For AS^{R_0}, it breaks the structures of both RMo^{R_0} and RMo^{R_1} (Fig. 5.13E$_1$). In the Rössler system, RMo^{R_0} is continuous in its phase space (Fig. 5.13E$_1$). However, for AS^{R_0}, its return map $RMa^{R_0}_{R_0}$ presents discontinuity, which is shown by a gap in Fig. 5.13E$_1$. Besides, RMo^{R_1} has an obvious longer left branch than the right branch. Nevertheless, $RMa^{R_1}_{R_0}$ has an almost equal length related to left side and right side branches (Fig. 5.13E$_1$). However, the deviations between the original and the artificial AS^{R_0} systems are diÿcult to be recognized in the phase plot of attractors (Fig. 5.13D$_1$).

For AS^{R_1}, new patterns are observed. In the phase plot of attractors (Fig. 5.13D$_2$), a limit cycle emerges when AS^{R_1} is initialized from the initial point $\boldsymbol{\nu}_0^P = \boldsymbol{\omega}_T^{R_0}$ (Fig. 5.13C). The point $\boldsymbol{\nu}_0^P$ approaches R_0 in the Rössler system via Eq. (F1) (Fig. 5.5). The differences between the original and the ML-mimetic attractors are also evident in the plot of return maps (Fig. 5.13E$_2$). A circle is observed from $RMa^{R_0}_{R_1}$, indicating the incapacity of AS^{R_1} to mimic R$_0$. Although $RMa^{R_1}_{R_1}$ follows the pattern of the left branch of RMo^{R_1}, deviations exist in the right branch of RMo^{R_1}. The deviation is shown by a divergence in the rightmost edge of $RMa^{R_1}_{R_1}$ (Fig. 5.13E$_2$).

Summary. From the trajectory-level experiment, we observe differences between the original and the artificial systems in producing coexisting attractors (Figs. 5.13D and 5.13E). The artificial systems, AS^{R_0} and AS^{R_1}, are incapable of simultaneously mimicking the coexisting attractors (Figs. 5.13E$_1$ and 5.13E$_2$). Also, for comparing trajectory-level behaviors between an original and artificial systems, a phase plot of return map is a better candidature than a phase plot of an attractor (Figs. 5.13D and 5.13E).

5.5.2 Basin-in-one-out machine behaviors

The second experiment is conducted on the Lorenz attractor whose basin is unbounded in $\mathbb{R}^3$. Fig. 5.14 presents the supposed and the actual behaviors.

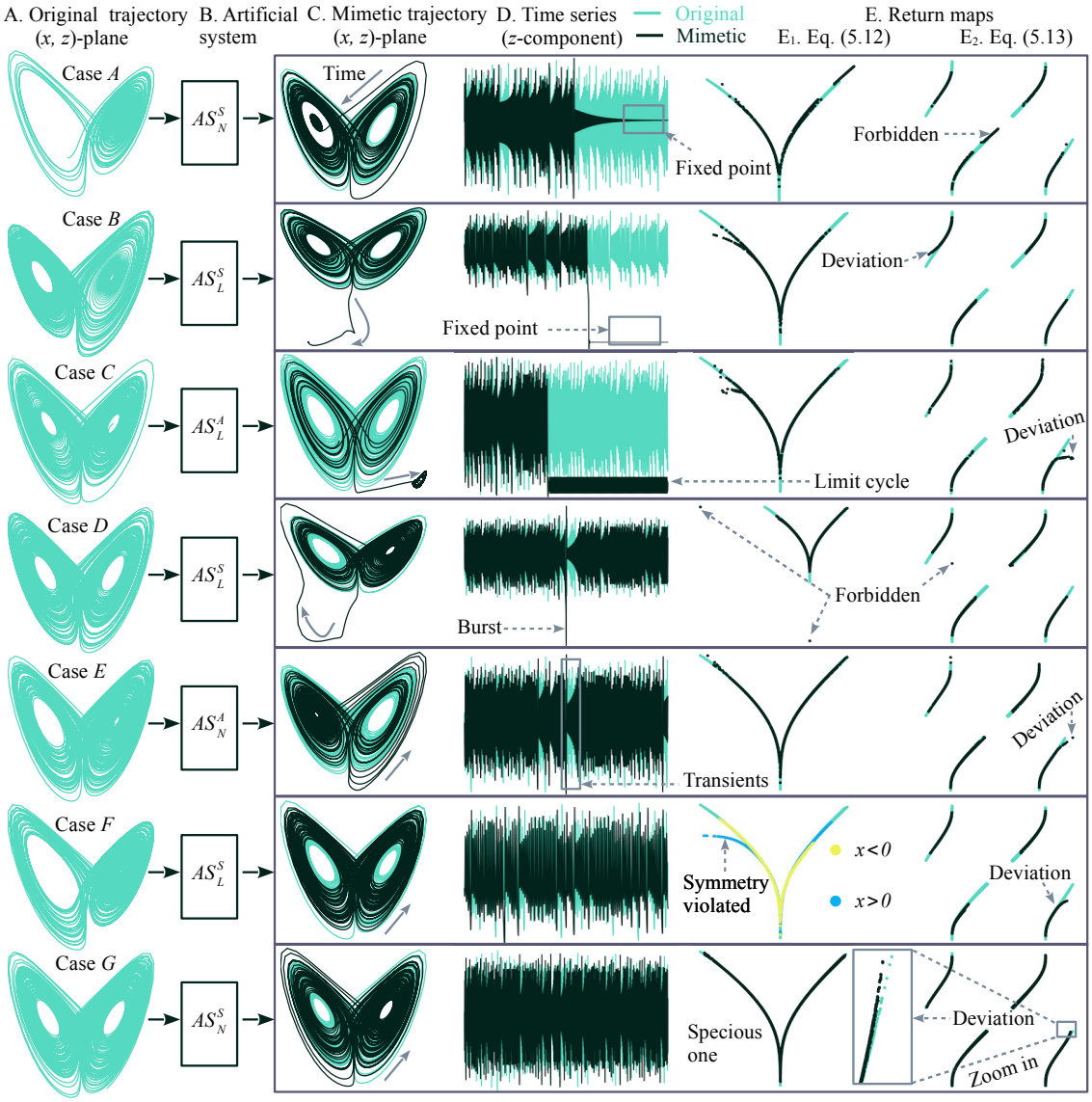

Figure 5.14 : Seven representative cases of system-level machine behaviors in mimicking the Lorenz attractor. Procedures A to E are consistent with the procedures that conduct a basin-in-one-out experiment (Figs. 5.6 and 5.7). Cases *A* and *B*: A mimetic trajectory stabilizes at a fixed point, which can be either related (*A*) or unrelated to (*B*) the fixed point of an original system. Case *C*: A mimetic trajectory stabilizes at a limit cycle. Case *D*: A mimetic trajectory presents abrupt changes in the amplitude of the time series. Case *E*: A mimetic trajectory carries the transients of an original trajectory. Case *F*: A mimetic trajectory breaks the symmetrical structure of an original attractor. Case *G*: A mimetic trajectory seemingly produce an original return map, however, a change of Poincaré section tells the deviations between the original and the mimetic trajectories.

Supposed behaviors. All initial conditions approach the Lorenz attractor. The return map that Eq. (5.12) defines has two branches (Fig. 5.14E_1). Here, the minimum represents the critical point. The left side of the minimum defines a left branch (Fig. 5.14E_1). The right side of the minimum defines a right branch (Fig. 5.14E_1). The return map that Eq. (5.13) defines has four branches (Fig. 5.14E_2), which are isolated in the phase plot of return maps. The four branches are positioned in the upper left, the upper right, the lower left, and the lower right (Fig. 5.14E_2), respectively.

Actual behaviors. The four artificial systems, AS_L^A, AS_L^S, AS_N^A, and AS_N^S, develop individual traits (Fig. 5.14) as Type I initial condition travels through the basin of the Lorenz attractor (Fig. 5.6). In advance of reporting the comprehensive comparisons of different artificial systems, we reveal the differences between the supposed and the actual behaviors in the seven representative cases that Fig. 5.7 outlines. According to the steady state dynamics of ML-mimetic attractors (Fig. 5.14), we classify six types of patterns. Cases *A* and *B* (Fig. 5.14) represent Type I pattern, converging to a fixed point. Case *C* (Fig. 5.14) represents Type II pattern, converging to a limit cycle. Case *D* (Fig. 5.14) represents Type III pattern, evolving with bursts. Case *E* (Fig. 5.14) represents Type IV pattern, carrying transients. Case *F* (Fig. 5.14) represents Type V pattern, breaking symmetry. Case *G* (Fig. 5.14) represents Type VI pattern, specious behavior. The six types of patterns satisfy the following features, respectively.

5.5.2.1 Different patterns in machine behaviors

Type I pattern: converging to a fixed point. Cases *A* and *B* in Fig. 5.14 show two stabilizing mechanisms that an artificial system approaches a fixed point. For case *A* (Fig. 5.14), a mimetic trajectory approaches a fixed point (columns C and D in Fig. 5.14). The point coincides with F_L, one of the three fixed points of the Lorenz system. For case *B*, a mimetic trajectory approaches a fresh fixed point (columns C and D in Fig. 5.14). The point is unrelated to the dynamics of the Lorenz system. The return map also shows the incapacity of mimicking the Lorenz attractor (columns E_1 and E_2 in Fig. 5.14). The

steady states of cases A and B are a single point. However, the return maps we present in cases A to C (Fig. 5.14) are not calculated on the steady states. The calculations are on the first 15,000 points for case A and the first 30,000 points for cases B and C. A return map with transients is to show that a deviation from the return map of an original system could cause Type I or Type II pattern.

In case A (Fig. 5.14), the mimetic trajectory shows a discontinuity in the two types of return maps that Eqs. (5.12) and (5.13) define. In column E_1 of case A (Fig. 5.14), the right branch of the return map is split into two isolated segments. In column E_2 of case A (Fig. 5.14), the return map of the mimetic trajectory has five isolated branches. However, the return map of the Lorenz attractor has and only has four branches (case A, Fig. 5.14E_2). This suggests that a forbidden branch emerges from the mimetic trajectory. In case B, the mimetic trajectory presents a deviation in the left branch related to the return map that Eq. (5.12) defines (column E_1 of case B in Fig. 5.14). The observation is that an additional branch occurs in the left branch. Besides, The return map that Eq. (5.13) yields shows a different curvature in the upper left branch between the original and the mimetic trajectories (column E_2 of case B in Fig. 5.14).

Type II pattern: converging to a limit cycle. Case C in Fig. 5.14 shows another mechanism that an artificial system stabilizes at steady states. In this pattern, a mimetic trajectory approaches a limit cycle that follows apparently chaotic behaviors durning transients (columns C and D of case C in Fig. 5.14). An abrupt switch to a limit cycle has occurred to an artificial system presented in [163, 292] as well. In case C, the return map that Eq. (5.12) defines has deviations in the left branch. Those deviations scatter among the left branch (column E_1 of case C in Fig. 5.14), rather than forming a new branch as shown in case B (column E_1 of case B in Fig. 5.14). In case C the return map that Eq. (5.13) defines further demonstrates a deviation. The way that the lower right branch of the return map (Eq. 5.13) bends is completely different between the original and the mimetic trajectories (column E_2 of case C in Fig. 5.14).

For Type I and II patterns, a mimetic trajectory eventually fails to approach the

chaotic Lorenz attractor. The failure can be identified from a phase plot (column C of cases *A* to *C* in Fig. 5.14) under enough iterations. Remaining patterns visit some neighborhoods of the Lorenz attractor, however, develop new behavior. It is diÿcult to show a deviation solely from a phase plot (column C of cases *D*-*G* in Fig. 5.14). Return maps become a crucial tool for showing a deviation.

Type III pattern: evolving with bursts. For case *D*, a mimetic trajectory exhibits bursting behaviors in the time series, evidenced by an abrupt change in the amplitude of the $z-$component (column D of case *D* in Fig. 5.14). In case *D*, a return map of a mimetic trajectory has outliers (column E of cases *D* in Fig. 5.14), which are away from branches that an original return map shows. For example, the return map that Eq. (5.12) defines has two outliers away from the left and the right branches of the Lorenz attractor (column E_1 of case *D* in Fig. 5.14). The return map that Eq. (5.13) defines has an obvious outlier between the upper left and the upper right branches (column E_2 of case *D* in Fig. 5.14). Those outliers occur in an area that the topology of the Lorenz attractor prohibits a return map from visiting. The appearance of a forbidden event indicates that a mimetic trajectory alters invariant property of deterministic chaos.

Type IV response: carrying transients. For case *E*, the artificial system AS_N^A has an obvious feature in the phase plot of attractors. The ML-mimetic attractor visits the transients of the Lorenz attractor. Two holes exist as the Lorenz attractor is projected onto the (x, z)-plane (column A of case *G* in Fig. 5.14). The transients correspond to the dynamics that a trajectory spires out of the holes. The initial conditions around F_L or F_R cause trajectories taking a bit long time to attenuate transients [213]. An observation can be found in the phase plot of the Lorenz attractor related to column A of cases *A, B, E* and *F* in Fig. 5.14. In case *E* the mimetic trajectory, however, recurrently spires in the left hole (column C of case *E* in Fig. 5.14). This indicates that AS_N^A is incapable of distinguishing between the transients and the steady-state dynamics.

In addition, case *E* shows that a choice of the Poincaré section is a decisive factor in identifying a deviation between an original and an artificial systems. It is diÿcult to

identify a deviation from the return map that Eq. (5.12) defines (column E_1 of case *E* in Fig. 5.14). However, the return map that Eq. (5.13) defines shows an obvious deviation in the curvature of the lower right branch (column E_2 of case *E* in Fig. 5.14).

Type V pattern: breaking symmetry. For case *F*, the artificial system AS_L^S has a feature evidenced in the return maps. The mimetic trajectory breaks the symmetrical topology of the Lorenz attractor. The violation of symmetry can be seen from the two types of return maps (Eqs. 5.12 and 5.13). For the mimetic trajectory, its return map that Eq. (5.12) defines has three branches (column E_1 of case *E* in Fig. 5.14), two left and one right branches. However, the Lorenz system uses identical dynamical template (the stretching and the tearing) to yield the left ($x < 0$) and the right ($x > 0$) sides as the attractor is projected onto the $(x, z)-$plane [56, 143]. The return map of the mimetic trajectory, however, has two different structures at where $x < 0$ and $x > 0$ (column E_1 of case *F* in Fig. 5.14).

In case *F* the return map that Eq. (5.13) defines is also capable of showing the deviations between the original and the artificial systems. The lower right branch has different curvatures between the two systems (column E_2 of case *F* in Fig. 5.14). This further indicates that AS_L^S synthesizes a mimetic trajectory by following a new topological mechanism, instead of preserving the topology of the Lorenz attractor. However, Type V pattern is diÿcult to be identified by a phase plot of the attractors or a plot of the time series (columns C and D of case *F* in Fig. 5.14).

Type VI pattern: specious behavior. For case *G*, the mimetic trajectory is the best approximation of the Lorenz attractor among all seven cases (Fig. 5.14). It has the following features. (1) The mimetic trajectory coincides with a trajectory of the Lorenz system in a phase plot and a time series. A phase plot is incapable of showing a difference between the original and the artificial systems (column C of case *G* in Fig. 5.14). (2) The time series of the mimetic trajectory is bounded by that of the Lorenz attractor (column D of case *G* in Fig. 5.14). (3) The return map that Eq. (5.12) defines is diÿcult to indicate a deviation between the original and the mimetic trajectories (column E_1

of case G in Fig. 5.14). A coincidence in one return map is thus observed. (4) For the mimetic trajectory, its return map that Eq. (5.13) defines follows the pattern of that of the Lorenz attractor in the upper left, the upper right, and the lower left branches (column E_2 of case G in Fig. 5.14). (5) A slight deviation occurs in the rightmost edge of the lower right branch (column E_2 of case G in Fig. 5.14).

In case G, a mimetic trajectory almost follows the return map of the Lorenz attractor (columns E_1 and E_2 of case G in Fig. 5.14). However, deviations exist in the return map (column E_2 of case G in Fig. 5.14) that Eq. (5.13) defines. This suggests that the artificial system AS_N^S is inequivalent to the Lorenz system. Case G also indicates that an optimal Poincaré section exists for a topological analysis of artificial chaos, although the dynamics of an original system is free from a choice of a Poincaré section. The reason is that the deviations in some Poincaré sections are diÿcult to be identified, such as Eq. (5.12) for the return map shown in column E_1 of case G in Fig. 5.14.

We have shown the effect of $\boldsymbol{\nu}_0^P$ on $\boldsymbol{f}^{\nu}|_{\boldsymbol{\nu}^P}$ (Eq. 5.2) by letting $\boldsymbol{\nu}_0^P$ travel through the basin of the Lorenz attractor (Figs 5.6 and 5.7). The six patterns (Fig. 5.14) have been shown in a phase plot, the time series, and the two types of return maps that Eqs (5.12) and (5.13) define. In the following subsection, we shall compare the behaviors of an identical artificial system under varying Type I initial conditions for understanding the effect of $\boldsymbol{\omega}$ on $\boldsymbol{f}^{\nu}|_{\boldsymbol{\nu}^P}$ (Eq. 5.2)

5.5.2.2 Sensitive dependence on Type I initial conditions

Cases B, D, and F use an identical artificial system AS_L^S to synthesize mimetic trajectories (column B in Fig. 5.14). Cases A and G use AS_N^S to synthesize mimetic trajectories (column B in Fig. 5.14). We therefore take those five cases to exemplify the effect of $\boldsymbol{\omega}$ on $\boldsymbol{f}^{\nu}|_{\boldsymbol{\nu}^P}$ (Eq. 5.2).

For cases B, D, and F, their sole difference is the original trajectory $\boldsymbol{\omega}$ that AS_L^S is fed with (column A in Fig. 5.14, Eq. 5.2). The original trajectories in cases B, D, and F are yielded by the Lorenz system, cf. Eq. (F2), however, different initial conditions are taken

(Eq. 5.1). For cases B and F, the corresponding original trajectories $\boldsymbol{\omega}$ exhibit transients (Fig. 5.14). For case D, the original trajectory $\boldsymbol{\omega}$ has no obvious transients (Fig. 5.14). However, the mimetic trajectories in cases B, D, and F exhibit three different patterns. This shows that AS_L^S responses individually to Type I initial condition. Therefore, AS_L^S is sensitive to Type I initial conditions, which behaves against the supposed behavior (Section 5.2).

On the other hand, a common feature is observed among the three cases. In phase plot, the mimetic trajectory of case D visits a small neighborhood of the fixed point that AS_L^S synthesizes in case B (column C of cases B and D in Fig. 5.14). The small neighborhood is far away from the Lorenz attractor, and the mimetic trajectory of case D exhibits an abrupt change in the amplitude for visiting the neighborhood. Besides, a deviation is only observed at $x < 0$ for cases B and D as Eq. (5.12) is applied for a return map of corresponding mimetic trajectories (column C of cases B and D in Fig. 5.14). The asymmetric way to deviate from the Lorenz attractor indicates that the mimetic trajectories of cases B and D break the symmetry as well. A choose of case F to represent Type V pattern is because the violation of symmetry in case F is the most obvious among the three cases (column E_1 of cases B, D, and F in Fig. 5.14).

Another artificial system AS_N^S has similar behaviors related to the sensitive dependence on Type I initial conditions. For cases A and G, AS_N^S is fed with an identical attractor and an identical equation, cf. Eq. (F2), however, different original trajectories. In case A the mimetic trajectory converges to a fixed point (case A in Fig. 5.14), whereas the mimetic trajectory of case G almost follows the return map of the Lorenz attractor (case G in Fig. 5.14). The individual behaviors in cases A and G indicate that AS_N^S is sensitive to Type I initial condition. The observation is against the supposed behavior that $\boldsymbol{f}^{\nu}|_{\boldsymbol{\nu}^P}$ should be insensitive to $\boldsymbol{\omega}$. The incapacity to preserve the insensitivity further demonstrates that the ML-mimetic attractor of case G exhibits a specious behavior in mimicking the Lorenz attractor. Moreover, for cases A and G a common feature exists in the lower right branch of the return map that Eq. (5.13) defines (column E_2 of cases A and G in Fig. 5.14). At that branch, the mimetic trajectories of cases A and G form

an upward curve to deviate from the Lorenz attractor (column E_2 of cases A and G in Fig. 5.14), as opposed to a downward curve in cases B to F (column E_2 of cases B to F in Fig. 5.14).

Summary. From the basin-in-one-out experiment, we observe six types of patterns in machine behaviors among seven cases (Fig. 5.14). The original trajectories that an artificial system is fed with approach an identical attractor and underly an identical equation via Eq. (F2). Results show that the artificial systems are sensitive to the original trajectories and develop unique features in mimicking the Lorenz attractor. The artificial systems, AS_L^A, AS_L^S, AS_N^A, and AS_N^S, exhibit a deviation from the Lorenz system. The deviations can be identified either from a phase plot of attractors in $\mathbb{R}^3$, the time series, or the return maps (Fig. 5.14). Moreover, AS_L^S has common behavioral features related to a violation of the symmetry of the Lorenz attractor (column E_1 of cases B, D, and F in Fig. 5.14). Also, AS_N^S has common features related to the way to deviate from an original return map (column E_2 of cases A and G in Fig. 5.14).

5.5.3 One-in-basin-out machine behaviors

The third and the last experiment is conducted on the Hénon map whose basin is fractal and visible in a two-dimensional space. Previous experiments on the Rössler (Fig. 5.13) and the Lorenz systems (Fig. 5.14) are analyzed based on qualitative behaviors. However, the following one-in-basin-out experiment (Fig. 5.8) are analyzed based on quantitative behaviors. The quantifications include machine learning basins (Fig. 5.15), the statistics of correlation dimension estimations (Fig. 5.16), and the climate of symbolic dynamics (Fig. 5.17). Machine learning basins quantify the sensitive dependence of an artificial system, AS^H, on Type II initial conditions (Fig. 5.8). The statistics of correlation dimension estimations quantify a statistical difference between an original and an ML-mimetic attractors. Moreover, the climate of symbolic dynamics quantifies a statistical difference in symbolic sequences for explaining observations in machine learning basins and the statistics of correlation dimension estimations.

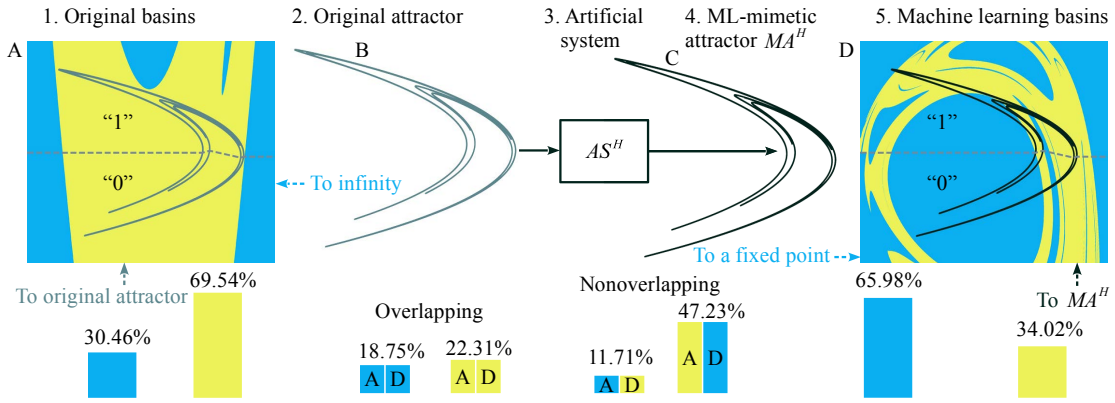

Figure 5.15 : System-level machine behaviors in mimicking the basins of the Hénon map. Procedures 1 to 5 are consistent with the procedures that conduct a one-in-basin-out experiment (Fig. 5.8). A. The basins of the Hénon map are calculated. Two types of behaviors exist. One type of points attract to infinity. The other type of points attract to the Hénon map. B. An original trajectory that approaches the Hénon map is fed into an artificial system AS^H. C. A mimetic trajectory that approaches the ML-mimetic attractor, MA^H (Fig. 5.11), is synthesized. In phase space, MA^H coincides with the Hénon map. D. Machine learning basins are calculated. Two types of behaviors exist. One type of points approach a fixed point (-422.7206, -41.8639). The other type of points approach MA^H. The percentage of points that approach a fixed point via the original and the artificial systems is 18.75%. The percentage of points that approach the Hénon map and MA^H via corresponding systems, respectively, is 22.31%. Under Eq. (5.14), a phase space is encoded with the two symbols "0" and "1" for a symbolic analysis of the Hénon map and MA^H.

5.5.3.1 Machine learning basins

Consistent with previous reports in the Rössler and the Lorenz systems, we first reveal observations in the Hénon map for the analysis of supposed behaviors, and then reveal observations in AS^H for the analysis of actual behaviors. Finally, actual behaviors are benchmarked against supposed behaviors.

Supposed behaviors. Fig. 5.15A shows the basins of the Hénon map. The original basins exhibit three features. (1) Two different attractors exist. The one initial poij ts in $\clubsuit_H$ attract to the Hénon map (Fig. 5.15B). The others attract to infinity. Among 2048^2 points (Fig. 5.8), the percentage of points to the Hénon map is 69.54%, whereas

that to infinity is 30.46% (Fig. 5.15). (2) The basin of the Hénon map contains the map itself. (3) Fractal basin boundaries exist to separate the two types of dynamics [3].

Actual behaviors. Fig. 5.15D shows the machine learning basins of the ML-mimetic attractor MA^H (Fig. 5.15C). No obvious deviations exist between the original and the ML-mimetic attractors (Figs. 5.15B and 5.15C). However, the original and the machine learning basins are different (Figs. 5.15A and 5.15D). The machine learning basins exhibit the following four features. (1) Two different attractors exist. The one points attract to MA^H (Fig. 5.15C). The others attract to a fixed point (Fig. 5.15D). Among 2048^2 points (Fig. 5.8), the percentage of points to MA^H is 34.02%, whereas that to the fixed point is 65.98% (Fig. 5.15). (2) A basin of an ML-mimetic attractor is incapable of containing the attractor itself in phase space. For example, MA^H travels across its own basin and the basin of the fixed point (Fig. 5.15D). (3) Basin boundaries become more complicated than the original one (Figs. 5.15A and 5.15D). (4) Machine learning basins are with tentacles, which are observed in high-dimensional systems due to twisted coexisting attractors [413].

Comparisons between the original and the machine learning basins indicate that AS^H are inequivalent to the Hénon map (Eq. F3), although the original and the mimetic trajectories coincide in a phase space (Figs. 5.15B and 5.15C). The sensitivity of the original and the artificial systems to initial conditions are quantitatively different. The percentage of the points in $\mathcal{B}_H$, taken as initial conditions, which approach the Hénon map in the original system and approach the ML-mimetic attractor in the artificial system, is 22.31% (Fig. 5.15) out of 2048^2 total points. The percentage of the points in $\mathcal{B}_H$, taken as initial conditions, which attract to infinity in the original system and stabilize at the fixed point in the artificial system, is 18.75% (Fig. 5.15) out of 2048^2 total points. The percentage of the points in $\mathcal{B}_H$, taken as initial conditions, which approach the Hénon map in the original system but stabilize at the fixed point in the artificial system, is 47.23% (Fig. 5.15) out of 2048^2 total points. The percentage of the points in $\mathcal{B}_H$, taken as initial conditions, which attract to infinity in the original system but approach the

ML-mimetic attractor in the artificial system, is 11.71% (Fig. 5.15) out of 2048^2 total points. Most of points (47.23%) are supposed to approach the original chaotic attractor, however, approach a fixed point. Also, 11.71% points do not belong to the basin of the original chaotic attractor, however, approach the ML-mimetic attractor. Comparisons between Figs. 5.15A and 5.15D indicate that AS^H is sensitive to Type II initial condition, which agrees with the supposed behaviors. However, AS^H quantitatively alters the original basins.

In addition, the organization of an attractor in its basin is different between an original and an ML-mimetic attractors. The Hénon map almost touches the basin boundary in the original basins (Fig. 5.15A). However, the basin of the ML-mimetic attractor is incapable of containing the attractor itself. The reason is that the ML-mimetic attractor is a projection of network states along the matrix W_{opt}^{out} (Figs. 5.1C and 5.4B). However, the dimension of network states is not necessarily equal to the dimension of an original attractor that an artificial system is designed to mimic. For example, for AS^H, the dimension of network states is 300 (Tab. 5.2), whereas the Hénon map is in two-dimensional phase space (Tab. 5.1). Moreover, machine learning basins are unable to preserve the fractal basin boundary of the original basins. Contrarily, octopuslike basins [413] are observed in machine learning basins (Fig. 5.15D).

5.5.3.2 Statistics of correlation dimension estimations

We have seen the differences between the original and the machine learning basins. An artificial system presents the sensitivity to Type II initial conditions, $\boldsymbol{\nu}_0^p$ (Eq. 5.2). However, the artificial system is incapable of preserving the invariant measure, a basin that quantifies the sensitivity to initial conditions. We then shall address the problem why an artificial system alters the original basin. To achieve it, we conduct the statistics of correlation dimension estimations. Fig. 5.16 presents the estimations of the original and the ML-mimetic attractors.

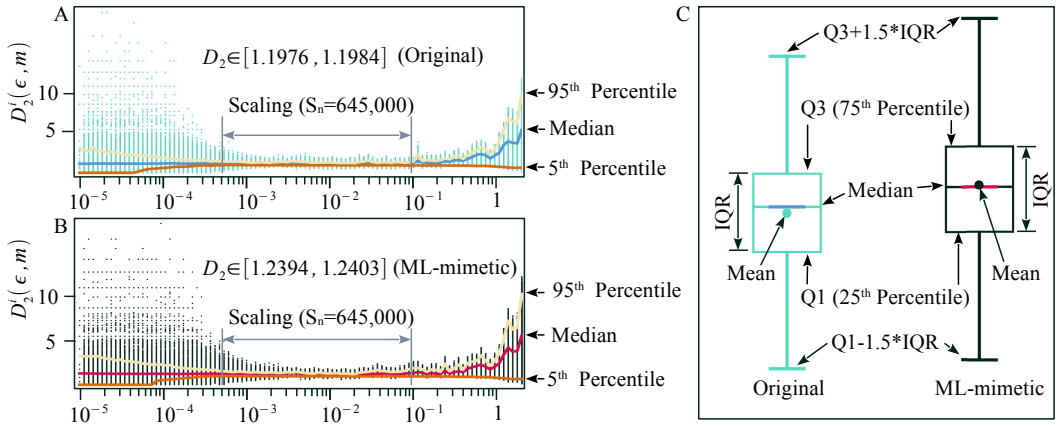

Figure 5.16 : A statistics of correlation dimension estimations to quantify a difference between the Hénon map and MA^H (Fig. 5.2D$_2$). A. For the Hénon map, its correlation dimension estimations $D_2^i(\epsilon, m)$ are presented as ϵ, m, and i increase. Here, ϵ is the size of an $\epsilon-$neighborhood, m is the embedding dimension, and i represents the index of an original trajectory. A scaling regime $\epsilon \in [p_s, P_S]$ with $p_s = 5.2214 \times 10^{-4}$ and $P_S = 9.8475 \times 10^{-2}$ is identified from trajectories that approach the Hénon map. B. For MA^H, its correlation dimension estimations $D_2^i(\epsilon, m)$ are presented as ϵ, m, and i increase. Here, i represents the index of a mimetic trajectory. The scaling regime $\epsilon \in [p_s, P_S]$ is applied for an estimation of correlation dimension. Also, $\mathrm{S_n} = 645{,}000$ estimations are in the scaling regime for both the Hénon map and MA^H. C. A boxplot is applied on corresponding $\mathrm{S_n}$ estimations, showing an overlap. However, the mean and the median in the Hénon map are different from that in MA^H.

Supposed behaviors. Fig. 5.16A shows a plateau $\epsilon \in [p_s, P_S]$ with $p_s = 5.221-\times 1-^{-4}$ and $P_S = 9.847-\times 1-^{-2}$. The plateau $\epsilon \in [p_s, P_S]$ represents a scaling regime. There are $\mathrm{S_n}$=645,000 correction dimension estimations $\mathrm{D}_2^i(\epsilon, m)$ that fall into the scaling regime (Fig. 5.16A). The statistics are conducted on those $\mathrm{S_n}$ correlation dimension estimations $\mathrm{D}_2^i(\epsilon, m)$. A 99% confidence interval of the mean of those $\mathrm{S_n}$ estimations is $D_2 \in \mathrm{CI}_{99} = [1.1976, 1.1984]$ (Fig. 5.16A).

Actual behaviors. Fixing $\epsilon \in [p_s, P_S]$ results in $\mathrm{S_n}$ correlation dimension estimations of the ML-mimetic attractor MA^H as well. A 99% confidence interval of the mean of those $\mathrm{S_n}$ estimations is $D_2 \in \mathrm{CI}_{99} = [1.2394, 1.2403]$ (Fig. 5.16B).

Three differences exist in the correlation dimension estimations between the original

and the ML-mimetic attractors. (1) The correlation dimension is different in the sense of 99% confidence interval of the estimations (Figs. 5.16A and 5.16B). (2) A box plot over corresponding S_n correlation dimension estimations also indicates a difference. The mean and the median of correlation dimension estimations are different, although some overlaps are observed in the interquartile range (IQR) (Fig. 5.16C). (3) The statistics of $D_2^i(\epsilon, m)$ differently fluctuates in the original and the ML-mimetic attractors as ϵ increases (Figs. 5.16A and 5.16B). For example, Fig. 5.16A and Fig. 5.16B have ups and downs at different positions for the corresponding 95^{th} percentile. In particular, at the left side where $1 \times 10^{-5} < \epsilon < 1 \times 10^{-4}$ and at the right side where $\epsilon > 1 \times 10^{-1}$, the fluctuation is different between the Hénon map (Fig. 5.16A) and MA^H (Fig. 5.16B).

The differences indicate that the ML-mimetic attractor MA^H just coincides with the Hénon map. However, MA^H does not preserve the fractality of the Hénon map. It is worth mentioning that the discrepancy between $D_2 \in \text{CI}_{99} = [1.1976, 1.1984]$ (original) and $D_2 \in \text{CI}_{99} = [1.2394, 1.2403]$ (ML-mimetic) is smaller than 0.05. The tiny deviation is identified thanks to a statistic over $1,000$ trajectories.

5.5.3.3 Climate of symbolic dynamics

We have shown that an ML-mimetic attractor is incapable of preserving the fractality of both the original attractor and the basins, although a coincidence is observed in phase space. We shall further look at why the incapacity happens by shifting the analysis from phase space to a space of symbols (Fig. 5.9). To achieve it, we conduct a symbolic analysis (Fig. 5.11). Fig. 5.17 shows the results of the climate of symbolic dynamics.

Supposed behaviors. Eq. (5.14) transforms an original orbit (trajectory) of length $200,000$ to a symbolic sequence of length $200,000$. We then calculate the $k-$words of the symbolic sequence with k ranging from 1 to 11. The result is consistent with existing findings [151]. The least length that forbidden words appear is 4. The corresponding forbidden 4-words are "0000", "0010", and "0110". The total number of different 4-words is 13 $(2^4 - 3)$. Consistent with [151], the total number of 4-words, 7-words, 8-words,

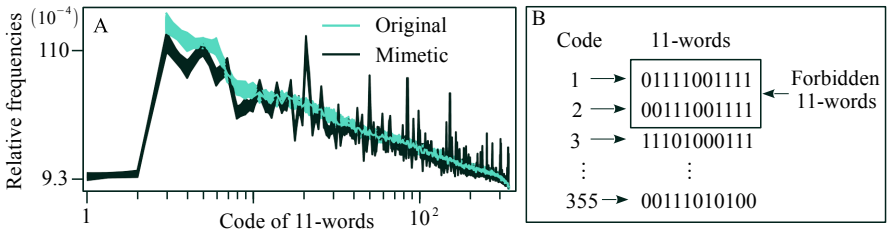

Figure 5.17 : The climate of symbolic dynamics to quantify a difference between the Hénon map and MA^H (Fig. 5.2D$_2$). A. The ML-mimetic attractor MA^H is incapable of following the climate of symbolic dynamics (11−words) of the Hénon map. B. At the length $k = 11$, the Hénon map has 353 different 11−words, however, MA^H has 355 different 11−words. The two additional 11-words are "01111001111" and "00111001111". They are forbidden 11−words of the Hénon map [151].

9-words and 11-words are 13, 53, 84, 133, and 353, respectively. For $k-$words with $k = 5, 6, 10$, there are no new forbidden words [151].

Actual behaviors. Eq. (5.14) is applied to $N_S = 1{,}000$ mimetic trajectories that approach the ML-mimetic attractor MA^H (Figs. 5.11 and 5.15C), yielding N_S symbolic sequences. The length of a mimetic trajectory and its symbolic sequence are 200,000. For an individual symbolic sequence, the total number of 4-words, 7-words, 8-words, 9-words and 11-words are 13, 53, 84, 133, and 355, respectively. The minimal length, at which the original and the mimetic trajectories have different $k-$words, appears at $k = 11$. The two 11-words, "01111001111" and "00111001111", are forbidden words of the Henon map [151] (Fig. 5.17B), however, appear in the symbolic sequence of the mimetic trajectories (Fig. 5.17B). The climate of symbolic dynamics is conducted on the 11−words of the original and the mimetic trajectories, respectively. Fig. 5.17A shows that the ML-mimetic attractor is incapable of following the climate of symbolic dynamics of the Henon map.

Summary. From the one-in-basin-out experiment, we observe that the ML-mimetic attractor MA^H coincides the Hénon map in a phase plot (Fig. 5.15). However, the coincidence does not lead to the preservations of the fractal basin boundary (Fig. 5.15),

Table 5.4 : Extracted equations of an original and corresponding mimetic trajectories. The extraction is based on a unique trajectory that approaches corresponding attractor.

Original	Equations and attractors		Equations and attractors	
Rössler	$\begin{cases} \dot{x} = -y - 0.999z \\ \dot{y} = x + 0.29y \\ \dot{z} = 0.1391 + z(0.996x - 4.504) \end{cases}$	R_0 (F4)	$\begin{cases} \dot{x} = -y - 0.999z \\ \dot{y} = x + 0.29y \\ \dot{z} = 0.1401 + z(0.998x - 4.51) \end{cases}$	R_1 (F5)
Rössler	$\begin{cases} \dot{x} = -1.001y - 0.998z \\ \dot{y} = 0.999x + 0.29y \\ \dot{z} = 0.1451 + z(0.997x - 4.504) \end{cases}$	$MA_{R_0}^{R_0}$ (F6)	$\begin{cases} \dot{x} = -y - 0.993z \\ \dot{y} = 0.996x + 0.29y \\ \dot{z} = 0.1141 + z(0.985x - 4.374) \end{cases}$	$MA_{R_0}^{R_1}$ (F7)
Rössler	$\begin{cases} \dot{x} = -0.112xz \\ \dot{y} = 0.925x \\ \dot{z} = z(1.006x - 4.742) \end{cases}$	$MA_{R_1}^{R_0}$ (F8)	$\begin{cases} \dot{x} = -1.001y - 0.993z \\ \dot{y} = x + 0.29y \\ \dot{z} = 0.1451 + z(x - 4.51) \end{cases}$	$MA_{R_1}^{R_1}$ (F9)
Lorenz	$\begin{cases} \dot{x} = -9.911x + 9.911y \\ \dot{y} = 27.209x - 0.846y - 0.978xz \\ \dot{z} = -2.636z + 0.988xy \end{cases}$	Lorenz (F10)	$\begin{cases} \dot{x} = -9.910x + 9.910y \\ \dot{y} = 27.224x - 0.861y - 0.977xz \\ \dot{z} = -2.636z + 0.987xy \end{cases}$	A (F11)
Lorenz	$\begin{cases} \dot{x} = -9.912x + 9.910y \\ \dot{y} = 27.207x - 0.849y - 0.978xz \\ \dot{z} = -2.636z + 0.989xy \end{cases}$	B (F12)	$\begin{cases} \dot{x} = -9.903x + 9.902y \\ \dot{y} = 27.232x - 0.832y - 0.979xz \\ \dot{z} = -2.642z + 0.992xy \end{cases}$	C (F13)
Lorenz	$\begin{cases} \dot{x} = -9.909x + 9.909y \\ \dot{y} = 27.205x - 0.846y - 0.978xz \\ \dot{z} = -2.635z + 0.988xy \end{cases}$	D (F14)	$\begin{cases} \dot{x} = -9.909x + 9.909y \\ \dot{y} = 27.228x - 0.841y - 0.978xz \\ \dot{z} = -2.635z + 0.988xy \end{cases}$	E (F15)
Lorenz	$\begin{cases} \dot{x} = -9.910x + 9.906y \\ \dot{y} = 27.130x - 0.838y - 0.976xz \\ \dot{z} = -2.635z + 0.988xy \end{cases}$	F (F16)	$\begin{cases} \dot{x} = -9.911x + 9.911y \\ \dot{y} = 27.210x - 0.846y - 0.978xz \\ \dot{z} = -2.636z + 0.988xy \end{cases}$	G (F17)
Hénon	$\begin{cases} x_{n+1} = 1.4001 - x_n^2 + 0.3y_n \\ y_{n+1} = x_n \end{cases}$	Hénon (F18)	$\begin{cases} x_{n+1} = 1.4001 - x_n^2 + 0.3y_n \\ y_{n+1} = x_n \end{cases}$	MA^H (F19)

or of the fractality of the original attractor (Fig. 5.16). Symbolic analysis shows that the ML-mimetic attractor exhibits the incapacity to synthesize the symbolic dynamics of the Hénon map (Fig. 5.17). In addition, the Hénon map has two forbidden 11−words. Those two 11−words , however, are allowed in the ML-mimetic attractor. This indicates an inequivalence between the Hénon map and AS^H.

5.5.4 Extracted equations

We have seen the differences between an original and an artificial systems from three perspectives. They are the dynamics in producing coexisting attractors, the six types of behavioral patterns, and the symbolic dynamics. Apart from nonlinear dynamics, we apply the SINDy algorithm [53] to extract the equations of an original and an ML-mimetic attractors (Fig. 5.12). Tab. 5.4 shows the extracted equations.

Supposed behaviors. Eq. (F4) is the extracted equation of the Rössler attractor R_0 and used for benchmarking against Eqs. (F6) and (F8). Eq. (F5) is the extracted equation of the Rössler attractor R_1 and used for benchmarking against Eqs. (F7) and (F9). Eq. (F10) is the extracted equation of the Lorenz attractor and used for benchmarking against Eqs. (F11) to (F17). Eq. (F18) is the extracted equation of the Hénon map and used to benchmarking against Eq. (F19).

Actual behaviors. Eqs. (F6) and (F7) are the extracted equations of mimetic trajectories that the artificial system AS^{R_0} synthesizes for mimicking R_0 and R_1 (Fig. 5.5), respectively. Eqs. (F8) and (F9) are the extracted equations of mimetic trajectories that the artificial system AS^{R_1} synthesizes for mimicking R_0 and R_1 (Fig. 5.5), respectively. Eqs. (F11) to (F17) are the extracted equations of mimetic trajectories that are synthesized in cases A to G (Fig. 5.7), respectively, for mimicking the Lorenz attractor. Eq. (F19) is the extracted equation of a mimetic trajectory that AS^H synthesizes for mimicking the Hénon map (Fig. 5.8).

For the trajectory-level experiment in the Rössler system (Figs. 5.5 and 5.13), Eq. (F6)

has identical terms with Eq. (F4), but the parameters of Eqs. (F6) and (F4) are different. Eq. (F8) has different terms with Eq. (F4), which is consistent to our observation of a limit cycle in Fig. 5.13D_2. Eqs. (F7) and (F9) have identical terms with Eq. (F5), but the parameters of Eqs. (F5), (F7), and (F9) are different.

For the basin-in-one-out experiment in the Lorenz system (Figs. 5.6, 5.7, and 5.14), Eq. (F10) and Eqs. (F11) to (F17) have identical terms, but different parameters. The result shows a limitation of a data-driven extraction of governing equations. For cases A to C, the mimetic trajectories stabilize at either a fixed point or a limit cycle. However, Eqs. (F11) to (F13) approximate the governing equation of the chaotic Lorenz attractor (Tab. 5.4). This indicates that the extracted equations may fail to reflect the dynamics of the time series. The limitation further highlights the importance of showing nonlinear dynamics of a mimetic trajectory.

For one-in-basin-out experiment in the Hénon map (Figs. 5.8, 5.15 to 5.17), Eqs. (F18) and (F19) have identical terms and parameters. We observe that if the ML-mimetic attractor coincides with the original attractor, then their extracted equations have identical terms. Also, the parameters of extracted equations are close. For example, the return map of $MA_{R_1}^{R_1}$ almost coincides with that of R_1(Fig. 5.13), and the parameters of Eqs. (F5) and (F9) are close. In case G the return map coincides with that of the Lorenz attractor (column E1 of case G in Fig. 5.14), and the parameters of Eqs. (F10) and (F17) are close.

Summary. From the extracted equations (Tab. 5.4), we observe that a coincidence of an ML-mimetic attractor with an original one in phase space corresponds to a reasonable approximation of the governing equations between the two attractors. However, the extraction of equations has a limitation when the time series has transients. The extraction may fail to indicate the stabilization either to a fixed point or to a limit cycle.

5.6 Summary and Discussions

Deterministic chaos is concerned with the sensitive dependence of a nonlinear system on its initial conditions [143, 333, 353, 398]. Machine learning methods are applied to mimic deterministic chaos [63, 293, 423]. The methods attract increasing attention as they offer a potential means for predicting deterministic chaos [293].

In computer science machine behavior is concerned with the behavioral patterns of an artificial intelligence system as initial settings are varied [304]. The understanding of machine behavior would improve the ability to control artificial intelligence systems and harvest their benefits [304]. An artificial system is a special artificial intelligence system that is equipped with machine learning methods and designed for mimicking deterministic chaos. We borrow the idea of machine behavior from computer science and regard the behavior of an artificial system under varying initial conditions as machine behavior. The comparisons of the sensitive dependence on initial conditions allow identifying a gap between an original $\boldsymbol{f}^{\omega}$ (mimicked, Eq. 5.1) and an artificial $\boldsymbol{f}^{\nu}|_{\boldsymbol{\nu}}$ (mimicking, Eq. 5.2) systems. Before we make discussions, we shall summarize the corresponding results.

5.6.1 Summary

We have identified three types of initial conditions that have an effect on an artificial system (Fig. 5.2A). Type I initial condition is an original trajectory (Fig. 5.1A), $\boldsymbol{\omega}$ (Eq. 5.2). The trajectory is yielded from an original chaotic system (Eq. 5.1) and fed to an artificial system in a training process (Fig. 5.1B, Eq. 5.2). Type II initial condition is an initial point, $\boldsymbol{\nu}_0^P$ (Eq. 5.2). The point is in phase space of an original attractor (Fig. 5.1C). Taking the point as initial conditions, an original system yields a chaotic trajectory, whereas an artificial system synthesizes a mimetic trajectory for mimicking that chaotic trajectory. Type III initial condition is initial network states (Figs. 5.1B), $\boldsymbol{X}_0$ and $\boldsymbol{X}_0^P$. They initialize a network in a training and a prediction processes, respectively. We have conducted three experiments for understanding the behavior of an artificial system under varying Type I or Type II initial conditions.

Results have been shown by comparing between the supposed ($\boldsymbol{f}^{\omega}$) and the actual ($\boldsymbol{f}^{\nu}|_{\boldsymbol{\nu}}$) behaviors.

The first experiment (Fig. 5.2C) focuses on a unique mimetic trajectory and its return map (Fig. 5.5), contributing to trajectory-level behaviors (Fig. 5.2C). The supposed behaviors are represented by two coexisting Rössler attractors (Fig. 5.13A), R_0 and R_1, and their return maps (Fig. 5.13E). Actual behaviors are synthesized by two artificial systems (Fig. 5.13B), AS^{R_0} and AS^{R_1}. An individual artificial system synthesizes two ML-mimetic attractors (Fig. 5.13E) as Type II initial conditions are varied. According to Eq. (5.11), we calculate the return map to quantify the differences between the supposed and the actual behaviors (Fig. 5.13F).

The second experiment (Fig. 5.2D_1) focuses on behavioral patterns of an identical artificial system as Type I initial conditions travel through a basin (Figs. 5.6 and 5.7), $\mathcal{B}_L$. System-level behaviors with a basin-in-one-out mode are collected from the second experiment (Fig. 5.2D_1). The supposed behaviors are represented by the unbounded basin of the Lorenz attractor (Fig. 5.6A). Actual behaviors are synthesized by four artificial systems (Figs. 5.6C and 5.7C), AS_L^A, AS_L^S, AS_N^A, and AS_N^S. An individual artificial system synthesizes 10^6 mimetic trajectories. We take seven representative cases to exemplify the behavior of an artificial system as Type I initial conditions are varied (Fig. 5.7). According to Eqs. (5.12) and (5.13), we calculate two types of return maps to show the supposed and the acutal behaviors (Fig. 5.14). Six types of patterns are identified in terms of a deviation in phase space (column C in Fig. 5.14), the time series (column D in Fig. 5.14), or return maps (column E in Fig. 5.14). The patterns include converging to a fixed point (cases A and B in Fig. 5.14) or to a limit cycle (case C in Fig. 5.14), evolving with bursts (case D in Fig. 5.14), carrying transients (case E in Fig. 5.14), breaking symmetry (case F in Fig. 5.14), and specious behavior (case G in Fig. 5.14).

The third experiment (Fig. 5.2D_2) focuses on quantitative differences between an original and an artificial systems as Type II initial conditions travel through different

basins (Fig. 5.8), $\mathcal{B}_H$. System-level behaviors with a one-in-basin-out mode are collected from the third experiment (Fig. 5.2D$_2$). Supposed behaviors are represented by the fractal basins of the Hénon map (Fig. 5.15A). Actual behaviors are synthesized by one artificial system, AS^H (Fig. 5.8C). Here, AS^H synthesizes 2048^2 mimetic trajectories. We use three quantifications, which are machine learning basins (Fig. 5.15), the statistics of correlation dimension estimations (Fig. 5.16), and the climate of symbolic dynamics (Fig. 5.17). Based on machine learning basins (Fig. 5.15A), the latter two quantifications are conducted on 1,000 trajectories (Fig. 5.11).

For a flow, either the coexisting Rössler attractors or the Lorenz attractor, return maps are an invariant measure to understand the topological organization of deterministic chaos [56, 313]. We thus use the return map to analyze and qualify the nonlinear dynamics of machine behaviors (Figs. 5.2C and 5.2D$_1$). An ML-mimetic attractor that the artificial system AS^H synthesizes almost coincides with the Hénon map (Figs. 5.15B and 5.15C). Besides, the basins of the Hénon map are well studied and quantifiable in a two-dimensional space [3]. We thus use three quantifications that are developed from the basins the of Hénon map to quantify the differences in nonlinear dynamics between an original and an artificial systems. The three quantifications examine nonlinear dynamics from different perspectives. Machine learning basins examine the fractality in basin boundary (Figs. 5.15A and 5.15D). The statistics of correlation dimension estimations examine the fractality of an ML-mimetic attractor (Fig. 5.16). Also, the climate of symbolic dynamics examines an equivalence between an original and an artificial systems from a space of symbols (Fig. 5.17). A shift map that critical points define ensures an equivalence between the nonlinear dynamics in phase space and the symbolic dynamics in a space of symbols [143, 151]. According to Eq. (5.14), we shift the focus from nonlinear dynamics in phase space to symbolic dynamics in a space of symbols (Fig. 5.9).

5.6.2 Discussions

Novel behavioral traits have been observed from the return maps of mimetic trajectories in mimicking either the Rössler attractors (Fig. 5.13) or the Lorenz attractor (Fig. 5.14).

Those traits indicate the diÿcult y of artificial chaos in preserving deterministic chaos. We also observe that an ML-mimetic attractor coincides with the Hénon map. However, the basins of the ML-mimetic attractor alter the basins of the Hénon map (Fig. 5.15). The correlation dimension estimations indicate a significantly statistical difference between the Hénon map and the ML-mimetic attractor (Fig. 5.16).

Moreover, we observe that the ML-mimetic attractor that coincides with the Hénon map is incapable of preserving the symbolic dynamics (Fig. 5.17). For example, two 11-words are forbidden in the Hénon map. Nevertheless, those two words are allowed in the ML-mimetic attractor (Fig. 5.17). The observations highlight that artificial chaos seems to mimic a chaotic attractor in phase space, however, may suffer from a deprivation of fractality that the chaotic attractor has. To be more detailed, we proceed by providing insights into the three questions introduced in section 5.1. The questions are concerned with the recurrence (Q.A) and the signatures (Q.B) of artificial chaos and the equivalence (Q.C) between deterministic and artificial chaos.

5.6.2.1 Recurrence of errors under perturbation

In this subsection, we shall discuss a limitation of universal approximation theorems "when machine learning meets complex dynamics" [363]. Universal approximation theorems offer an artificial system the ability to synthesize equations. The equations arbitrarily approach those of an original system [95, 112, 155, 194, 410]. We firstly discuss the effect of arbitrarily small approximation errors [155, 340] on artificial chaos and then provides insights into the recurrence of errors (Q.A) that artificial chaos induces under varying initial conditions.

In the three experiments (Figs. 5.5 to 5.8), we compare the supposed and the actual behaviors of artificial systems (Figs. 5.13 to 5.17). According to the comparisons, our results identify the differences between an original and an ML-mimetic attractors. This suggests that arbitrarily small approximation errors introduce a perturbation term to equations that an original system underlies. Universal approximation theorems provide the existence of an artificial system that leads to arbitrarily small approximation er-

rors [95, 112, 155, 194, 410]. However, the theorems disregard the recurrence of those arbitrarily small errors under perturbation.

The limitation results from the disregard of how those arbitrarily small errors recur. In complex dynamics, arbitrarily small errors have four implications for a nonlinear system. (1) Under fixed parameters of a known equation, errors in initial conditions result in different trajectories or different attractors [232, 333]. (2) Errors in parameters of a known equation induce bifurcations in nonlinear dynamics [159, 232]. (3) Errors by changing the term of an equation bring about a new system of similar dynamics or bifurcations [159]. (4) Errors can bring about a new system with dynamics unrelated to an original system. The existence of an arbitrarily small approximation error is incapable of indicating the insignificance of errors in complex dynamics.

However, a study of machine behaviors provides a tool for showing how an arbitrarily small error recurs as Type I or II initial conditions are varied. A basin of a state provides information about the recurrence of a dynamical system under global perturbations [257, 258]. Machine learning basins, as a basin of states, thus indicate how an arbitrarily small error recurs under global perturbations. The results show that machine learning basins alter the basins of the Hénon map (Figs. 5.15A and 5.15D). This suggests that the approximation errors of AS^H bring about a new system with different dynamics. The findings support the hypothesis that the arbitrarily small errors allow an artificial system to develop its own behavioral traits and deviate from supposed behaviors.

The incapacity to preserve symbolic dynamics confirms that an ML-mimetic attractor can use different organizations of topology to synthesize a mimetic trajectory (Fig. 5.17B), although the ML-mimetic attractor coincides with the original attractor (Figs. 5.15B and 5.15C). The finding emphasizes the importance of showing symbolic dynamics as a conclusion is drawn on a system-level relationship between an original $\boldsymbol{f}^{\omega}$ (Eq. 5.1) and an artificial systems $\boldsymbol{f}^{\nu}|_{\boldsymbol{\nu}}$ (Eq. 5.2), for example, a conclusion of the topological conjugation [80]. Showing machine behaviors could provide an effective tool to avoid the pitfalls [311] of machine learning methods as they meet complex dynamics.

5.6.2.2 Trajectory-centric behavior

In this subsection, we shall discuss the behavior of an artificial system under varying Type I initial condition. We firstly discuss the observations and then explain contradictions between the supposed and the actual behaviors. Solutions that may address the contradictions are discussed for providing insights into the signatures of machine behaviors (Q.B).

The supposed behaviors of an artificial system should be insensitive to Type I initial condition. An original system yields a chaotic trajectory as a result of some nonlinearity. The nonlinearity can be defined either by equations with nonlinear terms [219, 333] or by topological organizations of branches in phase space [56, 143, 219]. An artificial system, however, utilizes a new type of nonlinearity (Figs. 5.1 and 5.4) that a network defines via Eq. (5.2) for mimicking deterministic chaos. A mimetic trajectory that the artificial system synthesizes is thus not necessarily chaotic. For example, a mimetic trajectory can develop non-chaotic dynamics, a fixed point (case A and B in Fig. 5.14), a limit cycle (case C in Fig. 5.14), or novel dynamics (cases D to F in Fig. 5.14).

Although Type I initial conditions are varied, the governing equations of original trajectories with which an artificial system is fed keep unchanged. In theory, if the artificial system did behave as a function approximator, then varying Type I initial condition could not affect the mimetic trajectories for the governing equations of original trajectories are unchanged.

In practice, however, we observe trajectory-centric machine behaviors. In the experiment related to the Lorenz system (Fig. 5.14), AS_N^S produces a reasonable approximation of the governing equation of the Lorenz attractor in case G, cf. Eqs. (F10) and (F17) in Tab. 5.4. However, AS_N^S synthesizes a fixed point in case A (Fig. 5.14). Here, a unique difference between case A and G is Type I initial condition with which AS_N^S is fed. The phenomenon is observed in AS_L^S as well. The observation is that cases B, D, and F in Fig. 5.14 present individual behaviors under varying Type I initial conditions.

The contradiction between the supposed behaviors and observable phenomena can be

understood in this way. (1) Despite a coincidence in phase space, an original $\boldsymbol{f}^{\omega}$ (Eq. 5.1) and an artificial systems $\boldsymbol{f}^{\nu}|_{\boldsymbol{\nu}}$ (Eq. 5.2) develop different system-level behaviors. (2) An artificial system could develop its own signatures in the way to deviate from mimicked deterministic chaos. As Type I initial conditions are varied, both AS_N^S and AS_L^S fail to understand the mechanism that is responsible for the mimicked dynamics (Fig. 5.14). On the other hand, AS_N^S and AS_L^S leave a signature to mimetic trajectories (Fig. 5.14).

The contradiction may be addressed by an exploration of the parameter space of a network and a training process (Fig. 5.1), an extension of the length of the inputted trajectories, the size of a network, and so on. However, those improvements exactly reflect the sensitivity of $\boldsymbol{f}^{\nu}|_{\boldsymbol{\nu}}$ to Type I or III initial conditions. This again causes a contradiction between supposed and observable phenomena of $\boldsymbol{f}^{\nu}|_{\boldsymbol{\nu}}$. In this sense, a new machine learning framework should be proposed to achieve an equivalence between $\boldsymbol{f}^{\omega}$ and $\boldsymbol{f}^{\nu}|_{\boldsymbol{\nu}}$. Under the framework, an arbitrary segment of $\boldsymbol{\omega}$ or an arbitrary parameter choice chosen from parameter space would lead $\boldsymbol{f}^{\nu}|_{\boldsymbol{\nu}}$ to be a shallow of $\boldsymbol{f}^{\omega}$, an existence of uncountable original trajectories being close to a mimetic trajectory.

Recently, an advanced framework introduces automatic differentiation [27] to neural networks. Information related to the derivatives of data is thus captured by the new framework [27, 76]. Two different frameworks are popular. The one is neural ordinary differential equations (neuralODE). The other one is physics-informed neural network. NeuralODE allows consecutive layers of a neural network to make an infinitesimal step for approximating the deviates of the equations that the data underly [76]. Physics-informed neural networks allow a graph to represent the derivate values of an operation [305, 306]. The basic idea is that "all numerical computations are ultimately compositions of a finite set of elementary operations for which derivatives are known, and combining the derivatives of the constituent operations through the chain rule gives the derivative of the overall composition" [27]. An optimization is then constructed by considering "more-step errors" [187]. Instead of individual points in phase space (Fig. 5.1B), a continuous-time trajectory [76], which is a solution to ODE, is optimized and smoothed.

Incorporating derivatives may lead to a reduction of the occurrence of Type I to V patterns that we observe in Fig. 5.14, since cases A to F fail to preserve the derivative of the Lorenz attractor (column E Fig. 5.14). Let assume an artificial system, either neuralODE or physics-informed neural networks, is capable of approximating the n-th derivative of $\boldsymbol{\omega}$ within an arbitrarily small error for suÿcien t large n. Therefore, $\boldsymbol{\omega}$ and $\boldsymbol{\nu}^P$ are equivalent in the sense of identical n-th derivative with n being suÿcien t large. The artificial system then could produce a mimetic trajectory that is a shallow of true trajectories yielded via $\boldsymbol{f}^{\omega}$ (Eq. 5.1).

Indeed, our study does not reject the existence of machine learning methods that produce a shallow of $\boldsymbol{f}^{\omega}$ or are equivalent to $\boldsymbol{f}^{\omega}$. However, we introduce machine behavior for showing whether the shallow or the equivalence is achieved by a given $\boldsymbol{f}^{\nu}|_{\boldsymbol{\nu}}$. As "machine-learning tools can also turn up fool's gold – false positives, blind alleys and mistakes" [311], a study of machine behavior is for avoiding the pitfalls of machine learning that meets complex dynamics. An automatic differentiation applies "black-box differential equation solver" [76] for a solution. A study of machine behavior would allow showing that whether the n-th derivative is suÿcie nt large for a conclusive evidence on the shallow or the equivalence.

Our findings further demonstrate that a misleading conclusion could be drawn without the study of machine behaviors related to Type I initial conditions. For example, if case G was the only source to validate the eÿcie ncy of AS_N^S (Case G in Fig. 5.14), then the conclusion is that AS_N^S preserved the deterministic chaos of the Lorenz system. However, we let AS_N^S synthesize a mimetic trajectory in case A, a fixed point appears (Case A in Fig. 5.14) instead of chaotic dynamics. The observation thus supports that AS_N^S fails to preserve the governing equation and the nonlinear dynamics of the Lorenz attractor.

5.6.2.3 Machine learning embedding

In this subsection we shall interpret an equivalence of an original and an ML-mimetic attractors (Q.C). Machine learning embedding is an embedding that an artificial system

reconstructs [166]. The reconstruction is based on a conjecture that $\boldsymbol{f}^{\nu}|_{\boldsymbol{\omega}}$ (Fig. 5.1B) and $\boldsymbol{f}^{\omega}$ (Fig. 5.1A) are topologically conjugate [166]. We introduce a new term, *dynamics-preserving learning*, to represent a topological conjugacy between $\boldsymbol{f}^{\nu}|_{\boldsymbol{\nu}^P}$ (Eq. 5.2) and $\boldsymbol{f}^{\omega}$ (Eq. 5.1).

In theory, the conjecture imposes a too strict condition for a dynamics-preserving learning. The difference between $\boldsymbol{f}^{\nu}|_{\boldsymbol{\omega}}$ and $\boldsymbol{f}^{\nu}|_{\boldsymbol{\nu}}$ lies in initial conditions and the mechanism to be an autonomous system (Figs. 5.1B and 5.1C). Let assume that $\boldsymbol{f}^{\nu}|_{\boldsymbol{\omega}}$ and $\boldsymbol{f}^{\omega}$ were topologically conjugate, then there existed a one-to-one correspondence between $\{\boldsymbol{\omega}_i\}$ and $\{\boldsymbol{\nu}_i\}$ (Figs. 5.1A and 5.1B). Since the functions $\{\boldsymbol{\omega}_{i-1}\} \to \{\boldsymbol{X}_i\}$ and $\{\boldsymbol{X}_i\} \to \{\boldsymbol{\nu}_i\}$ are surjective (by the assumption), and $\{\boldsymbol{\omega}_i\}$ is a countable set because $\{\boldsymbol{\omega}_i\}$ is collected under iterations, there exists a one-to-one correspondence between $\{\boldsymbol{\omega}_i\}$, $\{\boldsymbol{X}_i\}$, and $\{\boldsymbol{\nu}_i\}$. According to the one-to-one correspondence, there exists a unique $\boldsymbol{X}_0^P$. Taken $\boldsymbol{X}_0^P$ as initial conditions, a dynamics-preserving learning is achieved. However, analytical solutions to optimization problems are often absent (Fig. 5.1B), so it is impracticable to find the unique $\boldsymbol{X}_0^P$. Indeed, $\boldsymbol{X}_0^P$ is often set to be zero or $\boldsymbol{X}_{T+1}$ when it comes to practical applications [64, 80, 166, 200, 293, 383, 423].

However, we observe that machine behaviors contain new traits. The traits are not attributed to the nonlinear dynamics of an original system. In the Rössler system, AS^{R_0} breaks symmetry that the return maps of coexisting Rössler attractors have (Fig. 5.13E). Also, AS^{R_1} mimics the return map of R_1 with a reasonable approximation (Fig. 5.13E_2), however, it is unable to simultaneously produce the coexisting attractors. Here, AS^{R_0} contains new traits of symmetry violated (Fig. 5.13E_1); and AS^{R_0} contains new traits by changing the sensitivity to initial conditions (Fig. 5.13E_1). In the Lorenz system, AS_L^A, AS_L^S, AS_N^A, and AS_N^S contain new traits through the way to deviate from the return map of an original attractor (Fig. 5.14).

Moreover, the new traits are reflected by statistical differences between supposed behaviors and machine behaviors in the Hénon map. In phase space, only 22.31% points, taken as initial condition, simultaneously approach the Hénon map and the ML-mimetic

attractor (Fig. 5.15). This suggests that AS^H has only 22.31% probability in producing a mimetic trajectory, which reasonably mimics the dynamics of the Hénon map. Besides, novel structures are observed in machine-learning basins such as basins with tentacles [413], which alter the basins of the Hénon map (Fig. 5.15D). Zhang and Strogatz [413] conclude basins with tentacles may be common in a high-dimensional system. Our calculation confirms the conclusion and exemplifies how machine learning basins with tentacles are fundamentally different from an original basin.

Our observations highlight that a coincidence in a single chaotic trajectory is insufficient to support an equivalence between machine learning and time delay embeddings. Takens' embedding theorem [324, 360] ensures an equivalence between an original attractor and the time delay embedding. However, a dynamic-preserving learning remains to be solved for machine learning that meets complex dynamics. It is thus impractical to ensure an equivalence between supposed and actual behaviors of an artificial system. A conclusive evidence of the equivalence should be based on supposed and actual behaviors under varying initial conditions, rather than a coincidence of a single chaotic trajectory at a given initial condition.

In complex dynamics, the study of deterministic chaos is concerned with the dynamics under varying initial conditions. However, the embrace of artificial chaos is often concerned with a good performance in a single chaotic trajectory. For avoiding machine learning pitfalls and misleading conclusions, our results indicate that artificial chaos should be concerned with the dynamics under Type I or II initial conditions. The findings highlight that machine behaviors provide qualifications and quantifications for showing the quality of artificial chaos. Besides, a coincidence in trajectory-level dynamics such as chaotic trajectories and a topology of a chaotic attractor is incapable of showing the relationship between an original and an artificial systems. However, machine behaviors provide information about the recurrence of arbitrarily small errors and the impact of the errors on an artificial chaos.

Chapter 6

Conclusions and new directions

In this thesis, dynamic pricing is modeled from dynamical systems' perspective and analyzed by nonlinear time series analysis. The focus is on a rational route to apparent randomness by a hypothetical model and a reconstruction of on-demand attractor. When dynamic pricing meets complex dynamics and machine learning, the sensitive dependence on initial conditions is compared between deterministic and artificial chaos.

6.1 Conclusions

This thesis has bridged three research fields, dynamic pricing, deterministic chaos, and machine learning methods that synthesize a mimetic trajectory for mimicking deterministic chaos. A hypothetical model has been proposed for justifying dynamics pricing from dynamical systems' perspectives (Fig. 1.1). A rational route contributes to uncertain demand by nonlinear interactions between consumers and a seller (Chapter 3). An on-demand attractor has been reconstructed for confirming the existence of a rational route in a ride-sharing market (Fig. 1.1). The attractor satisfies period-7 limit cycle oscillations. The reconstruction is based on recurrence plots and Pareto optimality by accumulating arrivals of transactions. Moreover, machine behaviors have been studied

for showing a gap between an original and an artificial systems (Fig. 1.1). Three types of initial conditions, including original trajectories (Type I), initial point (Type II), and initial network states (Type III), are identified. The sensitive dependence on Type I and II initial conditions is analyzed by conducting experiments that collect machine behaviors (Chapter 5). We condense the achievements of this work in the following sections.

6.1.1 Stochastic demand and border collision bifurcations

As explained in Chapters 3 and 4, demand dynamics poses a unique challenge in modeling dynamic pricing problems. In a theoretical setting, we show that nonlinear equations with a sine and a quadratic terms could contribute to volatile demand (Chapter 3). The results justify dynamic pricing strategy being a hedge against volatility. Besides, those nonlinear equations form a rational route to apparent randomness. The findings agree with Hu et al. [175] and Rump and Stidham [319] and indicate that consumers' nonlinear adaptation of price expectations could cause irregular demand (Chapter 3).

We emphasize the importance of identifying demand dynamics for practical dynamic pricing problems. The interactions among price, demand, and supply bring about irregular price expectations, thus contributing to unpredictability of demand. However, the unpredictability is due to the inaccuracy in initial conditions, rather than exogenous forces of a market. The inaccuracy could due to an incapacity to know the parameters that quantify a demand function [232], an incapacity to obtain a demand function that a market underlies [191], or a misspecification of a demand function [40].

We observe border collision bifurcations in the analytical demand mode (Chapter 3) and the time series of on-demand attractor (Chapter 4). den Boer and Keskin [102] introduce a piecewise continuous demand function. Their results show that the ignorance of discontinuity in demand can cause revenue losses. Hu et al. [175] use a piecewise continuous demand function to model consumers' reference price, thus observing border collision bifurcations. By contrast, the demand model we consider allows discrete price choices. The discontinuities result from a piecewise continuous demand function and optimizations together. We show that border collision bifurcations can emerge from

demand fluctuations (Chapter 3) and can be evidenced by irregularity in limit cycle oscillations (Chapter 4). The reconstructed on-demand attractor further provides real-life evidence of an occurrence of border collision bifurcations. Our analytics emphasize the importance of the understanding of demand functions, in particular, the consideration of discontinuities in the modeling of demand for avoiding revenue losses.

6.1.2 Recurrence-based attractor reconstruction

Based on recurrence plots and their quantifications, we propose a new approach to reconstruct an attractor from a univariate time series (Chapter 4). The approach explores the parameters of recurrence plots while exploiting the determinisms and the trapping time that are derived from recurrence plots. Pareto optimality allows the simultaneously exploring and exploiting and aims for finding optimal parameters for attractor reconstructions. The recurrence-based attractor reconstruction provides a tool to identify demand dynamics. Also, the new reconstruction improves the applicability of recurrence plots related to a signal contaminated with noise or nonstationarity.

6.1.3 Machine behaviors

Machine learning methods seem to have a great potential to realize a mode-free analysis of deterministic chaos [293]. Indeed, we observe that an artificial system is capable of synthesizing a mimetic trajectory that coincides with a chaotic trajectory of an original system (Chapter 5). Under the coincidence, the mimetic trajectory approaches the chaotic trajectory within arbitrarily small errors. The coincidence can be extended in phase space of an attractor and in that of a return map as well (Chapter 5). However, differences are identified between an original and an artificial systems as initial conditions are varied. This indicates that the existence of arbitrarily small errors is incapable of showing the recurrence of those errors under varying initial conditions. However, machine behaviors reflect the nonlinear dynamics of an artificial system. They provide insights into how those errors evolve by comparing the supposed and the actual dynamics of artificial chaos.

The study opens a new way to show artificial chaos through behaviors under varying initial conditions, instead of a coincidence in trajectories. For avoiding machine learning pitfalls, an artificial system should be performed under varying initial conditions and be compared with the sensitive dependence on initial conditions of an original system. The findings suggest that for artificial chaos, showing its sensitive dependence on initial conditions is as important as showing the coincidence of mimetic trajectories in phase space or return maps.

6.2 Managerial implications

We have drawn two main conclusions (Fig. 1.1). (1) Deterministic dynamics can be a constituent part of irregular demand. (2) The reliability of machine learning methods in mimicking deterministic chaos depends on their sensitive dependence on initial conditions, rather than a coincidence of a single chaotic trajectory or a single trajectory-based measure. In the following, we address what the conclusions imply in the sense of practical actions of agents in a market with irregular demand.

For a price maker, an irregular pricing strategy is optimal responding to irregular demand that underlies deterministic dynamics. Under border collision bifurcations, it is optimal to make the periodicity of a pricing strategy irregular. For example, a price maker can use two different frequencies to switch between a high and a low prices. Those two frequencies are relatively prime to each other.

On the other hand, machine learning methods are applied in addressing practical pricing problems [59, 157, 224, 253, 338, 417]. However, we observe that novel behavioral patterns occur in machine behavior. The observations indicate that an artificial system could mislead conclusions. For example, we observe an abrupt change in the amplitude of a mimetic trajectory (evolving with bursts, Chapter 5). The abrupt changes, however, are unrelated to the true dynamics that the inputted data underly.

For a price maker, the accuracy and the reliability of demand predictions are the main concerns. Three solutions exist to examine the accuracy and the reliability of

predictions that machine learning methods make. They are (A) a change of Type I initial conditions, (B) a change of Type II initial conditions, and (C) a use of another machine learning method. Here, (A) and (B) are related to the use of machine behaviors to validate predictions. A machine learning method for demand predictions can utilize different data sets (A) that come from an identical market to train its parameters, the results are then compared for validating the reliability of the method. In case of limited data, for example, a unique data set, an artificial system can be fed with the unique data. However, two or more predictions can be made by allowing the artificial system initialized from two or more points (B). Those points are from a small neighborhood of a target point. Different predictions are then compared for a cross-validation. In addition, different machine learning methods can be applied on an identical data set for a cross-validation of predictions to avoid pitfalls.

Discontinuity causes a new type of uncertainty in demand (Chapters 3 and 4), evidenced by border collision bifurcations. An ignorance of uncertain demand causes a policy maker out of a control of public welfare [84]. It is necessary to take discontinuity into considerations for the policy maker of governments. Besides, irregular pricing strategies adapt the sales price according to consumers' price expectations, thus being benefit to consumers' welfare as well .

6.3 New directions

This thesis draws conclusions and implications to bridge dynamic pricing, deterministic chaos, and artificial chaos. In the following, we recommend future work to gain guidelines for an improvement of dynamic pricing problems and for the reliability of artificial chaos.

1. As shown in this thesis, the dynamics of demand can be deterministic. It is important to propose a new optimization method to address the maximization of revenue solely based on an attractor. Current optimizations are based on known equations or statistics to harvest averaged revenue. An attractor can be reconstructed from a time series with a high accuracy. However, an equation that describes the evolu-

tion of the reconstructed attractor remains elusive. An attractor-based optimization method could address an optimal price by the topology of an attractor without any prior knowledge of the governing equation. For example, a method would use the deterministic structures of an attractor to harvest optimal revenue.

2. An alternative research direction could identify the governing equations of the on-demand attractor (Chapter 4). If an equation was identified, then contemporary optimizations could be applied to improve a pricing decision. Besides, a mode-free framework could be used to approximate the governing equation of an attractor. An attractor is with an invariant topology in phase space. A dynamic template of an attractor could be encoded. Regressions then could be applied to decode a template to a trajectory. The encoding and decoding framework would define an equation that approximates the attractor.

3. We have shown that recurrence plots and their quantifications increase the quality of attractor reconstructions. As we discuss in Chapter 4, another two or more than two recurrence quantifications would be used as the objective of Pareto optimality. Also, recurrence-based attractor reconstruction could be applied to other real-life scenarios for showing nonlinear dynamics of a signal.

4. Our study of machine behaviors is based on deterministic chaos without noise. It would be interesting to examine how artificial systems behave in mimicking deterministic chaos that is contaminated by noise. For example, experiments could be designed to collect machine behaviors as original trajectories are contaminated by noise. A physics-informed neural network is robust to a contamination of substantial noise [305, 307]. The behavior of the physics-informed neural network could be examined by a contamination of different levels of noise under varying Type I and II initial conditions. It would also be interested to conduct surrogate data between deterministic chaos contaminated by noise and artificial chaos in mimicking that. The null hypothesis could be related to a preservation of nonlinearity by an artificial system under a contamination of noise.

5. Trajectory-centric behaviors have been observed from artificial systems that satisfy universal approximation theorems. It is worth proposing an artificial system that universally approaches an original attractor within arbitrary small errors. The artificial system targets a chaotic attractor, rather than a chaotic trajectory. Similar to **2**, an artificial system could be based on the encoding and decoding framework.

6. We study dynamic pricing problems based on maximizing revenue of a single product within a single selling period (Chapter 3). It would be interesting to look at how discontinuities affect dynamic pricing problems for multiple products within multiple selling periods. We did some work for a single produce within multiple selling periods in Appendix B. Besides, our symbolic dynamics is analyzed based on an identification of critical points (Chapter 5), which could be a diÿcult task for some original systems. It would be interesting to investigate the climate of symbolic dynamics related to order patterns. An order pattern is based on comparing values of a time series, which has no need of critical points. We advanced some work related to order patterns in Appendix C.

Bibliography

[1] D. M. Abrams, H. A. Yaple, and R. J. Wiener. Dynamics of social group competition: modeling the decline of religious aÿliation. *Physical Review Letters*, 107(8): 088701, 2011.

[2] G. Abrate, G. Fraquelli, and G. Viglia. Dynamic pricing strategies: Evidence from european hotels. *International Journal of Hospitality Management*, 31(1):160–168, 2012.

[3] J. Aguirre, R. L. Viana, and M. A. Sanjuán. Fractal structures in nonlinear dynamics. *Reviews of Modern Physics*, 81(1):333, 2009.

[4] A. Ajorlou, A. Jadbabaie, and A. Kakhbod. Dynamic pricing in social networks: The word-of-mouth effect. *Management Science*, 64(2):971–979, 2018.

[5] J. Amigó. *Permutation complexity in dynamical systems*. Springer-Verlag, Berlin, 2010.

[6] J. Amigó, S. Zambrano, and M. A. Sanjuán. Combinatorial detection of determinism in noisy time series. *EPL (Europhysics Letters)*, 83(6):60005, 2008.

[7] J. M. Amigó, L. Kocarev, and J. Szczepanski. Order patterns and chaos. *Physics Letters A*, 355(1):27–31, 2006.

[8] J. M. Amigó, S. Zambrano, and M. A. Sanjuán. True and false forbidden patterns in deterministic and random dynamics. *EPL (Europhysics Letters)*, 79(5):50001, 2007.

[9] J. M. Amigó, S. Zambrano, and M. A. Sanjuán. Detecting determinism in time series with ordinal patterns: a comparative study. *International Journal of Bifurcation and Chaos*, 20(09):2915–2924, 2010.

[10] M. Anufriev, D. Radi, and F. Tramontana. Some reflections on past and future of nonlinear dynamics in economics and finance. *Decisions in Economics and Finance*, 41(2):91–118, 2018.

[11] M. Anufriev, L. Gardini, and D. Radi. Chaos, border collisions and stylized empirical facts in an asset pricing model with heterogeneous agents. *Nonlinear Dynamics*, 102:993–1017, 2020.

[12] V. F. Araman and R. Caldentey. Dynamic pricing for nonperishable products with demand learning. *Operations research*, 57(5):1169–1188, 2009.

[13] A. Arenas, A. Díaz-Guilera, J. Kurths, Y. Moreno, and C. Zhou. Synchronization in complex networks. *Physics reports*, 469(3):93–153, 2008.

[14] A. Avila and I. Mezić. Data-driven analysis and forecasting of highway traÿc dynamics. *Nature communications*, 11(1):1–16, 2020.

[15] Y. Aviv and A. Pazgal. Pricing of short life-cycle products through active learning. *Working paper,Washington University, St. Louis*, pages 1–32, 2002.

[16] Y. Aviv and A. Pazgal. A partially observed markov decision process for dynamic pricing. *Management Science*, 51(9):1400–1416, 2005.

[17] V. Avrutin and M. Schanz. On multi-parametric bifurcations in a scalar piecewise-linear map. *Nonlinearity*, 19(3):531, 2006.

[18] S. R. Balseiro, D. B. Brown, and C. Chen. Dynamic pricing of relocating resources in large networks. *Management Science*, 67(7):4075–4094, 2021.

[19] G.-Y. Ban and N. B. Keskin. Personalized dynamic pricing with machine learning: High-dimensional features and heterogeneous elasticity. *Management Science*, 2021.

[20] C. Bandt and B. Pompe. Permutation entropy: a natural complexity measure for time series. *Physical Review Letters*, 88(17):174102, 2002.

[21] S. Banerjee, C. Riquelme, and R. Johari. Pricing in ride-share platforms: A queueing-theoretic approach. *Available at SSRN 2568258*, 2015.

[22] M. Bardoscia, S. Battiston, F. Caccioli, and G. Caldarelli. Pathways towards instability in financial networks. *Nature Communications*, 8:14416, 2017.

[23] M. Barreiro, A. C. Marti, and C. Masoller. Inferring long memory processes in the climate network via ordinal pattern analysis. *Chaos*, 21(1):013101, 2011.

[24] S. Battiston, J. D. Farmer, A. Flache, D. Garlaschelli, A. G. Haldane, H. Heesterbeek, C. Hommes, C. Jaeger, R. May, and M. Scheffer. Complexity theory and financial regulation. *Science*, 351(6275):818–819, 2016.

[25] P. Bauer, A. Thorpe, and G. Brunet. The quiet revolution of numerical weather prediction. *Nature*, 525(7567):47–55, 2015.

[26] L. Bauwens and E. Otranto. Nonlinearities and regimes in conditional correlations with different dynamics. *Journal of Econometrics*, 217(2):496–522, 2020.

[27] A. G. Baydin, B. A. Pearlmutter, A. A. Radul, and J. M. Siskind. Automatic differentiation in machine learning: a survey. *Journal of Marchine Learning Research*, 18:1–43, 2018.

[28] R. Bellman. On the theory of dynamic programming. *Proceedings of the National Academy of Sciences of the United States of America*, 38(8):716, 1952.

[29] R. Bellman. Dynamic programming. *Science*, 153(3731):34–37, 1966.

[30] A. Belloni and V. Chernozhukov. Least squares after model selection in high-dimensional sparse models. *Bernoulli*, 19(2):521–547, 2013.

[31] S. Ben-David, P. Hrubeš, S. Moran, A. Shpilka, and A. Yehudayoff. Learnability can be undecidable. *Nature Machine Intelligence*, 1(1):44, 2019.

[32] R. Benzi, A. Sutera, and A. Vulpiani. The mechanism of stochastic resonance. *Journal of Physics A: mathematical and general*, 14(11):L453, 1981.

[33] R. Benzi, G. Parisi, A. Sutera, and A. Vulpiani. Stochastic resonance in climatic change. *Tellus*, 34(1):10–16, 1982.

[34] M. Bernardo, C. Budd, A. R. Champneys, and P. Kowalczyk. *Piecewise-smooth dynamical systems: theory and applications*, volume 163. Springer Science & Business Media, 2008.

[35] D. Bertsimas and V. V. Mišić. Decomposable markov decision processes: A fluid optimization approach. *Operations Research*, 64(6):1537–1555, 2016.

[36] O. Besbes and I. Lobel. Intertemporal price discrimination: Structure and computation of optimal policies. *Management Science*, 61(1):92–110, 2015.

[37] O. Besbes and C. Maglaras. Dynamic pricing with financial milestones: Feedback-form policies. *Management Science*, 58(9):1715–1731, 2012.

[38] O. Besbes and D. Sauré. Product assortment and price competition under multinomial logit demand. *Production and Operations Management*, 25(1):114–127, 2016.

[39] O. Besbes and A. Zeevi. Dynamic pricing without knowing the demand function: Risk bounds and near-optimal algorithms. *Operations Research*, 57(6):1407–1420, 2009.

[40] O. Besbes and A. Zeevi. On the (surprising) suÿciency of linear models for dynamic pricing with demand learning. *Management Science*, 61(4):723–739, 2015.

[41] O. Besbes, D. A. Iancu, and N. Trichakis. Dynamic pricing under debt: Spiraling distortions and eÿciency losses. *Management Science*, 64(10):4572–4589, 2018.

[42] O. Besbes, F. Castro, and I. Lobel. Surge pricing and its spatial supply response. *Management Science*, 67(3):1350–1367, 2021.

[43] J. Bezanson, A. Edelman, S. Karpinski, and V. B. Shah. Julia: A fresh approach to numerical computing. *SIAM review*, 59(1):65–98, 2017.

[44] K. Bimpikis, O. Candogan, and D. Saban. Spatial pricing in ride-sharing networks. *Operations Research*, 67(3):744–769, 2019.

[45] G. Bitran and R. Caldentey. An overview of pricing models for revenue management. *Manufacturing & Service Operations Management*, 5(3):203–229, 2003.

[46] G. R. Bitran and S. V. Mondschein. Periodic pricing of seasonal products in retailing. *Management Science*, 43(1):64–79, 1997.

[47] R. Bowen. ω-limit sets for axiom a diffeomorphisms. *Journal of differential equations*, 18(2):333–339, 1975.

[48] E. Bozzo, R. Carniel, and D. Fasino. Relationship between singular spectrum analysis and fourier analysis: Theory and application to the monitoring of volcanic activity. *Computers & Mathematics with Applications*, 60(3):812–820, 2010.

[49] T. Braun, V. R. Unni, R. Sujith, J. Kurths, and N. Marwan. Detection of dynamical regime transitions with lacunarity as a multiscale recurrence quantification measure. *Nonlinear Dynamics*, pages 1–19, 2021.

[50] P. G. Breen, C. N. Foley, T. Boekholt, and S. P. Zwart. Newton versus the machine: solving the chaotic three-body problem using deep neural networks. *Monthly Notices of the Royal Astronomical Society*, 494(2):2465–2470, 2020.

[51] W. A. Brock and C. H. Hommes. A rational route to randomness. *Econometrica: Journal of the Econometric Society*, 65(5):1059–1095, 1997.

[52] J. Broder and P. Rusmevichientong. Dynamic pricing under a general parametric choice model. *Operations Research*, 60(4):965–980, 2012.

[53] S. L. Brunton, J. L. Proctor, and J. N. Kutz. Discovering governing equations from data by sparse identification of nonlinear dynamical systems. *Proceedings of the National Academy of Sciences*, 113(15):3932–3937, 2016.

[54] S. L. Brunton, B. W. Brunton, J. L. Proctor, E. Kaiser, and J. N. Kutz. Chaos as an intermittently forced linear system. *Nature Communications*, 8(1):19, 2017.

[55] Budget-additive functions. Submodular set function, 2021. URL `https://en.wikipedia.org/wiki/Submodular_set_function`. Accessed 2021-07-04.

[56] G. Byrne, R. Gilmore, and C. Letellier. Distinguishing between folding and tearing mechanisms in strange attractors. *Physical Review E*, 70(5):056214, 2004.

[57] M. V. Caballero-Pintado, M. Matilla-García, and M. Ruiz Marín. Symbolic recurrence plots to analyze dynamical systems. *Chaos*, 28(6):063112, 2018.

[58] G. P. Cachon, K. M. Daniels, and R. Lobel. The role of surge pricing on a service platform with self-scheduling capacity. *Manufacturing & Service Operations Management*, 19(3):368–384, 2017.

[59] E. Calvano, G. Calzolari, V. Denicolo, and S. Pastorello. Artificial intelligence, algorithmic pricing, and collusion. *American Economic Review*, 110(10):3267–97, 2020.

[60] L. Cao. Practical method for determining the minimum embedding dimension of a scalar time series. *Physica D: Nonlinear Phenomena*, 110(1-2):43–50, 1997.

[61] P. Cao, N. Zhao, and J. Wu. Dynamic pricing with bayesian demand learning and reference price effect. *European Journal of Operational Research*, 279(2):540–556, 2019.

[62] L. C. Carpi, P. M. Saco, and O. Rosso. Missing ordinal patterns in correlated noises. *Physica A: Statistical Mechanics and its Applications*, 389(10):2020–2029, 2010.

[63] K. Champion, B. Lusch, J. N. Kutz, and S. L. Brunton. Data-driven discovery of coordinates and governing equations. *Proceedings of the National Academy of Sciences*, 116(45):22445–22451, 2019.

[64] A. Chattopadhyay, P. Hassanzadeh, and D. Subramanian. Data-driven predictions of a multiscale Lorenz 96 chaotic system using machine-learning methods: reservoir computing, artificial neural network, and long short-term memory network. *Nonlinear Processes in Geophysics*, 27(3):373–389, 2020.

[65] R. E. Chatwin. Continuous-time airline overbooking with time-dependent fares and refunds. *Transportation Science*, 33(2):182–191, 1999.

[66] B. Chen, J. Huang, and J. Ji. Control of flexible single-link manipulators having duÿng oscillator dynamics. *Mechanical Systems and Signal Processing*, 121:44–57, 2019.

[67] K. Chen, Y. Zha, L. C. Alwan, and L. Zhang. Dynamic pricing in the presence of reference price effect and consumer strategic behaviour. *International Journal of Production Research*, 58(2):546–561, 2020.

[68] L. Chen, A. Mislove, and C. Wilson. Peeking beneath the hood of uber. In *Proceedings of the 2015 internet measurement conference*, pages 495–508, 2015.

[69] L. Chen, A. Mislove, and C. Wilson. An empirical analysis of algorithmic pricing on amazon marketplace. In *Proceedings of the 25th international conference on World Wide Web*, pages 1339–1349, 2016.

[70] M. Chen and Z.-L. Chen. Recent developments in dynamic pricing research: multiple products, competition, and limited demand information. *Production and Operations Management*, 24(5):704–731, 2015.

[71] M. Chen and Z.-L. Chen. Robust dynamic pricing with two substitutable products. *Manufacturing & Service Operations Management*, 20(2):249–268, 2017.

[72] M. K. Chen and M. Sheldon. Dynamic pricing in a labor market: Surge pricing and flexible work on the uber platform. *Ec*, 455(10.1145):2940716–2940798, 2016.

[73] N. Chen and G. Gallego. Welfare analysis of dynamic pricing. *Management Science*, 65(1):139–151, 2019.

[74] N. Chen and G. Gallego. Nonparametric pricing analytics with customer covariates. *Operations Research*, 69(3):974–984, 2021.

[75] Q. Chen, S. Jasin, and I. Duenyas. Nonparametric self-adjusting control for joint learning and optimization of multiproduct pricing with finite resource capacity. *Mathematics of Operations Research*, 44(2):601–631, 2019.

[76] R. T. Chen, Y. Rubanova, J. Bettencourt, and D. K. Duvenaud. Neural ordinary differential equations. *Advances in neural information processing systems*, 31, 2018.

[77] X. Chen, P. Hu, and Z. Hu. Eÿcien t algorithms for the dynamic pricing problem with reference price effect. *Management Science*, 63(12):4389–4408, 2016.

[78] X. Chen, P. Hu, S. Shum, and Y. Zhang. Dynamic stochastic inventory management with reference price effects. *Oper. Res.*, 64(6):1529–1536, 2016.

[79] X. Chen, P. Hu, and Z. Hu. Eÿcien t algorithms for the dynamic pricing problem with reference price effect. *Management Science*, 63(12):4389–4408, 2017.

[80] X. Chen, T. Weng, H. Yang, C. Gu, J. Zhang, and M. Small. Mapping topological characteristics of dynamical systems into neural networks: A reservoir computing approach. *Physical Review E*, 102(3):033314, 2020.

[81] X. Chen, Z. Owen, C. Pixton, and D. Simchi-Levi. A statistical learning approach to personalization in revenue management. *Management Science*, 2021.

[82] Y. Chen and M. Hu. Pricing and matching with forward-looking buyers and sellers. *Manufacturing & Service Operations Management*, 22(4):717–734, 2020.

[83] W. C. Cheung, D. Simchi-Levi, and H. Wang. Dynamic pricing and demand learning with limited price experimentation. *Operations Research*, 65(6):1722–1731, 2017.

[84] M. C. Cohen, R. Lobel, and G. Perakis. The impact of demand uncertainty on consumer subsidies for green technology adoption. *Management Science*, 62(5): 1235–1258, 2016.

[85] M. C. Cohen, N.-H. Z. Leung, K. Panchamgam, G. Perakis, and A. Smith. The impact of linear optimization on promotion planning. *Operations Research*, 65(2): 446–468, 2017.

[86] M. C. Cohen, R. Lobel, and G. Perakis. Dynamic pricing through data sampling. *Production and Operations Management*, 27(6):1074–1088, 2018.

[87] M. C. Cohen, S. Gupta, J. J. Kalas, and G. Perakis. An eÿcien t algorithm for dynamic pricing using a graphical representation. *Production and Operations Management*, 29(10):2326–2349, 2020.

[88] M. C. Cohen, J. J. Kalas, and G. Perakis. Promotion optimization for multiple items in supermarkets. *Management Science*, 67(4):2340–2364, 2021.

[89] A. Corcos, J.-P. Eckmann, A. Malaspinas, Y. Malevergne, and D. Sornette. Imitation and contrarian behaviour: hyperbolic bubbles, crashes and chaos. *Quantitative Finance*, 2:264–281, 2002.

[90] K. Cosguner, T. Y. Chan, and P. B. S. Seetharaman. Dynamic pricing in a distribution channel in the presence of switching costs. *Management Science*, 64(3): 1212–1229, 2018.

[91] B. Coulter and S. Krishnamoorthy. Pricing strategies with reference effects in competitive industries. *International transactions in operational Research*, 21(2): 263–274, 2014.

[92] P. Cramton, R. R. Geddes, and A. Ockenfels. Set road charges in real time to ease traÿc. *Nature*, 560:23–26, 2018.

[93] J. Croft, C. Makrides, M. Li, A. Petrov, B. Kendrick, N. Balakrishnan, and S. Kotochigova. Universality and chaoticity in ultracold K+ KRb chemical reactions. *Nature Communications*, 8(1):1–8, 2017.

[94] Y. Cui, A. Y. Orhun, and I. Duenyas. How price dispersion changes when upgrades are introduced: Theory and empirical evidence from the airline industry. *Management Science*, 65(8):3835–3852, 2019.

[95] G. Cybenko. Approximation by superpositions of a sigmoidal function. *Mathematics of Control, Signals and Systems*, 2(4):303–314, 1989.

[96] H. Dankowicz and A. B. Nordmark. On the origin and bifurcations of stick-slip oscillations. *Physica D: Nonlinear Phenomena*, 136(3-4):280–302, 2000.

[97] G. Datseris. Dynamicalsystems.jl: A julia software library for chaos and nonlinear dynamics. *Journal of Open Source Software*, 3(23):598, mar 2018. URL `https://doi.org/10.21105/joss.00598`.

[98] A. M. Davis, V. Gaur, and D. Kim. Consumer learning from own experience and social information: An experimental study. *Management Science*, 67(5):2924–2943, 2021.

[99] D. P. De Farias and B. Van Roy. The linear programming approach to approximate dynamic programming. *Operations research*, 51(6):850–865, 2003.

[100] A. V. den Boer. Dynamic pricing and learning: historical origins, current research, and new directions. *Surveys in operations research and management science*, 20 (1):1–18, 2015.

[101] A. V. Den Boer. Tracking the market: Dynamic pricing and learning in a changing environment. *European journal of operational research*, 247(3):914–927, 2015.

[102] A. V. den Boer and N. B. Keskin. Discontinuous demand functions: estimation and pricing. *Management Science*, 66(10):4516–4534, 2020.

[103] A. V. den Boer and N. B. Keskin. Dynamic pricing with demand learning and reference effects. *Management Science, forthcoming, Available at SSRN: doi:10.2139/ssrn.3092745*, April 19, 2021.

[104] A. V. den Boer and B. Zwart. Simultaneously learning and optimizing using controlled variance pricing. *Management science*, 60(3):770–783, 2014.

[105] A. V. den Boer and B. Zwart. Dynamic pricing and learning with finite inventories. *Operations research*, 63(4):965–978, 2015.

[106] R. L. Devaney. *An Introduction to Chaotic Dynamical Systems*. Westview press, 2008.

[107] T. Devolder, D. Rontani, S. Petit-Watelot, K. Bouzehouane, S. Andrieu, J. Létang, M.-W. Yoo, J.-P. Adam, C. Chappert, S. Girod, V. Cros, M. Sciamanna, and J.-V. Kim. Chaos in magnetic nanocontact vortex oscillators. *Phys. Rev. Lett.*, 123: 147701, Oct 2019.

[108] M. Dinerstein, L. Einav, J. Levin, and N. Sundaresan. Consumer price search and platform design in internet commerce. *American Economic Review*, 108(7): 1820–59, 2018.

[109] R. Donner, U. Hinrichs, and B. Scholz-Reiter. Symbolic recurrence plots: A new quantitative framework for performance analysis of manufacturing networks. *The European Physical Journal Special Topics*, 164(1):85–104, 2008.

[110] B. M. Douglas Lind. *An Introduction to Symbolic Dynamics and Coding*. Cambridge Mathematical Library. Cambridge University Press, 2 edition, 2021. ISBN 9781108820288, 9781108899727.

[111] C. Du, W. L. Cooper, and Z. Wang. Optimal pricing for a multinomial logit choice model with network effects. *Operations Research*, 64(2):441–455, 2016.

[112] J. Dushoff, J. B. Plotkin, S. A. Levin, and D. J. Earn. Dynamical resonance can account for seasonality of influenza epidemics. *Proceedings of the National Academy of Sciences*, 101(48):16915–16916, 2004.

[113] D. Dutta and J. Bhattacharjee. Period adding bifurcation in a logistic map with memory. *Physica D: Nonlinear Phenomena*, 237(23):3153–3158, 2008.

[114] G. Dutta and K. Mitra. A literature review on dynamic pricing of electricity. *Journal of the Operational Research Society*, 68(10):1131–1145, 2017.

[115] C.-Y. Dye, C.-T. Yang, and C.-C. Wu. Joint dynamic pricing and preservation technology investment for an integrated supply chain with reference price effects. *Journal of the operational research society*, pages 1–14, 2017.

[116] J.-P. Eckmann and D. Ruelle. Ergodic theory of chaos and strange attractors. In *The Theory of Chaotic Attractors*, pages 273–312. Springer, 1985.

[117] J.-P. Eckmann, S. O. Kamphorst, and D. Ruelle. Recurrence plots of dynamical systems. *Europhys. Lett.*, 5:973–977, 1987.

[118] J. Eliasson et al. The stockholm congestion charges: an overview. *Stockholm: Centre for Transport Studies CTS Working Paper*, 7:42, 2014.

[119] W. Elmaghraby and P. Keskinocak. Dynamic pricing in the presence of inventory considerations: Research overview, current practices, and future directions. *Management science*, 49(10):1287–1309, 2003.

[120] V. F. Farias and B. Van Roy. Dynamic pricing with a prior on market response. *Operations Research*, 58(1):16–29, 2010.

[121] M. Feigenbaum. Universality in complex discrete dynamics. *Los Alamos Theoretical Division Annual Report*, 1976:1976, 1975.

[122] M. J. Feigenbaum. Quantitative universality for a class of nonlinear transformations. *Journal of statistical physics*, 19(1):25–52, 1978.

[123] J. Feng, X. Li, and X. Zhang. Online product reviews-triggered dynamic pricing: Theory and evidence. *Information Systems Research*, 30(4):1107–1123, 2019.

[124] Y. Feng and B. Xiao. A continuous-time yield management model with multiple prices and reversible price changes. *Management science*, 46(5):644–657, 2000.

[125] Y. Feng and B. Xiao. Integration of pricing and capacity allocation for perishable products. *European Journal of Operational Research*, 168(1):17–34, 2006.

[126] K. J. Ferreira, B. H. A. Lee, and D. Simchi-Levi. Analytics for an online retailer: Demand forecasting and price optimization. *Manufacturing & Service Operations Management*, 18(1):69–88, 2016.

[127] K. J. Ferreira, D. Simchi-Levi, and H. Wang. Online network revenue management using thompson sampling. *Operations research*, 66(6):1586–1602, 2018.

[128] U. Feudel and C. Grebogi. Multistability and the control of complexity. *Chaos: An Interdisciplinary Journal of Nonlinear Science*, 7(4):597–604, 1997.

[129] G. Fibich, A. Gavious, and O. Lowengart. Explicit solutions of optimization models and differential games with nonsmooth (asymmetric) reference-price effects. *Oper. Res.*, 51(5):721–734, 2003.

[130] M. Fisher, S. Gallino, and J. Li. Competition-based dynamic pricing in online retailing: A methodology validated with field experiments. *Management Science*, 64(6):2496–2514, 2017.

[131] R. FitzHugh. Impulses and physiological states in theoretical models of nerve membrane. *Biophysical journal*, 1(6):445–466, 1961.

[132] B. Futter, V. Avrutin, and M. Schanz. The discontinuous flat top tent map and the nested period incrementing bifurcation structure. *Chaos, Solitons & Fractals*, 45(4):465 – 482, 2012.

[133] G. Gallego and G. Van Ryzin. Optimal dynamic pricing of inventories with stochastic demand over finite horizons. *Management science*, 40(8):999–1020, 1994.

[134] G. Gallego and G. Van Ryzin. A multiproduct dynamic pricing problem and its applications to network yield management. *Operations research*, 45(1):24–41, 1997.

[135] G. Gallego and R. Wang. Multiproduct price optimization and competition under the nested logit model with product-differentiated price sensitivities. *Operations Research*, 62(2):450–461, 2014.

[136] L. Gammaitoni, P. Hänggi, P. Jung, and F. Marchesoni. Stochastic resonance. *Reviews of modern physics*, 70(1):223, 1998.

[137] E. Garbarino and O. F. Lee. Dynamic pricing in internet retail: effects on consumer trust. *Psychology & Marketing*, 20(6):495–513, 2003.

[138] L. Gardini, V. Avrutin, and I. Sushko. Codimension-2 border collision bifurcations in one-dimensional discontinuous piecewise smooth maps. *Int. J. Bifurcation Chaos*, 24(02):1450024, 2014.

[139] L. Gardini, I. Sushko, and K. Matsuyama. 2d discontinuous piecewise linear map: Emergence of fashion cycles. *Chaos: An Interdisciplinary Journal of Nonlinear Science*, 28(5):055917, 2018.

[140] A. Gershkov, B. Moldovanu, and P. Strack. Revenue-maximizing mechanisms with strategic customers and unknown, markovian demand. *Management Science*, 64 (5):2031–2046, 2018.

[141] C. Gibbs, D. Guttentag, U. Gretzel, L. Yao, and J. Morton. Use of dynamic pricing strategies by airbnb hosts. *International Journal of Contemporary Hospitality Management*, 2018.

[142] K. Giesecke, G. Liberali, H. Nazerzadeh, J. G. Shanthikumar, and C. P. Teo. Call for papers—management science—special issue on data-driven prescriptive analytics. *Management Science*, 64(6):2972–2972, 2018.

[143] R. Gilmore and M. Lefranc. *The Topology of Chaos*. John Wiley & Sons, Inc, 2011.

[144] N. Golrezaei, A. Javanmard, and V. Mirrokni. Dynamic incentive-aware learning: Robust pricing in contextual auctions. *Operations Research*, 69(1):297–314, 2021.

[145] I. Goodfellow, Y. Bengio, A. Courville, and Y. Bengio. *Deep learning*. MIT press Cambridge, 2016.

[146] B. Goswami, N. Boers, A. Rheinwalt, N. Marwan, J. Heitzig, S. F. Breitenbach, and J. Kurths. Abrupt transitions in time series with uncertainties. *Nature communications*, 9(1):1–10, 2018.

[147] G. A. Gottwald and I. Melbourne. Testing for chaos in deterministic systems with noise. *Physica D: Nonlinear Phenomena*, 212(1):100 – 110, 2005.

[148] A. Granados and G. Huguet. Gluing and grazing bifurcations in periodically forced 2-dimensional integrate-and-fire models. *Communications in Nonlinear Science and Numerical Simulation*, 2018.

[149] A. Granados, L. Alsedà, and M. Krupa. The period adding and incrementing bifurcations: from rotation theory to applications. *SIAM Rev.*, 59(2):225–292, 2017.

[150] P. Grassberger and I. Procaccia. Characterization of strange attractors. *Physical review letters*, 50(5):346, 1983.

[151] P. Grassberger, H. Kantz, and U. Moenig. On the symbolic dynamics of the hénon map. *Journal of Physics A: Mathematical and General*, 22(24):5217, 1989.

[152] C. Grebogi, S. M. Hammel, J. A. Yorke, and T. Sauer. Shadowing of physical trajectories in chaotic dynamics: Containment and refinement. *Physical Review Letters*, 65(13):1527, 1990.

[153] E. A. Greenleaf. The impact of reference price effects on the profitability of price promotions. *Marketing science*, 14(1):82–104, 1995.

[154] A. Griÿth, A. Pomerance, and D. J. Gauthier. Forecasting chaotic systems with very low connectivity reservoir computers. *Chaos: An Interdisciplinary Journal of Nonlinear Science*, 29(12):123108, 2019.

[155] L. Grigoryeva and J.-P. Ortega. Echo state networks are universal. *Neural Networks*, 108:495 – 508, 2018. ISSN 0893-6080.

[156] A. Groth. Visualization of coupling in time series by order recurrence plots. *Physical Review E*, 72(4):046220, 2005.

[157] S. Gu, B. Kelly, and D. Xiu. Empirical asset pricing via machine learning. *The Review of Financial Studies*, 33(5):2223–2273, 2020.

[158] A. Gualandi, J.-P. Avouac, S. Michel, and D. Faranda. The predictable chaos of slow earthquakes. *Science Advances*, 6(27):eaaz5548, 2020.

[159] J. Guckenheimer and P. Holmes. *Nonlinear oscillations, dynamical systems, and bifurcations of vector fields*, volume 42. Springer Science & Business Media, 2013.

[160] H. Guda and U. Subramanian. Your uber is arriving: Managing on-demand workers through surge pricing, forecast communication, and worker incentives. *Management Science*, 65(5):1995–2014, 2019.

[161] M. G. Güler, T. Bilgiç, and R. Güllü. Joint pricing and inventory control for additive demand models with reference effects. *Annals of Operations Research*, 226(1):255–276, 2015.

[162] Z. Guo and J. Ma. Dynamics and implications on a cooperative advertising model in the supply chain. *Communications in Nonlinear Science and Numerical Simulation*, 64:198–212, 2018.

[163] A. Haluszczynski and C. Räth. Good and bad predictions: Assessing and improving the replication of chaotic attractors by means of reservoir computing. *Chaos: An Interdisciplinary Journal of Nonlinear Science*, 29(10):103143, 2019.

[164] A. Haluszczynski, J. Aumeier, J. Herteux, and C. Räth. Reducing network size and improving prediction stability of reservoir computing. *Chaos: An Interdisciplinary Journal of Nonlinear Science*, 30(6):063136, 2020.

[165] P. Harsha and M. Dahleh. Optimal management and sizing of energy storage under dynamic pricing for the eÿcien t integration of renewable energy. *IEEE Trans. Power Syst.*, 30(3):1164–1181, 2015.

[166] A. Hart, J. Hook, and J. Dawes. Embedding and approximation theorems for echo state networks. *Neural Networks*, 128:234 – 247, 2020. ISSN 0893-6080.

[167] C. Haxholdt, E. R. Larsen, and A. van Ackere. Mode locking and chaos in a deterministic queueing model with feedback. *Management Science*, 49(6):816–830, 2003.

[168] R. Hegger, H. Kantz, and T. Schreiber. Practical implementation of nonlinear time series methods: The tisean package. *Chaos: An Interdisciplinary Journal of Nonlinear Science*, 9(2):413–435, 1999.

[169] M. Hénon. A two-dimensional mapping with a strange attractor. *Communications in Mathematical Physics*, 50:69–77, 1976.

[170] R. C. Hilborn et al. *Chaos and nonlinear dynamics: an introduction for scientists and engineers*. Oxford University Press on Demand, 2000.

[171] Y. Hirata. Recurrence plots for characterizing random dynamical systems. *Communications in Nonlinear Science and Numerical Simulation*, 94:105552, 2021.

[172] Y. Hirata and K. Aihara. Timing matters in foreign exchange markets. *Physica A: Statistical Mechanics and its Applications*, 391(3):760–766, 2012.

[173] T.-P. Hsieh and C.-Y. Dye. Optimal dynamic pricing for deteriorating items with reference price effects when inventories stimulate demand. *European Journal of Operational Research*, 262(1):136–150, 2017.

[174] Z. Hu. *Dynamic pricing with reference price effects*. PhD thesis, University of Illinois at Urbana-Champaign, 2015.

[175] Z. Hu, X. Chen, and P. Hu. Dynamic pricing with gain-seeking reference price effects. *Operations Research*, 64(1):150–157, 2016.

[176] Y. Huang, G. Kou, and Y. Peng. Nonlinear manifold learning for early warnings in financial markets. *European Journal of Operational Research*, 258(2):692–702, 2017.

[177] J. D. Hunter. Matplotlib: A 2d graphics environment. *Computing in Science & Engineering*, 9(3):90–95, 2007.

[178] Hyperparameter. Hyperparameter (machine learning), 2022. URL `https://en.wikipedia.org/wiki/Hyperparameter_(machine_learning)`. Accessed 2022-07-01.

[179] H. Jaeger and H. Haas. Harnessing nonlinearity: predicting chaotic systems and saving energy in wireless communication. *Science*, 304(5667):78–80, 2004.

[180] S. Jagabathula and P. Rusmevichientong. A nonparametric joint assortment and price choice model. *Management Science*, 63(9):3128–3145, 2017.

[181] P. Jain and S. Banerjee. Border-collision bifurcations in one-dimensional discontinuous maps. *Int. J. Bifurcation Chaos*, 13(11):3341–3351, 2003.

[182] P. L. Joskow and C. D. Wolfram. Dynamic pricing of electricity. *American Economic Review*, 102(3):381–85, 2012.

[183] D. Kahneman, Daniel and A. Tversky. Prospect theory: An analysis of decision under risk. *Econometrica*, 47(2):263–292, 1979.

[184] K. Kalyanam and T. S. Shively. Estimating irregular pricing effects: A stochastic spline regression approach. *Journal of Marketing Research*, 35(1):16–29, 1998.

[185] G. Kalyanaram and R. S. Winer. Empirical generalizations from reference price research. *Marketing science*, 14(3):G161–G169, 1995.

[186] E. Kamenica, S. Mullainathan, and R. Thaler. Helping consumers know themselves. *American Economic Review*, 101(3):417–22, 2011.

[187] H. Kantz and L. Jaeger. Improved cost functions for modelling of noisy chaotic time series. *Physica D: Nonlinear Phenomena*, 109(1):59–69, 1997.

[188] H. Kantz and T. Schreiber. *Nonlinear time series analysis*, volume 7. Cambridge university press, 2004.

[189] P. Kasthuri, I. Pavithran, A. Krishnan, S. A. Pawar, R. Sujith, R. Gejji, W. Anderson, N. Marwan, and J. Kurths. Recurrence analysis of slow–fast systems. *Chaos: An Interdisciplinary Journal of Nonlinear Science*, 30(6):063152, 2020.

[190] C. Kemper and C. Breuer. How eÿcien t is dynamic pricing for sport events? designing a dynamic pricing model for bayern munich. *International Journal of Sport Finance*, 11(1):4–25, 2016.

[191] N. B. Keskin and A. Zeevi. Dynamic pricing with an unknown demand model: Asymptotically optimal semi-myopic policies. *Operations Research*, 62(5):1142–1167, 2014.

[192] N. B. Keskin and A. Zeevi. Chasing demand: Learning and earning in a changing environment. *Mathematics of Operations Research*, 42(2):277–307, 2017.

[193] C. J. Keylock. Constrained surrogate time series with preservation of the mean and variance structure. *Phys. Rev. E*, 73:036707, Mar 2006.

[194] P. Kidger and T. Lyons. Universal approximation with deep narrow networks. In *Conference on Learning Theory*, pages 2306–2327, 2020.

[195] D. Kilminster. *Modelling dynamical systems via behaviour criteria.* University of Western Australia, 2002.

[196] B.-G. Kim, Y. Zhang, M. Van Der Schaar, and J.-W. Lee. Dynamic pricing and energy consumption scheduling with reinforcement learning. *IEEE Transactions on smart grid*, 7(5):2187–2198, 2015.

[197] S. Klus, F. Nüske, S. Peitz, J.-H. Niemann, C. Clementi, and C. Schütte. Data-driven approximation of the koopman generator: Model reduction, system identification, and control. *Physica D: Nonlinear Phenomena*, 406:132416, 2020.

[198] A. Komanduri, Z. Wafa, K. Proussaloglou, and S. Jacobs. Assessing the impact of app-based ride share systems in an urban context: Findings from austin. *Transportation Research Record*, 2672(7):34–46, 2018.

[199] A. Konak, D. W. Coit, and A. E. Smith. Multi-objective optimization using genetic algorithms: A tutorial. *Reliability engineering & system safety*, 91(9):992–1007, 2006.

[200] L.-W. Kong, H.-W. Fan, C. Grebogi, and Y.-C. Lai. Machine learning prediction of critical transition and system collapse. *Physical Review Research*, 3(1):013090, 2021.

[201] B. O. Koopman. Hamiltonian systems and transformation in hilbert space. *Proceedings of the national academy of sciences of the united states of america*, 17(5): 315, 1931.

[202] P. K. Kopalle and D. R. Lehmann. The effects of advertised and observed quality on expectations about new product quality. *Journal of Marketing Research*, 32(3): 280–290, 1995.

[203] P. K. Kopalle and J. Lindsey-Mullikin. The impact of external reference price on consumer price expectations. *Journal of Retailing*, 79(4):225 – 236, 2003.

[204] P. K. Kopalle and R. S. Winer. A dynamic model of reference price and expected quality. *Marketing Letters*, 7(1):41–52, 1996.

[205] P. K. Kopalle, A. G. Rao, and J. L. Assuncao. Asymmetric reference price effects and dynamic pricing policies. *Marketing Science*, 15(1):60–85, 1996.

[206] P. K. Kopalle, P. Kannan, L. B. Boldt, and N. Arora. The impact of household level heterogeneity in reference price effects on optimal retailer pricing policies. *Journal of Retailing*, 88(1):102–114, 2012.

[207] I. Kovacic and M. J. Brennan. *The Duffing equation: nonlinear oscillators and their behaviour*. John Wiley & Sons, 2011.

[208] K. H. Kraemer, R. V. Donner, J. Heitzig, and N. Marwan. Recurrence threshold selection for obtaining robust recurrence characteristics in different embedding dimensions. *Chaos: An Interdisciplinary Journal of Nonlinear Science*, 28(8): 085720, 2018.

[209] M. Kremer, B. Mantin, and A. Ovchinnikov. Dynamic pricing in the presence of myopic and strategic consumers: Theory and experiment. *Production and Operations Management*, 26(1):116–133, 2017.

[210] C. Kulp and L. Zunino. Discriminating chaotic and stochastic dynamics through the permutation spectrum test. *Chaos: An Interdisciplinary Journal of Nonlinear Science*, 24(3):033116, 2014.

[211] C. Kulp, J. Chobot, B. Niskala, and C. Needhammer. Using forbidden ordinal patterns to detect determinism in irregularly sampled time series. *Chaos*, 26(2): 023107, 2016.

[212] C. W. Kulp and S. Smith. Characterization of noisy symbolic time series. *Physical Review E*, 83(2):026201, 2011.

[213] N. Kuznetsov, T. Mokaev, O. Kuznetsova, and E. Kudryashova. The Lorenz system: hidden boundary of practical stability and the Lyapunov dimension. *Nonlinear Dynamics*, 102(2):713–732, 2020.

[214] D. La Torre, S. Marsiglio, and F. Privileggi. Fractal attractors in economic growth models with random pollution externalities. *Chaos: An Interdisciplinary Journal of Nonlinear Science*, 28(5):055916, 2018.

[215] G. Lancaster, D. Iatsenko, A. Pidde, V. Ticcinelli, and A. Stefanovska. Surrogate data for hypothesis testing of physical systems. *Physics Reports*, 748:1–60, 2018.

[216] L. Larger, B. Penkovsky, and Y. Maistrenko. Laser chimeras as a paradigm for multistable patterns in complex systems. *Nature Communications*, 6(1):1–7, 2015.

[217] P. S. Lavieri, F. F. Dias, N. R. Juri, J. Kuhr, and C. R. Bhat. A model of ridesourcing demand generation and distribution. *Transportation Research Record*, 2672(46):31–40, 2018.

[218] Y. LeCun, Y. Bengio, and G. Hinton. Deep learning. *Nature*, 521(7553):436, 2015.

[219] C. Letellier, E. Roulin, and O. E. Rössler. Inequivalent topologies of chaos in simple equations. *Chaos, Solitons & Fractals*, 28(2):337–360, 2006.

[220] A. Levi, J. Sabuco, and M. A. Sanjuán. Supply based on demand dynamical model. *Commun. Nonlinear Sci. Numer. Simul.*, 57:402–414, 2018.

[221] C. Li, W. Hu, J. C. Sprott, and X. Wang. Multistability in symmetric chaotic systems. *The European Physical Journal Special Topics*, 224(8):1493–1506, 2015.

[222] H. Li and W. T. Huh. Pricing multiple products with the multinomial logit and nested logit models: Concavity and implications. *Manufacturing & Service Operations Management*, 13(4):549–563, 2011.

[223] J. Li, N. Granados, and S. Netessine. Are consumers strategic? structural estimation from the air-travel industry. *Management Science*, 60(9):2114–2137, 2014.

[224] X. Li, W. Shang, and S. Wang. Text-based crude oil price forecasting: A deep learning approach. *International Journal of Forecasting*, 35(4):1548–1560, 2019.

[225] M. Liao, J. Ing, J. P. Chávez, and M. Wiercigroch. Bifurcation techniques for stiffness identification of an impact oscillator. *Communications in Nonlinear Science and Numerical Simulation*, 41:19–31, 2016.

[226] A. E. Lim and J. G. Shanthikumar. Relative entropy, exponential utility, and robust dynamic pricing. *Operations Research*, 55(2):198–214, 2007.

[227] S. Limmer. Dynamic pricing for electric vehicle charging—a literature review. *Energies*, 12(18):3574, 2019.

[228] K. Y. Lin. Dynamic pricing with real-time demand learning. *European Journal of Operational Research*, 174(1):522–538, 2006.

[229] Y. Liu, Q. Wang, and H. Xu. Bifurcations of periodic motion in a three-degree-of-freedom vibro-impact system with clearance. *Communications in Nonlinear Science and Numerical Simulation*, 48:1–17, 2017.

[230] E. N. Lorenz. Deterministic nonperiodic flow. *Journal of the Atmospheric Sciences*, 20(2):130–141, 1963.

[231] S. Lu, Z. Luo, G. Zhang, and S. Oberst. Order pattern recurrence plots: unveiling determinism buried in noise. In *University of Technology Sydney, FEIT Research Showcase*, Sydney, NSW, Australia, 14 Jun 2018.

[232] S. Lu, S. Oberst, G. Zhang, and Z. Luo. Bifurcation analysis of dynamic pricing processes with nonlinear external reference effects. *Communications in Nonlinear Science and Numerical Simulation*, 79:104929, 2019.

[233] S. Lu, S. Oberst, G. Zhang, and Z. Luo. Period adding bifurcations in dynamic pricing processes. In *IEEE CIFEr 2019: 2019 IEEE Conference on Computational Intelligence for Financial Engineering and Economics, Shenzhen, China*, May 4-5, 2019.

[234] S. Lu, S. Oberst, G. Zhang, and Z. Luo. Novel order patterns recurrence plot-based quantification measures to unveil deterministic dynamics from stochastic processes. In *ITISE 2018 (International conference on Time Series and Forecasting)*, September 19th-21th, 2018.

[235] Z. Lu, B. R. Hunt, and E. Ott. Attractor reconstruction by machine learning. *Chaos: An Interdisciplinary Journal of Nonlinear Science*, 28(6):061104, 2018.

[236] R. D. Luce. *Individual choice behavior: A theoretical analysis*. Courier Corporation, 2012.

[237] B. Lusch, J. N. Kutz, and S. L. Brunton. Deep learning for universal linear embeddings of nonlinear dynamics. *Nature Communications*, 9(1):4950, 2018.

[238] T. Lymburn, A. Khor, T. Stemler, D. C. Corrêa, M. Small, and T. Jüngling. Consistency in echo-state networks. *Chaos: An Interdisciplinary Journal of Nonlinear Science*, 29(2):023118, 2019.

[239] C. Maglaras and J. Meissner. Dynamic pricing strategies for multiproduct revenue management problems. *Manufacturing & Service Operations Management*, 8(2): 136–148, 2006.

[240] N. G. Mankiw. *Principles of economics*. Cengage Learning, 2014.

[241] R. T. Marler and J. S. Arora. Survey of multi-objective optimization methods for engineering. *Structural and multidisciplinary optimization*, 26(6):369–395, 2004.

[242] P. Martien, S. Pope, P. Scott, and R. Shaw. The chaotic behavior of the leaky faucet. *Phys. Lett. A*, 110:399–404, 1985.

[243] N. Marwan. How to avoid potential pitfalls in recurrence plot based data analysis. *International Journal of Bifurcation and Chaos*, 21(04):1003–1017, 2011.

[244] N. Marwan and J. Kurths. Comment on "stochastic analysis of recurrence plots with applications to the detection of deterministic signals" by rohde et al.[physica d 237 (2008) 619–629]. *Physica D: Nonlinear Phenomena*, 238(16):1711–1715, 2009.

[245] N. Marwan, A. Groth, and J. Kurths. Quantification of Order Patterns Recurrence Plots of Event Related Potentials. *Chaos and Complexity Letters*, 2:301–314, 2007.

[246] N. Marwan, M. C. Romano, M. Thiel, and J. Kurths. Recurrence plots for the analysis of complex systems. *Physics Reports*, 438(5-6):237–329, 2007.

[247] Matplotlib. Matplotlib 3.5.0 documentation. `https://matplotlib.org/stable/api/mlab_api.html#matplotlib.mlab.psd`, 2021. Accessed: 2021-12-13.

[248] A. Maus and J. Sprott. Neural network method for determining embedding dimension of a time series. *Communications in Nonlinear Science and Numerical Simulation*, 16(8):3294–3302, 2011.

[249] R. M. May. Simple mathematical models with very complicated dynamics. *Nature*, 261:459–467, 1976.

[250] T. Mazumdar, S. P. Raj, and I. Sinha. Reference price research: Review and propositions. *Journal of marketing*, 69(4):84–102, 2005.

[251] T. Mazumdar, S. P. Raj, and I. Sinha. Reference price research: Review and propositions. *Journal of marketing*, 69(4):84–102, 2005.

[252] M. McCullough, K. Sakellariou, T. Stemler, and M. Small. Regenerating time series from ordinal networks. *Chaos*, 27(3):035814, 2017.

[253] S. McNally, J. Roche, and S. Caton. Predicting the price of bitcoin using machine learning. In *2018 26th euromicro international conference on parallel, distributed and network-based processing (PDP)*, pages 339–343. IEEE, 2018.

[254] P. E. McSharry and L. A. Smith. Better nonlinear models from noisy data: Attractors with maximum likelihood. *Physical review letters*, 83(21):4285, 1999.

[255] J. A. Mead and D. M. Hardesty. Price font disfluency: Anchoring effects on future price expectations. *Journal of Retailing*, 94(1):102–112, 2018.

[256] A. Mehra, S. Kumar, and J. S. Raju. Competitive strategies for brick-and-mortar stores to counter "showrooming". *Management Science*, 2017.

[257] P. J. Menck, J. Heitzig, N. Marwan, and J. Kurths. How basin stability complements the linear-stability paradigm. *Nature physics*, 9(2):89–92, 2013.

[258] P. J. Menck, J. Heitzig, J. Kurths, and H. J. Schellnhuber. How dead ends undermine power grid stability. *Nature communications*, 5(1):1–8, 2014.

[259] I. Mezić. Spectral properties of dynamical systems, model reduction and decompositions. *Nonlinear Dynamics*, 41(1-3):309–325, 2005.

[260] I. Mezić. Analysis of fluid flows via spectral properties of the koopman operator. *Annual Review of Fluid Mechanics*, 45:357–378, 2013.

[261] S. Miao and X. Chao. Dynamic joint assortment and pricing optimization with demand learning. *Manufacturing & Service Operations Management*, 23(2):525–545, 2021.

[262] F. J. Milliken. Three types of perceived uncertainty about the environment: State, effect, and response uncertainty. *Academy of Management review*, 12(1):133–143, 1987.

[263] N. Mizik and R. Jacobson. Myopic marketing management: Evidence of the phenomenon and its long-term performance consequences in the seo context. *Marketing Science*, 26(3):361–379, 2007.

[264] J. M. Moore, D. C. Corrêa, and M. Small. Is bach's brain a markov chain? recurrence quantification to assess markov order for short, symbolic, musical compositions. *Chaos: An interdisciplinary journal of nonlinear science*, 28(8):085715, 2018.

[265] A. K. Naimzada and M. Pireddu. Fashion cycle dynamics in a model with endogenous discrete evolution of heterogeneous preferences. *Chaos: An Interdisciplinary Journal of Nonlinear Science*, 28(5):055907, 2018.

[266] K. Nakai and Y. Saiki. Machine-learning inference of fluid variables from data using reservoir computing. *Physical Review E*, 98(2):023111, 2018.

[267] T. Nakamura, M. Small, and Y. Hirata. Testing for nonlinearity in irregular fluctuations with long-term trends. *Physical Review E*, 74(2):026205, 2006.

[268] M. Nambiar, D. Simchi-Levi, and H. Wang. Dynamic learning and pricing with model misspecification. *Management Science*, 65(11):4980–5000, 2019.

[269] J. Nash. Non-cooperative games. *Annals of mathematics*, pages 286–295, 1951.

[270] J. Nasiry and I. Popescu. Dynamic pricing with loss-averse consumers and peak-end anchoring. *Oper. Res.*, 59(6):1361–1368, 2011.

[271] J. Nasiry and I. Popescu. Dynamic pricing with loss-averse consumers and peak-end anchoring. *Operations research*, 59(6):1361–1368, 2011.

[272] F. Nazarimehr, S. Jafari, S. M. R. Hashemi Golpayegani, M. Perc, and J. C. Sprott. Predicting tipping points of dynamical systems during a period-doubling route to chaos. *Chaos: An Interdisciplinary Journal of Nonlinear Science*, 28(7):073102, 2018.

[273] Neighbourhood. Neighbourhood (mathematics). `https://en.wikipedia.org/wiki/Neighbourhood_(mathematics)`, 2022. Accessed: 2022-01-04.

[274] H. E. Nusse and J. A. Yorke. Border-collision bifurcations including "period two to period three" for piecewise smooth systems. *Physica D: Nonlinear Phenomena*, 57(1-2):39–57, 1992.

[275] H. E. Nusse and J. A. Yorke. Border-collision bifurcations for piecewise smooth one-dimensional maps. *International Journal of Bifurcation and Chaos*, 05:189–207, 1994.

[276] S. Oberst. Nonlinear dynamics: Towards a paradigm change via evidence-based complex dynamics modelling. In *NOVEM 2018*, Ibiza, Spain, 7-9 May 2018.

[277] S. Oberst and J. Lai. Chaos in brake squeal noise. *Journal of Sound and Vibration*, 330(5):955–975, 2011.

[278] S. Oberst and J. Lai. A statistical approach to estimate the lyapunov spectrum in disc brake squeal. *Journal of Sound and Vibration*, 334:120 – 135, 2015. ISSN 0022-460X.

[279] S. Oberst and J. Lai. A statistical approach to estimate the Lyapunov spectrum in disc brake squeal. *Journal of Sound and Vibration*, 334:120–135, 2015.

[280] S. Oberst and J. Lai. A statistical approach to estimate the lyapunov spectrum in disc brake squeal. *Journal of Sound and Vibration*, 334:120–135, 2015.

[281] S. Oberst and S. Tuttle. Nonlinear dynamics of thin-walled elastic structures for applications in space. *Mechanical Systems and Signal Processing*, 110:469 – 484, 2018. ISSN 0888-3270.

[282] S. Oberst, G. Bann, J. C. Lai, and T. A. Evans. Cryptic termites avoid predatory ants by eavesdropping on vibrational cues from their footsteps. *Ecology letters*, 20 (2):212–221, 2017.

[283] S. Oberst, S. Marburg, and N. Hoffmann. Determining periodic orbits via nonlinear filtering and recurrence spectra in the presence of noise. *Procedia engineering*, 199: 772–777, 2017.

[284] S. Oberst, R. K. Niven, D. Lester, A. Ord, B. Hobbs, and N. Hoffmann. Detection of unstable periodic orbits in mineralising geological systems. *Chaos: An Interdisciplinary Journal of Nonlinear Science*, 28(8):085711, 2018.

[285] F. Olivares, A. Plastino, and O. A. Rosso. Contrasting chaos with noise via local versus global information quantifiers. *Physics Letters A*, 376(19):1577 – 1583, 2012. ISSN 0375-9601.

[286] P. E. Olsen, J. Laskar, D. V. Kent, S. T. Kinney, D. J. Reynolds, J. Sha, and J. H. Whiteside. Mapping solar system chaos with the Geological Orrery. *Proceedings of the National Academy of Sciences*, 116(22):10664–10673, 2019.

[287] E. Özkan and A. R. Ward. Dynamic matching for real-time ride sharing. *Stochastic Systems*, 10(1):29–70, 2020.

[288] S. Pan and K. Duraisamy. Data-driven discovery of closure models. *SIAM Journal on Applied Dynamical Systems*, 17(4):2381–2413, 2018.

[289] A. Panchuk, I. Sushko, and F. Westerhoff. A financial market model with two discontinuities: Bifurcation structures in the chaotic domain. *Chaos: An Interdisciplinary Journal of Nonlinear Science*, 28(5):055908, 2018.

[290] U. Parlitz, S. Berg, S. Luther, A. Schirdewan, J. Kurths, and N. Wessel. Classifying cardiac biosignals using ordinal pattern statistics and symbolic dynamics. *Computers in Biology and Medicine*, 42(3):319 – 327, 2012.

[291] R. Pascanu, T. Mikolov, and Y. Bengio. On the diÿcult y of training recurrent neural networks. In *International Conference on Machine Learning*, pages 1310–1318, 2013.

[292] J. Pathak, Z. Lu, B. R. Hunt, M. Girvan, and E. Ott. Using machine learning to replicate chaotic attractors and calculate Lyapunov exponents from data. *Chaos: An Interdisciplinary Journal of Nonlinear Science*, 27(12):121102, 2017.

[293] J. Pathak, B. Hunt, M. Girvan, Z. Lu, and E. Ott. Model-free prediction of large spatiotemporally chaotic systems from data: A reservoir computing approach. *Phys. Rev. Lett.*, 120:024102, Jan 2018.

[294] M. T. Pearce, A. Agarwala, and D. S. Fisher. Stabilization of extensive fine-scale diversity by ecologically driven spatiotemporal chaos. *Proceedings of the National Academy of Sciences*, 117(25):14572–14583, 2020.

[295] L. M. Pecora, L. Moniz, J. Nichols, and T. L. Carroll. A unified approach to attractor reconstruction. *Chaos: An Interdisciplinary Journal of Nonlinear Science*, 17(1):013110, 2007.

[296] R. Phillips, A. S. Şimşek, and G. Van Ryzin. The effectiveness of field price discretion: Empirical evidence from auto lending. *Management Science*, 61(8): 1741–1759, 2015.

[297] R. L. Phillips. *Pricing and revenue optimization*. Stanford University Press, 2005.

[298] A. Pikovsky, J. Kurths, M. Rosenblum, and J. Kurths. Synchronization: a universal concept in nonlinear sciences, 2003.

[299] A. N. Pisarchik and U. Feudel. Control of multistability. *Physics Reports*, 540(4): 167–218, 2014.

[300] I. Popescu and Y. Wu. Dynamic pricing strategies with reference effects. *Oper. Res.*, 55(3):413–429, 2007.

[301] M. Porfiri and M. R. Marín. Symbolic dynamics of animal interaction. *Journal of theoretical biology*, 435:145–156, 2017.

[302] Python package. scipy.integrate. `https://docs.scipy.org/doc/scipy/reference/generated/scipy.integrate.ode.html`, 2022. Accessed: 2022-05-16.

[303] T. Qin, K. Wu, and D. Xiu. Data driven governing equations approximation using deep neural networks. *Journal of Computational Physics*, 395:620–635, 2019.

[304] I. Rahwan, M. Cebrian, N. Obradovich, J. Bongard, J.-F. Bonnefon, C. Breazeal, J. W. Crandall, N. A. Christakis, I. D. Couzin, M. O. Jackson, et al. Machine behaviour. *Nature*, 568(7753):477, 2019.

[305] M. Raissi. Deep hidden physics models: Deep learning of nonlinear partial differential equations. *The Journal of Machine Learning Research*, 19(1):932–955, 2018.

[306] M. Raissi, P. Perdikaris, and G. E. Karniadakis. Physics-informed neural networks: A deep learning framework for solving forward and inverse problems involving nonlinear partial differential equations. *Journal of Computational physics*, 378: 686–707, 2019.

[307] M. Raissi, A. Yazdani, and G. E. Karniadakis. Hidden fluid mechanics: Learning velocity and pressure fields from flow visualizations. *Science*, 367(6481):1026–1030, 2020.

[308] B. Rakshit, M. Apratim, and S. Banerjee. Bifurcation phenomena in two-dimensional piecewise smooth discontinuous maps. *Chaos: An Interdisciplinary Journal of Nonlinear Science*, 20(3):033101, 2010.

[309] R. Rana and F. S. Oliveira. Real-time dynamic pricing in a non-stationary environment using model-free reinforcement learning. *Omega*, 47:116–126, 2014.

[310] RideAustin (2017). Ride-austin-june6-april13 [dataset], 2013. URL `https://data.world/ride-austin/ride-austin-june-6-april-13`. Accessed: 2021-05-19.

[311] P. Riley. Three pitfalls to avoid in machine learning. *Nature*, 572:27, 2019.

[312] C. Robinson. *Dynamical Systems: Stability, Symbolic Dynamics, and Chaos 2nd Edition (Studies in Advanced Mathematics)*. CRC Press, 2 edition, 1998. ISBN 0849384958, 9780849384950.

[313] M. Rosalie. Templates and subtemplates of rössler attractors from a bifurcation diagram. *Journal of Physics A: Mathematical and Theoretical*, 49(31):315101, 2016.

[314] O. E. Rössler. An equation for continuous chaos. *Physics Letters A*, 57(5):397–398, 1976.

[315] O. A. Rosso, H. A. Larrondo, M. T. Martin, A. Plastino, and M. A. Fuentes. Distinguishing noise from chaos. *Physical Review Letters*, 99(15):154102, 2007.

[316] O. A. Rosso, L. C. Carpi, P. M. Saco, M. G. Ravetti, A. Plastino, and H. A. Larrondo. Causality and the entropy–complexity plane: Robustness and missing ordinal patterns. *Physica A: Statistical Mechanics and its Applications*, 391(1):42 – 55, 2012. ISSN 0378-4371.

[317] O. A. Rosso, F. Olivares, L. Zunino, L. De Micco, A. L. Aquino, A. Plastino, and H. A. Larrondo. Characterization of chaotic maps using the permutation bandt-pompe probability distribution. *The European Physical Journal B*, 86(4): 116, 2013.

[318] S. H. Rudy, J. N. Kutz, and S. L. Brunton. Deep learning of dynamics and signal-noise decomposition with time-stepping constraints. *Journal of Computational Physics*, 396:483 – 506, 2019.

[319] C. M. Rump and S. Stidham. Stability and chaos in input pricing for a service facility with adaptive customer response to congestion. *Management Science*, 44 (2):246–261, 1998.

[320] P. Rusmevichientong, Z.-J. M. Shen, and D. B. Shmoys. Dynamic assortment optimization with a multinomial logit choice model and capacity constraint. *Operations research*, 58(6):1666–1680, 2010.

[321] P. Rusmevichientong, D. Shmoys, C. Tong, and H. Topaloglu. Assortment op-

timization under the multinomial logit model with random choice parameters. *Production and Operations Management*, 23(11):2023–2039, 2014.

[322] M. Saberi, H. Hamedmoghadam, M. Ashfaq, S. A. Hosseini, Z. Gu, S. Shafiei, D. J. Nair, V. Dixit, L. Gardner, S. T. Waller, et al. A simple contagion process describes spreading of traÿc jams in urban networks. *Nature communications*, 11 (1):1–9, 2020.

[323] M. Sangiorgio and F. Dercole. Robustness of lstm neural networks for multi-step forecasting of chaotic time series. *Chaos, Solitons & Fractals*, 139:110045, 2020.

[324] T. Sauer, J. A. Yorke, and M. Casdagli. Embedology. *Journal of statistical Physics*, 65(3):579–616, 1991.

[325] D. Sauré and A. Zeevi. Optimal dynamic assortment planning with demand learning. *Manufacturing & Service Operations Management*, 15(3):387–404, 2013.

[326] K. Schindler, H. Gast, L. Stieglitz, A. Stibal, M. Hauf, R. Wiest, L. Mariani, and C. Rummel. Forbidden ordinal patterns of periictal intracranial eeg indicate deterministic dynamics in human epileptic seizures. *Epilepsia*, 52(10):1771–1780, 2011.

[327] R. M. Schindler. The 99 price ending as a signal of a low-price appeal. *Journal of Retailing*, 82(1):71 – 77, 2006. ISSN 0022-4359.

[328] S. Schinkel, N. Marwan, and J. Kurths. Order patterns recurrence plots in the analysis of erp data. *Cognitive neurodynamics*, 1(4):317–325, 2007.

[329] C. Schlereth, B. Skiera, and F. Schulz. Why do consumers prefer static instead of dynamic pricing plans? an empirical study for a better understanding of the low preferences for time-variant pricing plans. *European Journal of Operational Research*, 269(3):1165–1179, 2018.

[330] R. Schlosser and M. Boissier. Dynamic pricing under competition on online marketplaces: A data-driven approach. In *Proceedings of the 24th ACM SIGKDD*

International Conference on Knowledge Discovery & Data Mining, pages 705–714, 2018.

[331] T. Schreiber and A. Schmitz. Surrogate time series. *Physica D: Nonlinear Phenomena*, 142(3-4):346–382, 2000.

[332] M. Schröder, D.-M. Storch, P. Marszal, and M. Timme. Anomalous supply shortages from dynamic pricing in on-demand mobility. *Nature communications*, 11(1): 1–8, 2020.

[333] H. G. Schuster and W. Just. *Deterministic Chaos: an Introduction*. John Wiley & Sons, 2006.

[334] Z.-J. M. Shen and X. Su. Customer behavior modeling in revenue management and auctions: A review and new research opportunities. *Production and operations management*, 16(6):713–728, 2007.

[335] A. Sherstinsky. Fundamentals of recurrent neural network (rnn) and long short-term memory (lstm) network. *Physica D: Nonlinear Phenomena*, 404:132306, 2020.

[336] N. Shukla, A. Kolbeinsson, K. Otwell, L. Marla, and K. Yellepeddi. Dynamic pricing for airline ancillaries with customer context. In *Proceedings of the 25th ACM SIGKDD International Conference on knowledge discovery & data mining*, pages 2174–2182, 2019.

[337] D. J. Simpson and J. D. Meiss. Simultaneous border-collision and period-doubling bifurcations. *Chaos: An Interdisciplinary Journal of Nonlinear Science*, 19(3): 033146, 2009.

[338] J. Sirignano and R. Cont. Universal features of price formation in financial markets: perspectives from deep learning. *Quantitative Finance*, 19(9):1449–1459, 2019.

[339] R. Slonim and E. Garbarino. Similarities and differences between stockpiling and reference effects. *Managerial and Decision Economics*, 30(6):351–371, 2009.

[340] S. Smale and D.-X. Zhou. Estimating the approximation error in learning theory. *Analysis and Applications*, 1(01):17–41, 2003.

[341] M. Small. *Applied nonlinear time series analysis: applications in physics, physiology and finance*, volume 52. World Scientific, 2005.

[342] M. Small, D. Yu, and R. G. Harrison. Surrogate test for pseudoperiodic time series data. *Physical Review Letters*, 87(18):188101, 2001.

[343] D. Sornette. *Critical phenomena in natural sciences: chaos, fractals, selforganization and disorder: concepts and tools*. Springer Science & Business Media, 2006.

[344] J. Sprott and A. Xiong. Classifying and quantifying basins of attraction. *Chaos: An Interdisciplinary Journal of Nonlinear Science*, 25(8):083101, 2015.

[345] J. C. Sprott. *Chaos and time-series analysis*, volume 69. Oxford: Oxford University Press, 2003.

[346] J. C. Sprott. *Chaos and time-series analysis*. Oxford University Press, 2006.

[347] J. C. Sprott and J. C. Sprott. *Chaos and time-series analysis*, volume 69. Citeseer, 2003.

[348] I. Stamatopoulos, N. Chehrazi, and A. Bassamboo. Welfare implications of inventory-driven dynamic pricing. *Management Science*, 65(12):5741–5765, 2019.

[349] M. Stender, M. Tiedemann, N. Hoffmann, and S. Oberst. Impact of an irregular friction formulation on dynamics of a minimal model for brake squeal. *Mechanical Systems and Signal Processing*, 107:439–451, 2018.

[350] M. Stender, S. Oberst, M. Tiedemann, and N. Hoffmann. Complex machine dynamics: systematic recurrence quantification analysis of disk brake vibration data. *Nonlinear Dynamics*, 97(4):2483–2497, 2019.

[351] M. Stender, M. Tiedemann, D. Spieler, D. Schoepflin, N. Hoffmann, and S. Oberst. Deep learning for brake squeal: Brake noise detection, characterization and prediction. *Mechanical Systems and Signal Processing*, 149:107181, 2021. ISSN 0888-3270.

[352] D.-M. Storch, M. Timme, and M. Schröder. Incentive-driven transition to high ride-sharing adoption. *Nature communications*, 12(1):1–10, 2021.

[353] S. H. Strogatz. *Nonlinear dynamics and chaos: with applications to physics, biology, chemistry, and engineering*. CRC Press, 2018.

[354] X. Su. A model of consumer inertia with applications to dynamic pricing. *Production and Operations Management*, 18(4):365–380, 2009.

[355] J. Subramanian, S. Stidham Jr, and C. J. Lautenbacher. Airline yield management with overbooking, cancellations, and no-shows. *Transportation science*, 33(2):147–167, 1999.

[356] C. Summerfield and F. P. De Lange. Expectation in perceptual decision making: neural and computational mechanisms. *Nature Reviews Neuroscience*, 15(11):745, 2014.

[357] I. Sushko, L. Gardini, and V. Avrutin. Nonsmooth one-dimensional maps: Some basic concepts and definitions. *Journal of Difference Equations and Applications*, 22(12):1816–1870, 2016.

[358] S. Suzuki, Y. Hirata, and K. Aihara. Definition of distance for marked point process data and its application to recurrence plot-based analysis of exchange tick data of foreign currencies. *International Journal of Bifurcation and Chaos*, 20(11): 3699–3708, 2010.

[359] N. Takeishi, Y. Kawahara, and T. Yairi. Learning koopman invariant subspaces for dynamic mode decomposition. In *Advances in Neural Information Processing Systems*, pages 1130–1140, 2017.

[360] F. Takens. Detecting strange attractors in turbulence. In *Dynamical Systems and Turbulence, Warwick 1980*, pages 366–381. Springer, 1981.

[361] K. T. Talluri and G. J. Van Ryzin. *The theory and practice of revenue management*, volume 68. Springer Science & Business Media, 2006.

[362] G. Tanaka, T. Yamane, J. B. Héroux, R. Nakane, N. Kanazawa, S. Takeda, H. Numata, D. Nakano, and A. Hirose. Recent advances in physical reservoir computing: A review. *Neural Networks*, 115:100 – 123, 2019. ISSN 0893-6080.

[363] Y. Tang, J. Kurths, W. Lin, E. Ott, and L. Kocarev. Introduction to focus issue: When machine learning meets complex systems: Networks, chaos, and nonlinear dynamics. *Chaos: An Interdisciplinary Journal of Nonlinear Science*, 30(6): 063151, 2020.

[364] N. Tereyagoglu, P. S. Fader, and S. Veeraraghavan. Multiattribute loss aversion and reference dependence: Evidence from the performing arts industry. *Management Science*, 64(1):421–436, 2018.

[365] The Prize in Economic Sciences 2010. Nobelprize.org. nobel prize outreach ab 2021. `https://www.nobelprize.org/prizes/economic-sciences/2010/summary/`, 2010. Accessed: 2021-12-01.

[366] The Prize in Economic Sciences 2010. Markets with search frictions. `https://www.nobelprize.org/uploads/2018/06/advanced-economicsciences2010.pdf`, 2010. Accessed: 2021-12-01.

[367] J. Theiler, S. Eubank, A. Longtin, B. Galdrikian, and J. D. Farmer. Testing for nonlinearity in time series: the method of surrogate data. *Physica D: Nonlinear Phenomena*, 58(1-4):77–94, 1992.

[368] J. D. Thompson. *Organizations in Action: Social Science Bases of Administrative Theory*. McGraw-Hill, 1st edition, 1967.

[369] R. Tibshirani. Regression shrinkage and selection via the lasso. *Journal of the Royal Statistical Society: Series B (Methodological)*, 58(1):267–288, 1996.

[370] TimeseriesSurrogates.jl. Timeseriessurrogates, 2022. URL `https://github.com/JuliaDynamics/TimeseriesSurrogates.jl.git`. Accessed: 2022-05-01.

[371] J. Timmer and M. Koenig. On generating power law noise. *Astronomy and Astrophysics*, 300:707, 1995.

[372] F. Tramontana and L. Gardini. Border collision bifurcations in discontinuous one-dimensional linear-hyperbolic maps. *Communications in Nonlinear Science and Numerical Simulation*, 16(3):1414–1423, 2011.

[373] T. D. Tsankov and R. Gilmore. Strange attractors are classified by bounding tori. *Physical Review Letters*, 91(13):134104, 2003.

[374] T. Tsuchiya and D. Yamagishi. The complete bifurcation diagram for the logistic map. *Zeitschrift für Naturforschung A*, 52(6-7):513–516, 1997.

[375] J. H. Tu, C. W. Rowley, D. M. Luchtenburg, S. L. Brunton, and J. N. Kutz. On dynamic mode decomposition: Theory and applications. *Journal of Computational Dynamics*, 1(2158-2491_2014_2_391):391, 2014. ISSN 2158-2491.

[376] N. B. Tufillaro, H. G. Solari, and R. Gilmore. Relative rotation rates: fingerprints for strange attractors. *Physical Review A*, 41(10):5717, 1990.

[377] A. Tversky and D. Kahneman. Loss aversion in riskless choice: A reference-dependent model. *The quarterly journal of economics*, 106(4):1039–1061, 1991.

[378] S.-M. Udrescu and M. Tegmark. AI feynman: A physics-inspired method for symbolic regression. *Science Advances*, 6(16):eaay2631, 2020.

[379] K. Valogianni, W. Ketter, J. Collins, and D. Zhdanov. Sustainable electric vehicle charging using adaptive pricing. *Production and Operations Management*, 29(6): 1550–1572, 2020.

[380] G. J. van Ryzin. *Models of demand*. The Oxford Handbook of Pricing Management, 2012.

[381] R. Vasconcellos and A. Abdelkefi. Nonlinear dynamical analysis of an aeroelastic system with multi-segmented moment in the pitch degree-of-freedom. *Communications in Nonlinear Science and Numerical Simulation*, 20(1):324–334, 2015.

[382] R. Vasconcellos, A. Abdelkefi, M. Hajj, and F. Marques. Grazing bifurcation in aeroelastic systems with freeplay nonlinearity. *Communications in Nonlinear Science and Numerical Simulation*, 19(5):1611–1625, 2014.

[383] P. R. Vlachas, W. Byeon, Z. Y. Wan, T. P. Sapsis, and P. Koumoutsakos. Data-driven forecasting of high-dimensional chaotic systems with long short-term memory networks. *Proceedings of the Royal Society A: Mathematical, Physical and Engineering Sciences*, 474(2213):20170844, 2018.

[384] M. Vogl and P. G. Rötzel. Chaoticity versus stochasticity in financial markets: Are daily s&p 500 return dynamics chaotic? *Communications in Nonlinear Science and Numerical Simulation*, 108:106218, 2022. ISSN 1007-5704.

[385] R. Wang. Capacitated assortment and price optimization under the multinomial logit model. *Operations Research Letters*, 40(6):492–497, 2012.

[386] R. Wang and Z. Wang. Consumer choice models with endogenous network effects. *Management Science*, 2016.

[387] W.-X. Wang, Y.-C. Lai, and C. Grebogi. Data based identification and prediction of nonlinear and complex dynamical systems. *Physics Reports*, 644:1 – 76, 2016. ISSN 0370-1573.

[388] Z. Wang. Intertemporal price discrimination via reference price effects. *Operations research*, 64(2):290–296, 2016.

[389] Z. Wang, S. Deng, and Y. Ye. Close the gaps: A learning-while-doing algorithm for single-product revenue management problems. *Operations Research*, 62(2): 318–331, 2014.

[390] G. Wanner and E. Hairer. *Solving ordinary differential equations I. Nonstiff Problems*. Springer Series in Computational Mathematics, Springer-Verlag, 1993.

[391] E. W. Weisstein. Farey sequence. From MathWorld–A Wolfram Web Resource. `https://mathworld.wolfram.com/FareySequence.html`, 2021. Accessed: 2021-12-07.

[392] E. W. Weisstein. Logistic map. From MathWorld–A Wolfram Web Resource. `https://mathworld.wolfram.com/LogisticMap.html`, 2022. Accessed: 2022-04-25.

[393] T. Weng, H. Yang, C. Gu, J. Zhang, and M. Small. Synchronization of chaotic systems and their machine-learning models. *Phys. Rev. E*, 99:042203, Apr 2019.

[394] T. Wenzel, C. Rames, E. Kontou, and A. Henao. Travel and energy implications of ridesourcing service in austin, texas. *Transportation Research Part D: Transport and Environment*, 70:18–34, 2019.

[395] B. Wernitz and N. Hoffmann. Recurrence analysis and phase space reconstruction of irregular vibration in friction brakes: Signatures of chaos in steady sliding. *Journal of Sound and Vibration*, 331(16):3887–3896, 2012.

[396] B. J. West. *Fractal physiology and chaos in medicine*, volume 16. World Scientific, 2012.

[397] T. Westerhold, N. Marwan, A. J. Drury, D. Liebrand, C. Agnini, E. Anagnostou, J. S. Barnet, S. M. Bohaty, D. De Vleeschouwer, F. Florindo, et al. An astronomically dated record of earth's climate and its predictability over the last 66 million years. *Science*, 369(6509):1383–1387, 2020.

[398] S. Wiggins. *Introduction to applied nonlinear dynamical systems and chaos*, volume 2. Springer Science & Business Media, 2003.

[399] S. Wu, Q. Liu, and R. Q. Zhang. The reference effects on a retailer's dynamic pricing and inventory strategies with strategic consumers. *Operations Research*, 63(6):1320–1335, 2015.

[400] J. J. Xu, S. P. Fader, and S. Veeraraghavan. Designing and evaluating dynamic pricing policies for major league baseball tickets. *Manufacturing & Service Operations Management*, 21(1):121–138, 2019.

[401] Y. Xu, M. Armony, and A. Ghose. The interplay between online reviews and physician demand: An empirical investigation. *Management Science*, 67(12):7344–7361, 2021.

[402] C. Yan, H. Zhu, N. Korolko, and D. Woodard. Dynamic pricing and matching in ride-hailing platforms. *Naval Research Logistics (NRL)*, 67(8):705–724, 2020.

[403] I. B. Yildiz, H. Jaeger, and S. J. Kiebel. Re-visiting the echo state property. *Neural Networks*, 35:1–9, 2012.

[404] S. Yin, J. Ji, G. Wen, and X. Wu. Use of degeneration to stabilize near grazing periodic motion in impact oscillators. *Commun. Nonlinear Sci. Numer. Simul.*, 66:20–30, 2019.

[405] Y. Yin and P. Shang. Multiscale recurrence plot and recurrence quantification analysis for financial time series. *Nonlinear Dynamics*, 85(4):2309–2352, 2016.

[406] Z. You, E. J. Kostelich, and J. A. Yorke. Calculating stable and unstable manifolds. *International Journal of Bifurcation and Chaos*, 1(03):605–623, 1991.

[407] X. Yuan and H. B. Hwarng. Stability and chaos in demand-based pricing under social interactions. *European Journal of Operational Research*, 253(2):472 – 488, 2016. ISSN 0377-2217.

[408] M. Zanin. Forbidden patterns in financial time series. *Chaos*, 18(1):013119, 2008.

[409] M. Zanin, L. Zunino, O. A. Rosso, and D. Papo. Permutation entropy and its main biomedical and econophysics applications: a review. *Entropy*, 14(8):1553–1577, 2012.

[410] L. Zdeborová. Machine learning: New tool in the box. *Nature Physics*, 13(5):420, 2017.

[411] J. Zhang, W.-y. K. Chiang, and L. Liang. Strategic pricing with reference effects in a competitive supply chain. *Omega*, 44:126–135, 2014.

[412] J. Zhang, J. Zhou, M. Tang, H. Guo, M. Small, and Y. Zou. Constructing ordinal partition transition networks from multivariate time series. *Scientific reports*, 7 (1):7795, 2017.

[413] Y. Zhang and S. H. Strogatz. Basins with tentacles. *Phys. Rev. Lett.*, 127:194101, Nov 2021.

[414] Z. Zhang, S. Oberst, and J. Lai. A non-linear friction work formulation for the analysis of self-excited vibrations. *Journal of Sound and Vibration*, 2018. ISSN 0022-460X.

[415] Z. Zhang, S. Oberst, and J. Lai. A non-linear friction work formulation for the analysis of self-excited vibrations. *Journal of Sound and Vibration*, 443:328 – 340, 2019. ISSN 0022-460X.

[416] W. Zhao and Y.-S. Zheng. Optimal dynamic pricing for perishable assets with nonhomogeneous demand. *Management science*, 46(3):375–388, 2000.

[417] Y. Zhao, J. Li, and L. Yu. A deep learning ensemble approach for crude oil price forecasting. *Energy Economics*, 66:9–16, 2017.

[418] N. Zheng and N. Geroliminis. Modeling and optimization of multimodal urban networks with limited parking and dynamic pricing. *Transportation Research Part B: Methodological*, 83:36–58, 2016.

[419] Y. Zhong, J. Tang, X. Li, B. Gao, H. Qian, and H. Wu. Dynamic memristor-based reservoir computing for high-eÿciency temporal signal processing. *Nature Communications*, 12(1):1–9, 2021.

[420] C. Zhou, L. Zemanová, G. Zamora, C. C. Hilgetag, and J. Kurths. Hierarchical organization unveiled by functional connectivity in complex brain networks. *Physical review letters*, 97(23):238103, 2006.

[421] Q. Zhu, H. Ma, and W. Lin. Detecting unstable periodic orbits based only on time series: When adaptive delayed feedback control meets reservoir computing. *Chaos: An Interdisciplinary Journal of Nonlinear Science*, 29(9):093125, 2019.

[422] Z. T. Zhusubaliyev and E. Mosekilde. *Bifurcations and chaos in piecewise-smooth dynamical systems*, volume 44. World Scientific, 2003.

[423] R. S. Zimmermann and U. Parlitz. Observing spatio-temporal dynamics of excitable media using reservoir computing. *Chaos: An Interdisciplinary Journal of Nonlinear Science*, 28(4):043118, 2018.

[424] L. Zunino, M. Zanin, B. M. Tabak, D. G. Pérez, and O. A. Rosso. Forbidden patterns, permutation entropy and stock market ineÿciency . *Physica A: Statistical Mechanics and its Applications*, 388(14):2854–2864, 2009.

Appendix A

Supplementary information of Chapter 3

A.1 Algorithm to run the map

Algorithm A.1: (Part A) Algorithm to run the map that Eq. (3.1) defines

1 Demand function $d(p)$, cf. Eq. (3.6);

Input : A given pair of (r_n^E, r_n^I) and a price p

Output: $d(p)$

Do : Calculate $d(p)$ according to Eq. (3.6)

Algorithm A.1: (Part B) Algorithm to run the map that Eq. (3.1) defines

2 The function f, cf. Eq. (3.9), for an optimal price;

Input : A given pair of (r_n^E, r_n^I), and finite price choices

$\mathbb{P}_\epsilon = \{\kappa\epsilon : \kappa = 0, 1, 2, \ldots, N_\epsilon\}$

Output: $p^{**}(r_n^E, r_n^I)$

Do : For each $p \in \mathbb{P}_\epsilon$

Do Procedure 1

Find the solution, $p^{**}(r_n^E, r_n^I) \in \mathbb{P}_\epsilon$, to Eq. (3.9).

Go to Procedure 3

3 The function (Eq. 3.1a) and the function h (Eq. 3.3), to update the IRP and the ERP, respectively;

Input : $p^{**}(r_n^E, r_n^I)$

Output: (r_{n+1}^E, r_{n+1}^I)

Do : Calculate the IRP according to Eq. (3.1a).

Calculate the ERP according to Eq. (3.3)

Go to Procedure 4

4 Map iteration;

Input : (r_{n+1}^E, r_{n+1}^I)

Output: $p^{**}(r_{n+1}^E, r_{n+1}^I)$

Do : $(r_n^E, r_n^I) \leftarrow (r_{n+1}^E, r_{n+1}^I)$

Go to Procedure 2

A.2 Correlation dimension estimation

Fig. A.1 shows a correlation dimension estimation D_2 of the dynamic pricing map. The calculation is based on the time series shown in Fig. ($3.4b_1$). The result of the calculation (cf. [279]) is $D_2 = 1.26 \in \mathrm{CI} = [1.11, 1.41]$, which helps to know the dynamics of the map (Eq. 3.1). The calculation is similar to a statistics of correlation dimension estimations detailed in section 5.4.5.4. However, a unique orbit is used for a calculation. "D2" algorithm is called as the size of an $\epsilon-$neighborhood and the embedding dimension m increase. A series of estimations $\mathrm{D}_2(\epsilon, m)$ are thus obtained. For a given ϵ, we calculate the median of $\{\mathrm{D}_2(\epsilon, m)\}$ under varying m. We follow Oberst and Lai [279] and conduct a statistics over D_2. The 10% estimations of the local maximum in the leftmost and the 10% estimations of the local maximum in the rightmost are cut off in the following plot.

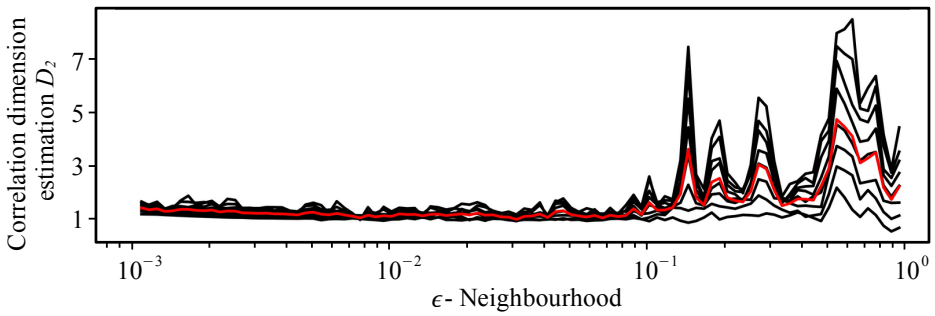

Figure A.1 : Correlation dimension estimation and its median for the time series given by Fig. ($3.4b_1$), cf. [279].

A.3 A visualization of the dynamics of the system

Fig. A.2 plots the $(r_n^E, r_n^I, p_n^{**})-$plane to visualize the map (Eq. 3.1). At $\mathscr{B} = 1$, we start from the initial condition $(r_0^E, r_0^I) = (0.3, 0.3)$, dispose the first $20,000$ iterations, and then record each point (r_n^E, r_n^I, p_n^{**}) to make a scatter plot.

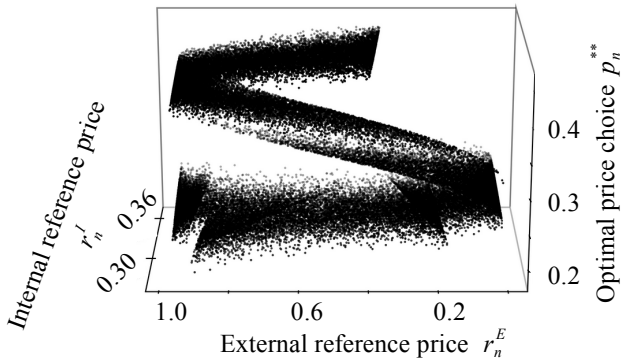

Figure A.2 : A visualization of the dynamics of the system from the $(r_n^E, r_n^I, p_n^{**})-$plane

Appendix B

Period adding bifurcations in dynamic pricing processes

Abstract

Price information enables consumers to anticipate a price and to make purchasing decisions based on their price expectations, which are critical for agents with pricing decisions or price regulations. A company with pricing decisions can aim to optimize the short-term or the long-term revenue, each of which leads to different pricing strategies thereby different price expectations. Two key ingredients play important roles in the choosing of the short-term or the long-term optimization objectives: the maximal revenue and the robustness of the chosen pricing strategy against market volatility. However the robustness is rarely identified in a volatile market. Here, we investigate the robustness of optimal pricing strategies with the short-term or long-term optimization objectives through the analysis of nonlinear dynamics of price expectations. Bifurcation diagrams and period diagrams are introduced to compare the change in dynamics of the optimal pricing strategies. Our results highlight that period adding bifurcations occur during the dynamic pricing processes studied. These bifurcations would challenge the robustness of an optimal pricing strategy. The consideration of the long-term revenue allows a

company to charge a higher price, which in turn increases the revenue. However, the consideration of the short-term revenue can reduce the occurrence of period adding bifurcations, contributing to a robust pricing strategy. For a company, this strategy is a robust guarantee of optimal revenue in a volatile market; for consumers, this strategy avoids rapid changes in price and reduce their dissatisfaction of price variations.

B.1 Introduction

Increased information eÿciency , e.g. higher price transparency due to the availability of novel information technologies, influences strongly consumer purchasing decisions [256]. For travel arrangements consumers tend to use online travel agents or meta-search engines which facilitate their purchasing decisions of an airline ticket [223]. Apart from that a lot of extra price information can be conveniently accessed over the internet, which allows consumers to compare prices from different channels and to anticipate a price as a reference point to support purchasing decisions [175].

When the anticipation of the price is based on historical values it is called the *internal reference price* [251] or *reference price* in short.

The reference price acts as a benchmark for consumer purchasing decisions [175, 205, 206, 300]. While a sales price lower than a reference price is perceived by the customer as a *gain*, a higher sales price is perceived as a *loss*. The experience of receiving a gain makes a consumer more likely to purchase something in the future. However, consumers who experience a loss rather tend to reject new purchases. The effect of the perceived gains/losses on the demand is called the reference effect [206].

Owing to reference effect, a decision maker with pricing decisions could set a lower price to attract a higher volume of consumers and so gain an increased short-term revenue. The decision maker, however, may suffer losses considering the long-term revenue since a low price decreases the reference price of consumers. A decreased reference price, however, makes consumers less likely to accept a higher price in the future [300].

Although the long-term revenue is critical, subjective reasons may influence the decision maker to emphasize the short-term revenue such as the quarterly earning expectations or the subjective job security cf. [263].

Another reason to focus on the short-term revenue is the computational complexity found in the associated optimization problem. An analytic solution is possible for optimizing the short-term revenue [79, 175]. However, when consumers behave asymmetrically towards gains and losses, the demand function becomes non-smooth, which challenges the optimization of the long-term revenue. So far, no explicit analytic solution but numerical approximations are available for this type of problem [79, 175, 205].

With regards to the advantages of a short-term revenue strategy, one question arises naturally: Can a decision maker benefit from a short-term revenue strategy and simultaneously gain insights from its detailed analysis to guide the pricing decision process for the long-term revenue?

Answering the question includes two criteria required to evaluate an optimal pricing strategy: what is the maximal revenue obtained from it? And what is the robustness against the volatile market and the optimization objectives.

To date it has been studied to compare the maximal revenue achieved from the short-term and the long-term optimization objective [300].

However, the studies neglect the robustness of the optimal pricing strategy. optimization responding to a changing environment, where the maximal revenue is not the unique criterion to choose an optimal pricing strategy [297, 361]. Therefore, in practice, a decision maker needs the robustness to evaluate optimal pricing strategies except if the maximal revenue is concerned [297, 361].

Also, consumers asymmetrically respond to gains and losses [175, 205, 300]. This leads to two different tangent slopes at the point in the demand curve where the reference price equals the sales price. As a result, the demand function becomes non-smooth .

Owing to the non-smoothness of the problem, border collision bifurcations have been

reported in mathematical models underlying dynamic pricing processes [175]. Border collision bifurcations or grazing bifurcations are also widely observed in other systems such as impact or friction oscillators [381, 404], and models of the financial market [289].

Period adding or period incrementing bifurcations are the cornerstones of border collision bifurcations [139, 265, 289]. For period incrementing bifurcations, the period either increases or decreases by a positive integer; for period adding bifurcations, the period follows the Farey summation rule with the changing bifurcation parameter [139, 265, 289]*.

Although dynamic pricing models are generally nonlinear with a non-smooth demand function, their bifurcation structures have not been studied to the best of the authors' knowledge. Here we aim to uncover these structures for the short-term and long-term revenue and introduce bifurcation and period diagrams to study the robustness of optimal pricing strategies.

B.2 Models

B.2.1 Reference price

Following a dynamic pricing process, the reference price evolves via

$$r_{n+1} = \alpha r_n + (1-\alpha)p_n \tag{B.1}$$

where r_n is the reference price at period n, p_n is the sales price at period n, and $\alpha \in [0,1]$ represents a memory factor.

For a given initial r_0, Eq. (B.1) can be transformed to

$$r_{n+1} = \alpha^{n+1} r_0 + (1-\alpha)(\alpha^n p_0 + \alpha^{n-1} p_1 + \cdots + \alpha^0 p_n) \tag{B.2}$$

In an extreme case when $\alpha = 0$ in Eq. (B.2), consumers only remember the latest price; for $\alpha > 0$ consumers start remembering past prices but slow down their adaptions to

*According to the Farey rule, a period-$m+n$ solution between the bifurcation parameters which generate period-m and period-n solution can been observed.

the past until for $\alpha = 1$, consumers memorize only r_0. Here, being consistent with Hu et al. [175], we define $r_0 \in [0, U]$ and $p_n \in [0, U]$ with U being the maximal price that a decision maker is allowed to charge.

B.2.2 Demand

Following Hu et al. [175], the demand $d(p_n, r_n)$ is composed of a linear base demand and nonlinear reference effects via

$$d(p_n, r_n) = \begin{cases} b - ap_n + \gamma^g (r_n - p_n), & \text{if } r_n > p_n, \quad \text{(B.3a)} \\ b - ap_n, & \text{if } r_n = p_n, \quad \text{(B.3b)} \\ b - ap_n + \gamma^l (r_n - p_n), & \text{if } r_n < p_n. \quad \text{(B.3c)} \end{cases}$$

Here, Eq. (B.3b) represents the base demand, a and b are parameters of the base demand, and γ^g and γ^l stand for the sensitivity of consumers to either a gain or a loss, respectively.

When $\gamma^g \neq \gamma^l$, the demand becomes *non-smooth*. Hu et al. [175] restricts their study to the special case of $\gamma^l = 0$. Yet, this assumption can result in losses [175] and should therefore be avoided from a management point of view. A more general scenario would be required to better understand the dynamics and to avoid losses. We therefore define a new parameter β to act as the relative sensitivity of consumers to losses and gains,

$$\beta = \gamma^l / \gamma^g : \quad \text{(B.4)}$$

- If $\beta = 1$, then $\gamma^g = \gamma^l$, and consumers are neutral and become equally sensitive to gains and losses;
- if $\beta \in [0, 1)$, then $\gamma^g > \gamma^l$, and consumers are gain-seeking; if $\beta = 0$, then $\gamma^l = 0$, and consumers are insensitive to losses; and
- if $\beta > 1$, then $\gamma^g < \gamma^l$, and consumers are loss-averse.

Gain-seeking consumers are observed in the market with promotion-driven consumers or highly stockable products [175]. In line with this observation, we focus here on gain-

seeking consumers and assume $\beta \in [0,1)$. In this setting, the demand becomes non-smooth due to being non-differentiable at the point $p_n = r_n$ (cf. Eq. (B.3a)-(B.3b)). Other scenarios (neutral and loss –averse consumers) require different modeling and optimization procedures and are therefore not considered here.

B.2.3 Short-term revenue

Suppose a decision maker aims to optimisze the short-term revenue, then optimal price choices are provided through

$$p_n^* = \arg \max_{p_n \in [0,U]} \Pi = p_n d(p_n, r_n). \tag{B.5}$$

Lemma 1: The reference price evolves via

$$r_{n+1} = \begin{cases} \alpha r_n + (1-\alpha)\frac{\gamma^l r_n + b}{2(a+\gamma^l)}, & \text{if } r_n \leq R \leq R_U \\ \alpha r_n + (1-\alpha)\frac{\gamma^g r_n + b}{2(a+\gamma^g)}, & \text{if } R < r_n, R \leq R_U, \text{and} \\ \alpha r_n + (1-\alpha)U & \text{if } R > R_U \end{cases} \tag{B.6}$$

where $R = \frac{b}{a+\sqrt{(a+\gamma^g)(a+\gamma^l)}}$, $R_U = \frac{2(a+\gamma^l)U - b}{\gamma^l}$, cf. [175].

B.2.4 Long-term revenue

When a decision maker focuses on the long-term revenue, the optimal price choices are determined by the following equation

$$\max_{p_n \in [0,U]} \sum_{n=0}^{\infty} \omega^n p_n d(p_n, r_n) \tag{B.7}$$

where $\omega \in (0,1]$ represents a discount rate, which is a rate to evaluate the present cash value of the discounted future revenue [175].

A numerical approximation solution p_n^* to Eq. (B.7) here is based on dynamic programming, which is described in more detail in [79, 175]. Plugging p_n^* into Eq. (B.1), we get a map that describes the evolution of the reference price for the long-term revenue scenario.

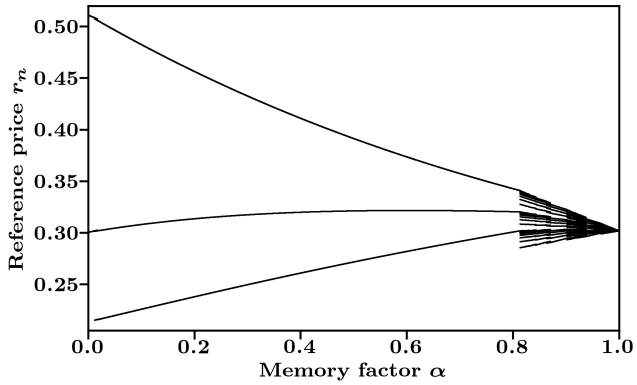

Figure B.1 : Bifurcation diagram of reference price against memory factor in the case of optimizing the short-term revenue.

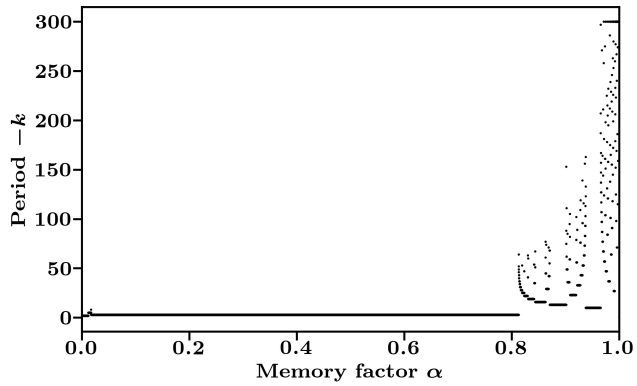

Figure B.2 : Period diagram of reference price against memory factor in the case of optimizing the short-term revenue.

Bifurcation diagrams summarize the entire behavior of the system as a significant parameter changes [347]. Bifurcation diagrams can analyze the change in the amplitude of the steady-state solutions as well as the change in the complexity of the solution. However, bifurcation diagrams may fail to detect the change in dynamics for border collision bifurcations [272]. Period diagrams record the period of solutions with the changing bifurcation parameter [132]. Period diagrams allows examining the robustness of steady-state solutions and allows comparing the optimizations with the short-term and the long-term revenue.

To generate the bifurcation and period diagrams, we assume the following parameters to be constant [175]:

$$b = 582, a = 569.4, \gamma^g = 2671.2, \omega = 0.9, U = 1, \tag{B.8}$$

The choosing of parameters given by Eq. B.8 is based on an empirical study [174, 175], where the parameters are estimated through ordinal least square to fit a given database [174]. Here, the memory factor α and β are chosen as the bifurcation parameter, respectively.

B.3 Dynamics in the short-term revenue strategy

Next the dynamic behavior of the reference price as evolved via Eq. (B.6) is investigated through numerical simulations. We focus on the reference price rather than the optimal price choices for two reasons. From Eq. (B.6), the dynamic behavior of the optimal price is in line with that of the reference price. Also, the evolution of the reference price provides critical information for a regulator to identify the behavior of a company in the market.

B.3.1 Variation of the memory rate α

In this section the relative sensitivity $\beta = 0$ is fixed and the memory rate α is varied which would be a conventional way of studying this type of equation [175].

Fig. B.1 depicts the results in form of a bifurcation diagram. When $\alpha \leq 0.813$, the reference price converges to three branches, however, when $\alpha \in (0.813, 1]$, more branches with the decreasing amplitude of reference price emerge until a constant value is reached. Jumps in the bifurcation diagram can indicate the occurrence of either sub-critical Hopf- or border collision bifurcations [404, 414].

Fig. B.2 depicts a period diagram. Except for a small interval $\alpha \in [0.012, 0.017]$ where the period changes from 3 to 8 and then to 5, the number of periods remains constant at 3. Complex changes in periodic behavior emerge from around $\alpha = 0.813$ up to unity, indicating the occurrence of border collision bifurcations [139, 181].

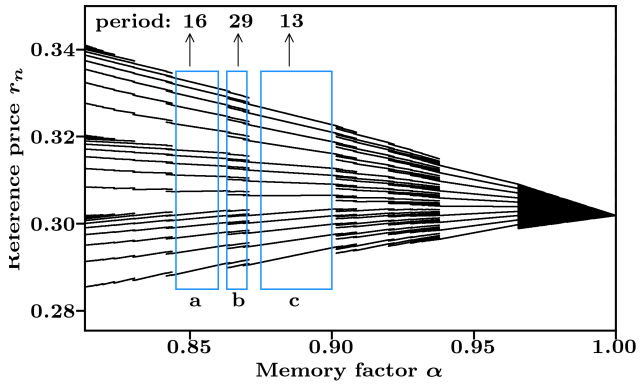

Figure B.3 : Zoom-in of Fig. B.1. Bifurcation diagram of reference price against the memory factor in the case of optimizing the short-term revenue. The branches in the window marked as 'b' are an overlap of its 'left' side branches marked as 'a' and its 'right' side branches marked as 'c'.

To investigate the dynamics in more detail as $\alpha \in (0.813, 1]$, we zoom into both, the bifurcation diagram of Fig. B.1 and the period diagram of Fig. B.2. The results are shown in Fig. B.3 and Fig. B.4.

Fig. B.3 highlights how branches overlap. The window marked with 'b' results from an overlap of branches found in window 'a' with those found in window 'c'. Fig. B.4 details these period adding cascades [149]. The period adding cascades within the period-13, period-16 and period-29 window are called period adding bifurcations as a result of border collisions [113, 138, 149]. According to this adding rule, there is a period-45 window between the period-16 and the period-29 window, and so forth.

For the short-term revenue, the reference price is robust to a change in the memory rate of consumers such that $\alpha < 0.813$, which leads to a robust and optimal period-3 pricing strategy. However, as $\alpha > 0.813$, period adding bifurcations emerge. This leads to a maximal revenue which is generated from a periodic pricing strategy based on a rapid changing period.

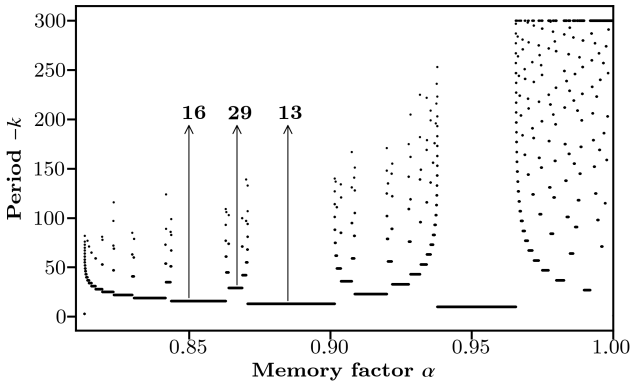

Figure B.4 : Period diagram of reference price against the memory factor in the case of optimizing the short-term revenue. Zoom-in of Fig. B.2 shows period adding cascades. Between the period-16 and the period-13 solutions, its sum, a period-29 solution, emerges.

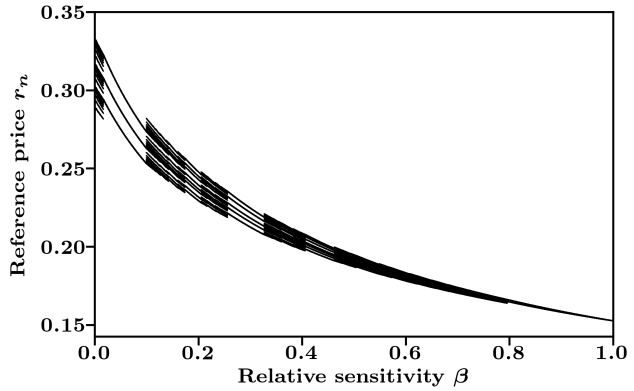

Figure B.5 : Bifurcation diagram of the reference price against the relative sensitivity of consumers in the case of optimizing the short-term revenue.

B.3.2 Variation of the relative sensitivity β

Next we set the the memory factor to be $\alpha = 0.85$, and alter the relative sensitivity β as shown in Fig. B.5. As β increases, the amplitude of the reference price decreases until a constant value is reached. Again, cascades of period adding bifurcations are observed. In the following Fig. B.6 illustrates two scenarios of period adding cascades as β increases:

1. For the window marked as 'a', the lowest period lies in the middle of the period adding cascade which is called in the following a U-cascade. In a U-cascade the

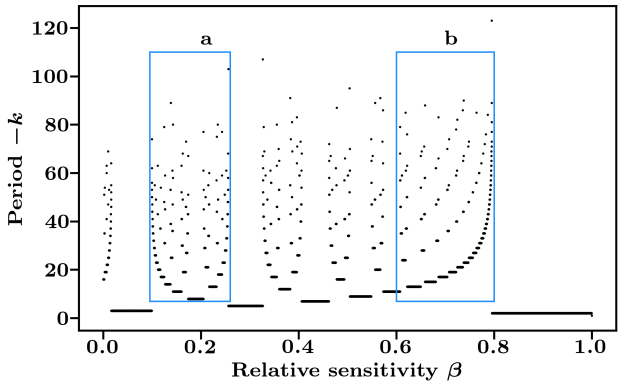

Figure B.6 : Period diagram of the reference price against the relative sensitivity in the case of optimizing the short-term revenue. The the window marked with an 'a' highlights a U-cascade which contains pairs of opposed period adding bifurcation cascades; the window marked by 'b' represents an S-cascade which only consists of period adding cascades of increasing order.

period of its right-hand side is greater than that of the left-hand side.

2. For the window marked with 'b', we observe an S-cascade of which period adding cascades have layers of increasing periods.

For the short-term revenue strategy, period adding bifurcations are observed only when $\beta < 0.795$. As the relative sensitivity to losses and gains approaches unity, the reference price becomes a period-2 solution, which is robust to the change in the relative sensitivity.

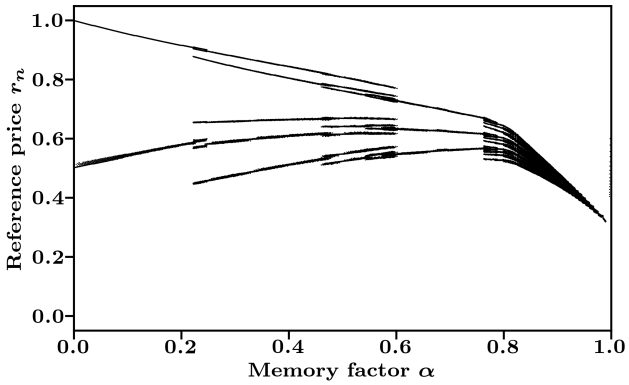

Figure B.7 : Bifurcation diagram of reference price against the memory factor in the case of optimizing the long-term revenue.

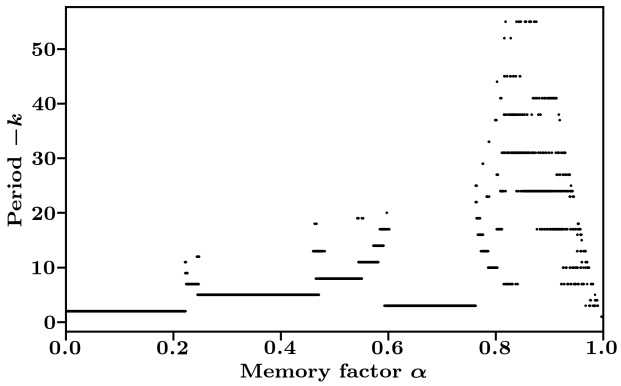

Figure B.8 : Period diagram of reference price against the memory factor in the case of optimizing the long-term revenue.

B.4 Dynamics in the long-term revenue strategy

This section investigates the nonlinear dynamics of reference price for a decision maker who aims at optimizing the long-term revenue.

B.4.1 Variation of memory rate α

The parameters used here are the same as those in section B.3.1 but a different objective function is used: The decision maker obtains the optimal price from the solutions to Eq. (B.7).

Fig. B.7 depicts the bifurcation diagram; again bifurcations in branches add up until α reaches a value of about 0.6, where the branches start merging into three main branches. This convergence is followed by the emergence of many branches and the shrinking amplitude until a constant value is reached.

However, when comparing the y-axis of Fig. B.1 and Fig. B.7, we find that for the same α, the reference price in the case of the long-term revenue can be higher than that in the case of the short-term revenue. The result is consistent with observations made by [300]: A company chooses usually a higher sales price to increase future reference prices and thereby to grow its long-term revenue.

Fig. B.8 depicts the change in dynamics with the changing α. As $\alpha \in (0, 0.222]$, the reference price becomes a period-2 solution. As $\alpha \in (0.222, 0.592)$, period adding bifurcations occur.

However, comparisons between the short-term (cf. Fig. B.2) and the long-term revenue (cf. Fig. B.8) in the interval $\alpha \in [0.018, 0.813)$ shows the robustness of the optimization of the short-term revenue. The solution in such interval of Fig. B.2 is a clear period-3 solution. In contrast, period adding bifurcations occur when the objective function is the long-term revenue (cf. Fig. B.8).

From the comparison between the behavior of the reference price and that of the amplitude and the period, a decision maker can charge a higher price when aiming for the long-term revenue. However, opposed to the short-term revenue strategy the consideration of the long-term revenue enables scenarios for which the reference price becomes prone to period adding bifurcations.

B.4.2 Variation of relative sensitivity β

The parameters are the same as section B.3.2. The optimal price is approximated according to Eq. (B.7).

Fig. B.9 shows the bifurcation diagram as the relative sensitivity changes. Similar to Fig. B.5, the branches show bifurcation adding cascades. Comparisons between Fig. B.9

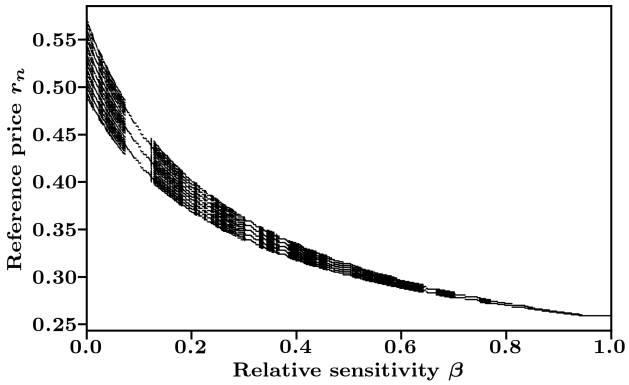

Figure B.9 : Bifurcation diagram of reference price against the relative sensitivity in the case of optimizing the long-term revenue.

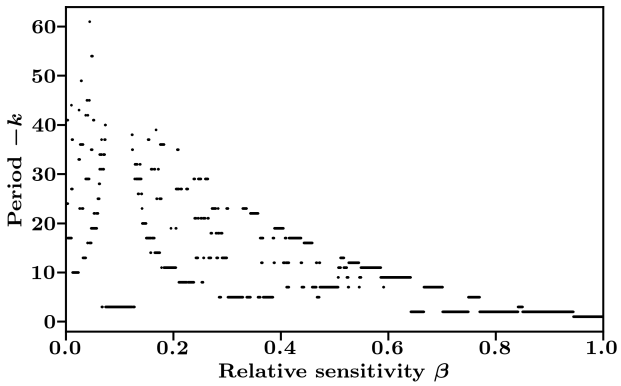

Figure B.10 : Period diagram of reference price against the relative sensitivity in the case of optimizing the long-term revenue.

and Fig. B.5 further validate our observations: a company can achieve a higher reference price for the long-term revenue strategy than in the short-term revenue strategy. Also, U-cascades shown in Fig. B.10 is not so obvious as in Fig. B.6. This observation indicates that the consideration of the long-term revenue reduce the variation in the period of the periodic reference price.

A reduced variation is due to a clairvoyant perspective in solving the optimization problem in the case of the long-term revenue. The underlying assumption is that the system does not follow any drift terms, evolves according to given equations and that

the 'maximal generating revenue' price path is chosen. The decision maker has full information of the market evolution.

This information helps the decision maker to reduce unnecessary transitions to steady-state solutions. As a result, the long-term consideration reduces the amplitude of the change in dynamics when the period adding bifurcations emerge both in the short-term and the long-term revenue strategy.

B.5 Conclusion

We have studied bifurcation and period diagrams to examine the nonlinear dynamics in a dynamic pricing model considering reference effects. Comparisons between a short-term and a long-term revenue strategy have been conducted. Period adding bifurcations are observed as the market environment changes. According to the order of the left and the right hand side of the period adding cascades, we classify two types of cascades: the U-cascade and the S-cascade [148]. These two types of cascades enable us to identify different bifurcation structures which belong to different revenue strategies.

The consideration of optimizing the long-term revenue has two advantages over optimizing the short-term revenue. A decision maker could charge temporarily a higher price to increase the reference price. Also, the long-term revenue strategy induces a less variation in the period. Further, this reduced variability lowers the amplitude of the period of the reference price. However, optimizing the long-term revenue breaks a supposedly robust pricing strategy in some situations (here $\alpha \in (0.222, 0.592)$). In this situation, the short-term revenue generates a robust periodic solution with a fixed period, which avoids period adding bifurcations. Knowing of such a robust period would enable a decision maker to reduce price volatility and manage consumer price expectations.

Our focus is on the periodic solution of the reference price and solutions with a period smaller than 300 using period diagrams. This limitation, however, makes it diÿcult to distinguish between higher periodic, quasi-periodic or chaotic solutions. Symbolic analyzes or order pattern recurrent plots and associated quantifiers may provide further

condensation of the complex information contained in bifurcation diagrams [234].

Future work will concentrate on the development of a theoretical framework on how to determine all parameters. Also the classification of cascades will further be used to characterize period adding bifurcations into different evolution of rotation numbers. Whether structures as calculated here are realistic or whether the model needs to be further adjusted is unknown to-date but is currently verified using real-life business data.

Appendix C

Novel order patterns recurrence plot-based quantification measures to unveil deterministic dynamics from stochastic processes

Abstract

Forbidden ordinal patterns are known to be useful to discriminate between chaotic and stochastic systems. However, while uncorrelated noise can be separated from deterministic signals using forbidden ordinal patterns, correlated noise exhibits apparently forbidden ordinal patterns, which can impede distinguishing noise from chaos.

Here, we introduce order patterns recurrence plots to visualize the difference among deterministic chaotic systems, and stochastic systems of uncorrelated and correlated noise. In an order pattern plot of a chaotic system with an optimal embedding dimension, the diagonal lines remain preserved, while uncorrelated noise shows up as thinly isolated dots and correlated noise forms clusters. We propose two measures, the mean and the median of relative frequencies of order patterns that appear in a time series to distinguish those dynamics. The effectiveness of the two measures is analyzed through bifurcation diagrams of the logistic map,

the tent map, the delayed logistic map and the Hénon map.

Our results show, that both, the mean and the median, distinguish chaos from quasi-periodicity in the delayed logistic map. The mean of relative frequencies of order pattern is reciprocal to the number of order patterns that occur in a given time series, thus can be a measure of forbidden structures - which becomes unbounded. While the mean is robust to the change of parameters in the bifurcation diagrams, the median exhibits sensitive changes, which is significant to characterize chaotic signals.

C.1 Introduction

Given a measured time series, irregularity often dominates. The irregularities can emerge in economics [214], finance [289], natural sciences (physics [66], biology [282], chemistry [353], geology [284], medicine [396] or engineering [277, 349, 395]). For real data it is often necessary to distinguish between stochastic dynamics (random noise, high dimensional) and deterministic dynamics which can also be chaotic, either low or high dimensions.

However, both a stochastic system and a chaotic system generate a broadband power spectrum in the frequency domain, which often hinders their disentanglement [315]. The situation complicates when it comes to real-life data or natural information (life sciences) since measurements here are inextricably contaminated by omnipresent dynamical or observational noise [210, 276, 283, 315].

To discriminate chaotic systems with observational noise from stochastic systems, [20] developed a symbolization scheme, the Bandt-Pompe(BP) methodology, which encodes a time series into order patterns. An order pattern with embedding dimension m represents a permutation of the set $\{0, 1, ..., m-1\}$, which is an invariant under the process of monotonous transformations and known to be robust with regards to observational Gaussian noise [20]. Owing to this robustness, order patterns have attracted a growing interest [23, 211, 290, 301, 412].

Two streams of studies have been devoted to quantify order patterns and the degree

of determinism on the basis of the BP method. The first stream is that of *forbidden ordinal patterns* [7, 8, 317, 326, 408, 409, 424], which are non-occurring permutations in a time series [5, 8, 62, 210, 316].

The occurrence of forbidden ordinal patterns is related to structures of deterministic processes. For a deterministic map $x_{i+1} = f(x_i)$, the number of intersections of $f^0(x) = x$,$f^1(x)$,...,$f^{m-1}(x)$ determines the number of order patterns. As a result, when the number of intersections is smaller than $m!$ (and exponentially growing with m), the map exhibits *forbidden pattern* [8, 9, 317].

However, there is a minimal embedding dimension to detect the outgrowth of forbidden ordinal patterns [317]. For the logistic map ($x_{i+1} = 4x_i(1 - x_i)$), as $m = 3$, the number of intersections of f^0, f^1, f^2 is 6, hence the number of order patterns equals 5 and the permutation $(2, 1, 0)$ is forbidden, irrespective of the time series' length [8]. Also, the number of forbidden ordinal patterns is robust to low degrees of sampling irregularities as the time series is generated from irregular time intervals [211].

To visualize forbidden ordinal patterns, Kulp and Smith [212] and Kulp and Zunino [210] introduce a permutation spectrum test, which plots the counts of frequencies of each permutation of $\{0, 1, ..., m-1\}$. A permutation that counts 0 is a forbidden ordinal pattern and indicates determinism. However, this plot fails to discriminate determinism from correlated noise, which is stochastic but shows missing order pattern. Both forbidden and missing order pattern are pattern structures that does not show up in a time series. However, while the forbidden order patterns is unrelated to the length of the time series, the missing order patterns have small probability to show up but will show up as long as the time series are long enough. Permutation entropy is further needed to facilitate the identification of determinism based on this plot [285, 316, 317].

On the other hand, the second stream of measures applied the BP method is to visualize and estimate recurrent behaviour of order patterns, using order patterns recurrence plot (OPRP). OPRP was developed by Groth [156] to visualize the dependencies between two time series. While a conventional recurrence plot (RP) is based on the

(phase) spatial and temporal closeness to define recurrent and laminar behaviour [246], a recurrence in an OPRP is that the same order pattern recurs [57, 156].

However, literature is scarce on interpreting recurrence quantification analysis (RQA) measures extracted from an OPRP [57]. Schinkel et al. [328] and Marwan et al. [245] employ the RQA to detect determinism of event-related potentials of brain responses using electroencephalography (EEG). Donner et al. [109] use RQA to investigate short-term dynamics of discrete-valued data. McCullough et al. [252] regenerate a time series using an ordinal network to compare the dynamics of the original time series and a surrogate time series designed from ordinal network data using the RQA and OPRP. Apart from ordering a time series, Caballero-Pintado et al. [57] define a new OPRP using a symbolic correlation integral by ordering the time series relative to the original.

Motivated by the study of Lu et al. [231], our goal here is to connect these two streams of studies and show that OPRP can visualize the effect of an exponential increase of forbidden ordinal patterns through the increase of embedding dimension m. To unveil the change of dynamics as the parameters of the dynamical system change, we introduce and validate two new measures, the mean and the median of the relative frequencies of order patterns that occur in a time series. To examine the evolution of those two measures, as deterministic test models, we apply the logistic map, the delayed logistic map, the tent map and the Hénon map; as stochastic test models we use white and Brown noise.

C.2 Methodology

Underlying a one-dimensional time series ($\{x_t\}_{t=1}^{N}$) with length N, order patterns of $\{x_t\}_{t=1}^{N}$ depend on the time delay τ and the embedding dimension m [20]. We encode x_t to its order pattern through ranked elements in the vector $\overrightarrow{x(t)} = (x_t, x_{t+\tau}, ..., x_{t+(m-1)\tau})$ [156]. Here, we study order patterns in the case of $\tau = 1$, and then rank $\overrightarrow{x(t)} = (x_t, x_{t+1}, ..., x_{t+(m-1)})$, where 0 corresponds to the smallest element in $\overrightarrow{x(t)}$. To guarantee the uniqueness of order patterns, when $x_{t+i} = x_{t+j}, i < j$, we assume $s_i < s_j$, where

s_i is the rank of x_{t+i} in $\overrightarrow{x(t)}$. As a result, order patterns of $\{x_t\}_{t=1}^{N}$ are permutations of $\{0,1,...,m-1\}$,and the length of order patterns equals to the embedding dimension m with the number of well-defined order patterns in $\{x_t\}_{t=1}^{N}$ equalling $N-m+1$. An order pattern of $\{x_1=4,x_2=1,x_3=7,x_4=5\}$, with embedding dimension $m=4$ corresponds to the permutation (ordered sequence) $(1,0,3,2)$ since 7 is the largest number corresponding to the symbol 3 and 1 being the smallest element corresponding to the symbol 0.

C.2.1 Order patterns recurrence plot

Given a time series, an OPRP [156, 246] visualizes its order patterns (i.e. ordered sequences) and analyzes recurrent order structures via the following matrix

$$R_{i,j}(m)=\begin{cases}1,\pi_i=\pi_j\\ 0,\pi_i\neq\pi_j\end{cases}\quad i,j=1,2,...,N-m+1 \tag{C.1}$$

where π_i and π_j are the order patterns of the i^{th} and j^{th} element of $\{x_t\}_{t=1}^{N}$,respectively.

C.2.2 Forbidden ordinal patterns

Let $\Pi_m=\{\pi_{\xi_1},...,\pi_{\xi_n}\}$ be the set of order patterns that occur in $\{x_t\}_{t=1}^{N}$ with embedding dimension m and C_i be the frequency of $\pi_{\xi_i}\in\Pi_m$, then

$$\sum_{i=1}^{n}C_i=N-m+1 \tag{C.2}$$

where n is the number of order patterns that appear in $\{x_t\}_{t=1}^{N}$.

The maximal value of n is $m!$ when $N\geq m!+m-1$. This leads to all possible order patterns showing up and the number of forbidden ordinal patterns becoming zero. If the time series is long enough to allow every possible order pattern ($N\gg m!$) to show up, then the number of forbidden ordinal patterns (FOP) becomes

$$\text{FOP}=m!-n \tag{C.3}$$

with $n < m!$. The relative frequency (RF) of π_{ξ_i} is then provided by

$$\mathrm{RF}_{\pi_{\xi_i}} = \frac{C_i}{N-m+1} \tag{C.4}$$

The mean of relative frequencies (MRF) is then given by

$$\mathrm{MRF} = \sum_{i=1}^{n} \mathrm{RF}_{\pi_{\xi_i}}/n = \sum_{i=1}^{n} \frac{C_i}{n(N-m+1)} = \frac{1}{n} \tag{C.5}$$

Kulp and Zunino [210] observe that a few order patterns of the fractional Brown noise have high frequencies. This leads to a skewed frequency distribution. The median is a better indicator to look at the statistic property of the frequency distribution. The reason is in that the median can reduce the influence of outliers [147]. The median of relative frequencies (MDRF) can be expressed via

$$\mathrm{MDRF} = \mathrm{median}\{\mathrm{RF}_{\pi_{\xi_1}}, ..., \mathrm{RF}_{\pi_{\xi_n}}\} = \frac{\mathrm{median}\{C_1, ..., C_n\}}{N-m+1} \tag{C.6}$$

However, the MRF and the MDRF may variate in a small interval. This hinders visualizing a small variation in the MRF and the MDRF. We therefore take the negative value of the logarithm of the mean (mean^l) and the median (median^l) of all relative frequencies. This approach is consistent with that of Bandt and Pompe [20] for a calculation of the permutation entropy. Here, the mean^l and the median^l are expressed via

$$\mathrm{mean}^l = -\log \mathrm{MRF} = \log n \tag{C.7}$$

$$\mathrm{median}^l = -\log \mathrm{MDRF} = \log(N-m+1) - \log(\mathrm{median}\{C_1, ..., C_n\}). \tag{C.8}$$

Plugging Eq. C.3 into Eq. C.7 yields

$$\mathrm{mean}^l = \log(m! - \mathrm{FOP}). \tag{C.9}$$

where Eq. (C.9) describes the relationship between the mean^l and the FOP. A pseudo algorithm to calculate the mean^l and the median^l is provided in Algorithm C.1.

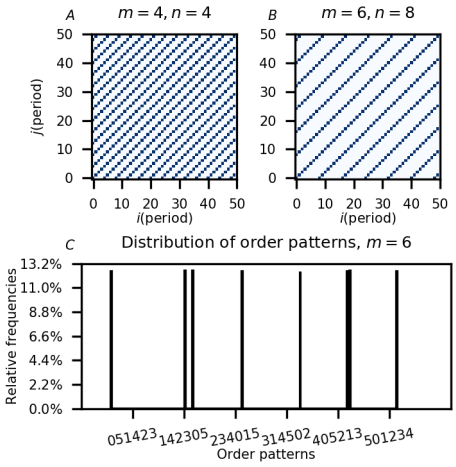

(A) OPRP of a periodic system

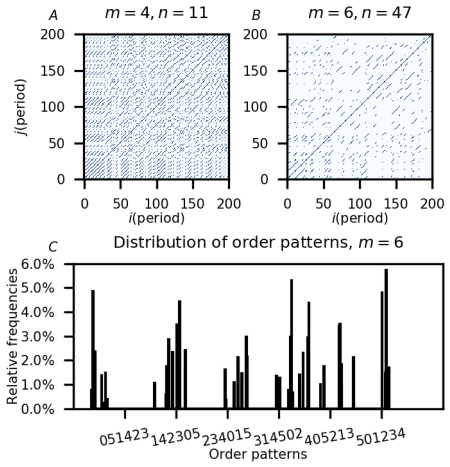

(B) OPRP of a chaotic system

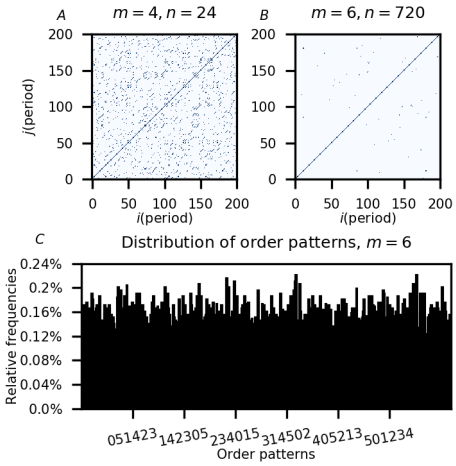

(C) OPRP of Gaussian noise

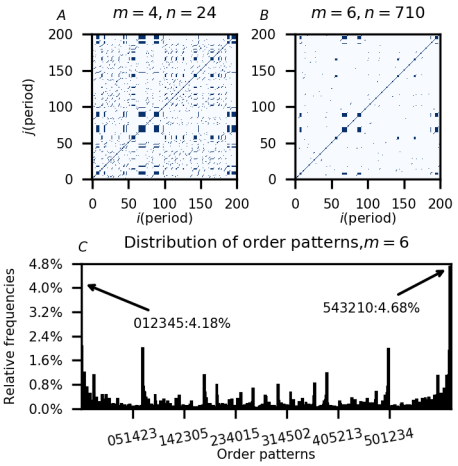

(D) OPRP of Brown noise

Figure C.1 : OPRPs as m increases.The embedding dimension m is 4 (A) and 6 (B). (C) is the distribution of order patterns. (1) and (2) logistic map $x_i = \alpha x_{i-1}(1-x_{i-1})$ for $\alpha = 3.55$ (periodic) and 3.91 (chaotic), respectively;(3) Gaussian noise (20,000 samples chosen from $\mathcal{N}(0,1)$); (4) Brown noise (20,000 samples chosen from power spectrum $S(f) = (1/f)^2$, with $f \sim \mathcal{N}(0,1)$ [371].)

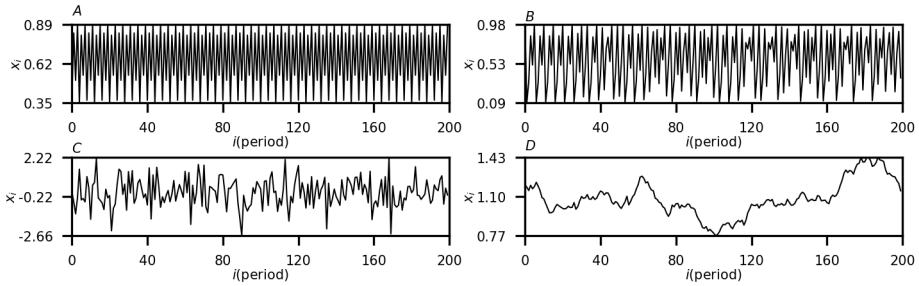

Figure C.2 : Time series. (1) and (2) logistic map (periodic,$r = 3.55$); and (chaotic,$r = 3.91$); (3) Gaussian noise of Fig C.1C; (4) Brown noise of Fig C.1D; parameters of noise as provided previously.

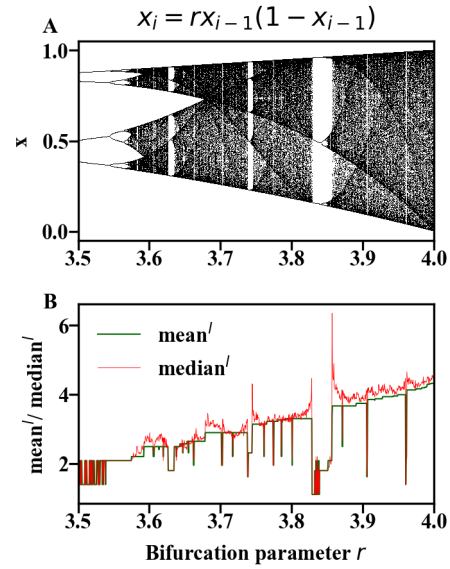

(A) Logistic map

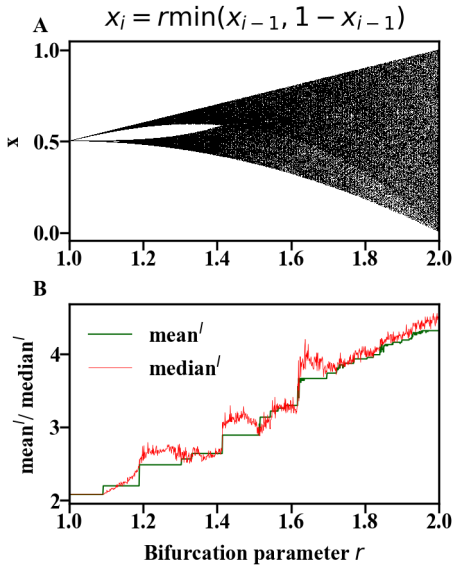

(B) Tent map

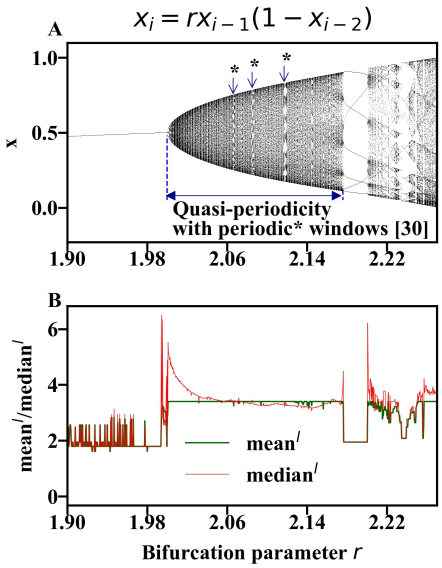

(C) Delayed logistic map

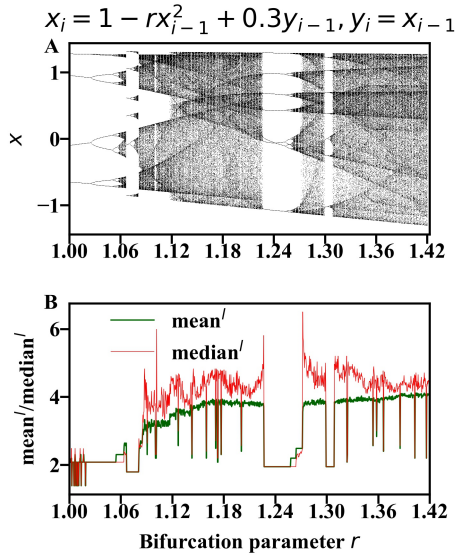

(D) x component of Hénon map

Figure C.3 : Bifurcation diagrams (A) and the evolution of the mean^l and the median^l (B). (1)-(4) correspond to logistic map, tent map, delayed logistic map and Hénon map, respectively.

Algorithm C.1: Calculation of the mean^l and the mean^l

procedure TIME SERIES TO SYMBOLIC SEQUENCES THROUGH THE BP METHOD
    if $i < N - m + 1$, where $N = 20,000, m = 6$.
    Order patter $\pi_j = (j_0, \cdot, j_5) \leftarrow \{x_i, \cdot, x_{i+5}\}$
    Record the frequency: $\pi_j : C_j$, where $j \leq n$.
procedure RELATIVE FREQUENCY OF EACH π_j
    Calculate the MRF and MDRF of each π_j according to Eq. C.5 and Eq. C.6.
procedure CALCULATE THE mean^l AND THE median^l
    Calculate the mean^l and the mean^l according to Eq. C.7 and Eq. C.8.

C.3 Results

C.3.1 Order patterns recurrence plot

For Gaussian noise (Fig C.1C), the increase of m makes the OPRP sparse. In Fig C.1C (A,B), we use Gaussian noise and see that the OPRP is denser for $m = 4$ than for $m = 6$. However, the OPRP of Brown noise (Fig C.1D) preserves many points indicating that the system has the order pattern of which the relative frequency is high. For the periodic or the chaotic system under study (Fig C.1A and Fig C.1B), the OPRPs show distinctly more diagonal lines than the cases of Gaussian or Brown noise. As highlighted by Rosso et al. [317], a minimal embedding dimension allows the occurrence of forbidden ordinal patterns and their exponential growth. An OPRP can then have an optimal embedding dimension that rules out Gaussian noise.

The reasons for a sparse OPRP in case of Gaussian noise are that no forbidden ordinal patterns exist [8] and that the relative frequencies of every order pattern is close [6]. Therefore as m increases (Fig C.1C(C)), the number of order patterns that occurs is up to $m!$, and thus the probability of an order pattern that recurs in a given time window is $\frac{1}{m!}$, which is low for large m, leading to a spare distribution of points in a given time window.

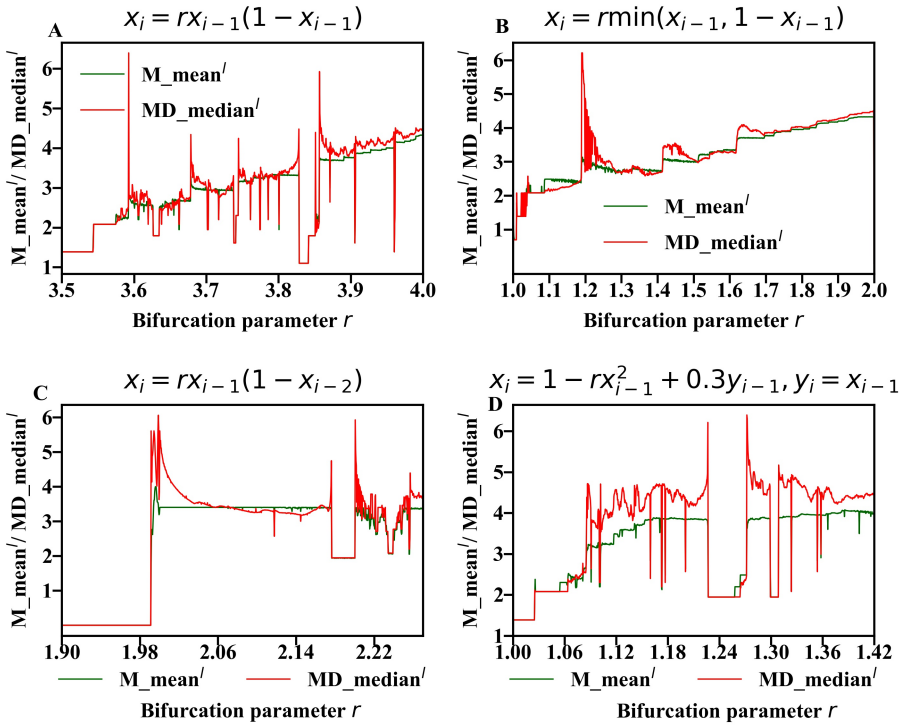

Figure C.4 : Analysis of the mean^l and the median^l as more initial conditions are considered. The M_mean^l represents the mean of the mean^l; the MD_median^l is the median of the median^l. The bifurcation diagram is plotted on a $1{,}000 \times 1{,}000$ grid with each point in the $x-$ axis having 1,000 samples of randomised conditions. (A) Logistic map; (B) tent map; (C) delayed logistic map; (D) Hénon map.

However, for Brown noise, in a given time window, the time series shows an upward (downward) tendency (Fig C.2(D)). As the upward (downward) tendency lasts for six time intervals, it forms the order pattern 012345 (543210). If the tendency lasts for over six time intervals, the order pattern does not change and forms a cluster in the OPRP (Fig C.1D(C)).

Due to the tendencies in the time series, Brown noise shows high relative frequencies (over 4%) of order patterns (012345 and 543210) (Fig C.1D(C)), compared with Gaussian noise (below 0.24%) (Fig C.1C(B)). As consistent with [316], Brown noise shows missing ordinal patterns ($n = 710 < 6! = 720$) (Fig C.1D(B-C)).

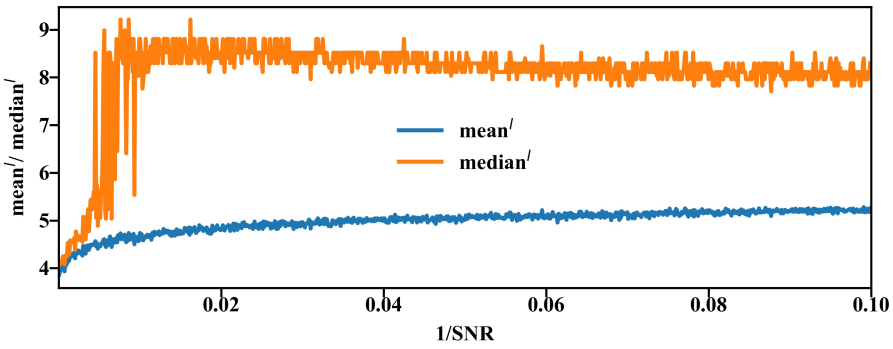

Figure C.5 : Influence of noise on the mean^l and the median^l of the logistic map as $r = 3.91$. SNR represents the signal-to-noise ratio. Here SNR=$\delta^2_{\text{signal}}/\delta^2_{\text{noise}}$, where $\delta^2_{\text{signal}} = 0.0926$. The noise is additive and follows $\mathcal{N}(0, \delta^2_{\text{noise}})$.

C.3.2 Bifurcation diagrams

Caballero-Pintado et al. [57] showed that RQA in the OPRP can detect changing dynamics. Now, we show how the mean^l and median^l unveil a change in dynamics and are able to uncover details in bifurcation diagrams. The embedding dimension is $m = 6$ in the following.

Fig C.3 shows that the change of the mean^l is like a staircase as bifurcation parameters change. That is, the number of forbidden ordinal patterns is robust to the change in dynamics. This result is complementary to the observation that forbidden ordinal patterns are robust to irregular sampling time [211].

From Fig C.3AB, Fig C.3BB, Fig C.3CB and Fig C.3DB, we find that the median^l quickly responds to a small change in the bifurcation parameter. As a result, the median^l is non-robust to a change in dynamics. In a periodic window, the median^l is close or equal to the mean^l. However, in a chaotic window, the median^l and the mean^l become more visible. Also, the median^l abruptly decreases to fit with the mean^l in a periodic point or a periodic window. In contrast, a sudden increase of the mean^l is found at points where the system switches between chaotic and periodic dynamics.

In a periodic window, the length of a time series may cause the number of some

order patterns to become slightly higher than the order patterns of the neighbouring regimes*. For the same length of the time series, as the periodicity increases, this difference becomes smaller. However, the difference may be visualized in a low periodic window such as the period-3 window. This is possible since a low periodicity leads to a high relative frequency for each order pattern. The unit difference of low periodicity induces a higher difference between the median^l and the median^l than that of a high periodicity (Fig C.3AB).

Whereas in a periodic window the order patterns are evenly distributed without consideration of the unit difference, in a chaotic window, the order patterns are not necessary evenly distributed [210]. An uneven distribution of order patterns can result in a difference of median^l and mean^l. Fig C.3A and Fig C.3B show that the mean^l changes step by step even in a chaotic region, contributing to the number n of order patterns which are robust against the change in dynamics. According to Eq. C.3, when n is robust, FOP is robust as well. Therefore, our results support that the number of forbidden ordinal patterns show some degree of robustness to the changes of dynamics since the mean^l is related to the number of forbidden ordinal patterns.

As shown by Sprott [345], for the delayed logistic map, it is diÿc ult to distinguish chaos from quasi-periodicity using a bifurcation diagram. However, fig C.3CB shows different structures of the change of the median^l and mean^l under the two kinds of dynamics. In the window of quasi-periodicity (see fig C.3CA), where the maximal Lyapunov exponent remain at zero [280, 345], the mean^l shows no evident variations, and the median^l has no abrupt changes. Also, different from periodic windows, the evolution of the median^l does not fit with that of the mean^l, showing a different quality in changes.

Next, we study the influence of randomized initial conditions on the mean^l and

*For example, in our numerical experiments, $N = 20,000, m = 6$, for the logistic map with $r = 3.55$, eight order patterns appear, so that the total amount of these eight order patterns is $N - m + 1 = 19,995$. However, $19,995$ cannot be divided by 8, so the count of some order patterns is $2,500$, that of the others is $2,499$, resulting in the difference of unity between the mean and the median of $\{C_1, \cdots, C_n\}$. This further shows the difference between the mean^l and the median^l according to Eq. C.7 and Eq. C.8.

the median^l as bifurcation parameters change. We implement the Algorithm C.1 using 1,000 randomised initial conditions for each r_i. For logistic map and tent map, initial conditions are chosen from U$(0,1)$; for the delayed logistic map, both the x_0 and x_1 are chosen from U$(0.4,0.8)$; for the Hénon map, both the x_0 and y_0 are chosen from U$(0,1)$. The mean^l and median^l are calculated in each sample. Then the $y-$axis records the mean of the mean^l or the median of the median^l. Fig C.4 shows the results. Fig C.4 (C) and fig C.3CB have the same phenomena in the almost quasi-periodic window: the mean^l is almost fixed.

The influence of noise on the two measures studying a noise contaminated regime of the logistic map is examined in Fig. C.5. Variations in the mean^l is less than those of the median^l. This result is consistent with the observation that the FOP is robust against Gaussian noise [6]. Since the mean$^l = \log(m! - FOP)$, a robust FOP leads to a more robust mean^l against Gaussian noise. However, the median^l shows persistent variations, which reflects the system is changing. Yet, whether this robustness will lead to similar prediction quality over a wide range of bifurcation parameters as shown for purely deterministic regimes and different or even different and varying SNRs will need to be studied in the future in more detail.

C.4 Conclusion

We have used the mean (mean^l) and the median (median^l) of the relative frequency of order patterns to characterize chaotic signals and stochastic signals. Although the mean and the median are common measurements in statistics, our definitions provide new measurements for order pattern recurrence plots to distinguish between chaotic signals and stochastic signals and to detect the change in dynamics in a purely chaotic signals. Here, the mean^l quantifies the number of forbidden order patterns (FOP, see Eq. C.9) for the first time.

Also, monitoring the embedding dimension can be used to qualify chaotic versus stochastic dynamics in an OPRP. An optimally embedded OPRP preserves diagonal

lines for a chaotic system, leads in the case of uncorrelated noise to thinly distributed isolated points and in the case of correlated noise to small clusters. However, whether this holds true for any system especially if noise contaminated systems are considered needs to be verified in the future.

While the mean^l is robust to changing bifurcation parameters, the median^l is sensitive to the change in the dynamics. Using the difference between the mean^l and the median^l and their fluctuations, we can distinguish chaos from quasi-periodic dynamics for the delayed logistic map.

The calculation of the median^l and the mean^l is easily accomplished and computationally inexpensive, which makes the median^l and the mean^l a cost effective analysis tool to tell deterministic signals from stochastic signals.

Further, the mean^l shows the robustness to Gaussian noise. However, the median^l is not robust to Gaussian noise. Since the relative frequencies of each order pattern of Gaussian noise are close in value to each other, the mean^l and the median^l of deterministic signals being buried in Gaussian noise, would likely to be different from that of pure noise.

From a practical viewpoint, especially low-dimensional deterministic signals are often contaminated by high-dimensional processes (noise); yet only the lower dimensional scales are often of interest. Cleaning these signals by employing dynamics-preserving nonlinear (geometric) filters as conducted by Oberst et al. [283, 284] could expand utilizing the measures, which are suggested here to real-life data problems. Especially studying border-collision/grazing bifurcations the measures could potentially assist in detecting of tipping points in bifurcation diagrams of maps and flows related to discontinuous dynamics, cf. [175, 272].